UNIVERSITÉ LAVAL

Integrated Bragg Gratings in silicon-on-insulator

Thèse

Alexandre D. Simard

Doctorat en Génie Électrique
Philosophiæ Doctor (Ph. D.)

Québec, Canada

Résumé

Dans la littérature, les réseaux de Bragg intégrés sur silicium sont relativement simples par rapport à leurs contreparties fibrées. Cependant, la fabrication de réseaux plus élaborés permettrait d’améliorer la capacité de traitement du signal des circuits sur silicium. Cette thèse s’attarde donc aux difficultés encourues lors de la conception, de la fabrication et de la caractérisation de réseaux de Bragg sur silicium ayant une réponse spectrale élaborée.

Tout d'abord, afin de caractériser la réponse spectrale complexe des réseaux, l’utilisation de filtrage temporel est proposée afin de supprimer les réflexions parasites. Cela a permis d’utiliser des algorithmes de reconstruction fournissant une caractérisation complète de ces structures. De plus, l’ajout d’un filtrage des hautes fréquences spatiales a permis de réduire considérablement le bruit des mesures.

Par la suite, les principales sources de distorsions de la réponse spectrale des réseaux ont été identifiées, soit la rugosité des guides et la variation de leur épaisseur. L’impact de ces phénomènes a été étudié numériquement et analytiquement et, pour la première fois, la longueur de corrélation de ces sources de bruit a été caractérisée expérimentalement sur une longueur suffisante. Finalement, deux techniques permettant de diminuer l’impact de ces phénomènes ont été proposées, ce qui a permis de fabriquer les réseaux de Bragg sur silicium ayant la plus petite largeur de bande publiée à ce jour.

Également, nous avons fait les premières démonstrations d’apodisation de réseaux de Bragg utilisant uniquement la phase de ces derniers (c.-à-d. apodisation en phase et par superposition). Contrairement aux techniques déjà proposées, ces dernières ont l'avantage de ne pas introduire de distorsions de l'indice effectif, ils sont plus robuste aux erreurs de fabrication et sont compatibles avec l’apodisation de réseaux à corrugations de très petites amplitudes.

Finalement, afin d'augmenter la longueur des réseaux tout en gardant leur dimension compatible avec la taille des puces de silicium, les réseaux ont été courbés en forme de spirale compacte. Pour ce faire, la période des réseaux a été modifiée afin de compenser l'effet de la courbure sur l'indice effectif. Ainsi, nous avons démontré que des réseaux de 2 mm de long

pouvaient être intégrés sur une surface de 200 µm x 190 µm sans ajout de dégradation spectrale et, surtout, sans restriction sur la structure du design.

Ces résultats sont significatifs, car un contrôle précis de la phase et de l’amplitude des réseaux combinés avec la capacité de fabriquer de réseaux longs sont nécessaire afin de réaliser des filtres optiques intégrés avec des réponses spectrales élaborées. Ainsi, le travail présenté dans cette thèse ouvre la porte à de nouveaux designs à base de réseaux de Bragg.

Abstract

In the literature, integrated Bragg gratings in Silicon-on-Insulator are relatively simple compared to their fibre Bragg grating counterpart. However, elaborate gratings could improve the signal processing capability of the silicon platform. Thus, this thesis addresses the issues that prevent the design, the fabrication and the characterization of Bragg gratings having elaborate spectral response in the silicon platform.

Firstly, in order to precisely characterize Bragg gratings complex spectral response, we proposed to suppress parasitic reflections using temporal filtering. The results obtained with measurement technique, when used with an integral layer peeling algorithm, allowed us to retrieve the amplitude and phase profiles of the grating thus providing a complete characterization of the structure. Moreover, the addition of a low-pass spatial filter allowed improving the characterization process by reducing the measurement noise.

Secondly, the main sources of distortion of Bragg gratings spectral response have been identified to be the sidewall roughness and the wafer height fluctuation. An exhaustive study of the impact of these phenomena has been done both numerically and analytically. Furthermore, for the first time, the autocorrelation of these noise sources has been characterized experimentally on a sufficient length. Finally, improvements in the waveguide designs have reduced significantly these effects which allowed the fabrication of Bragg gratings in silicon with the smallest bandwidth published to date.

Thirdly, the first demonstration of apodized Bragg gratings using only phase modulation of the structure has been done (i.e. phase apodisation and superposition apodisation). Unlike already published techniques, the later ones have the advantage to be robust to deep-UV lithography and fabrication errors. Furthermore, they do no introduce distortions into the grating phase profile and they are compatible with gratings having small recesses.

Finally, in order to increase the grating length while keeping their dimension compatible with the silicon chip size, we proposed to bend them in a compact spiral shape. To do this properly, the curvature impact on the effective index has been modeled and compensated successfully by modifying the grating period. Thus, we have shown that 2 mm long gratings can be integrated on

a surface of 200 µm x 190 µm without the addition of spectral degradation and without restrictions on the design structure.

These results are of importance because longer grating structures with weaker coupling coefficients and a precise control both on its phase and amplitude are required in order to achieve integrated optical filters with elaborate spectral responses. Thus, we believe that the work presented in this thesis open the door to many new grating-based optical filter designs compatible with integrated optics technologies.

Contents

Résumé ... **iii**

Abstract ... **v**

Contents ... **vii**

List of Tables ... **ix**

List of Figures ... **xi**

List of Symbols ... **xvii**

List of Acronyms ... **xxi**

Remerciements ... **xxiii**

Preface ... **xxix**

Introduction ... **1**

Chapter 1: Bragg Gratings ... **9**

1.1 – Integrated Bragg gratings ... 9

1.2 – Fabricated gratings ... 13

1.3 – Bragg grating coupled equations ... 17

1.4 – Numerical simulations of Bragg grating response ... 22

1.5 – Grating reconstruction ... 25

1.6 – Elaborate grating structures ... 27

1.7 – Characterization of integrated Bragg gratings ... 32

Chapter 2: Impact of Sidewall Roughness on Integrated Bragg Gratings ... **37**

2.1 – Abstract ... 37

2.2 – Introduction ... 38

2.3 – Sidewall roughness model ... 39

2.4 – Sidewall roughness model for IBG analysis ... 41

2.5 – Emulator ... 42

2.6 – Numerical analysis ... 48

2.7 – Weak grating analysis ... 53

2.8 – Discussion ... 62

2.9 – Conclusion ... 62

2.10 – Supplementary information ... 63

Chapter 3: Characterization and Reduction of Spectral Distortion in Silicon-on-Insulator Integrated Bragg Grating ... **67**

3.1 – Abstract ... 67

3.2 – Introduction ... 68

3.3 – Phase-noise model 70
3.4 – Phase-noise characterization 73
3.5 – Phase-noise reduction techniques 85
3.6 – Conclusion 90
3.7 – Supplementary information 91
Chapter 4: Apodized Silicon-on-Insulator Bragg Gratings........ 99
4.1 – Abstract 99
4.2 – Introduction........ 100
4.3 – Design and post processing 101
4.4 – Superposition-apodized Bragg gratings 102
4.5 – Phase-apodized Bragg gratings 103
4.6 – Discussion 105
4.7 – Conclusion 106
4.8 – Supplementary information 107
Chapter 5: Integrated Bragg Gratings in Spiral Waveguides 109
5.1 – Abstract 109
5.2 – Introduction........ 109
5.3 – Waveguide and grating design 111
5.4 – Grating characterization........ 118
5.5 – Experimental results and discussion 119
5.6 – Conclusion 125
Conclusion........ 127
References 131
Appendix A: Coupled-Mode Equation Derivation........ 141
A.1 – Simplification of Maxwell equations........ 141
A.2 – Excitation of modes........ 142
A.3 – Calculation of the polarisation 145
A.4 – General coupled-mode equations 146
Appendix B: Sidewall Roughness Modeling........ 149
B.1 – Detuning distribution autocorelation 149
B.2 – Derivation of O(4)........ 150

List of Tables

Table 1: Characteristics of the grating from now on named “Straight Grating #1” 16
Table 2: Characteristics of the grating from now on named “Straight Grating #2” 16
Table 3: Characteristics of the grating from now on named “Spiral Grating #3” 17
Table 4: The inputs describe the phase noise characteristic used for the emulations presented in section 2.6 while the outputs is final standard deviation of the Bragg wavelength used in these simulations and the waveguide width that has the same emulation results considering the phase noise parameter measured in this chapter 94
Table 5: Spectral measurement of IBG samples 106

List of Figures

Fig. 1: Type of structural modification used to fabricate IBG : a) top IBG [38], b) lateral IBG [39], c) pillar IBG [40]. 10

Fig. 2: Typical singlemode a) photonic wire, b) ridge waveguide with a thin slab and c) ridge waveguide with a thick slab cross-section. 11

Fig. 3: a) Variation of the fabricated waveguides width (or line width) as a function of exposure dose [52] and the designed waveguide line width. b) Sensitivity of the effective index of the TE_0 mode to photonic wire width at 1550 nm. The height of the wire is 220 nm. The gray region depicts the cutoff region [53]. 13

Fig. 4: 3D view and top-view of the schematic of the third order 2 mm-long IBGs used in this thesis 15

Fig. 5: Schematic of the ILP algorithm 26

Fig. 6: a) Simulated reflection spectrum b) dispersion, c) Bragg wavelength profile and d) coupling coefficient profile of a uniform Bragg grating (in black) and a gaussian apodized grating (in red). The gratings length is respectively 80 µm and 105 µm. 28

Fig. 7: a) Simulated reflection spectrum b) dispersion, c) Bragg wavelength profile and d) coupling coefficient profile of a gaussian apodized grating (in red) and a tailored dispersion-less flattop Bragg grating (in blue). The gratings length is respectively 105 µm and 1600 µm. 29

Fig. 8: a) Simulated reflection spectrum b) dispersion, c) Bragg wavelength profile and d) coupling coefficient profile of the same tailored dispersion-less flattop Bragg grating cut at different distance from the main coupling coefficient lobe. The length of the grating in blue is 1600 µm while the grating in cyan and red are respectively 950 µm and 600 µm. 30

Fig. 9: a) Simulated reflection spectrum b) dispersion, c) Bragg wavelength profile and d) coupling coefficient profile of tailored square-shape-zero-dispersion Bragg grating for coarse (in blue) and dense (in cyan) WDM application. The gratings length is respectively 1600 µm and 12 000 µm. 31

Fig. 10: a) Amplitude of the impulse response as a function of propagation distance in the device. b) Reflection spectrum without time-filtering (black) and with the section C time-filtered (red) 34

Fig. 11: a) Comparison of the experimental reflection spectrum of an unapodized grating (red) to the reconstructed spectrum without spatial filtering (black), with Δλ = 3 nm (green) and Δλ = 1.5 nm (blue). The retrieved b) λ_B and c) Δn profiles associated to the spectrum of a) 36

Fig. 12: Waveguide geometry. 40

Fig. 13: SWR spectral power density as a function of spatial frequencies for different values of autocorrelation length. 40

Fig. 14: Comparison of an IBGs simulated without using the low-pass filtering approach (in blue) and with a low-pass filter having a cut-off frequency defined by equation (2.10) (in red). The bandwidth of interest is a) $2\Delta\lambda$ = 10 nm (f_c = 1.8x10^4 m^{-1}) and b) $2\Delta\lambda$ =20 nm (f_c = 3.6x10^4 m^{-1}). 45

Fig. 15: Numerical simulations of chirped IBG with σ_{SWR} and $L_{c,\ SWR}$ of, respectively a) 4 nm and 300 nm, b) 4 nm and 30 nm c) 2 nm and 300 nm, and d) 2 nm and 30 nm. 46

Fig. 16: Comparison of 2.8 mm experimental (red), emulated (blue) and unperturbed (black) a) weak uniform gratings, b) strong uniform gratings, and c) chirped gratings. 48

Fig. 17: Distribution of a) the SLSR and b) of the central wavelength of uniform IBGs having σ_{SWR} =4 nm and $L_{c,SWR}$ =300 nm. The dotted red lines represent the results of an ideal uniform grating. The solid black line of a) is a smoothed curve of the simulated data while on b) it is a Gaussian fit. 50

Fig. 18: Probability density function of a) the SLSR and b) of central wavelength of uniform IBGs having different SWR parameters. The numbers in a) are the average SLSR values. 51

Fig. 19: Probability density function of a) the SLSR and of b) the central wavelength of IBGS with Gaussian apodization and different SWR parameters. The numbers above the curves of a) are the average SLSR values. The dotted red line is the ideal SLSR, the dotted green line is the SLSR of the ideal unapodized grating having the same length and $\int\kappa(z)dz$ while the dotted blue line is the SLSR of the ideal unapodized grating having the same length and same maximum κ value. 52

Fig. 20: Calculated spectral response of uniform gratings with κL=2.8 and various phase noise parameters. The blue curves show the averaged spectrum of 1000 gratings. The black curves delimit the insertion loss values that enclose 90 % of the simulated spectra while the red curves are typical spectra. 54

Fig. 21: Calculated spectral response of apodized gratings with $\int\kappa(z)dz$=1.3 and various phase noise parameters. The blue curves are the calculated averaged spectrum of 1000 gratings. The black curves delimit the insertion loss values that enclose 90 % of the simulated spectra while the red curves are typical spectra. 54

Fig. 22: Comparison between analytical analysis (black) of the mean spectrum of uniform grating with SWR (Eqs. (2.13) and (2.15)) and the average of 1000 spectrum numerically simulated (blue). The red curves are the unperturbed spectral responses. a) → b) shows the impact of increasing L, b) → c) shows the impact of increasing $L_{c,SWR}$, c) → d) shows the impact of increasing σ_{SWR}, c) → e) shows the impact of increasing κL 57

Fig. 23: Comparison of R_n of three gratings having the same κL but different lengths. 58

Fig. 24: Comparison of R_n of three gratings having the same length but different κL. 59

Fig. 25: Comparison between analytical analysis (black) of the standard deviation of uniform grating with SWR and the standard deviation of 1000 spectrum numerically simulated (blue). The noise and grating parameters correspond to the parameters of Fig. 22-a), b) and e). 60

Fig. 26: The blue curve shows the theoretical mean spectrum of a 1 mm long grating having a κL = 0.8, L_c = 20 nm and σ, $_{SWR}$ = 4 nm while the black curves delimit the reflection values that enclose ~70 % of the spectra while the red curve is a typical simulated spectrum. 61
Fig. 27: Spectral response of a 700 periods uniform grating simulated by a FDTD simulator and by a matrix solution of the coupled mode equations. This figure also shows the spectrum of similar gratings but with high frequency modulation. 64
Fig. 28: Typical top-down SEM image of a photonic wire 75
Fig. 29: Typical intensity profile of a pixel column (taken at the position of the red line in Fig. 28. 75
Fig. 30: Typical top-down SEM image converted into a binary image with the threshold shown by the black line in Fig. 29. The red lines are the outer waveguide sidewalls. 76
Fig. 31: Typical superposition of the waveguide width fluctuation from every image of a set of measurement. The thick blue line is the linear regression of the average waveguide width fluctuation per pixel (black curve). 78
Fig. 32: Waveguide width fluctuation obtained from top-down SEM taken at the same location with different working distance. 79
Fig. 33: Dependency of the average waveguide width caused by a variation of the working distance. 80
Fig. 34: Typical overlap of the waveguide width fluctuation between three consecutive images (red, blue and green). The black curve is the averaged waveguide width as a function of position. 81
Fig. 35: Typical waveguide width fluctuation profile as a function of position. The black line is the raw data while the blue line is a filtered version of the waveguide width profile. 81
Fig. 36: Autocorrelation function of the waveguide width fluctuation of the filtered (blue) and unfiltered (black) curve of Fig. 35. The red curve is the decaying exponential autocorrelation fit. 82
Fig. 37: Probability density functions of the SWR. The red curve is a Gaussian function. 83
Fig. 38: a) Comparison of the experimental reflection spectrum of a typical straight grating on a 1200 nm wide waveguide (in red) with the reconstructed reflection spectrum (in black). Retrieved b) λ_B and c) Δn profiles, which are used to calculate the black curve of a). 85
Fig. 39: Bragg wavelength standard deviation as a function of the waveguide width. The black curve contains both the impact of the SWR and the WHFs, while the blue and red curve takes those to effect independently. The cyan lines are the optical measurement of 2 mm-long IBGs while the purple line is the optical measurement for spiral IBGs. 86
Fig. 40: Schematic of spiral IBGs 88
Fig. 41: Typical spectral response of 2 mm-long a) straight grating on a 800 nm wide waveguide, b) straight grating on a 1200 nm wide waveguide and c) spiral grating on a 1200 nm wide waveguide. The blue curves are the designs while the black curves are the experimental results. 89

Fig. 42: Superposition of every Bragg wavelength fluctuation measurements for a) 800 nm straight waveguide, b) 1200 nm straight waveguide and c) 1200 nm spiral waveguide. 90

Fig. 43: α_{Lc} is plotted in blue as a function of N_{Lc}. The red curve is a smoothed version of the blue markers while the black line is highlighting the N_{Lc} value used in this chapter and the green lines highlight the minimal N_{Lc} value suggested in [112]–[114]. 92

Fig. 44: Bragg wavelength standard deviation as a function of the waveguide width. The black curve contains both the impact of the SWR and the WHFs (already presented in Fig. 39) while the red curve presents the same result but with a larger $L_{c,SWR}$ (to consider a possible underestimation of the parameter due to the window size). The cyan lines are the optical measurement of 2 mm-long IBGs while the purple line is the optical measurement for spiral IBGs (already presented in Fig. 39). 93

Fig. 45: The black line is an example of the shape of the corrugations of an IBG mask layout, the red lines shows a possible fabricated sidewall of an IBG while the arrows illustrate the position shifts of the sidewall that can happens after fabrication. 95

Fig. 46: a) Exponential decaying autocorrelation function (in red) and a linear fit (in black) and b) the associate power density function. The vertical dotted lines are the frequency content relevant for IBGs spectral response 96

Fig. 47: Experimental autocorrelation function of the data presented in this paper but where the SEM images are analysed independently (without the picture alignment procedure). The thick black curve is the exponential fit having a 42.2 nm autocorrelation length. 97

Fig. 48: a) Comparison of the experimental reflection spectrum of an unapodized grating (in red) with the reconstructed reflection spectrum (in black) and the designed spectrum (in blue). Retrieved b) λ_B and c) Δn profiles, which are used to calculate the black curve of a). 101

Fig. 49: a) Comparison of the experimental reflection spectrum of the superposition-apodized grating #1 (in red) with the reconstructed spectrum (in black) and the designed spectrum (in blue). Retrieved b) λ_B and c) Δn profiles, which are used to simulate the black curve of a). The blue curve in c) is the target apodization profile. 103

Fig. 50: a) Comparison of the experimental reflection spectrum of the phase-apodized grating #1 (in red) with the reconstructed spectrum (in black) and the designed spectrum (in blue). Retrieved b) λ_B and c) Δn profiles which are used to simulate the black curve of a), blue curve is the target apodization. 104

Fig. 51: a) Comparison of the experimental reflection spectrum of the superposition-apodized grating #1 (in red) with the reconstructed spectrum (in black) and the designed spectrum (in blue). Retrieved b) λ_B and c) Δn profiles, which are used to simulate the black curve of a). The blue curve in c) is the target apodization profile. This figure is a reproduction of Fig. 49 on which the simulated spectrum of the reconstructed apodization profile with an ideal Bragg wavelength profile is added in green. 107

Fig. 52: a) Comparison of the experimental reflection spectrum of the phase-apodized grating #1 (in red) with the reconstructed spectrum (in black) and the designed spectrum (in blue). Retrieved b) λ_B and c) Δn profiles which are used to simulate the black curve of a), blue curve is the target apodization. This figure is a reproduction of Fig. 50 on which the simulated spectrum of the reconstructed apodization profile with an ideal Bragg wavelength profile is added in green. 108

Fig. 53: Three different schematic of spiral gratings having α values of 0.3355, 0.671 and 1.0065 (red, black and blue curve respectively). The red dots represents the position where Δx_s becomes negligible.......... 112

Fig. 54: a) CAD mask of the spiral IBGs used in this chapter (α value of 0.671); b) Optical microscope image of the first spiral-IBG row. 113

Fig. 55: a) Radius of curvature of the spirals shown in Fig. 53. 115

Fig. 56: Variation of the effective index of a 1200 nm x 220 nm silicon waveguide with top-oxyde as function of its radius of curvature. 116

Fig. 57: Phase function that must be incorporated in the grating structure to compensate the effective index variation caused by the curvature of the spirals shown in Fig. 53. 117

Fig. 58: The grating period of the spiral shown in Fig. 53. The black line is the uncorrected grating period.......... 117

Fig. 59: a) Comparison of the experimental reflection spectrum of an uncompensated spiral IBG (in red) with the reconstructed reflection spectrum (in black) and the designed uniform grating response (blue curve). Retrieved b) λ_B and c) Δn profiles, which are used to calculate the black curve of a). 119

Fig. 60: a) Comparison of the experimental reflection spectrum of a phase compensated spiral IBG (in red) with the reconstructed reflection spectrum (in black) and the designed uniform grating response (blue curve). Retrieved b) λ_B and c) Δn profiles, which are used to calculate the black curve of a). 120

Fig. 61: a) Interleaved spiral having R_0 = 59 µm, Δw_s = 15 µm and α = 0.671 and a minimal radius of curvature of 20 µm for the blue and red waveguides and 25 µm for the black (central) waveguide. b) Radius of curvature of a typical interleaved spiral as function of the position on the spiral waveguide. c) Phase function that must be incorporated in the grating structure to compensate the effective index variation caused by the curvature 121

Fig. 62: a) Comparison of the experimental reflection spectrum of a compensated interleaved spiral IBG (in red) with the reconstructed reflection spectrum (in black) and the designed uniform grating response (blue curve). Retrieved b) λ_B and c) Δn profiles, which are used to calculate the black curve of a). 122

Fig. 63: a) Comparison of the experimental reflection spectrum of a compensated Gaussian-apodized CBG (in red) with the reconstructed reflection spectrum (in black). The blue curve is the spectrum obtained with the ideal Gaussian apodization profile shown in c) and an ideal Bragg wavelength while the green curve is the spectrum calculated with the noisy apodization profile but without phase noise (ideal Bragg wavelength). Retrieved b) λ_B and c) Δn profiles, which are used to calculate the black curve of a). 124

List of Symbols

This section contains the list of symbols used in this thesis. Even if they are listed by chapters, corresponding to the chapter of their first appearance, their definition is valid throughout the thesis.

Chapter 1: Bragg gratings

Symbol	Definition
w_0	Waveguide average width
Δw	Grating recess amplitude
Λ_p	Grating physical period
z	Axis of propagation
A and B	Amplitude of the forward and backward propagating modes
$\mathrm{K}_{\mu\nu}^{z}$ and $\mathrm{K}_{\mu\nu}^{z}$	Tangential and longitudinal coupling coefficient between mode μ and ν
β	Propagation constant
x	Cross-section axis of the waveguide (tangential to the wafer surface)
y	Cross-section axis of the waveguide (normal to the wafer surface)
c	Speed of light in vacuum
$n(\lambda)$	Effective index of the TE-like mode
λ	Free-space wavelength
ε	Permittivity
$\Delta\varepsilon$	Deviation of the permittivity from the nominal distribution
κ	Bragg grating coupling coefficient
G	Grating phase
Λ	First order grating period having a resonance near the C-band
m'	Grating order
Δn	Grating effective index perturbation having a resonance near the C-band
θ	Bragg grating phase variation
n_i	Coefficients of the truncated Taylor series modeling the effective index
λ_0	Reference wavelength of the truncated Taylor series modeling the effective index
n_g	Group index

δ	Bragg grating detuning
δ_0	Designed Bragg grating detuning
u and v	Slowly varying amplitude of the forward and backward waves
Δn_z	z-varying component of the effective index
Φ	Phase term that takes into account all the z-varying parameter of the gratings
λ_B	Grating Bragg wavelength
L	Grating length
r and t	Grating complex spectral response in reflection and transmission
h	Grating impulse response in reflection
f_c	Cut-off spatial frequency of the low-pass filter
$\Delta\lambda$	Measurable spectrum width (taken at the noise floor)
$\overline{\lambda}_B$	Average Bragg wavelength

Chapter 2: Impact of Sidewall Roughness on Integrated Bragg Gratings

Symbol	**Definition**
$G_{\Delta x}$	Sidewall roughness spectral density function
$R_{\Delta x}$	Sidewall roughness autocorrelation function
Δx	Deviation of the sidewall from its average position
Δz	Spatial shift along the waveguide propagation axis
σ_{SWR}	Waveguide sidewall roughness standard deviation
$L_{c,SWR}$	Waveguide sidewall roughness autocorrelation length
f_z	Spatial frequency (along the z-axis)
Δw_z	Waveguide width variation related to sidewall roughness
C_{SWR}	Effective index variation associate to a waveguide width variation
σ_n	Effective index standard deviation
$\Delta\delta_z$	Waveguide detuning variation related to sidewall roughness
σ_δ	Detuning standard deviation
ϕ	Phase modulation amplitude
δ_d	Designed detuning factor
$\delta_j(z)$	Detuning distribution
R_n	Noise contribution to the grating spectral response
R_{δ_j}	Autocorrelation function of the detuning distribution

σ_R^2 / σ_R	Spectral response variance / standard deviation

Chapter 3: Characterization & Reduction of Integrated Bragg Grating Spectral Distortion

Symbol	**Definition**
Δy	Deviation of the wafer height from its average position
σ_{WHF}	Wafer height fluctuation standard deviation
$L_{c,WHF}$	Wafer height fluctuation autocorrelation length
C_{WHF}	Effective index variation associate to a waveguide thickness variation
$\tilde{\sigma}_{SWR}$	Filtered sidewall roughness standard deviation (portion relevant to IBGs)
$\tilde{\sigma}_{WHF}$	Filtered wafer height fluctuation standard deviation (portion relevant to IBGs)
$\tilde{\sigma}_{\lambda_B}$	Filtered Bragg wavelength deviation (portion relevant to IBGs)
$\tilde{\sigma}_n$	Filtered effective index standard deviation (portion relevant to IBGs)
N_{Lc}	Ratio of the measurement length and the measured autocorrelation length
α_{Lc}	Ratio between the calculated autocorrelation length and the generated autocorrelation length

Chapter 4: Apodized Silicon-on-Insulator Bragg Gratings

Symbol	**Definition**
$F_i(z)$	Phase functions used to achieve a superposition apodisation
Λ_m	Phase modulation period
ϕ	Phase modulation amplitude
$f(z)$	Target apodization profile

Chapter 5: Integrated Bragg Gratings in Spiral Waveguides

Symbol	**Definition**
S	Spiral path in the complex domain
Δx_s	Shift of the center of rotation on the real axis in the (complex) domain where the spiral is defined (not to confuse with Δx chapter 2)
P	Angle of rotation
$R(\rho)$	Local radius of curvature (when $\Delta x_s \rightarrow 0$)
R_0	Minimal value of the radius of curvature (when $\Delta x_s \rightarrow 0$)
Δw_s	Spacing between two consecutive waveguides in the spiral (not to confuse with Δw and Δw_z defined in chapter 1)
A	This parameter controls the rate of change of the center of rotation as function of ρ
$R(z)$	Radius of curvature as a function of the position on the spiral path

$\vec{N}$	Local unitary normal vector of S
$\delta n(R)$	Effective index perturbation caused by a curvature
$\Omega(z)$	Phase term added to the grating to compensate for the effective index distortion $\delta n(R(z))$

List of Acronyms

This section contains the list of acronyms used in this thesis. Even if they are listed by chapters, corresponding to the chapter of their first appearance, their definition is valid throughout the thesis.

Introduction

Acronyms	Definition
PIC	Photonic Integrated Circuit
WDM	Wavelength Division Multiplexing
AWG	Arrayed-Waveguide Gratings
SOI	Silicon-On-Insulator
CMOS	Complementary Metal-Oxyde Semiconductor
DUV	Deep Ultra-Violet
DC	Data-Center
FBG	Fiber Bragg Grating
MMI	Multimode interferometer
MZI	Mach-Zehnder Interferometers
IBG	Integrated Bragg Grating

Chapter 1: Bragg gratings

Acronyms	Definition
SWR	SideWalls Roughness
SEM	Scanning Electron Microscope
ILP	Integral Layer Peeling
OFDR	Optical Frequency Domain Reflectometer
SLSR	Side-Lobe Suppression Ratio
TE-mode	Transverse Electric mode

Chapter 2: Impact of Sidewall Roughness on Integrated Bragg Gratings

Acronyms	Definition
WHF	Wafer Height Fluctuation

FDTD	Finite Difference Time Domain

Chapter 3: Characterization & Reduction of Integrated Bragg Grating Spectral Distortion

Acronyms	**Definition**
FOV	Field-Of-View
AFM	Atomic Force Microscope

Chapter 5: Integrated Bragg Gratings in Spiral Waveguides

Acronyms	**Definition**
ESW	Equivalent Straight Waveguide
CAD	Computer-Aided Design

Remerciements

Je tiens à profiter de cette section pour exprimer ma reconnaissance à tous ceux qui ont rendu la réalisation de ce travail possible d'une façon ou d'une autre.

En tout premier lieu, je tiens tout d'abord à remercier ma directrice de recherche, Sophie. Je la remercie de m'avoir accueilli dans son groupe de recherche, d'avoir dirigé ce travail et de m'avoir donné ma première chance (et plusieurs autres par la suite). Sa disponibilité, son support, ses encouragements et ses conseils furent indispensables afin de traverser les obstacles inhérents à la recherche. J'ai énormément appris à son contact et j'ai fortement apprécié travailler avec elle durant toutes ces années (je récidive donc avec plaisir). Je remercie également mon co-directeur, Yves, d'avoir été disponible tout au long de ce travail. Ses judicieux conseils et suggestions ont considérablement haussé la qualité de ce travail. À vous deux, votre esprit critique, votre professionnalisme et vos connaissances du domaine ont fortement forgé le chercheur que je suis en train de devenir.

Je voudrais aussi remercier mes collègues qui ont fortement contribué à la réalisation des travaux présentés dans ce document. Tout d'abord, j'aimerais souligner mes collègues du groupe de photonique sur silicium, c'est-à-dire Nicolas, Kéven et Nezih. Nicolas, qui m'accompagne depuis le début, fut d'une grande aide à plusieurs niveaux, que ce soit pour la programmation, la prise de mesures ou d'un point de vue personnel. Merci beaucoup. Je remercie (et je m'excuse auprès de) Kéven pour la caractérisation exhaustive des chips de réseaux courbées. Également, je remercie Nezih pour les simulations de guides courbées qu'il a faites.

D'un point de vue technique, je tiens à remercier Serge et Philippe. Le premier contribua grandement à l'élaboration du premier montage d'injection optique et le second l'améliora un gazillion de fois. D'ailleurs, Philippe représente une des forces du COPL, c'est-à-dire la présence de personnels techniques extrêmement compétents. Son aide, lors des expériences, fut significative et facilita grandement ces travaux qui furent généralement ardus. Chul Soo, en tant que superviseur de laboratoire, fut également une ressource très importante lorsque venait le temps de travailler au deuxième sous-sol. Mentionnons également Hugues pour son aide lors de la caractérisation de guides en silicium à l'AFM et Stéphane, Daniel et Guillaume pour leurs efforts lors de la caractérisation de ces mêmes guides au SEM. Une mention particulière à

Guillaume, de l'Université de Sherbrooke, qui a pris plusieurs milliers d'images SEM pour la réalisation du travail sur la caractérisation de la rugosité. Merci beaucoup pour ce travail de longue haleine.

Également, je désire remercier Wing Chau, qui fut une aide précieuse pour les derniers miles de l'analyse théorique de l'impact du bruit de phase sur les réseaux de Bragg intégrés. Je remercie également tous mes collègues des groupes de Sophie et de Leslie. L'ambiance de recherche créée par ces collègues fut très stimulante. Mentionnons particulièrement Mehrdad, Yousra, David, Léonard, Cang, An, Bora, Li Xian, Ramtin … Finalement, j'aimerais remercier Benoit pour deux raisons. D'une part, je le remercie simplement parce qu'il apprécie se faire remercier (ça fait plaisir) et d'autre part, parce qu'il fut d'un grand support scientifique (pour la modélisation des milieux de gain en semi-conducteur) et personnel (le palladium peut en témoigner). Merci beaucoup Benoit !

Malgré que le contenu présenté dans cette thèse n'inclut pas les travaux menés sur le design, la fabrication et la caractérisation de laser à verrouillage de phase avec control actif sur le taux de répétitions conçu à base de réseaux de Bragg superposées, d'un point de vue personnel, le stage que j'ai fait à l'« University of Glasgow » fut très enrichissant. Les gens qui ont contribué à ce travail mérite donc une part de remerciement. Tout d'abord, j'aimerais remercier Marc d'avoir accepté de mener le projet que Sophie et moi lui avons proposé et de m'avoir accueilli dans son groupe pour six mois. Également, ce projet n'aurait certainement pas abouti à ces résultats intéressants sans l'importante contribution de Michael, qui a participé grandement à l'élaboration du design, à la fabrication du composant, la caractérisation et à l'analyse des résultats. De plus, je remercie Vincenzo d'avoir pris en charge la fabrication du laser. Sans la minutie et le travail de précision de ce dernier, ce projet serait évidemment tombé à l'eau. Finalement, j'aimerais remercier Marco et Piotr qui furent des ressources très importantes lors de la caractérisation de lasers que j'ai faits dans les laboratoires de Marc. En bref, un grand merci à cette équipe formidable.

Je tiens à remercier grandement Dan Deptuck de CMC microsystem. Dan fut une personne ressource très importante lors du design des composants et de la fabrication du layout. Un grand merci d'avoir fait le pont (à défaut d'une meilleure expression) entre notre vision photonique et le milieu de la fabrication CMOS. Par ailleurs, en rétrospective, je suis convaincu que le cours de nano-fabrication passif donné par Lukas Chrostowski de l'« University of British Columbia » a accéléré la réalisation de mes études doctorales d'au moins un an. Un grand merci pour ce travail qui me fut extrêmement bénéfique.

Pour conclure le volet professionnel, je remercie les évaluateurs de mon examen pré-doctoral et de ma soutenance qui n'ont pas déjà été remercié jusqu'ici, c'est-à-dire, les professeurs Leslie Rusch, Amr Helmy, Wei Shi et Odile Liboiron-Ladouceur. Ces gens ont investi beaucoup de temps et m'ont fait des commentaires et suggestions extrêmement constructives. Je tiens donc à les remercier.

Beaucoup d'heures de travail furent nécessaires pour mener à bien le projet présenté dans cette thèse. Malheureusement, beaucoup de ces heures furent amputées sur mon temps personnel. Ainsi, une grande part des résultats présentés dans cette thèse est due à la compréhension et au support de ma conjointe Nancy. Son humour, sa bonne humeur et sa joie de vivre m'ont également permis de garder un bon moral même lors des moments difficiles. Je dois également faire une mention toute spéciale à mon fils Nicolas, qui a fortement contribué au succès de mes études doctorales en faisant des nuits de 6 heures dès sa dixième journée. J'aurais pu dire sa neuvième journée si son père ne l'avait pas bêtement réveillé pour le nourrir…enfin. Finalement, je dois mentionner le support de longue haleine fourni par ma mère et mon père qui ont prodigué respectivement une quantité phénoménale et modérée de conseils et de recommandations utiles. Avec toutes ces années d'études derrière moi, je suis maintenant en mesure d'apprécier l'importance du soutien que ma famille m'a apporté.

A tous, merci beaucoup !

The activity you are most
avoiding contains your
biggest opportunity.

R. Sharma

Preface

The main chapters of this thesis are reproductions of published papers aside for some minor modifications to improve the thesis uniformity. In this section, as required by the "*Faculté des Études Supérieures et Postdoctorales de l'Université Laval*", a short description of the contribution of the respective authors is made.

Section 1.6 has been presented at

> "*A. D. Simard, Y. Painchaud, and S. LaRochelle, "Characterization of Integrated Bragg Grating Profiles," in Bragg Gratings, Photosensitivity, and Poling in Glass Waveguides, Colorado Springs, USA, 2012, p. BM3D.7.*"

The author of this thesis contributed to the idea, conducted the experimental characterisation, the data processing and the writing of the manuscript. S. LaRochelle and Y. Painchaud contributed to the overall work with many suggestions that significantly improved the quality and completeness of the manuscript. They also both actively participated in the edition of the manuscript.

Chapter 2 has been published in

> *"A. D. Simard, N. Ayotte, Y. Painchaud, S. Bedard, and S. LaRochelle, "Impact of Sidewall Roughness on Integrated Bragg Gratings," J. Lightwave Technol., vol. 29, no. 24, pp. 3693–3704, Dec. 2011."*

The author of this thesis developed the model and the emulator, did the numerical simulations and led the analytical derivation and the redaction of the manuscript. N. Ayotte and S. Bedard provided help in the mathematical derivation of the analytical model. S. LaRochelle and Y. Painchaud contributed to the overall work with many suggestions that significantly improved the quality and completeness of the manuscript. They also both actively participated in the edition of the manuscript. A preliminary portion of this works has also been presented at

> *"A. D. Simard, N. Ayotte, Y. Painchaud, and S. LaRochelle, "Impact of Sidewall Roughness on Integrated Bragg Gratings" CLEO: Applications and Technology, Baltimore, USA, 2011"*

Chapter 3 has been published in

> *"A. D. Simard, G. Beaudin, V. Aimez, Y. Painchaud, and S. LaRochelle, "Characterization and reduction of spectral distortions in Silicon-on-Insulator integrated Bragg gratings," Opt. Express, vol. 21, no. 20, pp. 23145–23159, Oct. 2013."*

The author of this thesis contributed to the idea and the manuscript redaction, developed the model, and conducted the optical characterisation and the data processing. G. Beaudin and Vincent Aimez conducted the scanning electron microscope characterization. S. LaRochelle and Y. Painchaud contributed to the overall work with many suggestions that significantly improved the quality and completeness of the manuscript. They also both actively participated in the edition of the manuscript.

Chapter 4 has been has been published in

> *"A. D. Simard, N. Belhadj, Y. Painchaud, and S. LaRochelle, "Apodized Silicon-on-Insulator Bragg Gratings," IEEE Photon. Technol. Lett., vol. 24, no. 12, pp. 1033 – 1035, Jun. 2012."*

The author of this thesis contributed to the idea, conducted the experimental characterisation, the mask layout, the data processing and the writing of the manuscript. N. Belhadj assisted in the mask layout drawing. S. LaRochelle and Y. Painchaud contributed to the overall work with many suggestions that significantly improved the quality and completeness of the manuscript. They also both actively participated in the edition of the manuscript.

Chapter 5 has been has been published in

> *"A. D. Simard, Y. Painchaud, and S. LaRochelle, "Integrated Bragg gratings in spiral waveguides," Opt. Express, vol. 21, no. 7, pp. 8953–8963, 2013."*

The author of this thesis contributed to the idea, conducted the experimental characterisation, the mask layout, the data processing and the writing of the manuscript. S. LaRochelle and Y. Painchaud contributed to the overall work with many suggestions that significantly improved the quality and completeness of the manuscript. They also both actively participated in the edition of the manuscript. Preliminary portions of this works has also been presented at

> *"A. D. Simard, Y. Painchaud, and S. LaRochelle, "Integrated Bragg Gratings in Curved Waveguides," in the 23rd Annual Meeting of the Photonics Society, Denver, USA, 2010, p. ThU3"*

> *"A. D. Simard, Y. Painchaud, and S. LaRochelle, "Small-footprint Integrated Bragg Gratings in SOI Spiral Waveguides," CLEO Europe 2013, Munich, Germany, May 2013"*

Introduction

Photonic integrated circuits (PIC) allow an optical system to be made more compact compared to its discrete free-space version. These devices have better mechanical vibration immunity and they have the advantage to be automatically aligned through a very precise fabrication process which eliminates the feedback loop often necessary to maintain a good alignment in free space optical circuits. However, the most promising advantage is the potential to achieve mass-production at a very low cost. Hopefully, the integration of optical components will follow a similar path as electronics, where the integration allowed transistor-based electronics to evolve into circuits with ever growing complexity and capability. PIC has many potential applications, such as imagery, spectroscopy systems, sensors and "lab-on-chip" for medical diagnostics, optical logic circuits and so on [1]. However, the focus applications of this thesis are optical communication systems for which key components are required, such as light sources, wavelength division multiplexing (WDM) multiplexers/demultiplexers, modulators, amplifiers and photodetectors. In current fiber optic telecommunication systems, such devices are used as discrete components, but significant benefits could come with monolithic integration.

Unlike electronic integrated circuits, where silicon is the dominant material and the transistor is the dominant device, integrated photonics circuits require a large variety of devices as mentioned above, which have been independently optimized on different substrates due to their respective properties. For example, the lithium niobate crystal is well known for its good electro-optical property that makes them exceptional modulators. Silica-on-silicon exhibits very low propagation loss and has a very low temperature sensitivity, which makes it interesting for passive devices such as arrayed-waveguide gratings (AWG) frequently used as optical multiplexers/demultiplexers in WDM systems. Semiconductor materials, such has GaAs and InP based devices, can amplify optical waves which also allows the fabrication of laser sources and amplifiers. Finally, photo-detectors with high sensitivity, fast response, low noise, low cost, and high reliability are usually fabricate in InGaAs or germanium for operation in the telecommunication band. The fact that all these components are fabricated in such many different materials makes challenging the monolithic integration of PIC.

Silicon is also an interesting material for PIC since the crystal quality is very good, which results in a negligible amount of absorption loss and its native oxide can be used as a good waveguide cladding. Silicon-on-insulator (SOI) wafers fabricated with the SMARTCUT technology [2] are of great quality and the high index contrast between the crystal $(n(@1550\text{ nm}) = 3.41)$ and its native oxide $(n(@1550\text{ nm}) = 1.444)$ allows the guided optical wave to be extremely confined. This fact results in the possibility to achieve bends with small radius of curvature (~ 5 µm) without significant losses, thus creating extremely compact circuits. Furthermore, since silicon is the dominant material for electronic, the use of this material could enable co-integration of photonics with transistor based electronics which are fabricated with the complementary metal–oxide–semiconductor (CMOS) technology. This high volume and low-cost production technique opens a wide range of applications for PIC since their fabrication follows similar step than that used in CMOS circuits which involves deep ultra-violet (DUV) photolithography to imprint the designed pattern on the photoresist, etching to transfer the pattern on the silicon layer, and material deposition/epitaxy to fabricate multilayered structures. The photonic community has only recently started to exploit the vast experience in the fabrication processes and the mature platform developed in the last decades by the electronic community.

Even though silicon is not the best material for modulating and emitting light, tremendous work has already been made in both these domains to enable this platform to offer a complete set of components. Many optical modulator designs have been proposed in the last decades [3]–[6]. Some Mach-Zehnder modulators with travelling wave electrodes achieved data rate up to 26 Gb/s with a very low RF energy consumption of 146 fJ/bit [6]. 50 Gb/s bit rate has already been achieved [4] and even higher bit rates have been obtained with advanced modulation format [7]. More compact modulators than traveling wave Mach-Zehnder can be obtained with microring or microdisk resonators [8]–[11]. However, such modulators have narrow optical bandwidth. Up to 40 Gb/s data rate has been obtained using such structures [12]. As for optical sources, even though silicon has an indirect bandgap, some schemes have been proposed to integrate light sources in a CMOS compatible environment [13]. For example, the bonding of unpatterned III–V active semiconductors layers on an SOI wafer can provide the gain required for laser emissions. It is possible to use either ultra-thin bonding layer and to consider the active section as an hybrid waveguide [14], [15] or to use a mode converter that couples the light in the III-V section and provide gain to the optical wave [16]. There is also the possibility to grow germanium on the silicon layer. Although this material also has an indirect bandgap, it can be stress-engineered to achieve light emission [17]. Finally, there is always the possibility to use external light sources with the advantage that a significant heat source is off-chip but with the drawback of reduced integration capability and increased difficulty for high volume production. Despite these difficulties, recent work have demonstrated the feasibility to fabricate the building blocks required for optical communications [18], [19] in SOI.

The choice between optical and electrical transmissions for communication systems is made based on a number of trade-offs [20]. Typically, optical communication systems are chosen over copper based transmission lines when a high bandwidth is required and when the system spans over long distances; i.e. when the bit-rate distance product is high, optical communications becomes a viable and, potentially, a better solution compared to electrical communications. As a result, fiber optic communications has initially been introduced in long-haul systems and metro-area networks. However, nowadays, in the telecommunication era, with ever increasing data traffic, the bit-rate distance product is very high even for shorter links. Fiber optic communications are now well established in local area networks.

Optical communications keep invading communication systems with shorter and shorter links. Recently, a significant portion of the computing and the data storage has moved from personal computers to data-centers (DC) which makes them a key infrastructure. This is due to the increasing popularity of cloud computing. While a significant part of the traffic is between these DCs and individual users, a much bigger portion of the traffic occurs within each DC [21]. The rapid increase in the required bit rate makes this application very appealing for photonic technology innovations targeting energy-efficient and high-speed devices. To further scale the density and reach higher data rates, PICs using WDM is a well-considered approach [21].

If we consider even smaller communication distance, it is well known that transistor performances significantly improves when their size is reduced, but this does not apply to the interconnections between them because copper wires generate an unacceptable amount of heat and induce significant losses when their cross-section dimension is reduced and when their length is increased. These properties make copper wires unsuitable for the next interconnect generation

[22]. Optical communications may solve the power and bandwidth problems of electronics [23]. Optical solutions have been proposed for inter-chip interconnects as well as for intra-chip interconnects, both for signal and clock distribution [20]. Obviously, intra-chip optical interconnects are not expected to replace copper-based interconnects, but could be beneficial for long interconnects in upper metal layers. Similarly, for inter-chip interconnects, the idea is to increase the bandwidth or decrease the power per bit for the data transferred over the long interconnects between chips. In both case, the focus is made on designs that take advantage of the unique properties of optical architectures, such as WDM networks.

Thus, there is a strong motivation to work on the monolithic integration of components already used in fiber optic telecommunications since, on one side, WDM communication systems appear to be a credible solution both for DC [21] and chip-to-chip communications [19], [22] as it was for fiber optic telecommunications decades ago and, on the other side, such devices could also be beneficial to already existing fiber optic telecommunications links. Specifically, power efficient laser sources, modulators, photodetectors and switches are required as well as precise filtering devices. The latter ones are usually obtained using multimode interferometers (MMI), AWGs, Mach-Zehnder interferometers (MZI), micro-rings or integrated Bragg grating (IBG) filters and this thesis focuses on the last type of filters.

Micro-ring resonator based devices are compact components capable of performing many functions required in an optical communication network. However, their periodic spectral response limits the amount of WDM channels that can be supported. Furthermore, their narrow Lorenztian spectral response distorts and attenuates optical signals and decreases the performance of high data rate systems. Finally, their resonant wavelengths are very sensitive to fabrication errors or process variations, which make them almost impossible to predict precisely. As a result, thermal tuning is frequently used to adjust the ring resonances, which requires a significant part of the power budget. MZI and generalized MZI interferometer are also very important for the silicon photonic platform, however, as micro-ring resonators, their periodic spectral response might be problematic for complex filtering devices. MZI are however a key building blocks for high-speed modulators. Finally, although MMIs and AWG are important for the fabrication of PICs, their filtering capabilities are restricted and they are mostly used for power splitters and WDM multiplexers respectively.

In comparison, Bragg gratings are exceptional filter. They are a key component in the field of semiconductor lasers, but with a proper phase and amplitude design, they can also provide tailored spectral response which can be used in a wide variety of applications. For example, Bragg gratings can be used as pulse shapers [24], as temporal differentiator and integrator [25], as phase engineering devices or multichannel dispersion compensation [26], [27], as wavelength stabiliser [28], as multi-wavelength lasers resonant cavity [29], as add/drop multiplexers [30] and so on [31]. As a result, the SOI platform could benefit from the integration of high-quality grating structures. However, a question remains: "*can the progress made in the last twenty years for fiber Bragg gratings be transferred to the SOI platform?*" Until now, IBG have been very simple, which limits their potential applications. At the start of this PhD work, five main issues could be identified as limiting or even preventing the fabrication of IBGs having elaborate spectral responses with a CMOS compatible process:

1) There was a lack of reliable procedure to fully characterize IBGs in reflection. Spectral distortion were observed but the origin could not be identified
2) Due to the high confinement of silicon waveguides, very small waveguide deformations create a high level of phase noise, which induces severe distortions in IBGs spectrum.
3) There was a lack of reliable apodization technique compatible with small corrugations.
4) The device length requirement for IBGs to design elaborate spectral response, which might go up to the cm-scale, was not compatible with most PIC device chip size;
5) Magnetic materials are not compatible with CMOS processes, which results in a lack of isolator/circulator and prevent the use of IBGs in reflection in PICs.

This thesis addressed the first four points while the fifth one has been solved in the meantime by other groups by using contra-directional Bragg grating couplers [32]–[34]. More specifically, this thesis is structured as follows:

Chapter 1 provides the theoretical background on Bragg grating structures and presents the state-of-the-art in IBGs, mainly in silicon, but also in other materials if the notions are necessary in the context of this thesis. This chapter also presents techniques to simulate the grating spectrum; it introduces an algorithm that reconstructed IBGs structure from experimental measurements and shows how to properly characterize IBGs in order to allow the use of such algorithm (issue #1). This experimental procedure is going to be used throughout this thesis.

Chapter 2 and 3 discuss in detail the phase distortion sources affecting IBGs in SOI and their impact on the grating spectral response (issue #2). In chapter 2, a technique to emulate IBG spectral responses in the presence of an imperfect waveguide was proposed. This work is useful to determine the fabrication parameters required to guarantee a target fabrication yield. In order to save computation time, the analysis also shows that only the low frequency components of the noise are significant to the IBG spectral response. Finally, an analytic study of the impact of sidewall roughness for weak gratings having small variance is presented. This analysis gives a good understanding of the impact of sidewall roughness and grating parameters on the spectral response. In chapter 3, the wafer height fluctuation, another important source of spectral distortion for IBGs, was incorporated in the model elaborated in the previous chapter and was characterized experimentally. Furthermore, a new technique to characterize roughness of silicon-on-insulator photonic waveguides is presented, thus providing the experimental parameters required in the model developed in chapter 2. Finally, two techniques were demonstrated to reduce IBG spectral distortions which allowed fabricating high quality IBGs.

Chapter 4 presents two fabrication-friendly apodization techniques that are compatible with deep UV lithography usually used in CMOS processes. The fabricated apodized gratings show very good agreement with the designed apodization profile. The proposed techniques are reliable even for weak index modulation amplitudes.

Finally, chapter 5 addressed the problem of integrating long IBGs in a way compatible with typical PIC chip size (issue #4). Specifically, this chapter demonstrate the integration of Bragg gratings with mm-lengths in spiral waveguides having a footprint of 200 x 190 μm^2 without degradation of their spectral response. The phase compensation technique that was used to overcome the distortion created by the waveguide curvature is presented. Furthermore, the integration capability has been increased by using interleaved spirals. Finally, it is shown that the spiral designs are compatible with the phase modulation apodisation technique presented in chapter 4.

Chapter 2 to 5 of this thesis are reproductions of published papers aside for some minor modifications such as symbol definitions made to improve the thesis uniformity, figure reshaping made for the reader convenience, the removal of the fabricated devices and the characterization procedure (which is done only once in section 1.2 and 1.7 respectively). Before the abstracts of each chapter, a short (unpublished) introduction of the paper is made in order to put it in the context of the work presented in this thesis and, whenever required, the last section contains (unpublished) results and discussion that were considered necessary for the completeness of the thesis.

Chapter 1: Bragg Gratings

In this chapter, the Bragg grating structure is introduced. Section 1.1 is discussing the state of the art of IBGs in SOI. A discussion on the different approaches used to create Bragg reflection is done as well as their respective limitations in the context of designing long IBGs with elaborate spectral responses. Section 1.2 presents a short description of the IBGs that were fabricated for this thesis and points out the differences in their structures. Section 1.3 outlines the derivation of the coupled mode equations applied to Bragg gratings. Section 1.4 focuses on the spectral simulation of such structure. The discussion is limited to the transfer matrix formalism, the approach that has been used in this thesis, and to the weak grating approximation, which is used in chapter 2. The calculation of the spectrum is often referred to as a direct scattering problem. Inversely, section 1.5 presents the inverse scattering algorithm used throughout this thesis to reconstruct the grating structure from the measured IBG complex spectral response in reflection. Section 1.4 and 1.5 are not meant to be an exhaustive literature review on Bragg gratings modeling but only to provide the tools that have been used for the completion of the work presented here. In this thesis, many references are made to the fabrication of "elaborate gratings". In section 1.6, this concept is discussed in detail. Finally, section 1.7 focuses on IBGs experimental characterisation. Due to the fact that these structures are embedded between reflective structures (grating couplers, cleaved fibers and/or cleaved facets) which interferes with the wave reflected form the IBGs, special care must be taken to retrieve the grating spectral response. This subsection is strongly inspired by reference [35] which was presented at the OSA topical meeting *Bragg Gratings, Photosensitivity, and Poling in Glass Waveguides* in 2012. It fully describes the experimental procedure used throughout the thesis to characterize IBGs.

1.1 – Integrated Bragg gratings

A few techniques have been proposed to fabricate an integrated component having an effective index periodic perturbation. For a reader familiar with FBGs, a straightforward way to modulate the effective index is to modify the material. In a silicon waveguide, it is possible to dope the silicon layer to reduce the refractive index through a modification of the carrier density [36]. However, this approach is not common since the typical minimum feature size achievable with carrier implementation is much larger than the lithography/etching minimum features size. Even though some researchers successfully achieved such grating structure [37], this approach is not accessible to most research group, including ours, since the photoresist with high resolution usually used in CMOS compatible foundries has a thickness too thin to be used as the implantation screen mask. As a result, in [37] they had to develop their own approach to decrease the minimal feature size of carrier implantation.

IBGs are usually fabricated by perturbing the waveguide structure such as a modification of its height (top IBGs as shown in Fig. 1-a)) [38], its width (lateral IBGs as shown in Fig. 1-b)) [39] or by adding pillar structure on the waveguide sides (pillar IBGs as shown in Fig. 1-c)) [40].

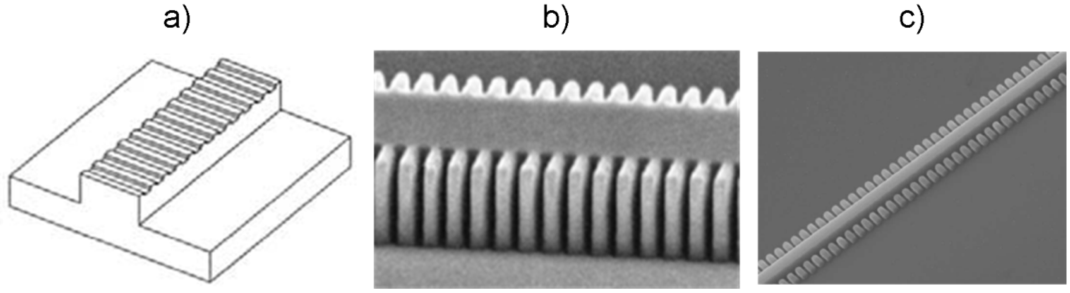

Fig. 1: Type of structural modification used to fabricate IBG : a) top IBG [38], b) lateral IBG [39], c) pillar IBG [40].

Top gratings are the least flexible of the three approaches. To fabricate such IBGs, a lithography/etching step must be used to define the waveguide and another one to define the grating, which increases the cost of the components, unless such fabrication step are already used for other components on the chip. Furthermore, this etching step depth is usually not flexible in CMOS compatible fabrication facilities. For example, the smallest etching depth of IMEC, a foundry optimized for the fabrication of photonic circuits, is fixed at 70 nm, which prevent an IBG designer to specify the grating coupling amplitude. As a result, such structure will not be used in this thesis.

The two last approaches have the advantage to be defined by the same lithographic/etching step of the waveguide which allows the designers to control the grating coupling amplitude (through a variation of the recess or the pillar-waveguide distance). However, the high confinement of photonic wires in SOI results in a high amount of optical power at the waveguide sidewalls. The waveguide cross-section with dimensions providing singlemode operation is shown in Fig. 2-a). This phenomenon combined with the waveguide sidewall roughness (SWR), which results from the fabrication process and creates effective index variation as a function of position, strongly distorts IBGs spectra. It creates a phase noise in the grating structure that is amplified if the mode intensity is strong near the waveguide walls. To reduce this effect, we suggested in [41], [42] (chapters 2 and 3) to use hybrid singlemode/multimode waveguides. These waveguides are composed of a multimode section which contains the grating, surrounded by two singlemode waveguides connected with adiabatic tapers that force the optical mode to be coupled in the fundamental mode of the multimode waveguide. The grating presented in this thesis are made with lateral corrugations (Fig. 1-b)) instead of pillars (Fig. 1-c)) since the coupling amplitude that could be obtained with the latter approach would be unreasonably small.

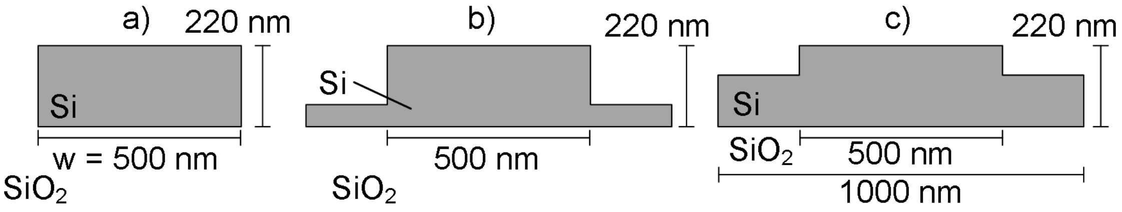

Fig. 2: Typical singlemode a) photonic wire, b) ridge waveguide with a thin slab and c) ridge waveguide with a thick slab cross-section.

Finally, it is also possible to fabricate IBGs in a ridge waveguide. This type of waveguide comes in two different configurations. The first one has micrometers waveguide thickness [38], [43]–[45] while the other one implements the same type of waveguide geometry but on sub-micrometer thick silicon layer [46], [47]. A large portion of the silicon photonic community has oriented their efforts towards sub-micrometer silicon thickness (typically 220 nm) because of the high modal confinement of such structures. However, many relevant works have also been published with larger waveguides since these devices have better propagation and coupling loss performances. Compared to micrometer-size cross-sections, sub-micrometer can be bent with very tight radius of curvature which is necessary to the design of highly integrated circuits (and the work presented in chapter 5). Considering that the silicon layer thickness cannot be modified easily in a photonic circuit, waveguides having thickness of the order of micrometers have been discarded (and the work presented in this thesis is entirely done with waveguides having thickness of 220 nm). As for the sub-micrometer ridge waveguide, this category can be split into two categories. The first one, shown in Fig. 2-b), has a thin slab layer which is usually used in active devices to connect the waveguide to a PN junction. The second one, shown in Fig. 2-c), has a thick slab layer. This latter waveguide is quite interesting for passive IBGs since it provides coupling coefficient that is compatible to long structure and the phase-noise properties caused by the SWR are certainly better than for singlemode photonic wires. However, it is not clear if this waveguide have better performances than the hybrid singlemode/multimode waveguide approach proposed in chapter 2 and 3 and this approach have been discarded due to the miss-alignment that can happen between the two lithographic steps required to fabricate such waveguides which could result in a reduced fabrication yield. Considering the long time required to achieve an experimental iteration loop (design, fabrication, characterization), which is roughly one year in a fabless research group, this possible source of error could have brought significant delay in the presentation of this work without bringing significant design improvement. Other research groups have used this approach [46], [47], but phase measurements were not available to accurately compare IBGs phase noise robustness. Anyhow, this type of waveguide is potentially a good one to explore in the future.

As mentioned above, in order to design an IBG with a specific spectral response, it is necessary to have a complete control over the amplitude and phase of the effective index modulation. In order to control the grating coupling amplitude (i.e. the grating apodization), many approaches have already been proposed, such as a variation of the corrugation recess amplitude [39], [48] or of the duty cycle [49]. Those techniques modify the grating coupling amplitude, but at the expense of an effective index variation. As a result, the grating phase is modified which is problematic since it distorts the spectral response. The only approach that has been used to apodize IBGs without involving a systematic spectral distortion consist of varying the IBGs corrugation recess and the local waveguide width in order to obtain the desired amplitude and phase profiles [50], [51]. In principle, this approach is very flexible since it allows the fabrication of tailored grating structure. However, it is unclear if the desired waveguide width and corrugation recess profiles are going to be robust to fabrication errors such as exposure dose variation. As mentioned in [52] and shown in Fig. 3-a), the fabricated waveguide width (or line width) is varying as a function of exposure dose and as a function of etching condition and the optimal exposure dose is a function of the waveguide width. Furthermore, the effective index variation is not linear as a function of the waveguide width, as shown in Fig. 3-b). As a result, a bias in the average waveguide width will distort both the apodization profile and the average effective index profile. Thus, to be robust to fabrication uncertainty, an IBG should have a constant average waveguide width as well as constant corrugation recess amplitude. In this situation, a bias in the waveguide width only introduces a constant effective index shift and a bias in the corrugation recess will only change the average grating coupling amplitude. For both profiles, no distortion is added to the grating structure. Chapter 4 is proposing two approaches to fabricate such apodized IBGs. As for the control of the phase, this problem is addressed in chapter 2 and 3.

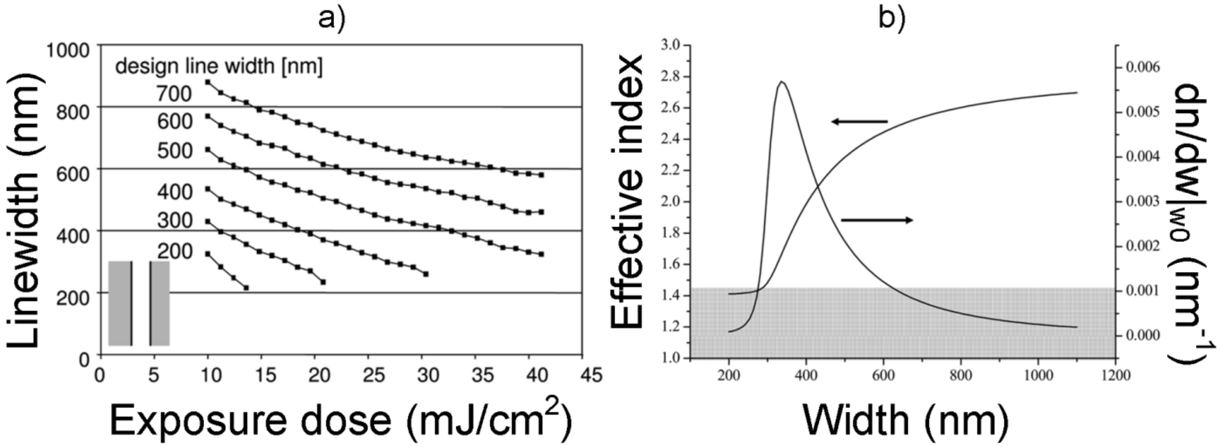

Fig. 3: a) Variation of the fabricated waveguides width (or line width) as a function of exposure dose [52] and the designed waveguide line width. b) Sensitivity of the effective index of the TE$_0$ mode to photonic wire width at 1550 nm. The height of the wire is 220 nm. The gray region depicts the cutoff region [53].

Even if good quality, long and elaborate grating structure have not been used extensively yet in silicon due to the aforementioned issues, short and simple ones with strong reflectivity have already been demonstrated in SOI waveguides with good spectral responses [54] and integration of such short uniform gratings on a contra-directional IBG-couplers, a four ports structure, has allowed operating the gratings in reflection [32]. This later contribution has a significant importance due to the absence of CMOS compatible isolators and circulators and has already been used for on-chip pulse compression applications [33]. Signal processing filter, such as on chip optical differentiator, have been obtained using a π phase shifted grating [55]. Furthermore, the demonstration of tunable gratings using the charge carrier effect [37], the thermo-optic effect [44], [45], [56] and of contra-directional IBG-couplers using the charge carrier effect [57] suggest potential use of these devices for modulation and switching.

1.2 – Fabricated gratings

The gratings fabricated for this thesis were very simple in order to characterize the SOI platform. They had a weak reflectivity to ease the convergence of the reconstruction algorithm presented in section 1.5 and they were 2 mm long uniform grating unless mentioned otherwise (in chapter 4 and 5, some gratings are Gaussian apodized with a full-width at half maximum of 1 mm). The IBGs were fabricated on strip waveguides having a width (w_0) of 1200 nm (without ridge structure), except in chapter 3 where the impact of the waveguide width on the phase noise was studied and some gratings were fabricated on 800 nm wide waveguides. The recess amplitude (Δw) was 30 nm and 10 nm for 1200 nm and 800 nm wide waveguide respectively. The recess amplitude was modified to obtain a similar grating reflectivity. The nominal silicon layer thickness was 220 nm.

Fig. 4 shows the schematic of the devices characterized for this thesis. Singlemode sections with adiabatic couplers are placed before and after the multimode section in order to predominantly excite the fundamental mode of the multimode section as suggested in chapter 2. As a result, the grating is behaving as if it were in a singlemode waveguide, but with less distortion. Input/output light coupling is achieved with grating couplers [58] having etched depth of 70 nm in 10 μm wide waveguides (except for spiral gratings presented in chapter 3 and 5 where compact focusing grating couplers [59] were used). These couplers are followed by 600 μm long adiabatic tapers that lead to single-TE mode waveguides having a width of 500 nm and a length of 190 μm (for spiral gratings, the taper was no longer necessary because of the focusing grating and was replaced by a simple singlemode waveguide longer than 800 μm). Then two 125 μm-long adiabatic tapers connect the single-TE mode waveguides to the multimode waveguide that contains the 2 mm-long IBG.

For the grating period, there is a limitation due to the smallest feature size available at IMEC, the CMOS facilities used to fabricate the gratings discussed in this thesis (except for the spiral gratings presented in chapter 3 and 5, which were fabricated at IME). The smallest structure that can be fabricated at IMEC has a dimension of 140 nm. Thus, a grating having a 50 % duty cycle must have a period larger than 280 nm. However, as mentioned previously, the waveguide used in this thesis are wide enough to require a grating period very close to 280 nm to have a resonance in the C-band. As a result, third order gratings were used with a duty-cycle of 25 % to ensure a resonance around 1550 nm. The 25 % duty-cycle is necessary since the corrugation amplitudes used in this thesis are much smaller than the process resolution. Thus, designed IBGs having rectangular corrugations are likely to become IBGs with sinusoidal-like corrugations [60] that are characterized, in theory, by a null third order resonance. With a 25 % duty cycle, although the third order will be attenuated, a significant portion should remain[I]. The following tables summarize the grating characteristics mentioned above and will be referred to in subsequent chapters.

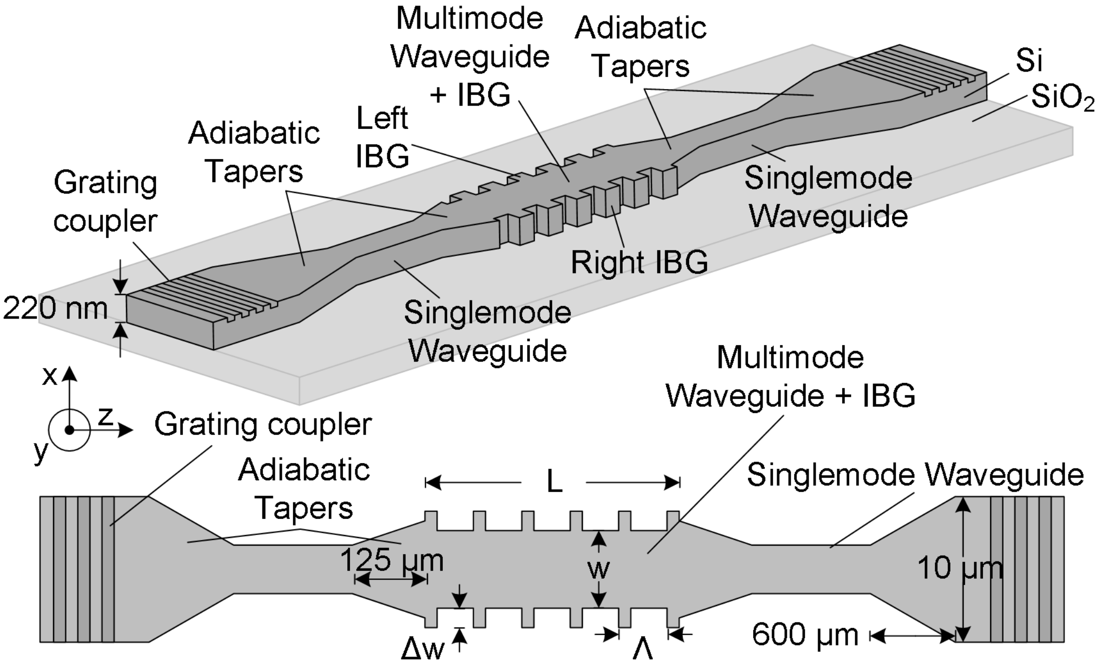

Fig. 4: 3D view and top-view of the schematic of the third order 2 mm-long IBGs used in this thesis

---

[I] Technically, the required period for 1200 nm wide waveguide is ~286 nm to have a resonance close to 1550 nm. However, third order grating has been fabricated since phase-apodized gratings experience local period smaller than the 280 nm limit. As a result, to prevent the comparison of IBGs with different grating order, all of them were fabricated with a third order resonance at 1550 nm. This comment also includes the spiral gratings fabricated at IME.

Table 1: Characteristics of the grating from now on named "Straight Grating #1"

Parameter	Values
Waveguide width	1 200 nm
Silicon thickness	220 nm
Top-silica layer	No
Grating physical period (Λ_p)	858 nm
Grating length	2 mm
Grating duty-cycle	25 %
Corrugation amplitude	30 nm
Shape	Straight gratings
External circuit on each side	Grating couplers + 600 µm long adiabatic tapers + 500 nm wide and 190 µm long waveguide + 125 µm-long adiabatic tapers
CMOS foundry	IMEC
Chapters	3-4
Comments	193 nm DUV lithography

Table 2: Characteristics of the grating from now on named "Straight Grating #2"

Parameter	Values
Waveguide width	800 nm
Silicon thickness	220 nm
Top-silica layer	No
Grating physical period (Λ_p)	873 nm
Grating length	2 mm
Grating duty-cycle	25 %
Corrugation amplitude	10 nm
Shape	Straight gratings
External circuit on each side	Grating couplers + 600 µm long adiabatic tapers + 500 nm wide and 190 µm long waveguide + 125 µm-long adiabatic tapers
CMOS foundry	IMEC
Chapters	3
Comments	Same fabrication run than Straight Grating #1

Table 3: Characteristics of the grating from now on named "Spiral Grating #3"

Parameter	Values
Waveguide width	1 200 nm
Silicon thickness	220 nm
Top-silica layer	Yes
Grating physical period (Λ_p)	858 nm
Grating length	2 mm
Grating duty-cycle	25 %
Corrugation amplitude	30 nm
Shape	Spiral gratings
External circuit on each side	Focusing grating couplers + 500 nm wide waveguide (longer than 800 µm) + 125 µm-long adiabatic tapers
CMOS foundry	IME (OpSIS)
Chapters	3-5
Comments	1) This fabrication run was the first OpSIS public run. The 248 nm DUV lithography results in weaker gratings 2) The fabricated spiral gratings are phase compensated unless told otherwise 3) The spiral waveguide characteristics are described in chapter 5.

1.3 – Bragg grating coupled equations

The derivation of the coupled mode equations has already been done many times [61]–[65] (to name a few). However, considering the extensive reference made to those equations throughout this thesis, a derivation of those equations from the Maxwell equations was considered essential and is done in Appendix A. Those equations can be used to model many physical phenomena, however, since this thesis focuses on Bragg gratings, this section considers that only one mode contains the energy and that the permittivity modulation induces a coupling between this mode and its contra-directional equivalent. Considering only the presence of those two modes, Eq. (A.33) and (A.34) reduces to

$$\frac{\partial A}{\partial z} = iB\left(\mathrm{K}_{\mu\nu}^{t} - \mathrm{K}_{\mu\nu}^{z}\right)e^{-i2\beta z} \qquad (1.1)$$

$$\frac{\partial B}{\partial z} = -iA\left(\mathrm{K}^{t}_{\mu\nu} - \mathrm{K}^{z}_{\mu\nu}\right)e^{i2\beta z} \ , \tag{1.2}$$

where z is the axis of propagation, A and B are the amplitude of the forward and backward propagating modes, β is the propagation constant and $\mathrm{K}^{t}_{\mu\nu}$ and $\mathrm{K}^{z}_{\mu\nu}$ are the tangential and longitudinal coupling coefficient between mode μ and v given by

$$\begin{aligned} \mathrm{K}^{t}_{\mu\nu} &= \frac{\pi}{\lambda}\left[\frac{2c}{n(\lambda)}\int_{-\infty}^{\infty}\int_{-\infty}^{\infty} dxdy\Delta\varepsilon \vec{E}_{t\nu}\vec{E}^{*}_{t\mu}\right] \\ \mathrm{K}^{z}_{\mu\nu} &= \frac{\pi}{\lambda}\left[\frac{2c}{n(\lambda)}\int_{-\infty}^{\infty}\int_{-\infty}^{\infty} dxdy\frac{\varepsilon\Delta\varepsilon}{\varepsilon+\Delta\varepsilon}\vec{E}_{z\nu}\vec{E}^{*}_{z\mu}\right] . \end{aligned} \tag{1.3}$$

In Eq. (1.3) x and y are respectively the cross-section axis tangential and normal to the wafer surface as shown in Fig. 4, c is the speed of light, $n(\lambda)$ is the effective index, λ is the free-space wavelength, ε is the permittivity and $\Delta\varepsilon$ is the deviation of the permittivity from the nominal waveguide profile. Since a Bragg grating is created by a periodic perturbation of the permittivity, the periodicity of the coupling coefficient can be made explicit by expending Eq. (1.3) with a Fourier series and by keeping only the term that has a resonance near the C-band such as

$$\begin{aligned} \mathrm{K}^{t}_{\mu,-\mu} - \mathrm{K}^{z}_{\mu,-\mu} &= \frac{2\pi}{\lambda}\Delta n \cos\left(\frac{2\pi}{\Lambda}z + \phi(z)\right) \\ &= \kappa\left(\mathrm{e}^{iG(z)} + e^{-iG(z)}\right) \end{aligned} , \tag{1.4}$$

where κ is the effective coupling coefficient, which takes into account both the tangential and the normal coupling, $G(z)$ is the grating phase and Δn is a unit less parameter representing the grating effective index perturbation. This latter term is introduced to express the coupling coefficient term in a similar manner as for FBG. Finally, Λ is the first order grating period having a resonance near the C-band (i.e. $\Lambda = \Lambda_p/m'$ where m' is the grating order). The effective index of a waveguide containing a grating can then be written in the form

$$\begin{aligned} n(z,\lambda) &= n(\lambda) + \Delta n\cos\left(G(z)\right) \\ &= n(\lambda) + \Delta n\cos\left(\frac{2\pi}{\Lambda}z + \theta(z)\right), \end{aligned} \tag{1.5}$$

where $\theta(z)$ includes any z-varying function that might be introduced into the grating period and

$$n(\lambda) = n_0 + n_1(\lambda - \lambda_0) \tag{1.6}$$

is the average effective index of the unperturbed waveguide, which is wavelength dependent. The n_i are the terms of the truncated Taylor series modeling the effective index and λ_0 is the reference wavelength of the truncated Taylor series, in the present case 1550 nm. It is also convenient to write Eq. (1.6) as a function of the group index (n_g), which gives

$$n(\lambda) = n_g + n_1\lambda \ . \tag{1.7}$$

In this thesis, the coupling coefficient is not calculated explicitly. Instead, a reconstruction algorithm, applied to experimental complex spectral measurements, provides the average effective index fluctuations as well as the grating coupling coefficient or, equivalently, Δn. As discussed in the previous section, the gratings fabricated in the context of this thesis are third order grating (i.e. Λ_p is equal to 858 nm and Λ = 286 nm). However, this fact does not bring confusions or errors since the Δn function displayed in this thesis comes from reconstruction of experimental measurement, which already takes into account the Δn amplitude reduction related to the grating order and corrugation shape.

The required corrugation amplitude for long gratings is typically much smaller than the minimum feature size allowed by CMOS compatible facilities. As a result, the lithography and etching steps severely modify the corrugation shapes (i.e. a rectangular corrugation will be severely rounded). As a result, if one is interested to predict the fabricated coupling coefficient, the appropriate permittivity variation profile must be determined. To do so, it is possible to either use an algorithm modeling the fabrication effect on the design [60] or to use a scanning electron microscope (SEM) image to measure it. Afterwards, the waveguide width variation should be parameterized using an appropriate function (i.e. square function, triangular function, sinusoidal function, rounded square wave function). Then, the Fourier term corresponding to the target resonant wavelength should be calculated. Furthermore, the importance of the longitudinal coupling coefficient should be evaluated. Obviously, this is not a trivial work and was not considered necessary for this thesis.

Inserting Eq. (1.4) into Eqs. (1.1) and (1.2), the coupled mode equations can be simplified to

$$\begin{aligned} \frac{\partial A}{\partial z} &= iB\kappa\left(e^{-i(2\beta z-G(z))}+e^{-i(2\beta z+G(z))}\right) \\ \frac{\partial B}{\partial z} &= -iA\kappa\left(e^{i(2\beta z+G(z))}+e^{i(2\beta z-G(z))}\right) \end{aligned}. \tag{1.8}$$

If we define a detuning parameter, such as,

$$\delta=\beta-\frac{1}{2}\frac{\partial G}{\partial z} \tag{1.9}$$

$$\begin{aligned} \delta(z) &= \frac{2\pi n(\lambda)}{\lambda}-\frac{\pi}{\Lambda}-\frac{1}{2}\frac{\partial\theta(z)}{\partial z} \\ &= \delta_0-\frac{1}{2}\frac{\partial\theta(z)}{\partial z} \end{aligned}, \tag{1.10}$$

where δ_0 is the designed detuning parameter, we obtain

$$\begin{aligned} \frac{\partial A}{\partial z} &= iB\kappa e^{-i2\delta z} \\ \frac{\partial B}{\partial z} &= -iA\kappa e^{i2\delta z} \end{aligned}, \tag{1.11}$$

where the higher harmonics have been neglected since they do not lead to phase matched mode coupling. Finally, using the following change of variable

$$\begin{aligned} A &= u\,\mathrm{e}^{-i\delta z} \\ B &= v\,\mathrm{e}^{i\delta z} \end{aligned}, \tag{1.12}$$

Eq. (1.11) becomes the well-known coupled equations [66]

$$u'=i\left(\delta u+\kappa v\right) \tag{1.13}$$

$$v'=-i\left(\delta v+\kappa u\right), \tag{1.14}$$

where *u* and *v* are the slowly varying amplitude of the forward and backward waves. It must be pointed out that if the effective index is varying along the *z*-axis, as it is the case when phase noise is considered (refer to Chapter 2 and 3) or whenever the waveguide width is voluntary modified [50], Eq (1.10) becomes

$$\begin{aligned}\delta(z) &= \frac{2\pi\left[n(\lambda)+\Delta n_z\right]}{\lambda} - \frac{\pi}{\Lambda} - \frac{1}{2}\frac{\partial\theta(z)}{\partial z} \\ &= \frac{2\pi n(\lambda)}{\lambda} - \frac{\pi}{\Lambda} - \frac{1}{2}\frac{\partial\theta(z)}{\partial z} + \frac{2\pi\Delta n_z}{\lambda}\end{aligned} \tag{1.15}$$

$$\begin{aligned}\delta(z) &= \frac{2\pi n(\lambda)}{\lambda} - \frac{\pi}{\Lambda} - \frac{1}{2}\frac{\partial\Phi(z)}{\partial z} \\ &= \delta_0 - \frac{1}{2}\frac{\partial\Phi(z)}{\partial z}\end{aligned}, \tag{1.16}$$

where a new phase term, given by

$$\Phi(z) = \theta(z) - \frac{2\pi}{n_0\Lambda}\int_0^z dz'\Delta n_z(z') \tag{1.17}$$

is defined to take into account all the *z*-varying parameter of the gratings i.e. including the new effective index variation along the z-axis parameter given by Δn_z (the label "*z*" has been used to prevent confusion with the grating effective index perturbation symbol "Δn"). In Eq. (1.17), the wavelength has been approximated to be equal to the designed Bragg wavelength at 1550 nm (i.e. $2n_0\Lambda$). In subsequent chapters, the experimentally retrieved grating phase information is going to be represented by the Bragg wavelength (λ_B) which, using Eqs. (1.7) and (1.16), can be associated to the grating parameters by the following expression:

$$\lambda_B(z) = \frac{2n_g\Lambda}{1 + \frac{\Lambda}{2\pi}\frac{\partial\Phi(z)}{\partial z} - 2n_1\Lambda}. \tag{1.18}$$

1.4 – Numerical simulations of Bragg grating response

In this section, two techniques that solve Eqs. (1.13) and (1.14) for arbitrary gratings are considered. The boundary conditions are $u(-L/2) = 1$ and $v(L/2) = 0$, where L is the grating length. The first technique uses the transfer matrix formalism while the second one considers the special case of weak gratings.

1.4.1 – Transfer matrix solution

The transfer matrix approach links the field u and v at the input of the grating to the field at its output with the following matrix

$$\begin{bmatrix} u(-L/2) \\ v(-L/2) \end{bmatrix} = \begin{bmatrix} 1/t & r^*/t^* \\ r/t & 1/t^* \end{bmatrix} \begin{bmatrix} u(L/2) \\ v(L/2) \end{bmatrix}, \tag{1.19}$$

where r and t are the complex reflection and transmission coefficient of the structure. Fortunately, the coupled-mode equations have an analytical solution for the special case of uniform gratings ($\kappa(z) = \kappa_0$ and $\delta(z) = \delta_0$). The reflection and transmission coefficient are given by

$$r = -\frac{\kappa_0 \sin(\sqrt{\delta_0^2 - \kappa_0^2}\,L)}{\delta_0 \sin(\sqrt{\delta_0^2 - \kappa_0^2}\,L) + i\sqrt{\delta_0^2 - \kappa_0^2}\cos(\sqrt{\delta_0^2 - \kappa_0^2}\,L)} \tag{1.20}$$

$$t = \frac{i\sqrt{\delta_0^2 - \kappa_0^2}}{\delta_0 \sin(\sqrt{\delta_0^2 - \kappa_0^2}\,L) + i\sqrt{\delta_0^2 - \kappa_0^2}\cos(\sqrt{\delta_0^2 - \kappa_0^2}\,L)}. \tag{1.21}$$

As a result, the spectral response of any tailored gratings can be calculated by decomposing it in many short sections, short enough to consider the grating uniform over the section length. The field is then propagated along the grating structure. The total matrix of the structure can be calculated numerically and, by using the appropriate boundary condition, the grating reflection and transmission coefficient are found. The simulation tool used in this thesis is quite similar to those already presented in the literature [66], [67]. More specifically, using Eq. (1.20) and (1.21) to obtain 1/*t* and *r*/*t* gives

$$\frac{1}{t} = \cosh(\sqrt{\kappa_0^2 - \delta_0^2} L) - \frac{i\delta_0}{\sqrt{\kappa_0^2 - \delta_0^2}} \sinh(\sqrt{\kappa_0^2 - \delta_0^2} L) \tag{1.22}$$

$$\frac{r}{t} = \frac{i\kappa_0}{\sqrt{\kappa_0^2 - \delta_0^2}} \sinh(\sqrt{\kappa_0^2 - \delta_0^2} L). \tag{1.23}$$

The insertion of Eqs. (1.22), (1.23) in (1.19) give the same transfer matrix discussed in [67]. Other approaches exist to solve the coupled-mode equations. For example, it is possible to solve them, once reduced to a single Riccati differential equation, using a Runge-Kutta algorithm [68]. However, this approach might lead to excessive convergence time. Bragg gratings spectral responses can also be simulated using the Rouard method [69], [70] which consist of discretizing the grating in a succession of discrete reflectors. This technique provides the grating reflectivity product by a “sinc” function which depends on the discrete reflector thickness. This approach might create numerical error, especially for gratings with wide spectrum. Thus, because of its flexibility and reliability, the transfer matrix approach has been chosen for this thesis.

1.4.2 – Weak grating approximation

The last approach discussed in this chapter to solve the coupled mode equations considers the special case where the grating coupling coefficient is small (also called the Born approximation). This approximation provides an analytical solution to the coupled-mode equations [64], [71]. More specifically, Eqs. (1.13) and (1.14) can be simplified by neglecting the coupling between the modes in Eq. (1.13). As a result, it can be found that $u = \exp\left[i \int dz \delta(\mathrm{z}) \right]$, which means that the mode simply propagates through the structure. Inserting this solution into Eq. (1.14) gives

$$v' = -i\left(\delta v + \kappa \, \mathrm{e}^{i \int dz \delta(\mathrm{z})} \right). \tag{1.24}$$

Such first order differential equation can be solved analytically [72]. When the boundary conditions stated in the previous section are applied, we find that the grating complex reflectivity is given by

$$r = -\int_{-L/2}^{L/2} dz\kappa\left(z\right)e^{2i\int_0^z dz'\delta(z)} . \tag{1.25}$$

Although the latter equation is the one used in chapter 2, it is interesting to make the detuning *z*-dependency explicit. Considering Eq. (1.16), we obtain

$$\begin{aligned} r(\delta_0) &= -\int_{-L/2}^{L/2} dz\kappa\left(z\right)e^{-2i\int_0^z dz'\left(-\delta_0+\frac{1}{2}\Phi'(z')\right)} \\ &= -\int_{-L/2}^{L/2} dz\kappa\left(z\right)e^{-i\Phi(z)}e^{2i\delta_0 z} \\ &= -\int_{-\infty}^{\infty} dz\frac{\kappa\left(z/2\right)}{2}e^{-i\Phi(z/2)}e^{i\delta_0 z} \end{aligned} , \tag{1.26}$$

where the last equality is obtained by making the change of variable 2*z* ⟶ *z* and by extending the integral interval over infinity. This latter operation does not add any error since $\kappa = 0$ for $|z| > L/2$. By doing this change of variable, we see that the grating physical structure

$$-\frac{\kappa\left(z/2\right)}{2}e^{-i\Phi(z/2)}$$

is forming a Fourier transform pair with its complex reflectivity. Furthermore, the Fourier transform of *r* is also the grating impulse response (*h*). Thus, according to (1.26), since

$$\mathrm{FT}\left\{r\right\} = -\frac{\kappa\left(z/2\right)}{2}e^{-i\Phi(z/2)} , \tag{1.27}$$

the Born approximation allows associating the grating structure to the grating impulse response (*h*), such as [73]

$$\kappa\left(z\right)e^{-i\Phi(z)} = -2h\left(2z\right). \tag{1.28}$$

This equation will be used in the following section to achieve the grating reconstruction.

Knowing that the weak grating spectral response is linked with a Fourier transform to its physical structure provides a good intuition of gratings behaviour. Moreover, it is important to mention that many of the Fourier transforms properties such as translation, frequency shift and scaling can be applied even to strong gratings. These properties are formally derived in [74], [75].

1.5 – Grating reconstruction

As discussed previously, when the grating structure is known, the complex spectral response of the grating can be calculated and this operation is referred to the direct scattering problem [73]. However, in some situation, it is essential to calculate the physical structure of the grating from a complex spectral response. This inverse scattering problem may happen in two different contexts: 1) in a synthesis problem, where the grating physical profiles are calculated from the desired spectral response and 2) in a reconstruction problem, where the grating physical profiles are retrieved from experimental measured complex spectral responses. This latter problem is the one that needed to be solved in the context of this thesis.

Several approaches have been proposed to solve the inverse scattering problem of Bragg gratings, however, in this thesis, the integral layer peeling (ILP) algorithm has been preferred [73] since it allows the reconstruction of strongly reflective gratings, which is a necessary feature for integrated gratings in SOI due to the high index contrast of silicon and silica. For more information on other approaches to solve the inverse scattering problem, the reader should refer to [73], [76] and the references therein.

Briefly, the algorithm separates the structure in M layers having a length Δz. Each layer, labeled by "m", is composed of non-uniform amplitude and phase profiles. These variables are shown on the schematic of Fig. 5. This approach reduces the error of the reconstruction, especially for strong gratings, since the algorithm considers that the reflectivity may decrease significantly from one facet of the layer to the other. The local position within a layer is identified by z'. When the layers are small enough to use the Born approximation, the local reflectivity of a single layer can be considered small even for strong gratings which leads to the simple recursive formula

$$r_{m+1} = \exp\left(-2i\delta_0\Delta z\right)\frac{r_m\left(\delta_0\right)-\overline{r}_m\left(\delta_0\right)}{1-r_m\left(\delta_0\right)\overline{r}_m^*\left(\delta_0\right)}, \tag{1.29}$$

where

$$\overline{r}_m\left(\delta_0\right) = \int_{-\infty}^{2\Delta z} d\tau h_m\left(\tau\right)\exp\left(i\delta_0 t\right). \tag{1.30}$$

The recursive formula allows calculating the local reflection coefficient before the next layer. The grating structure of the m^{th} + 1 layer is thus given by the local impulse response, such as

$$\kappa\left(m\Delta z + z'\right)e^{-i\Phi\left(m\Delta z+z'\right)} = -2h_m\left(2z'\right) \qquad 0 \le z' \le \Delta z \ . \tag{1.31}$$

Eq. (1.29), (1.30) and (1.31) are the one that has been used to reconstruct the grating structure presented in this thesis.

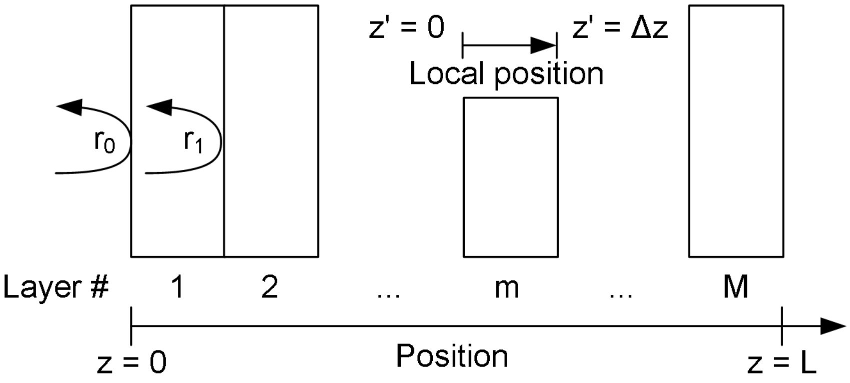

Fig. 5: Schematic of the ILP algorithm

The algorithm works as follow: r_0 is the experimentally measured complex spectral response of the grating. The first layer structure is found by applying a fast-Fourier transform algorithm on r_0, which provides h_0. Afterward, using Eq. (1.31), one can obtain the grating coupling amplitude and phase information of the first layer. Subsequently, $\overline{r}_0$ is found with h_0 and Eq. (1.30) and r_0 and $\overline{r}_0$ are used to obtain r_1 with Eq. (1.29). This procedure is reproduced over the whole grating length. Every spectral measurement taken in this thesis has been obtained with a commercial optical frequency domain reflectometer (OFDR) from LUNA technologies.

1.6 – Elaborate grating structures

In this thesis, many references are made to the fabrication of “elaborate gratings” or “complex spectral responses”. Obviously, the complexity of a grating is a qualitative description and the goal of this section is to illustrate more precisely how the complexity of a grating structure can improve the filter response. Unfortunately, when the grating complexity is increased, the fabrication yield is likely to be reduced, which is why designing elaborate gratings must be done carefully. The grating complexity is higher when the grating coupling amplitude and phase vary significantly (i.e. $|\partial\kappa/\partial z|$ and $|\partial\lambda_B/\partial z|$). Moreover, the difficulty in fabricating a grating is strongly dependant on the material. For example, designing FBGs having large κ can be challenging due to the relatively small index change that can be photo-induced. For IBGs in SOI, the main issue comes from random geometrical variations of the waveguide which induce phase noise (refer to chapter 2 and 3). As will be shown in chapter 2, the phase noise impact on the grating spectral response increases as the square of κL and as a square root of L. In other words, when the grating reflectivity or when the grating length is increased, spectral distortions are going to be stronger. Thus, the fabrication yield is decreased. However, increasing the grating complexity, or equivalently designing filter with tailored spectral responses, is beneficial (and sometime necessary) for many applications [24]–[31].

To illustrate this concept, we consider the design of a WDM add/drop filter having a designed reflectivity and bandwidth of respectively -0.04 dB (99 %) and 8 nm (i.e. appropriate for coarse WDM network). As a first tryout, let’s consider a uniform grating. In this example, the target reflectivity defines the κL product and the grating length is fixed using the bandwidth requirement (i.e. $\kappa = 36.5\ \mathrm{mm}^{-1}$ and $L = 82\ \mu\mathrm{m}$). As can be seen in black in Fig. 6 (which shows the reflection amplitude and dispersion in a) and b) respectively and the grating Bragg wavelength and coupling coefficient in c) and d)), the use of a uniform grating for WDM filter might not be appropriate due to the low side-lobe suppression ratio (SLSR). Low SLSR creates crosstalk between channels and, ultimately, increases the bit error rates. However, it is possible to increase the SLSR by increasing the complexity of the grating coupling amplitude profile (apodizing the grating) as shown in red in Fig. 6. This Gaussian apodization, which has a full-width at half-maximum of 70 μm, increases the SLSR by 13 dB. To maintain the same bandwidth and reflectivity, the maximal value of κ as well as the grating length had to be slightly increased to 43 mm^{-1} and 105 µm respectively.

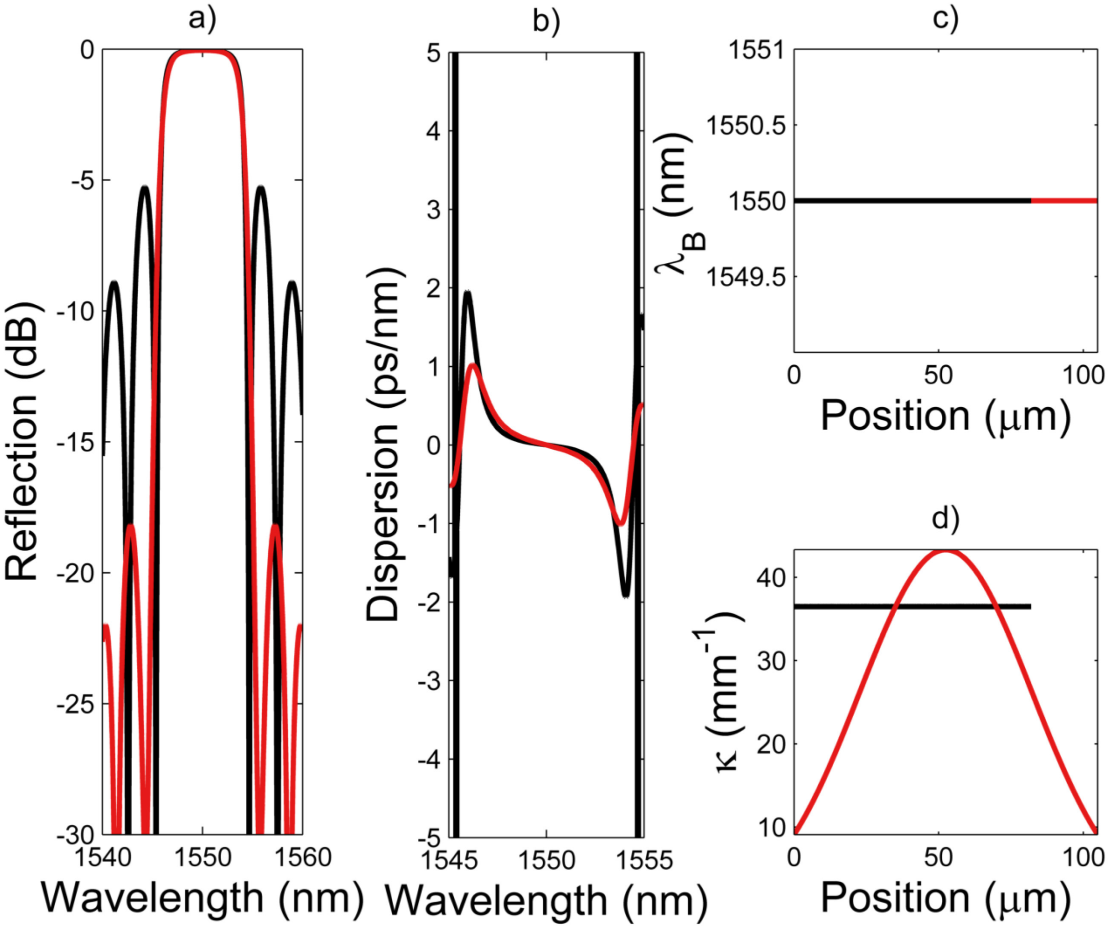

Fig. 6: a) Simulated reflection spectrum b) dispersion, c) Bragg wavelength profile and d) coupling coefficient profile of a uniform Bragg grating (in black) and a gaussian apodized grating (in red). The gratings length is respectively 80 µm and 105 µm.

In order to further improve the filter shape, one might be interested to design a grating having flat-top dispersion-less response. Such grating structure, obtained with the ILP algorithm described in section 1.5 and shown in blue in Fig. 7, has an increased complexity since the Bragg wavelength and coupling coefficient profiles variations are much more important. Moreover, compared to the Gaussian apodized uniform grating structure (shown in red), the grating length had to be increased significantly (from 105 µm to 1600 µm). This can be understood with the Fourier transform scaling property, discussed in section 1.4.2 since faster variations in one domain (i.e. sharp edges in the spectral domain) result in longer structures in the other. However, the improvements obtained with this elaborate grating can be beneficial since the filter SLSR is increased by another 13 dB, the sharpness of the amplitude response is increased and fit closely to the WDM channel bandwidth and the optical phase does not experience significant chirp anymore, which could be desirable at high bit-rate. This example clearly shows the benefit that can be obtained by increasing the grating complexity (amplitude, phase and length).

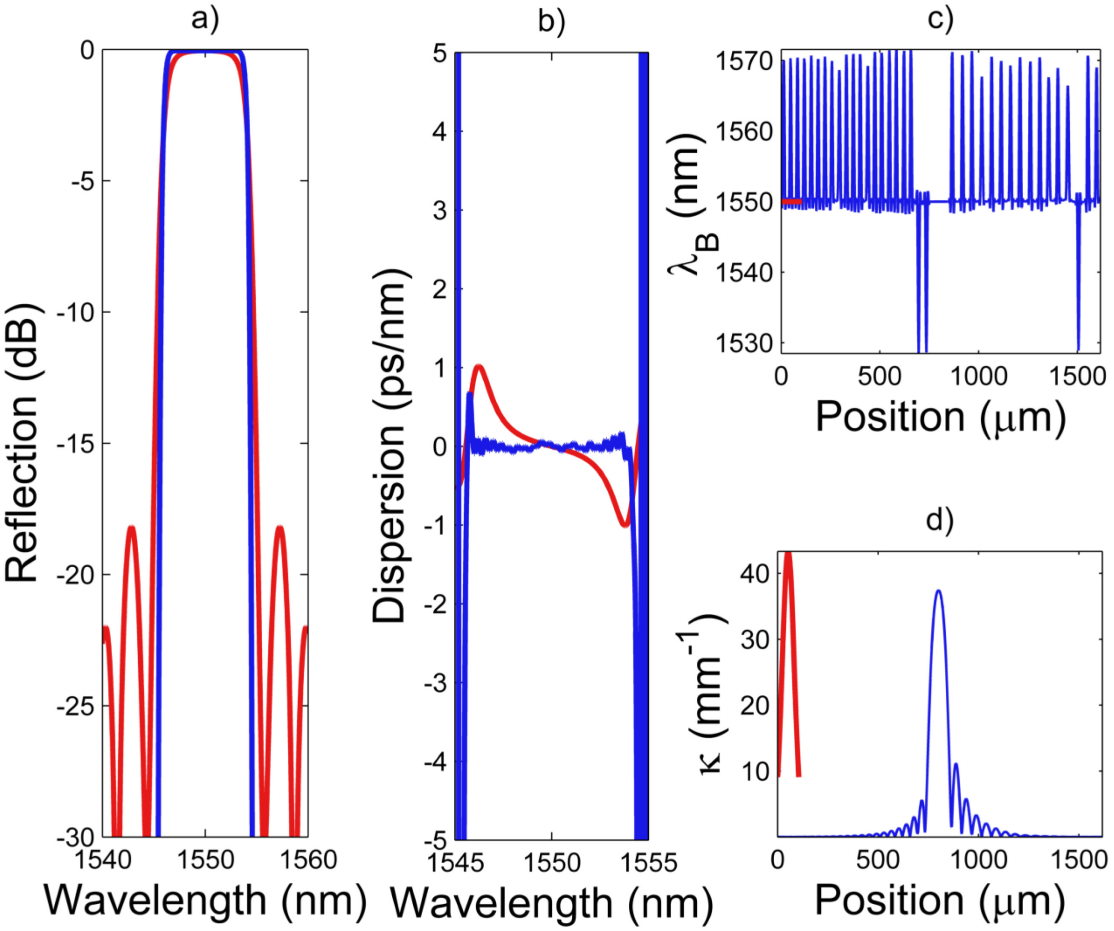

Fig. 7: a) Simulated reflection spectrum b) dispersion, c) Bragg wavelength profile and d) coupling coefficient profile of a gaussian apodized grating (in red) and a tailored dispersion-less flattop Bragg grating (in blue). The gratings length is respectively 105 μm and 1600 μm.

For this filter to be feasible experimentally the apodization technique must be reliable in order to define correctly the sinc-like shape and the phase noise must not be too significant otherwise the grating spectral response will be severely distorted compared to the design. An interesting point that can be seen from Fig. 7-d) is that as the grating complexity increases (the blue curves), the required grating coupling coefficient is likely to be reduced, at least at some specific positions (on the grating sides in the example discussed here). As a result, there is a strong motivation to develop apodisation techniques compatible with small κ values (work done in chapter 4). If the fabrication technology limits the grating length and/or the minimum coupling coefficient that can be fabricated, the designed grating response is going to be distorted, as shown in Fig. 8 where the tailored grating presented above is cut closer to the coupling coefficient main lobe (the gratings in cyan and red are 950 µm and 600 µm long respectively). Thus, this figure shows that a reduction of the grating length will increase the oscillation in the phase of the spectral response of the grating. This grating design has been chosen in this section especially because the optical phase is particularly sensitive which illustrates well the necessity to develop a reliable technology to fabricate long IBGs compatible with weak coupling coefficients. A short mention should also be made on the Bragg grating profile. As can be seen in Fig. 7-c) and Fig. 8-c), a series of phase shift structure are required at the location of the zeroes of the apodization profile. However, since

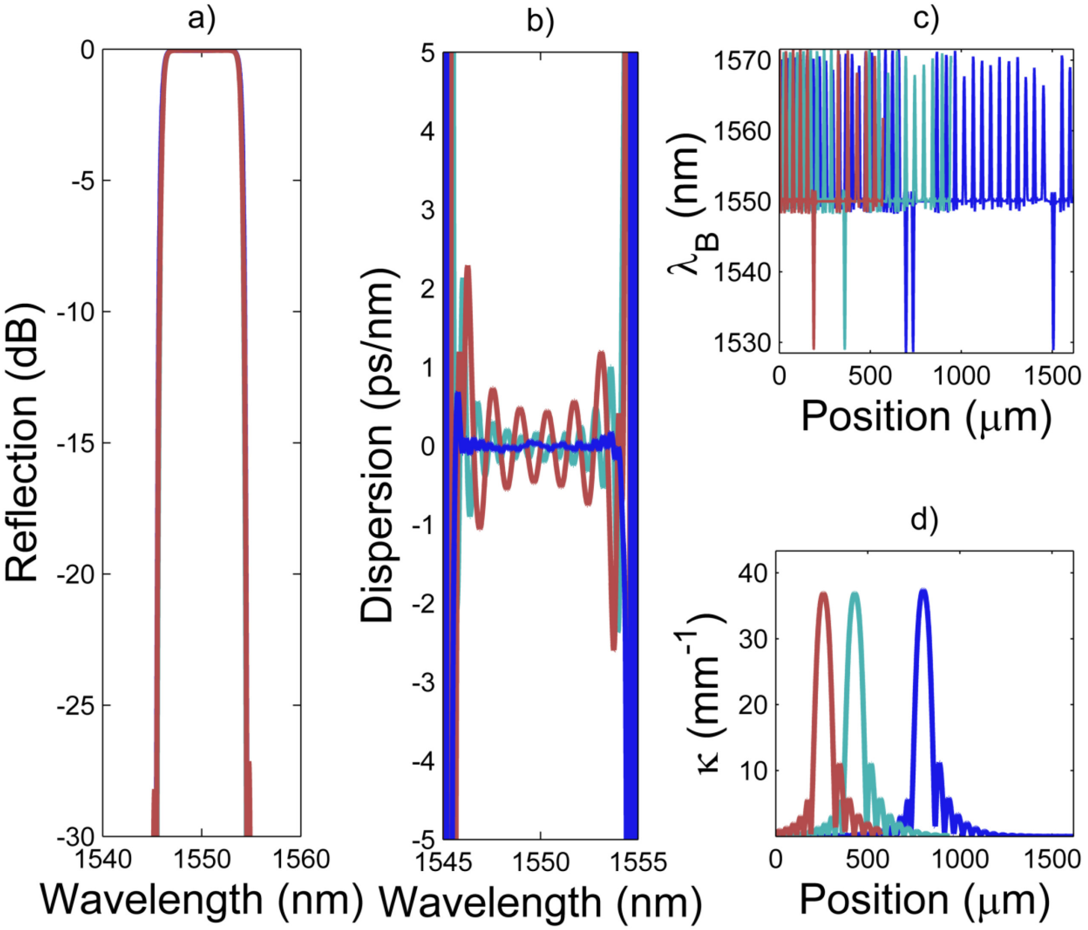

Fig. 8: a) Simulated reflection spectrum b) dispersion, c) Bragg wavelength profile and d) coupling coefficient profile of the same tailored dispersion-less flattop Bragg grating cut at different distance from the main coupling coefficient lobe. The length of the grating in blue is 1600 µm while the grating in cyan and red are respectively 950 µm and 600 µm.

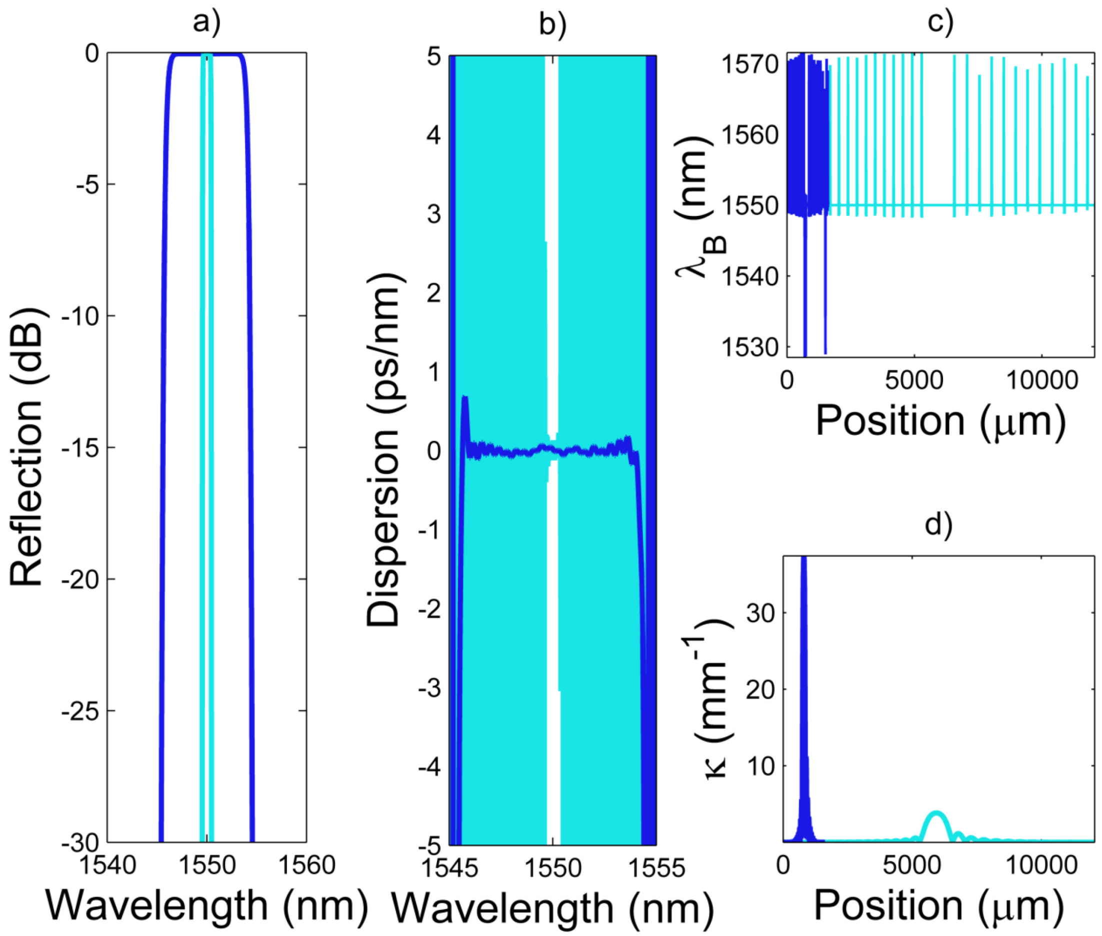

Fig. 9: a) Simulated reflection spectrum b) dispersion, c) Bragg wavelength profile and d) coupling coefficient profile of tailored square-shape-zero-dispersion Bragg grating for coarse (in blue) and dense (in cyan) WDM application. The gratings length is respectively 1600 μm and 12 000 μm.

Bragg gratings are not affected by high frequency variations (as discussed in chapter 2), the reconstruction algorithm cannot provide discrete phase shifts. Thus, before fabricating this structure, a performance comparison should be made between this structure and one where these distributed phase shifts are replaced by discrete phase shifts that are easier to fabricate.

Finally, to further increase the data-traffic in a WDM system, one could also be interested to design a similar filter, but for dense WDM applications. In this situation, the channel bandwidth is reduced to 100 GHz (in this example). Once again, the Fourier transform scaling property involves an increase in the required grating length, as shown in Fig. 9 where the length of the grating in cyan is 12 mm. The phase noise inherent to IBG in SOI will reduce the yield of such filter. As a result, this narrow band filter is a much more complex structure to fabricate. However, the increased data-rate that can be obtained with dense WDM network, compared to coarse

WDM network, is a strong motivation to keep improving the Bragg grating fabrication capabilities.

1.7 – Characterization of integrated Bragg gratings

Most work focusing on integrated Bragg gratings only provides the spectral response amplitude in transmission, which incompletely characterizes the grating. Indeed, phase measurement is difficult because the device under test is embedded between reflective structures (grating couplers, cleaved fibers and/or cleaved facets) that interfere with the wave reflected form the IBGs. This section which is strongly inspired by [35], a conference paper presented at *Bragg Gratings, Photosensitivity, and Poling in Glass Waveguides* in 2012, addresses this issue by providing a technique to post process the retrieved complex spectral response of the component, reduce the measurement high frequency noise and reconstruct the grating structure. This procedure is used throughout this thesis to optically characterize IBGs phase noise (chapter 3), to confirm the reliability of the apodization technique (chapter 4) and to confirm that the phase compensation of spiral-waveguides was done correctly (chapter 5). Briefly, the main steps used to characterize IBGs are: 1) characterizing the complex spectral response in reflection using and OFDR, 2) applying a time filter to suppress spurious reflections, 3) reconstructing the grating structure using the ILP algorithm to obtain the spatial profiles of the IBG and 4) comparing the measured and reconstructed spectral response.

1.7.1 – Complex spectral response measurement in reflection

When the light is injected in the SOI chip, spurious reflections can interfere and distort the grating reflection spectrum. Recently, a data processing approach was used to retrieve the grating spectral response when using butt coupling [77]. In this work, the authors considered that their gratings were surrounded by two waveguide (propagation region) and two strong reflectors (created by the silicon-air interface), which allows them to successfully isolate the IBG spectral response from the Fabry-Perot response. However, this method cannot be applied to most elaborate photonic integrated circuits since many reflections might occur at different positions.

Fig. 10-a) shows a typical time response of an IBG in reflection. Specifically, this IBG is a straight grating described in Table 1 and represented in Fig. 4. The origin of the graph

corresponds to the reflection from the input fiber end and time-to-position conversion is done to match the 4 mm component length (the grating has a length of 2 mm). Although this procedure neglects possible effective index changes along the waveguide, it still gives precious information on the position of each event.

1.7.2 – Time filtering of the measured impulse response

The impulse response shown in Fig. 10-a) is separated in five distinct sections. Sections A and E correspond to the reflection coming respectively from the input and output cleaved fiber end. Sections B and D correspond to the grating coupler, the subsequent taper and the singlemode waveguide. These latter sections can be separate in two subsections; one without significant reflected amplitude (first half of section B and second half of section D) which corresponds mostly to the tapers, and one with relatively important reflection amplitude compared to the grating (second half of B). As shown in Fig. 4, these subsections correspond to the 500 nm wide single transverse electric mode (TE-mode) waveguides. As discussed in [78], the measured reflection is a SWR induced reflection. This backscattered light due to SWR is depending on the waveguide width and, as it increases, the mode intensity on the sidewall is reduced which involves a reduction of the backscattered light. Thus, the measured reflection is significant only on a limited interval in section B and D since the 500 nm wide waveguides are surrounded by adiabatic tapers. From IBG perspective, this measurement shows that singlemode waveguides suffer from backscattered light induced by SWR that might have amplitude comparable to an IBG. This phenomenon should be suppressed as much as possible since it increases the measured noise level in reflection which reduces the grating characterization precision using the ILP algorithm. Finally, it can be noticed that there is a reflection spike in section B that is not present in section D although both sections are nominally identical. This spike is likely coming from a discrete reflection that happens at the bottom of the silicon substrate, which has a thickness of ~ 700 μm. It can appear if the IBG resonance does not match the grating coupler resonance. As a result, the fiber injection angle must be modified to match these resonances and, in this situation, the injection angle was close to a normal injection which allowed some light to be coupled back in the input fiber.

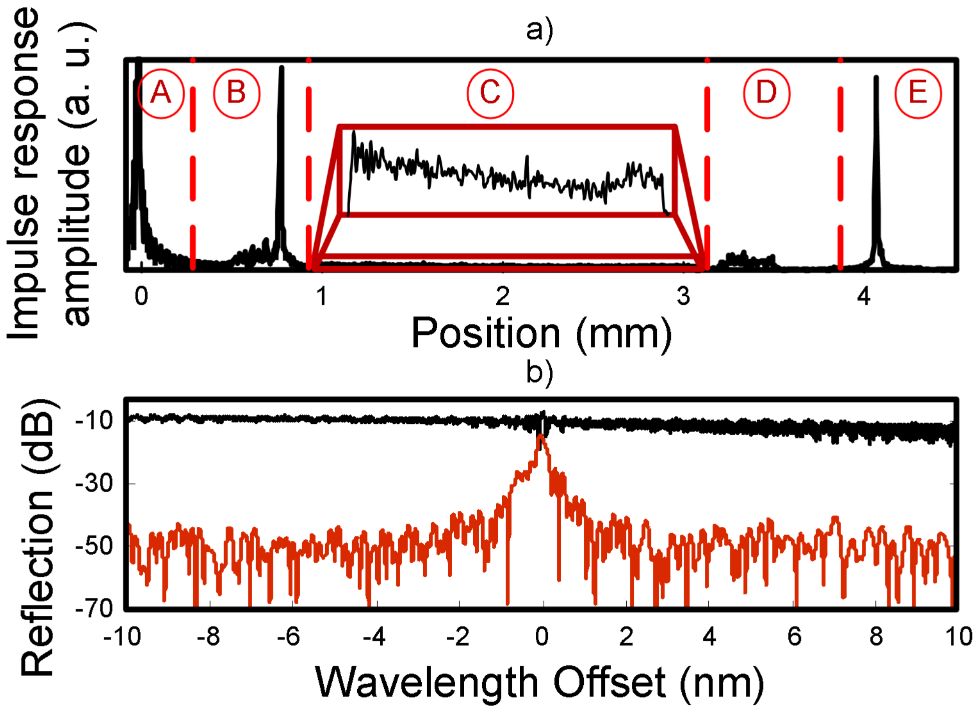

Fig. 10: a) Amplitude of the impulse response as a function of propagation distance in the device. b) Reflection spectrum without time-filtering (black) and with the section C time-filtered (red)

The four sections mentioned above, when time filtered independently, do not exhibit any resonance at the IBG frequency. They are wideband reflection. Section C corresponds to the IBG. As mentioned previously, the singlemode waveguides (section B and D) are important to excite the fundamental mode of the multimode section. Fig. 10-b) shows the spectral response of the raw data (black) and of the one obtained with a rectangular time window to extract section C (red). On this figure, the insertion loss caused by the grating coupler has been removed. The processed data clearly shows the resonance of a weak grating, which was unclear using the raw data.

1.7.3 – Grating reconstruction using the ILP algorithm

To characterize the IBG amplitude and phase profiles, the ILP presented above is applied to the processed data. Due to the recurrent use of the fast-Fourier transform algorithm in the ILP algorithm, the spatial resolution of those profiles depends on the measured optical bandwidth and, since IBGs are narrowband filters, most of the information is noise (corresponding to a wavelength offset larger than ~ ±1.5 nm for the grating shown in Fig. 11-a)). As a result, the phase and amplitude profiles, shown in Fig. 11-b) and c), contain both low frequency variations that alter the grating spectrum and higher frequency variations that are artefacts, due to out-of-band measurement noise, hiding the relevant information. Consequently, the retrieved profiles should be low-pass filtered. As shown in [41][II], IBGs reflection spectrum are distorted by spatial frequencies lower than $f_c \approx \left(2n_g/\overline{\lambda_B}\right)\left(\overline{\lambda_B}/\Delta\lambda - 1\right)^{-1}$, where $\Delta\lambda$ is the spectrum width taken at the noise level and $\overline{\lambda_B}$ is the average Bragg wavelength which, in the special case of a uniform grating, is given by

$$\overline{\lambda_B} = \frac{2n_g\Lambda}{1-2n_1\Lambda}. \tag{1.32}$$

1.7.4 – Comparison of the reconstructed and measured spectra

The spectral response can then be reconstructed from the retrieved and filtered grating coupling amplitude and phase profiles with a standard transfer matrix solution of the coupled mode equations. Fig. 11-a) compares the grating experimental spectrum with reconstructed one with different cut-off frequencies: the reconstructed spectrum without spatial filtering is shown by the black curve while the green and blue curves are reconstructed spectra with cut-off frequencies corresponding to $\Delta\lambda$ = 3 nm and $\Delta\lambda$ = 1.5 nm respectively. All the reconstructed spectra follow closely the experimental one for wavelength offset smaller than 1.5 nm which gives good confidence in the reconstruction technique. It should be noted that in this thesis, the value $\Delta\lambda$ is determined by the grating bandwidth at the measurement noise floor ($\Delta\lambda$ = 1.5 nm for the example above).

[II] Chapter 2 is a reproduction of paper [41]; the derivation of f_c is made in this chapter.

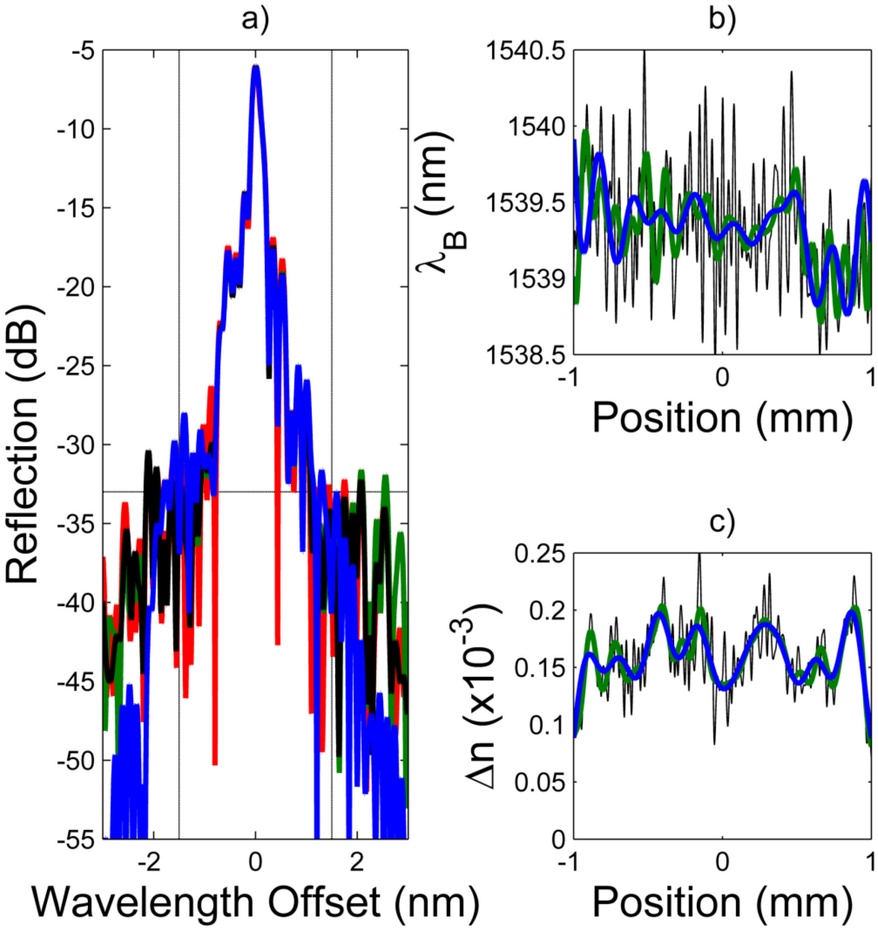

Fig. 11: a) Comparison of the experimental reflection spectrum of an unapodized grating (red) to the reconstructed spectrum without spatial filtering (black), with Δλ = 3 nm (green) and Δλ = 1.5 nm (blue). The retrieved b) λ_B and c) Δn profiles associated to the spectrum of a)

Chapter 2: Impact of Sidewall Roughness on Integrated Bragg Gratings

A wide variety of waveguide size has been used in the SOI platform. However, the silicon photonic community has oriented its effort mostly towards sub-micrometer silicon thickness (typically 220 nm) because of the high modal confinement. Such structure, compared to micrometer-size cross-sections, is beneficial to the design of highly integrated circuits, since it allows tight curvature.

To be compatible with other integrated silicon components, singlemode waveguides having both sub-micrometer thickness and width have first been considered at the start of this project. Unfortunately, such highly confined waveguides suffer from a high level of phase noise which distorts the Bragg grating spectral response. This issue is addressed in the two following chapters. This chapter, a reproduction of [41] published in the "*Journal of Lightwave Technology*" in 2011, models numerically and analytically the SWR impact on the grating spectral response. The analysis has been done solely on SWR since this effect is the dominant one for singlemode photonic wires. The conclusion drawn in this chapter has led us to use hybrid singlemode/multimode waveguides in subsequent works (chapter 3 to 5).

2.1 – Abstract

A major issue in the fabrication of IBG filters in highly confined waveguides is the average effective index fluctuations caused by SWR. In this work, we model the impact of this effect on IBG spectral responses and we identify key parameters that need to be controlled in order to minimize distortions. We show that only low spatial frequency components of the noise are relevant to the calculation of the IBG spectral response, which decreases considerably the computation time. Furthermore, we present an IBG emulator that allows estimation of expected fabrication yield of specific gratings given that the fabrication process is well characterized. The analysis of apodized gratings is used as an example to illustrate how this modeling can help to reduce development cost by first studying robustness of IBG designs to fabrication limitations. Finally, we study analytically the impact of SWR having short correlation lengths and small roughness variances on the spectral response of weak gratings.

2.2 – Introduction

There are currently major research efforts worldwide to develop photonic integrated circuits for telecommunication applications using SOI. The goal is to provide a low-cost small-footprint platform to integrate several functions on the same photonic chip. One type of components typically required for WDM systems are optical filters with flexible and precise spectral responses. IBG structures in SOI could provide greater tuning properties, compared to FBGs, through the plasma dispersion [79], [80] or the thermo-optic [81], [82] effects. To obtain IBGs with complex spectral responses, long structures must be used (tens of thousands of periods). Very recently, footprint reduction of long IBGs has been proposed using curved waveguides [83], [84]. Large scale integration of IBGs could be achieved with a photonic wire in a spiral shape without having a significant impact on the grating spectral response [83]. However, long grating structures are more sensitive to phase noise induced by SWR.

Over the past few years, a lot of work has been dedicated to model propagation losses caused by SWR [85]–[87]. Simultaneously, other researchers have focused their efforts on reducing the waveguides roughness by optimizing the lithography techniques and etching conditions [88], [89]. Furthermore, the effect of SWR on Bragg gratings in silica waveguides has been studied theoretically in [90]. However, this work is limited to the analysis of the average impact of the noise, which does not provide any information on the resulting distortion of the grating spectral response. In addition, in waveguides with high index contrast, such as photonic wires in SOI, SWR severely degrades the performance of long IBGs because small waveguide width variations induce significant modifications of the mode effective index. Consequently, since this effect cannot be neglected in SOI waveguides, as it is the case for silica waveguides, there is great interest in modeling it in order to develop robust grating designs that will lead to reasonable fabrication yields. The model can also be useful to guide future refinement of fabrication processes by establishing targets for desired roughness parameters.

This work is structured as follows: section 2.3 summarizes briefly the SWR model used in this chapter. In section 2.4, we describe how our model converts the SWR information in an effective index variation. This information will be used in the following sections to model the grating spectral response. In section 2.5, an IBG emulator based on coupled-mode theory is presented and simulated spectra are qualitatively compared to experimental ones in order to examine the validity of the approach. We also examine the noise spatial frequencies that are needed in order to accurately model the grating spectral responses. We find that the noise spectral density content below a cutoff frequency of typically 0.1 μm^{-1} is the most relevant. Section 2.6 presents numerical results of unapodized and apodized uniform-period gratings obtained with this IBG emulator in order to evaluate the apodization resistance to SWR. This section shows how to use the emulator in order to predict IBG yield, hence saving a huge amount of time, effort and resources. Section 2.7 presents analytical results on the behavior of weak gratings in the presence of SWR. In this section, we use the weak grating approximation of the usual coupled-mode equations. Finally, section 2.8 proposes some approaches to mitigate the impact of SWR on IBG spectral responses.

2.3 – Sidewall roughness model

As discussed in [85]–[87], SOI platforms have very high quality Si/SiO$_2$ interfaces due to the high precision of the wafer fabrication process. However, the etching process typically leaves vertical stripes [91], as illustrates in Fig. 12, creating sidewall fluctuations that follow a normal distribution. The spatial frequency content of a random process, X, is described by its power spectral density function, G_X, which is the Fourier transform of its autocorrelation function, R_X. Thus, the spatial frequency content is described by the spectral density function, G_{SWR}, which is the Fourier transform of the sidewall autocorrelation function, R_{SWR}, defined by

$$R_{SWR}\left(\Delta z\right) = \lim_{L\to\infty} \frac{1}{L}\int_{-L/2}^{L/2} \Delta x(z)\Delta x(z+\Delta z)dz\,, \tag{2.1}$$

where Δx is the deviation of the sidewall from its average position and Δz is the spatial shift along the waveguide propagation axis. Throughout this thesis, many random processes will be discussed (i.e. the effective index, the Bragg wavelength, the SWR, the wafer height fluctuation (WHF), etc.). To simplify the notation, σ_X is going to refer to the standard deviation of the process. Similarly, $L_{c,X}$ is going to refer to the autocorrelation length of X. For lithographically-defined waveguides, the autocorrelation function is typically given by [92]

$$R_{SWR}\left(\Delta z\right) = \sigma_{SWR}^2 \exp\left(\frac{-\left|\Delta z\right|}{L_{c,SWR}}\right), \tag{2.2}$$

where σ_{SWR} is the waveguide sidewall position standard deviation and $L_{c,SWR}$ is the autocorrelation length. Consequently, the spectral power density function is given by

$$G_{SWR}\left(f_z\right)=\frac{2\sigma_{SWR}^2 L_{c,SWR}}{1+4\pi^2 L_{c,SWR}^2 f_z^2}, \tag{2.3}$$

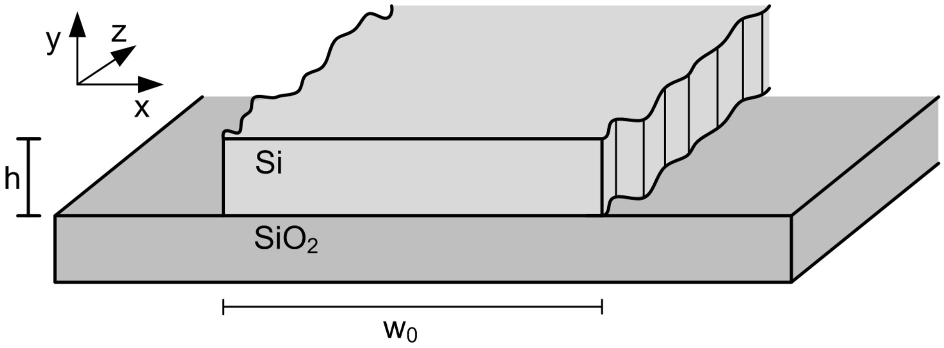

Fig. 12: Waveguide geometry.

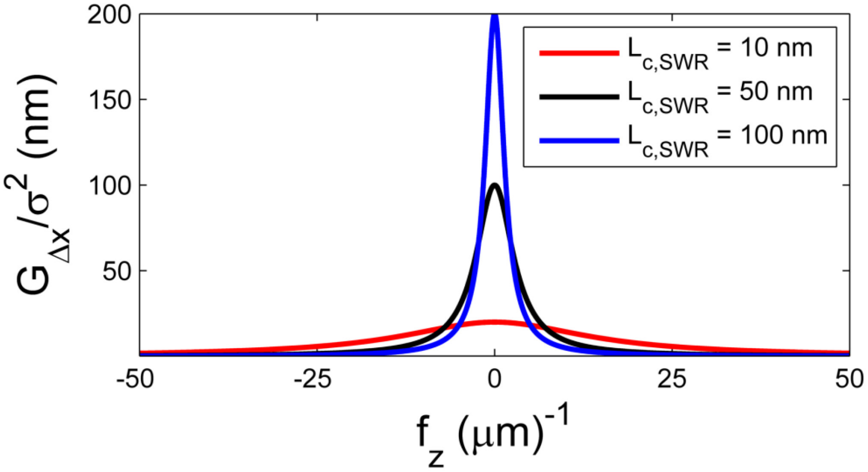

Fig. 13: SWR spectral power density as a function of spatial frequencies for different values of autocorrelation length.

where f_z is the spatial frequency (along the z-axis). Typical values for σ_{SWR} and $L_{c,SWR}$ are, respectively, from ~ 2 to 4 nm and 50 to 500 nm[III]. Fig. 13 shows the spectral power density

---

[III] Those estimated values were provided by a CMOS compatible foundry (IMEC). However, these values do not properly model the phase noise affecting IBGs spectral response since the related spatial frequency are too high (see section 2.5), which is why the work of the next chapter was necessary. The results obtained in Chapter 3 shows that the sidewall roughness standard deviation is around 2 nm and the autocorrelation length that is affecting IBGs is of the order of ~ 10 µm.

normalized by σ_{SWR}^2 for different values of $L_{c,SWR}$. As expected, as $L_{c,SWR}$ increases so does the spectral density at low frequencies. In section 2.5, we show that it is mostly these slow fluctuations that are damaging to the in-band IBG spectral response. Thus, small $L_{c,SWR}$ will result in better spectral response performances.

2.4 – Sidewall roughness model for IBG analysis

For Bragg grating analysis, the waveguide sidewall perturbations must be transposed to effective index perturbations. These effective index perturbations will then create a detuning with respect to the designed grating. It is this additional detuning that is used to model the grating spectral response using coupled-mode theory. This theory is assumed to be valid since this work focuses on long grating structures in order to fabricate complex spectral responses that involve weak local coupling coefficient and negligible mode profile variations.

In order to obtain a concise analysis of the impact of SWR on IBGs, three approximations are made:

1) This work does not consider any random process associated to Λ[IV] or κ[V]. Those parameters are considered noiseless.
2) Since the SWR amplitude is relatively small (i.e. < 1 % of the waveguide width), the effective index variation as a function of width variation (Δw_z) is assumed to be linear around the average waveguide width (w_0). The proportionality constant ($C_{SWR} = dn/dw|_{w_0}$) has been found using a finite element method mode solver [93]. For example, Fig. 1 of [53] and reproduced in this thesis in Fig. 3-b) shows the dependency of C_{SWR} as a function of w_0 for a photonic wire of height of 220 nm. The C_{SWR} used in this chapter is 1.9×10^{-3} nm^{-1}, value associated with $w_0 = 500$ nm.

[IV] This hypothesis has not been discussed in detail in this publication but, in the context of this thesis, it was necessary to discuss this point in more detail. This is done at section 3.7.3.

[V] The justification of this approximation is done in section 4.8 where it is shown that the amplitude noise has a much smaller impact on the grating spectral response than the phase noise.

3) Although the dispersion is strong in photonic wires, the effective index perturbation due to a small width variation has a negligible wavelength dependency in the telecom band. Consequently, $\Delta n_z = C_{SWR}\Delta w_z$ is evaluated at λ = 1550 nm.

Due to approximations 2 and 3 above, the effective index standard deviation is given by

$$\sigma_n \approx \sqrt{2} C_{SWR} \sigma_{SWR} \ . \tag{2.4}$$

The factor √2 comes from the fact that both sides of the waveguides are independent random processes following a normal distribution. This waveguide width variation can also be included in the detuning parameter since, as shown in Eq. (1.15), a waveguide effective index variation along the *z*-axis is given by

$$\Delta\delta_z = \frac{2\pi\Delta n_z}{\lambda} \approx \frac{\pi\Delta n_z}{n_0\Lambda} \ . \tag{2.5}$$

As a result, the standard deviation of this process is

$$\sigma_\delta \approx \frac{\sqrt{2}\pi C_{SWR}\sigma_{SWR}}{n_0\Lambda} . \tag{2.6}$$

The detuning has an autocorrelation function still given by Eq. (2.2) where σ_{SWR} is replaced by σ_δ, since δ and Δx are linearly dependant.

2.5 – Emulator

The IBG emulator, coded in MATLAB, is constructed as follows. The necessary inputs parameters are the coupling coefficient and the local detuning, both being vectors along the *z*-axis. Once the noise-less parameters are fixed by the target grating design, a white Gaussian noise is filtered by the function given by Eq. (2.3) to introduce random detuning variations. At this point the filtered white Gaussian noise standard deviation corresponds to Eq. (2.6) provided that the amount of points used to generate the white Gaussian noise is large enough to ensure the presence of all the relevant frequencies shown in Fig. 13. For calculation purposes, a grating suffering from a SWR noise of $L_{c,SWR}$ ~100 nm should typically be divided in sections of ~ 1 to

10 nm[VI]. Those sections are considered uniform when calculating the transfer function using coupled-mode equations. As discussed below, because high frequencies do not impact the spectral response of a narrow band grating, the filtered Gaussian noise can be filtered a second time by a low-pass filter having a cut-off frequency described above by f_c. This procedure allows using sections lengths of ~ 1 to 10 µm, which reduces considerably the computation time. Finally, the grating spectral response is simulated using coupled-mode equations [67].

To examine the validity of this low-pass filtering operation, we consider the index profile of an IBG as shown by Eq. (1.5) on which we add a phase modulation of frequency f_c and amplitude ϕ, i.e.

$$n(z,\lambda) = n(\lambda) + \Delta n \cos\left(\frac{2\pi}{\Lambda} z + \theta(z) + \phi \sin(2\pi f_c z)\right). \tag{2.7}$$

Eqs. (1.15) and (1.17) show that an effective index variation along the z axis (Δn_z) is equivalent to a z-varying grating phase and, as shown by Eq. (1.17), the phase function that would represent such an effective index variation can be written as

$$-\frac{2\pi}{n_0 \Lambda} \int_0^z dz' \Delta n_z(z'). \tag{2.8}$$

In other words, both approaches can be used to examine grating phase noise. By expanding the term $\phi \sin(2\pi f_c z)$ with a Fourier series and using the Bessel function integral definition, Eq. (2.7) becomes

$$n = n(\lambda) + \Delta n \sum_{m=-\infty}^{\infty} J_m(\phi) \cos\left(\frac{2\pi}{\Lambda} z + m 2\pi f_c z\right). \tag{2.9}$$

[VI] The relevance of having such small layer thickness is discussed in section 2.10

Eq. (2.9) shows that a periodic perturbation of the phase of the grating creates side resonances around the fundamental grating. If we focus on the order $m = 1$, the cosine term can be rewritten as

$$\cos\left(\frac{2\pi z}{\left(\Lambda/(1+\Lambda f_c)\right)}\right).$$

This form is insightful since it shows that the $m = 1$ order has an equivalent grating period of $\Lambda_{m=1} = \Lambda/(1+\Lambda f_c)$ and that this resonance is shifted farther as f_c is increased. Consequently, the high noise frequencies have an out-of-band impact on the grating spectral response. Knowing that we have gratings of period Λ and $\Lambda_{m=1}$ and knowing that the resonances occur at wavelengths given by Eq. (1.18), the spectral spacing between those two gratings ($\Delta\lambda$ – which is equivalent to the measurable spectrum width taken at the noise floor discussed in section 1.6) is given by

$$\Delta\lambda = \frac{f_c \Lambda \overline{\lambda}_B}{1 - 2n_1\Lambda + f_c\Lambda}$$

or inversely, the low-pass filter cut-off frequency as a function of the spectral band of interest is given by

$$f_c = \frac{2n_g}{\overline{\lambda}_B\left(\overline{\lambda}_B/\Delta\lambda - 1\right)}. \tag{2.10}$$

An illustration of the appropriateness of using only the noise components with spatial frequencies lower than Eq. (2.10) is shown in Fig. 14-a) and b) which compares two simulated spectra. The simulated grating has a length of 3 mm, $\kappa = 1000$ m^{-1}, and the noise properties are $L_{c,SWR} = 200$ nm and $\sigma_{SWR} = 3$ nm. The white Gaussian noise was first generated randomly but the same noise vector was used for all curves. The blue curves, identical on both graphs, are the simulation results without a low-pass filter performed with grating sections length of ~ 10 nm. Therefore, the highest spatial frequency accurately modeled in this simulation is 50 μm^{-1}, which is enough to cover 99 % of the noise Lorentzian spectral power density. The 1 % left is composed of higher spatial frequency components and is considered negligible. The red curves were calculated with the same grating parameters, but the noise was low-pass filtered to model the grating spectral response on a bandwidth of 2Δλ = 10 nm and 2Δλ = 20 nm for Fig. 14 a) and b) respectively using Eq. (2.10).

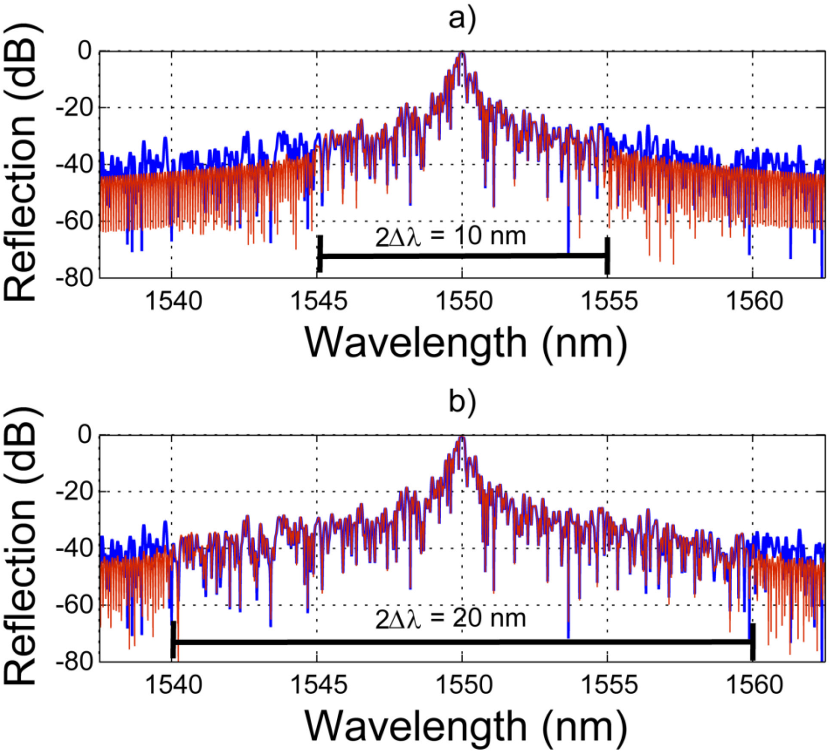

Fig. 14: Comparison of an IBGs simulated without using the low-pass filtering approach (in blue) and with a low-pass filter having a cut-off frequency defined by equation (2.10) (in red). The bandwidth of interest is a) 2Δλ = 10 nm (f_c = 1.8x10^4 m^{-1}) and b) 2Δλ =20 nm (f_c = 3.6x10^4 m^{-1}).

The very good correspondence between the red and blue curves in the inner part of the spectrum of those two figures confirms that only the low spatial frequencies are relevant in the analysis of narrow-band IBG spectral responses. The higher frequencies do not have any impact around the Bragg grating resonance. Similarly the low-pass filter has totally suppressed the noise in the outer part of the spectrum. Finally, a comparison between those two figures shows that Eq. (2.10) is a very good approximation to determine the low-pass filter cut-off frequency as a function of the desired analysis bandwidth.

Fig. 15 shows typical spectra simulated with this emulator with 1st order gratings of length 2.8 mm and linear chirp of 14 nm/cm. The SWR standard deviation of figures a) and b) correspond to σ_{SWR} ~ 4 nm while figures c) and d) correspond to σ_{SWR} ~ 2 nm. The SWR autocorrelation length of figure a) and c) are equal to 300 nm while the autocorrelation length of figure b) and d) are 10 times smaller. From Fig. 15, it is clear that both $L_{c,SWR}$ and σ_{SWR} are important parameters in IBG design which must be maintained as low as possible to allow the fabrication of complex grating structures.

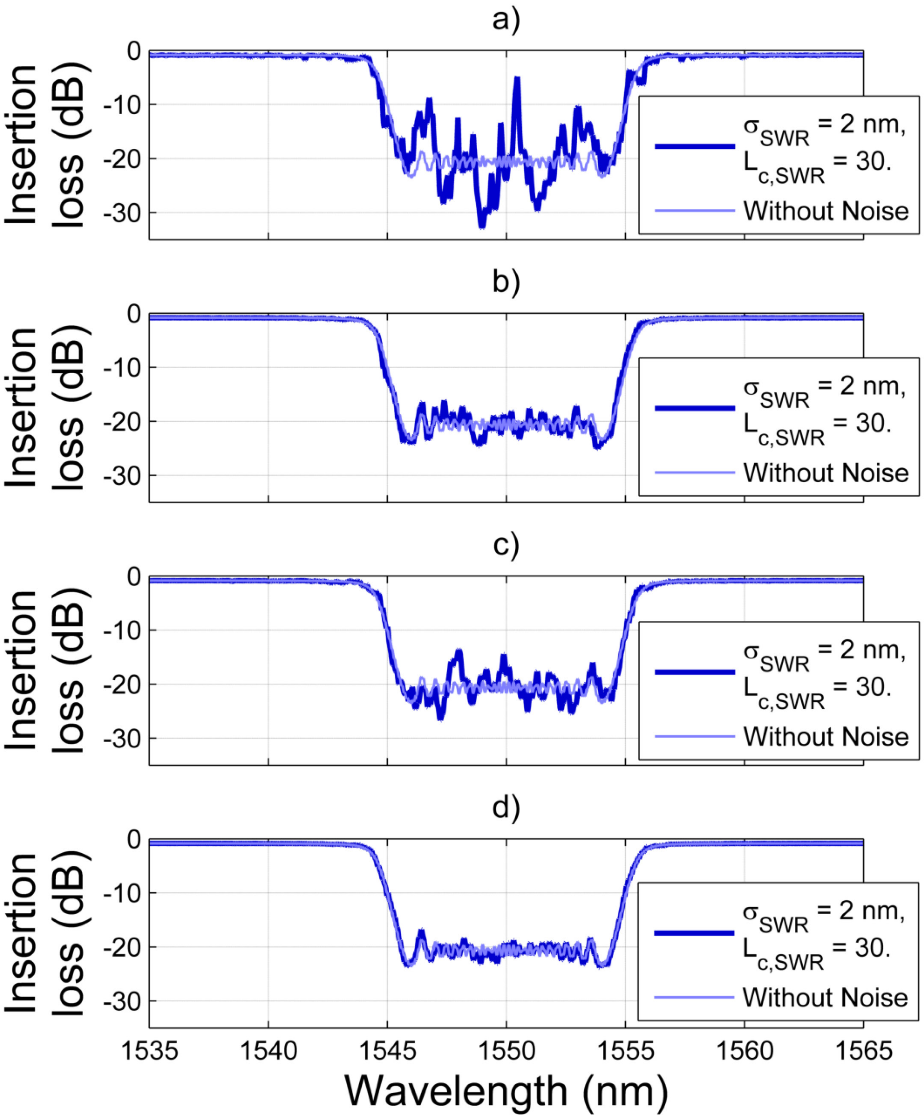

Fig. 15: Numerical simulations of chirped IBG with σ_{SWR} and $L_{c,\,SWR}$ of, respectively a) 4 nm and 300 nm, b) 4 nm and 30 nm c) 2 nm and 300 nm, and d) 2 nm and 30 nm.

After a set of simulation, this emulator gives the fraction of the fabricated gratings that will meet specified requirements with the available roughness parameters. Consequently, if the yield is not sufficient, design modifications can be done without actually requiring fabrications and measurements, hence saving a huge amount of time, effort and resources. It should be noted that when the SWR parameters are too high, strong resonances might appear in the spectrum. This kind of structure can be seen in Fig. 15-a) around 1550.5 nm. Those phase-shifts like structures are very damaging to the filtering performance, since it decreases the extinction ratio considerably and increases the ripple amplitude.

To confirm the validity of this model, Fig. 16 compares typical experimental results of IBGs to simulations done using $\sigma_{SWR} \sim 4$ nm and $L_{c,SWR} \sim 300$ nm [94]. Of course, since a random process is involved, this comparison remains qualitative and the idea is not to retrieve experimental roughness parameters, which should be done by analyzing scanning electron microscope images of the waveguide sidewalls in order to obtain the experimental autocorrelation function[VII] [95]–[97]. Nonetheless, the observed similarities between experimental and simulated spectra shown in Fig. 16 confirm the validity of this model.

More specifically, in Fig. 16-a), the main similarity is the phase-shift like resonance in the uniform grating spectrum which adds a strong ripple in the main lobe. Another feature observed both experimentally and numerically is the reduction of the SLSR. In the case of the strong uniform gratings shown in Fig. 16-b), the ripples seen on the edge of the transmitted spectrum are similar in terms of amplitude and wavelength band. Experimentally, the measured spectrum has a noise floor around -40 dB due to a measurement limitation while the numerical simulation has a floor located at about -120 dB. In the chirped grating case of Fig. 16-c), the experimental ripple amplitude seems to be higher than the emulated one, which suggests that the emulated roughness parameters might be too small. However, since we are dealing with a random process, it is more reasonable to reproduce the analysis on a larger number of samples before drawing any conclusions. Nonetheless, the emulated results are close enough to the experimental ones to confirm that a major source of ripples is effectively coming from the phase noise created by SWR.

[VII] This work is done in the next chapter

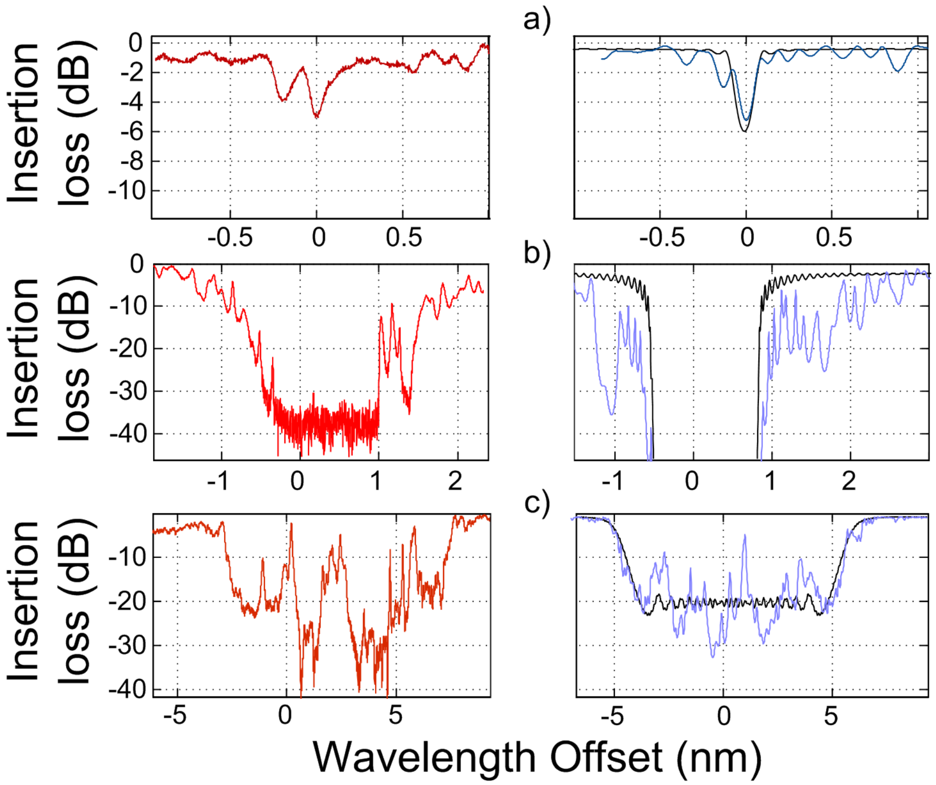

Fig. 16: Comparison of 2.8 mm experimental (red), emulated (blue) and unperturbed (black) a) weak uniform gratings, b) strong uniform gratings, and c) chirped gratings.

2.6 – Numerical analysis

In this section, we use the emulator developed in the last section to evaluate the roughness parameters necessary to achieve IBG apodized filters. If SWR is too large, its effect will damage or, ultimately, completely cancel the positive effects of grating apodization. To do this analysis, uniform and Gaussian apodized uniform gratings, which improves the SLSR, are analyzed and compared. The procedure presented here can be used to study any grating design in order to determine its expected fabrication yield against specific quality factors, i.e. SLSR, ripple amplitude, central wavelength position, etc.

2.6.1 – Uniform gratings

For uniform gratings, the performance criteria are the accuracy of the central wavelength and the SLSR. The central wavelength is obtained with a weighted mean of the emulated spectrum (i.e. The central wavelength is given by $\lambda_c = \sum_{i=1}^{N'} |r(\lambda_i)|^2 \lambda_i \Big/ \sum_{i=1}^{N'} |r(\lambda_i)|^2$ where *N’* is the length of the wavelength vector and $|r(\lambda_i)|^2$ is the reflection amplitude at λ_i.). To retrieve the SLSR, an ideal grating is simulated in order to obtain the spectral width of the main lobe and the ideal SLSR (shown in Fig. 17-a) by the dotted red line). Furthermore, using the spectral reflection of the emulated gratings, an algorithm determines which pair of zeros surrounding the main lobe is closest to this ideal width. This step is delicate since the emulated spectrum might be considerably affected by the phase noise. Those two zeros separate the main lobe and the side-lobes regions. The SLSR is the difference, in dB, between the maximum reflectivity of the main-lobe and side-lobe regions. Finally, because ripples in the main lobe are undesirable, only gratings with a smooth spectral response in the main-lobe region are considered usable. Unusable gratings are assigned a 0 dB SLSR. To identify them, the width of every grating, taking at the first zeroes of the spectrum, has been calculated. If this value was smaller than 60 % of the ideal grating width, it was assumed that the phase noise distortion of the central lobe spectrum was too high (i.e. it meant that a strong notch was present in the main lobe).

In this section, four sets of gratings having $L = 2.8$ mm, $\kappa = 1000$ m^{-1} and roughness parameters values [σ_{SWR}, $L_{c,SWR}$] of respectively [4 nm, 300 nm], [4 nm, 50 nm], [2 nm, 300 nm], and [2 nm, 50 nm] have been simulated. Each set is composed of 1000 gratings.

Fig. 17 shows the distribution obtained for the set [4 nm, 300 nm], which is the worst of the four. The dotted red lines represent the results of an ideal uniform grating. First, it should be mentioned that only ~ 65 % of the grating do not exhibit unwanted resonance and ripples in the main lobe. This decreases considerably the design yield and explains the large amount of SLSR occurrence smaller than 1 dB. As seen on the top figure, the SWR is very damaging for the SLSR. If a SLSR > 3 dB is required, those simulations shows that only ~ 10 % of the fabricated grating could be used. The thick black curve of Fig. 17-a) is a smoothed curve fit of the simulated data while the black curve of the bottom figure is a Gaussian fit. The calculated central position of the distribution is 1549.998 nm and the standard deviation is 42.37 pm, which strongly suggest that the mean grating wavelength, on average, is unaffected by the SWR, which is in agreement with the weak grating analysis presented in section VI. Those fits are used in Fig. 18 to compare results with different SWR parameters.

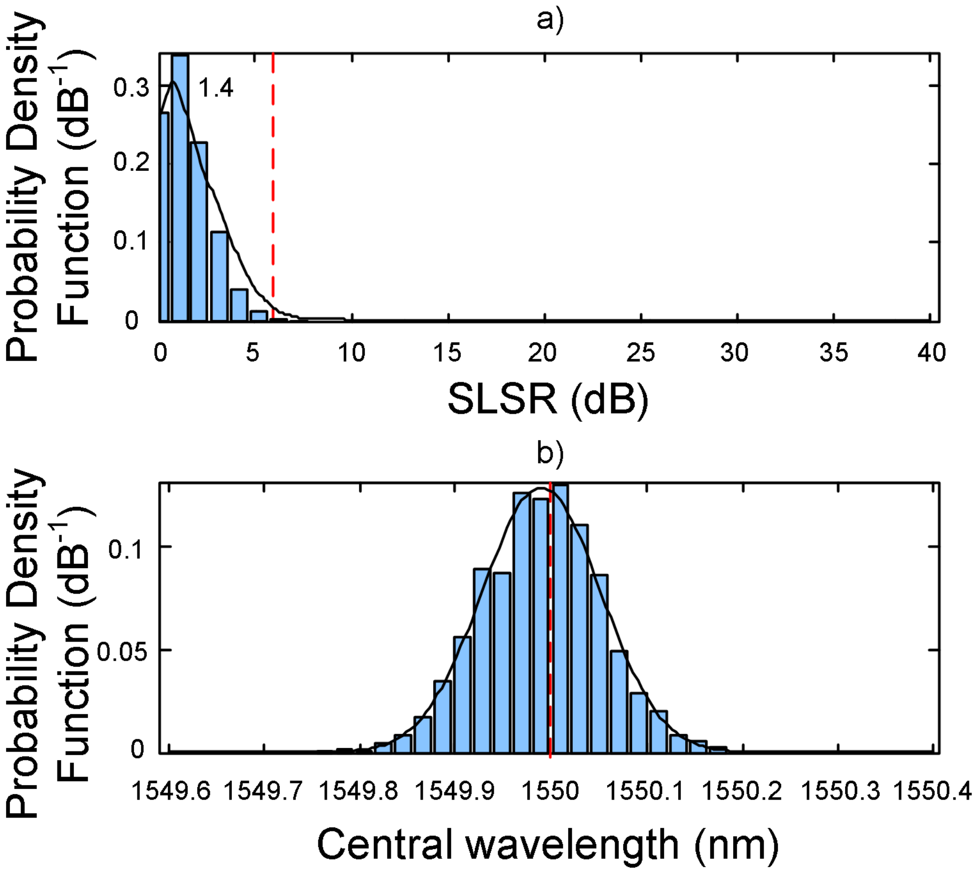

Fig. 17: Distribution of a) the SLSR and b) of the central wavelength of uniform IBGs having σ_{SWR} =4 nm and $L_{c,SWR}$=300 nm. The dotted red lines represent the results of an ideal uniform grating. The solid black line of a) is a smoothed curve of the simulated data while on b) it is a Gaussian fit.

For the three other sets of simulations, the ripples in the main lobe are considerably reduced and less than 1 % of the gratings exhibit strong ripples with phase-shift like structures. For the set [4 nm, 50 nm], about 55 % of the grating exhibit SLSR > 3 dB while for the set [2 nm, 300 nm], it is about 45 %. For the set [2 nm, 50 nm], 95 % of the grating exhibits a SLSR larger than 3 dB and 30 % a SLSR larger than 5 dB.

2.6.2 – Apodized gratings

Apodized-amplitude uniform-period gratings are typically used to increase SLSR. In this section, we verify if a Gaussian apodization profile can be efficient in the presence of SWR having the same parameters as in section 2.6.1. We consider an apodization function having a full-width at half maximum of 1.2 mm, which gives in the ideal case (without noise) a SLSR of ~ 42 dB. For comparison sake, the ideal uniform grating (without noise and apodization) having the same length and strength (i.e. $\int \kappa(z)dz$ is not varied) should have a SLSR of ~ 10 dB while the ideal uniform grating having the same length and same maximum κ value, presented in section 2.6.1, should have a SLSR of ~ 6 dB.

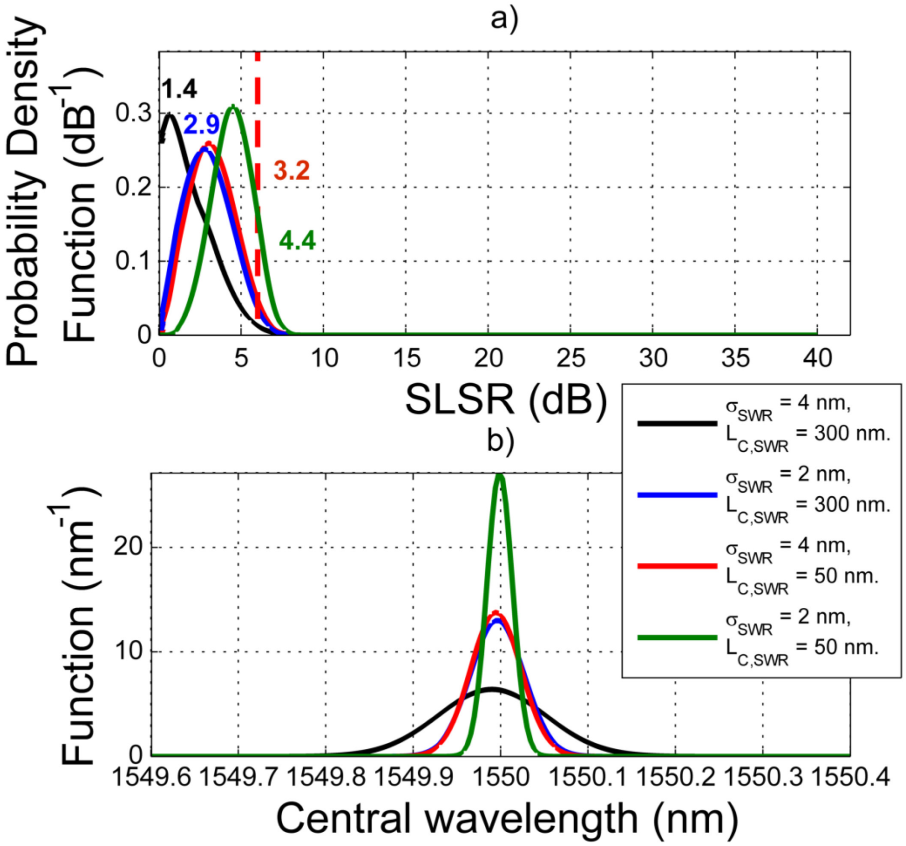

Fig. 18: Probability density function of a) the SLSR and b) of central wavelength of uniform IBGs having different SWR parameters. The numbers in a) are the average SLSR values.

The occurrence density distribution of both SLSR and central wavelength are shown in Fig. 19. As expected, the noise reduces the SLSR improvement; for the set [4 nm, 300 nm], the average SLSR is only 7.3 dB, for the set [4 nm, 50 nm], the SLSR is 15.9 dB, for the set [2 nm, 300 nm], the SLSR is 14.6 dB and for the set [2 nm, 50 nm], the SLSR is 23.1 dB.

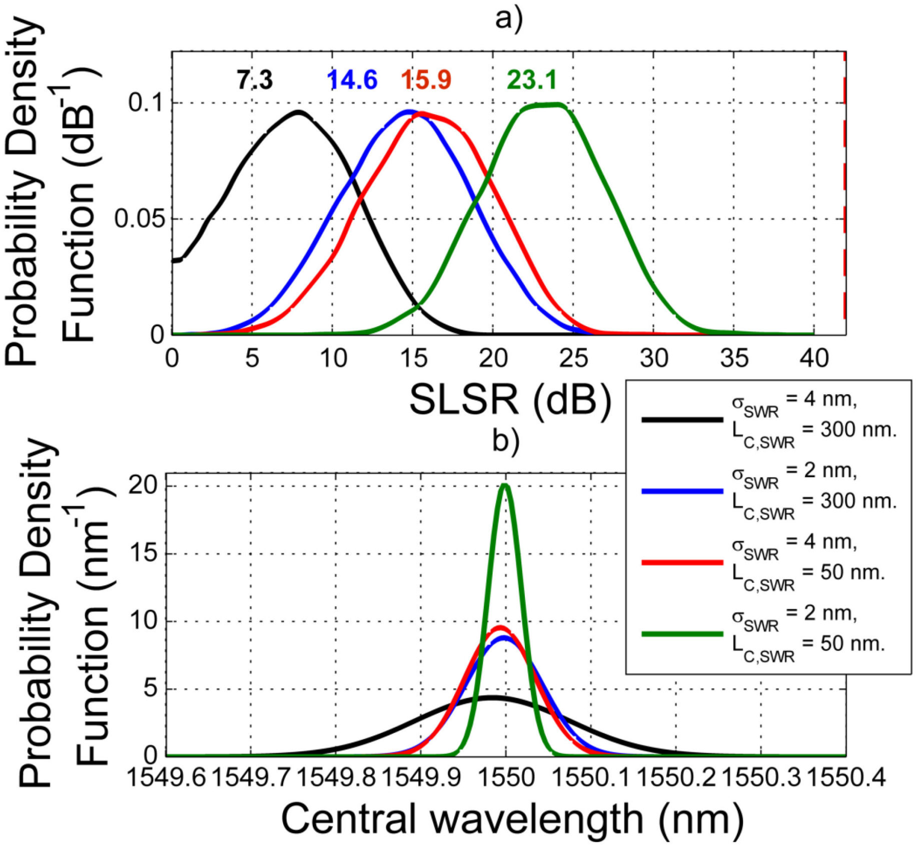

Fig. 19: Probability density function of a) the SLSR and of b) the central wavelength of IBGS with Gaussian apodization and different SWR parameters. The numbers above the curves of a) are the average SLSR values. The dotted red line is the ideal SLSR, the dotted green line is the SLSR of the ideal unapodized grating having the same length and $\int\kappa(z)dz$ while the dotted blue line is the SLSR of the ideal unapodized grating having the same length and same maximum κ value.

2.6.3 – Discussion

In Fig. 20-a) to d) we compare the spectrum of the four sets of unapodized gratings simulated with different roughness parameter. The blue curves are the average of all calculated spectrum (1000 gratings). The black curves delimit the insertion loss values which enclose 90 % of the simulated spectra while the red curves are typical simulated spectrum. A comparison between Fig. 20-a) and d) shows that, as the roughness parameters improve, the resonance of uniform gratings becomes more defined. Fig. 21 presents similar results but for the Gaussian-apodized grating case. Fig. 21-a) shows that, on average, apodization in the presence of high SWR parameters does not have much impact on the grating spectrum since the blue and the black curves are almost identical. However, when the SWR parameters are improved (Fig. 21-d)), the apodization becomes more efficient, i.e. variations in the main lobe are strongly limited as seen from the black curves and the SLSR of this structure is considerably improved by apodization.

We conclude that when the roughness parameters of fabricated waveguides are of the order of magnitude discussed in this article, IBG design should include a statistical analysis of the impact of SWR to provide the expected fabrication yield. This modeling can further be used to improve the design robustness to given SWR parameters.

2.7 – Weak grating analysis

The previous section gives information on grating performance limitations due to SWR through numerical analysis of figure of merits such as the SLSR. In this section we examine whether an analytical approach could provide more insights on the impact of the grating and phase noise parameters on the obtained spectral responses. We use an approach similar to [90] to derive the grating averaged spectral response in reflection and we compare it to the ideal grating response. This analytical approach is of interest because it gives the averaged grating spectrum without having to emulate thousands of identical IBG structures. We validate our analytical formulation by comparing it to the average of 1000 simulated spectra. Unfortunately, as can be seen by comparing the blue and the red curves of Fig. 20 and Fig. 21, the ensemble average does not reflect how much a typical spectrum is distorted. Consequently, this analysis cannot provide information on the fabrication yield of IBGs. More information on this aspect can be obtained by the calculation of the variance of grating spectral responses in the presence of SWR. We derive an analytical expression for this parameter that is valid for low reflectivity gratings and we compare it to the spectral reflectivity variance calculated numerically.

We restrict our analysis to the case of weak gratings, for which we can obtain an analytical solution. We further restrict our analysis to SWR having small $L_{c,SWR}$ and σ_{SWR}. Considering the weak grating approximation [64], with a real coupling coefficient and a detuning that varies as a function of the position, the grating reflectivity is given by Eq. (1.25). However, since the only random process is in the term $\exp\left(2i\int_0^z dz'\delta(z')\right)$, we separate the random term from the designed detuning (δ_d) factor and rewrite (1.25) as

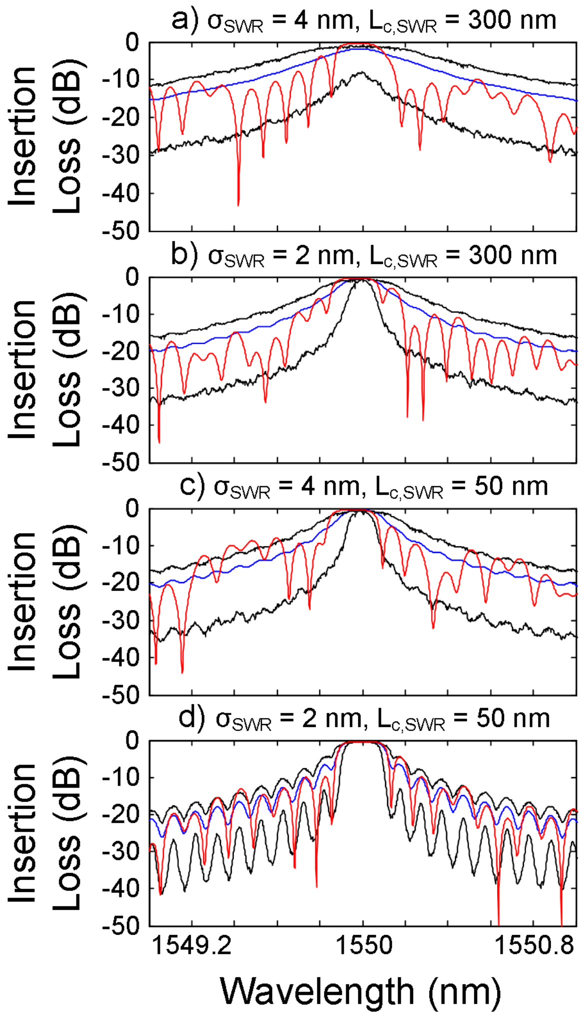

Fig. 20: Calculated spectral response of uniform gratings with κL=2.8 and various phase noise parameters. The blue curves show the averaged spectrum of 1000 gratings. The black curves delimit the insertion loss values that enclose 90 % of the simulated spectra while the red curves are typical spectra.

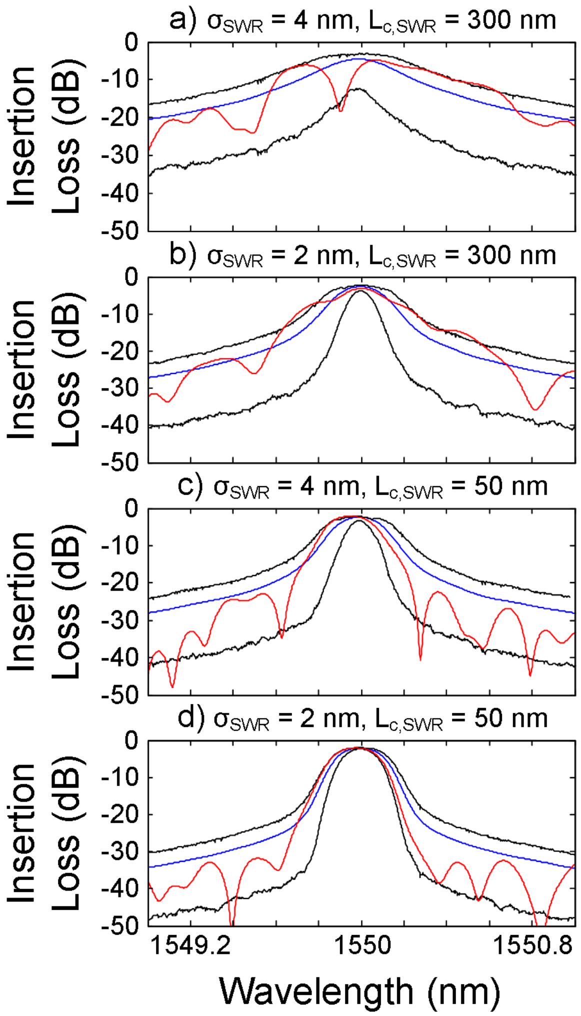

Fig. 21: Calculated spectral response of apodized gratings with $\int\kappa(z)dz$=1.3 and various phase noise parameters. The blue curves are the calculated averaged spectrum of 1000 gratings. The black curves delimit the insertion loss values that enclose 90 % of the simulated spectra while the red curves are typical spectra.

$$r = -\int_{-L/2}^{L/2} dz\,\kappa(z)\, e^{i\delta_{\int}(z)}\, e^{2i\int_0^z dz'\delta_d(z')} , \qquad (2.11)$$

where a new random distribution, $\delta_{\int}(z)$, has been defined. We name $\delta_{\int}(z)$ the detuning distribution and the index ∫ refers to the integral from 0 to z. The autocorrelation function of this distribution is obtained in Appendix B.1 for small $L_{c,SWR}$ values. It should be mentioned that this approximation is still valid for $L_{C,SWR}$ up to ~ 100 µm. To analyze the impact of SWR on the grating spectral response, the average reflection in intensity of “noisy gratings” is obtained and compared to the ideal grating reflection. We use the expected value operator ($E[\ldots]$) and the n^{th} moment of a probability distribution of a random process, $X(t)$ defined by

$$E\left[X(t)^n\right] = \int_{-\infty}^{\infty} x^n p_X(x)dx ,$$

where p_X is the probability density function of the random process $X(t)$. $E[rr^*]$, where * refers to the complex conjugate, is the 1st moment, or the mean value, of the random process rr^* and is given by

$$E\left[rr^*\right] = E\left[\int_{-L/2}^{L/2} dz\kappa(z)e^{i\delta_{\int}(z)}e^{2i\int_0^z dz'\delta_d(z')}\int_{-L/2}^{L/2} d\zeta\kappa(\zeta)e^{-i\delta_{\int}(\zeta)}e^{-2i\int_0^{\zeta} d\zeta'\delta_d(\zeta')}\right].$$

Since $E[\ldots]$ is a linear operator, it can be interchanged with the integral, which allows us to write $E[rr^*]$ as

$$E\left[rr^*\right] = \int_{-L/2}^{L/2} dz \int_{-L/2}^{L/2} \left\{ d\zeta E\left[e^{-i\delta_{\int}(\zeta)}e^{i\delta_{\int}(z)}\right] \right. \\ \left. \kappa(\zeta)e^{-2i\int_0^{\zeta} d\zeta'\delta_d(\zeta')}\kappa(z)e^{2i\int_0^z dz'\delta_d(z')} \right\} .$$

Considering only the situation where the noise amplitude is relatively small, the exponential in the expected value operator can be expanded with a Taylor series, which gives

$$E\left[rr^*\right] \approx \int_{-L/2}^{L/2} dz \int_{-L/2}^{L/2} \left\{ d\zeta \left(1 + E\left[\delta_{\int}(z)\delta_{\int}(\zeta)\right]\right) \right. \\ \left. \kappa(\zeta)e^{-2i\int_0^{\zeta} d\zeta'\delta_d(\zeta')}\kappa(z)e^{2i\int_0^z dz'\delta_d(z')} \right\} . \tag{2.12}$$

Finally, Eq. (2.12) can be simplified to

$$E\left[rr^*\right] \approx R + R_n , \tag{2.13}$$

where R is the IBG reflection spectrum without noise, which can be simulated either by Eq. (1.25) or by the usual transfer matrix solution of the coupled mode theory, and R_n, the noise contribution, is given by

$$R_n = \int_{-L/2}^{L/2} \left\{ dz\kappa(z) e^{2i\int_0^z dz'\delta_d(z')} \int_{-L/2}^{L/2} d\zeta R_{\delta_{\smallint}}(z,\zeta)\kappa(\zeta) e^{-2i\int_0^\zeta d\zeta'\delta_d(\zeta')} \right\},$$

where $R_{\delta_{\smallint}} = E\left[\delta_{\smallint}(z)\delta_{\smallint}(\zeta)\right]$ is the detuning distribution autocorrelation function derived in Appendix B.1. We thus obtain

$$\begin{aligned} R_n = 2L_c \left(\frac{2\sqrt{2}\pi C_{SWR}\sigma}{n_0\Lambda} \right)^2 \int_{-L/2}^{L/2} \Bigg\{ & dz\kappa(z) e^{2i\int_0^z dz'\delta_d(z')} \\ & \left[\int_{-L/2}^{z} d\zeta\zeta\kappa(\zeta) e^{-2i\int_0^\zeta d\zeta'\delta_d(\zeta')} + z\int_{z}^{L/2} d\zeta\kappa(\zeta) e^{-2i\int_0^\zeta d\zeta'\delta_d(\zeta')} \right] \Bigg\} \end{aligned} \tag{2.14}$$

and, in the case of uniform grating, Eq. (2.14) simplifies to

$$R_n = 2L_c \left(\frac{2\sqrt{2}\pi C_{SWR}\sigma}{n_0\Lambda} \right)^2 \frac{\kappa^2 L}{2} \frac{1}{\delta_d^2} \left[\cos^2\left(L\delta_d\right) - \frac{\sin\left(2L\delta_d\right)}{2L\delta_d} \right]. \tag{2.15}$$

To examine the validity of this approach, Fig. 22 compares Eq. (2.13) and (2.15) to the mean of a thousand emulated weak uniform gratings having different phase noise characteristics. The correspondence between those curves is very good for the considered grating strength and phase noise. Of course we expect this model to become less accurate as larger coupling coefficient and phase noise values are used. Remember that the purpose of this analysis is to get a better understanding of the impact of each parameter and not to achieve precise analysis of specific grating designs.

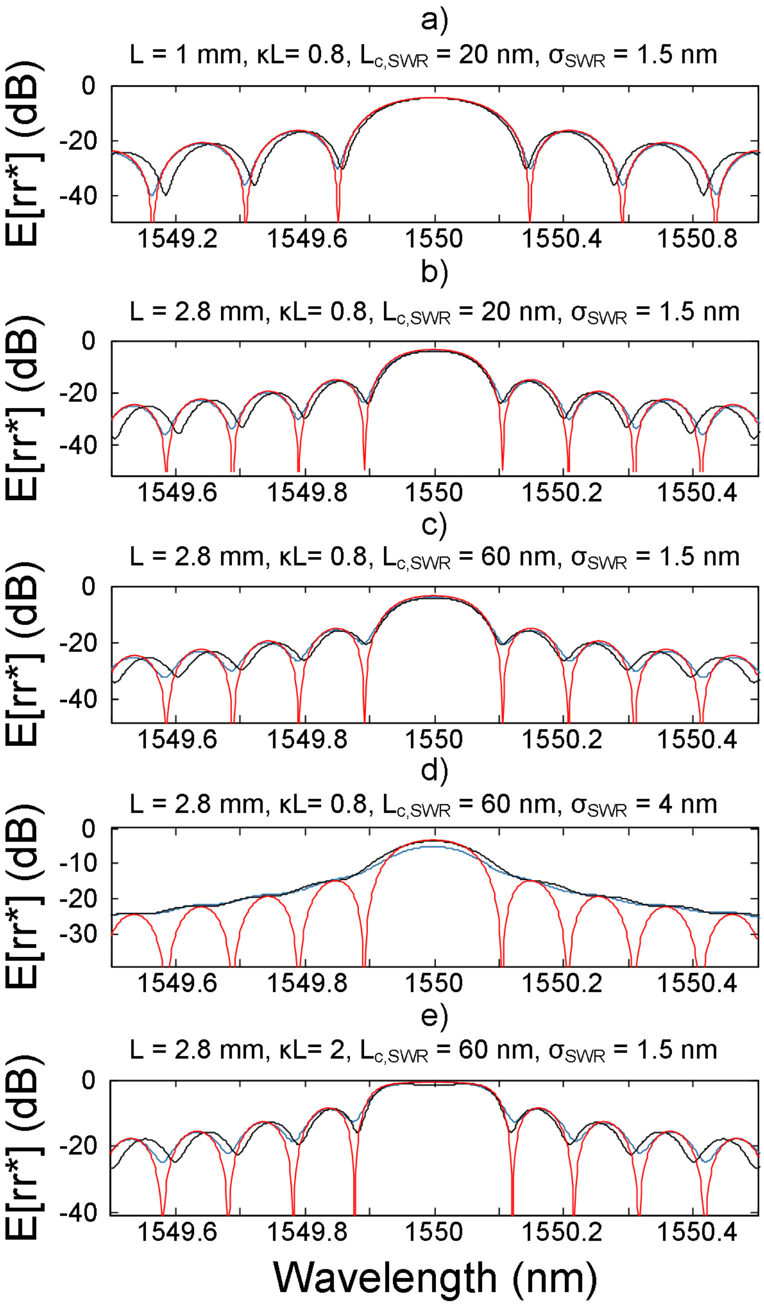

Fig. 22: Comparison between analytical analysis (black) of the mean spectrum of uniform grating with SWR (Eqs. (2.13) and (2.15)) and the average of 1000 spectrum numerically simulated (blue). The red curves are the unperturbed spectral responses. a) → b) shows the impact of increasing L, b) → c) shows the impact of increasing $L_{c,SWR}$, c) → d) shows the impact of increasing σ_{SWR}, c) → e) shows the impact of increasing κL

As shown by Eq. (2.13), the mean reflection spectrum of a noisy grating is composed of the sum of the ideal reflection spectrum and another term (R_n) associated to the noise contribution, which is plotted in Fig. 23 and Fig. 24 for various grating parameters. In [90], E[rr^*] was obtained by solving the coupled mode equations by a perturbative approach. The conclusion of the study was that the visibility of the grating resonances is strongly decreased by the presence of

SWR, as can be observed in Fig. 22. However, an analysis only based on the study of the mean spectrum does not show how the spectrum of a single grating is distorted, which can lead to a wrong interpretation of the impact of the SWR on the grating spectrum. Consequently, since we are interested by knowing how much a grating is expected to deviate from the ensemble average, the remaining part of this section is dedicated to the study of the spectral response variance, σ_R^2, and the standard deviation, σ_R, of a uniform grating. In this case, the second moment of *rr** is given by

$$\begin{aligned} E\left[rr^*rr^*\right] = E\Big[& \int_{-L/2}^{L/2} dz e^{i\delta_{\int}(z)} \kappa e^{2i\delta_d z} \int_{-L/2}^{L/2} dz' e^{-i\delta_{\int}(z')} \kappa e^{-2i\delta_d z'} \\ & \int_{-L/2}^{L/2} d\zeta e^{i\delta_{\int}(\zeta)} \kappa e^{2i\delta_d \zeta} \int_{-L/2}^{L/2} d\zeta' e^{-i\delta_{\int}(\zeta')} \kappa e^{-2i\delta_d \zeta'} \Big] . \end{aligned} \tag{2.16}$$

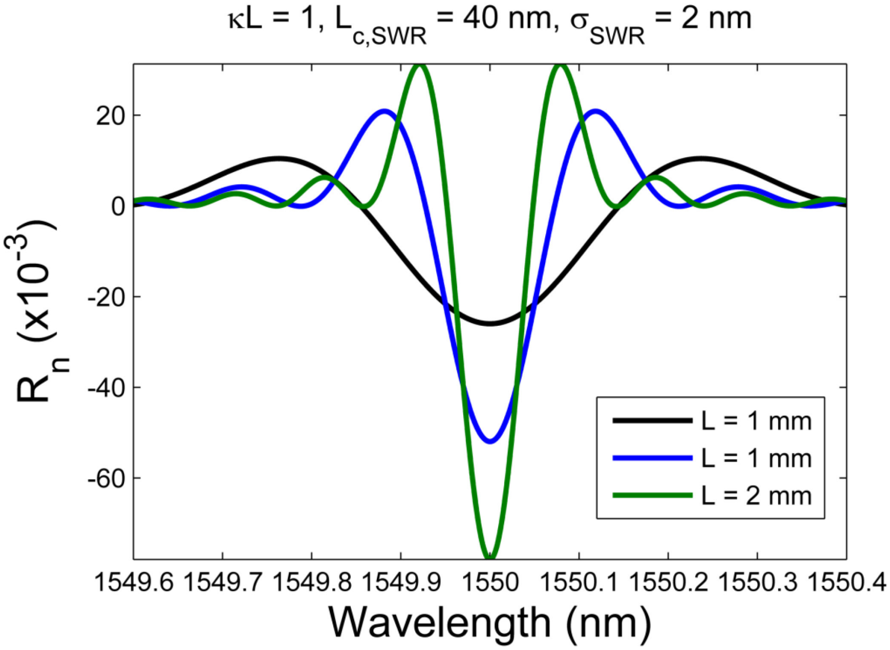

Fig. 23: Comparison of R_n of three gratings having the same κL but different lengths.

Once again, if we only consider cases where the noise amplitude is relatively small, the second moment is

$$E\left[rr^*rr^*\right] = R^2 + 4RR_n - 2RR_{n,r} + O(4) , \tag{2.17}$$

where $R_{n,r}$, the term that involves *E[δ(z)δ(ζ)]* and *E[δ(z')δ(ζ')]*, is given by

$$R_{n,r} = 2L_c \left(\frac{2\sqrt{2}\pi C_{SWR}\sigma}{n_0 \Lambda} \right)^2 \frac{\kappa^2 L}{2\delta^2} \left(\frac{\sin(2\delta L)}{4\delta L} - \frac{1}{2} \right) \tag{2.18}$$

and $O(4)$, the term that involves the fourth moment of $\delta(z)$, is given in appendix B.2. Finally, the variance of rr^* is given by

$$\begin{aligned} \sigma_R^2 &= E\left[rr^* rr^*\right] - \left(E\left[rr^*\right]\right)^2 \\ &= \left(R^2 + 4RR_n - 2RR_{n,r} + O(4)\right) - \left(R + R_n\right)^2 . \\ &= 2R\left(R_n - R_{n,r}\right) - R_n^2 + O(4) \end{aligned} \tag{2.19}$$

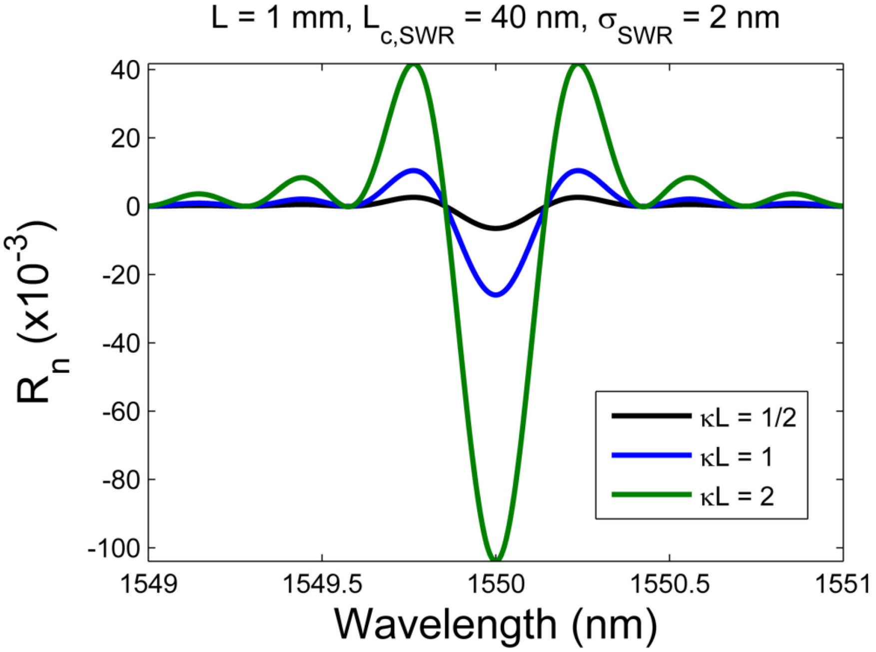

Fig. 24: Comparison of R_n of three gratings having the same length but different κL.

Fig. 25 compares σ_R calculated with Eq. (2.19) to the numerical one obtained from the simulation of a 1000 gratings. The analytical approximation of the σ_R is very close to the numerical once, except for Fig. 25-c). In this case, the grating reflection is too high to obtain a good approximation of the second moment.

Those curves show that the spectral distortions are relatively small near the Bragg wavelength and that the distortions exhibit two strong maxima on both sides of the grating main lobe. This explains why, as the noise increases, the central wavelength of the gratings shifts from the unperturbed one as shown in Fig. 17. In Eq. (1.25), the operations that link the noise of the waveguide width to the grating spectral response are linear. Consequently, the distribution of rr^* remains normal and one can evaluate with Eqs. (2.13) and (2.19) the percentage of gratings that will be within a specified spectral mask. For example, the area delimited by the curves

$$\begin{aligned} R_{\text{upper bound}}(\lambda) &= R + R_n + \sigma_R \\ R_{\text{lower bound}}(\lambda) &= R + R_n - \sigma_R \end{aligned} \tag{2.20}$$

encloses ~70 % of the ensemble spectra as shown in Fig. 26. Consequently,

$$SLSR_{th} = R_{\text{lower bound}}(\lambda_B) - R_{\text{upper bound}}(\lambda_{\text{first lobe}}) R_{up} \tag{2.21}$$

gives the SLSR threshold ($SLSR_{th}$) that will be met by 70 % of the gratings.

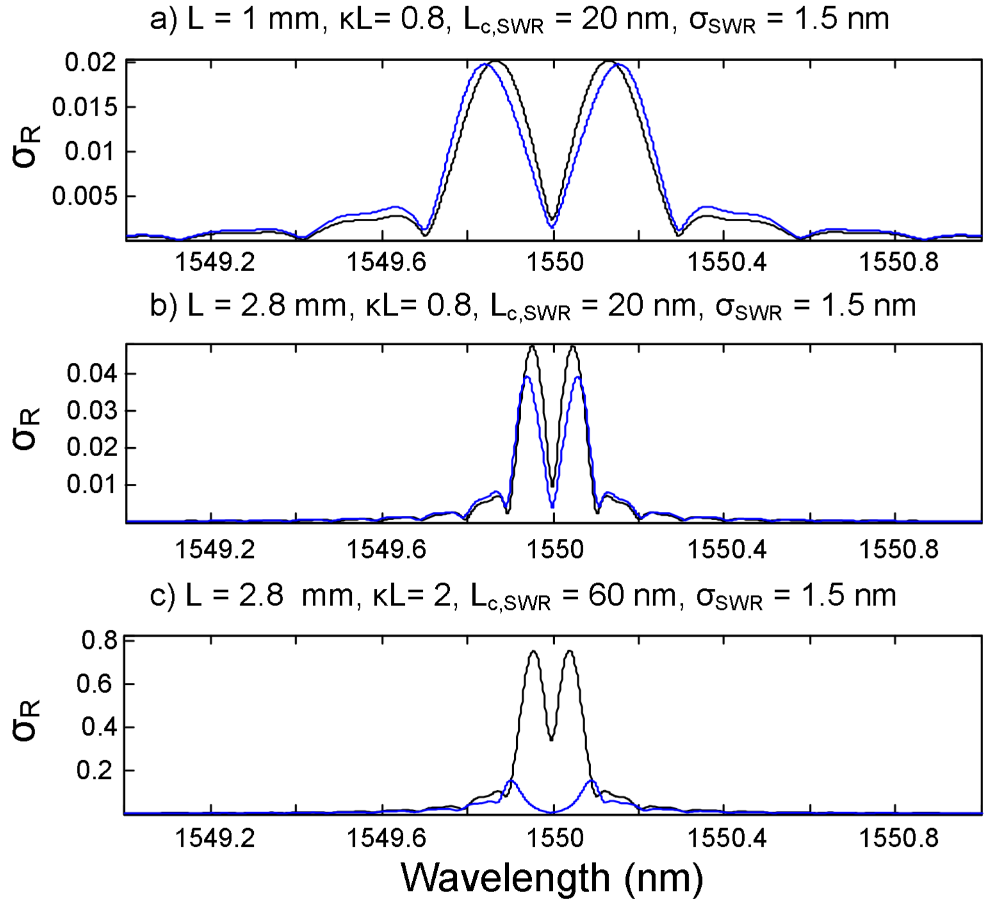

Fig. 25: Comparison between analytical analysis (black) of the standard deviation of uniform grating with SWR and the standard deviation of 1000 spectrum numerically simulated (blue). The noise and grating parameters correspond to the parameters of Fig. 22-a), b) and e).

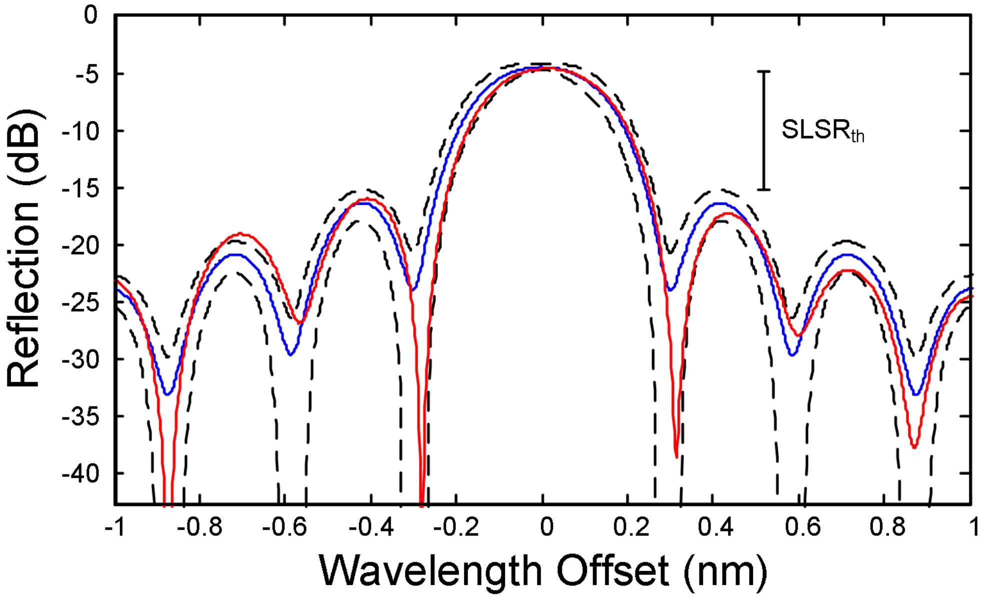

Fig. 26: The blue curve shows the theoretical mean spectrum of a 1 mm long grating having a κL = 0.8, L$_c$ = 20 nm and σ, $_{SWR}$ = 4 nm while the black curves delimit the reflection values that enclose ~70 % of the spectra while the red curve is a typical simulated spectrum.

To obtain more information on the parameters leading to large spectral reflectivity distortion we examine more closely the maxima of σ_R for which the dominant term is $2R\left(R_n - R_{n,r}\right)$, which gives

$$\sigma_R \approx 4\sqrt{L_{c,SWR}L}\left(\frac{\pi C_{SWR}\sigma\kappa^2 L^2}{n_0\Lambda}\right)\left\{\frac{\sin^2\left(\delta L\right)}{\delta^2 L^2}\left(\frac{\cos^2\left(\delta L\right)}{\delta^2 L^2} + \frac{1}{2\delta^2 L^2} - \frac{3\sin\left(2\delta L\right)}{4\delta^3 L^3}\right)\right\}^{1/2}. \tag{2.22}$$

We find that the maxima are located at

$$\delta L \approx \pm 1.315 \quad \rightarrow \quad \lambda \approx \frac{2\pi n_g}{\frac{\pi}{\Lambda} - 2\pi n_1 \pm \frac{1.315}{L}} \tag{2.23}$$

and that

$$\max\left(\sigma_R\right) \approx \frac{4}{\sqrt{10}}\sqrt{L_{c,SWR}L}\,\frac{\pi C_{SWR}\sigma}{n_0\Lambda}\left(\kappa L\right)^2. \tag{2.24}$$

Eq. (2.24) gives good insights on the important parameters defining grating noise amplitude, such as the grating length, strength and resonant wavelength as well as the SWR properties (σ_{SWR} and $L_{c,SWR}$). Eq. (2.24) shows that long gratings are more affected by SWR since max(σ_R) is proportional to the square of κ and to $L^{5/2}$. That means that for two uniform gratings with the same reflectivity (identical κL) but different lengths, max(σ_R) increases with $\sqrt{L}$. Eq. (2.24) also shows that the noise contribution to the grating distortion increases as the square of κL, but linearly with σ_{SWR} and C_{SWR}, and as a square root function with $L_{c,SWR}$. Finally, a careful analysis of Eq. (2.24) shows that using the Bragg filter at higher λ (i.e. higher $n_0\Lambda$) will improve its robustness to SWR.

2.8 – Discussion

We now examine how we can reduce the impact of SWR on IBG spectral response. Eq. (2.4) indicates that careful waveguide design can decrease the impact of fabrication-limited SWR. For example, the use of waveguides with width larger than $w_0 \sim 400$ nm causes C_{SWR} to decrease [53] (Fig. 3-b)). This approach should be done carefully since the waveguide becomes multimode for $w_0 > \sim 600$ nm, however selective mode excitation could be achieved with a hybrid waveguide structure [98]. This design would connect a multimode waveguide, containing the IBG, to a single TE-mode waveguides with adiabatic tapers thus coupling the power solely in the fundamental TE-mode of the multimode waveguide.

The use of other types of waveguide such as quasi-planar waveguides [99], which are intermediate structures between highly confined photonic wires and micrometer scale ridge waveguides, could also reduce $\sigma_{\lambda B}$ through a smaller C_{SWR}. However, less confined waveguides are more affected by curvatures and the use of those waveguides will diminish the capability to achieve large scale integration of IBGs [83].

2.9 – Conclusion

In this chapter, we have examined and modeled the importance of SWR on IBGs spectral response. Both the roughness amplitude and correlation length have been shown to be critical to IBGs performance. We proposed a technique to emulate IBG spectral responses in the presence of an imperfect waveguide. This numerical analysis is useful to design the long IBG structures necessary to develop filters with elaborate spectral responses. This tool should prove useful in establishing the fabrication parameters required to obtain a target fabrication yield for IBG fabricated in SOI nanowires. This technology has SWR that is far from being negligible but that could be improved through future process developments. In order to save computation time, our analysis also showed that only the low frequency components of the noise are significant to the IBG spectral response.

Finally, we have presented an analytic study of SWR for weak gratings having short correlation lengths and small roughness variances. A general analytical expression of the averaged spectrum in presence of the phase noise caused by SWR has been obtained, which could be used to analyze more complex weak gratings. Using weak uniform gratings as an example, we found an analytical expression for the standard deviation of the spectral response that gives information on the spread of the grating reflection spectra around the average. This analysis shows why the noise has a relatively small impact on the reflection strength at the Bragg wavelength while larger distortions appear on each side of the main reflection peak. The analytical expressions also help to evaluate how the noise impact depends on other grating parameters. We have shown that the noise contribution to the grating distortion increases as the square of κL, but linearly with σ_{SWR} and C_{SWR}, and as a square root function with $L_{c,SWR}$.

2.10 – Supplementary information

This section discusses the compatibility of the coupled mode theory with transfer matrices having short layer thickness and with the presence of high spatial frequency content. It is usual in references on Bragg gratings to have the requirement that the layer thickness should be larger than the grating period for the coupled mode theory to be valid [100]. However, the “restrictive” approximation is that the optical field should be varying slowly (approximation done at Eq. (1.11)). As a result, if the “excessive” discretization done in section 2.5 does not lead to an optical field that is varying too fast, the coupled mode theory should remain valid. Fig. 14 shows that it is the case in this work since there are negligible variations in the grating band between the simulations done with different layer thickness (~ 10 nm and ~ 10 μm) which implies that the algorithm does not diverge as the layer thickness decreases. Furthermore, even if the grating structure is varying rapidly, due to the SWR for example, the coupled mode equations are still valid if the roughness effect on the spectrum can be seen as a small perturbation [90].

To confirm this point, numerical simulation has been done with a finite difference time domain (FDTD) simulator. The program is FDTD Solution from Lumerical. The 2D simulation has been done has followed: first, the spectral response of a 700 period's uniform grating has been simulated (in blue in Fig. 27). The grating has corrugation amplitudes of 50 nm on a 850 nm wide waveguide. The period is constant at a value of 280 nm and the grid size along the waveguide axis is 10 nm. The same simulation has been done using the coupled mode theory solved by the transfer matrix approach. The coupling coefficient has been matched to fit the maximal reflectivity value and the result is shown in black in Fig. 27. As expected, the two curves correspond well to each other over the whole grating band, which confirm the validity of the coupled mode equations in this situation. This is so because the grating coupling coefficient is relatively weak (~ 90 cm^{-1}) as well as the mode overlap mismatch between the two sections within a period (< 2 %); thus the two main approximations required for the coupled mode equations to be valid are respected.

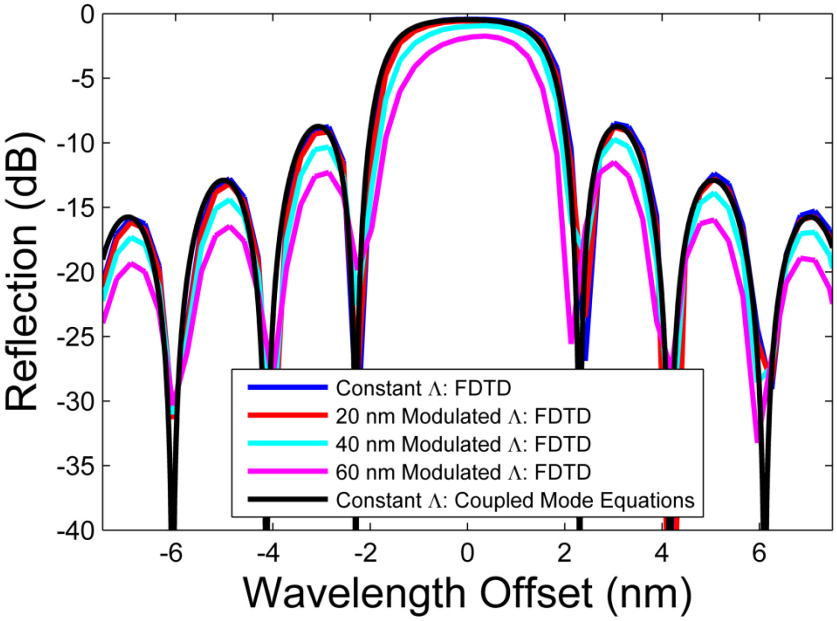

Fig. 27: Spectral response of a 700 periods uniform grating simulated by a FDTD simulator and by a matrix solution of the coupled mode equations. This figure also shows the spectrum of similar gratings but with high frequency modulation.

Another FDTD simulation has been done, and shown in red in Fig. 27, with the exact same parameters but with the difference that the period was modified alternatively by 20 nm (i.e. 260 nm, 300 nm, 260 nm and so on) which introduce a high frequency variation in the grating structure but with the same average period. Interestingly, the differences between this latter simulation and the two previous one are negligible. This result, is predicted by the coupled mode theory which allows us to conclude that this latter theory is still valid with the presence of high frequency perturbations having a small amplitude (i.e. with the presence of SWR). Another very important conclusion that can be drawn from these simulations is that even if CMOS foundries have grid rules, which mean that the position of each polygon lattices is discretized, it does not have an impact on the grating spectral response. As a result, it is possible to design a grating with a local period of 302.5 nm on a 5 nm grid, for example, if the local period is alternated between 300 nm and 305 nm. This knowledge is particularly useful to fabricate gratings with a continuously varying period.

Finally, two more simulations have been done, but with larger phase modulation amplitude. The period was modified alternatively by 40 nm and 60 nm around the average period. As shown in cyan and purple in Fig. 27, when the modulation amplitude is increased, the grating reflectivity is decreased. According to Eq. (2.9), when ϕ increases, $J_0(\phi)$decreases, which reduces the Bragg grating reflectivity to the benefit of the higher order phase modulation terms, since the terms $J_m(\phi)$ (for $m \neq 0$) increase. Thus, this result is predicted both by the coupled mode equations and by FDTD simulations. However, the asymmetry shown in the main lobe of the purple curve shows that, for high spatial frequency fluctuations having significant amplitude, FDTD and coupled mode equations predictions diverge from each other's. Furthermore, although the coupling coefficient is weak in this example, the correspondence between the coupling coefficient strength obtained with 3D-FDTD simulation and Eq. (1.3) should be done to fully understand the limit of the coupled mode equation model; the accuracy of the model is expected to be reduced for narrower waveguides. Further simulations in these directions should be done to analyse thoroughly the limit of the coupled mode theory of silicon photonic IBGs, but this work falls out of the scope of this thesis since the gratings that have been used are much weaker and the phase modulation added to the grating structure had much lower frequency (chapter 4 and 5).

Chapter 3: Characterization and Reduction of Spectral Distortion in Silicon-on-Insulator Integrated Bragg Grating

The main difficulty that arises when using the model developed in the previous chapter is to obtain the values describing the SWR (σ_{SWR} and $L_{c,SWR}$) from CMOS compatible foundries. It was initially anticipated that the SWR would be a "guaranteed" parameter from those foundries in a similar manner as the waveguide propagation loss. Unfortunately, this information is not known by the fab or, at least, not disclosed. To show the impact of the SWR on the grating spectral response, in section 2.5 and 2.6, we estimated these values from the partial information divulgated by the foundries at the time. Although this "guess" was appropriate to describe how to use the model, it is not suitable to obtain quantitative information on the grating response, the fabrication yield prediction and so on. As a result, the retrieval of these parameters is a critical issue.

In chapter 2, the relevant parameters that influence the phase noise have been identified and the implementation of IBGs in hybrid singlemode/multimode waveguides has been proposed to significantly reduce their impact. This hybrid approach is used in chapters 3 to 5. However, when using such hybrid waveguides, the SWR is not the dominant phase noise source anymore which is why, in this chapter, we also have improved the model by incorporating the effect of the WHF. This chapter also partially characterizes this phenomenon and provides another approach to reduce this second phase noise source: the use of compact IBG in spiral waveguides. Using both phase noise reduction techniques, we fabricated the IBG on SOI having, to our knowledge, the narrowest 3 dB bandwidth (i.e. 0.14 nm). This chapter is a reproduction of [42], a paper published in *Optics Express* in 2013 while the work on spiral IBGs is presented in detail in chapter 5 [101].

3.1 – Abstract

A major issue in the fabrication of IBG filters in highly confined waveguides is the average effective index fluctuations caused by waveguide dimension variations. Lateral variations are caused by the SWR created during the etching process while vertical variations are coming from the silicon waveguide thickness non-uniformity. Grating spectral distortions are known to result

solely from the low spatial frequency components of these variations. As a result, in this work, we present an experimental method to quantify such relevant spatial components by stitching a hundred high-resolution SEM images. Additionally, we propose two techniques to reduce, in the design, the phase noise impact on IBGs without relying on fabrication process improvements. More specifically, we show that the use of hybrid multimode/singlemode waveguides reduce by more than one order of magnitude the effect of SWR on IBGs while we show that the fabrication of ultra-compact gratings in spiral waveguides mitigate the impact of the silicon layer thickness variations.

3.2 – Introduction

Due to its compatibility with CMOS processes, silicon photonics has emerged as an attractive solution for the fabrication of low-cost small-footprint photonic integrated circuits. Alongside these developments, FBGs provide filters with versatile and precise spectral responses, but their footprint could be significantly reduced if integrated in SOI platform. IBGs with complex spectral responses require long structures with tens of thousands of periods but, unfortunately, these long gratings are sensitive to phase noise [41]. The grating phase defines the local Bragg wavelength or, equivalently, the grating detuning coefficient whereas the grating strength refers to the coupling coefficient. In this chapter, we therefore use the term “phase noise” to regroup perturbations that have an impact on the local Bragg wavelength of the grating [41]. Any perturbation to the waveguide geometry that changes its effective refractive index is thus a source of phase noise that can induce distortion in the grating spectral response. Recent work reported significant spectral distortions of IBGs in SOI due to waveguide dimension variations that perturb the mode effective index [41], [102]. This effect is significant due to the high index contrast of SOI waveguides. Waveguide width variations are caused by the SWR introduced by the lithography and etching processes whereas the height variations are caused by the silicon layer thinning and polishing processes, i.e. WHF. Since these phenomena modify the waveguide effective index, they consequently perturb the grating phase or equivalently introduce variations in the local Bragg wavelength along the waveguide.

The study of waveguide non-uniformities in SOI has recently received growing attention due to the associated performance degradation observed for many devices. The impact of SWR was mostly studied in the context of waveguide group delay [103], propagation losses [85], [104] and spectral distortions in IBGs [41], while WHF was recently identified as a major concern in the reproducibility of micro-ring [105] and IBGs [47] resonances. Furthermore, much work was already dedicated to reduction of the SWR [88], [89], [106], [107] as well as to the improvement of silicon thickness uniformity [108].

The modeling of SWR and its impact on IBG spectral responses was discussed in [41] (the previous chapter), but this work did not include the effect of WHF. Furthermore, the experimental characterization of those two random processes has never been done in the context of IBGs that are more sensitive to dimension variations with low spatial frequency components, in contrast to propagation loss that is more severely affected by the high spatial frequency components and less by the low frequency ones. Thus, the first objective of this chapter is to present an experimental method to quantify the phase noise terms that affect the quality of IBG spectral responses. Those parameters can be used as inputs to a Bragg grating emulator in order to predict device yield [41]. The second objective is to demonstrate how the phase noise can be reduced by appropriate design, i.e. without relying on fabrication process improvements. It should be mentioned that propagation loss also affects IBGs spectral response. However this phenomenon can already be considered by adding a complex index of refraction in the coupled-mode equations.

This chapter is organized as follows: section 3.3 presents the phase-noise model that links the SWR and WHF random processes to the Bragg wavelength fluctuations observed in IBGs. Previous studies have already addressed the characterization of the SWR random process using scanning electron microscope (SEM) images ([95], [104], [109], [110] to name a few). However, these previous reports did not characterize the low spatial frequency content of SWR, which is critical to predict spectral distortions of IBGs, because the required characterization length exceeds the field-of-view (FOV) of SEM images. Consequently, we propose in section 3.4 an experimental method to increase the length over which the waveguide is analyzed, thus enabling the characterization of the low spatial frequency content of SWR. We also discuss how to extract the parameters characterizing WHF from IBGs optical measurements. Finally, section 3.5 presents two techniques to improve IBG robustness to phase noise: the first one is to fabricate IBGs on wider waveguide to reduce the impact of SWR, while the second one proposes to fabricate ultra-compact gratings to mitigate the impact of the WHF, i.e. using spiral IBGs [83], [101].

3.3 – Phase-noise model

This section presents the theoretical background that links the parameters of the SWR and the WHF random processes to the standard deviation of the grating Bragg wavelength profile. These two processes are modeled by a normal distribution and an exponentially decaying autocorrelation function [86], [92], [111]. In section 3.4, we will show that this model provides a good fit to the SWR experimental results and we assume that this model could be extended to the WHF. The good correspondence between the model and the experimental results presented in the following sections supports this hypothesis. For the random processes SWR and WHF, the autocorrelation function are defined by

$$\begin{aligned} R_{SWR}\left(\Delta z\right) &= \lim_{L\to\infty}\frac{1}{L}\int_{-L/2}^{L/2}\Delta x(z)\Delta x(z+\Delta z)dz \\ R_{WHF}\left(\Delta z\right) &= \lim_{L\to\infty}\frac{1}{L}\int_{-L/2}^{L/2}\Delta y(z)\Delta y(z+\Delta z)dz \end{aligned}, \qquad (3.1)$$

where Δy is the wafer height deviation from the average silicon thickness (Δx and Δz were defined in the previous section). The axes are indicated on the SEM image of Fig. 28-a), which shows a typical top-down image of a photonic wire. We use the usual exponential function to model the autocorrelation function of the SWR and the WHF processes, which is given by [92]

$$\begin{aligned} R_{SWR}\left(\Delta z\right) &= \sigma_{SWR}^{2}\exp\left(\frac{-\left|\Delta z\right|}{L_{c,SWR}}\right) \\ R_{WHF}\left(\Delta z\right) &= \sigma_{WHF}^{2}\exp\left(\frac{-\left|\Delta z\right|}{L_{c,WHF}}\right) \end{aligned}. \qquad (3.2)$$

Resulting from Eq. (3.2), the power spectral density functions are given by

$$
\begin{aligned}
G_{SWR}\left(f_z\right) &= \frac{2\sigma_{SWR}^2 L_{c,SWR}}{1+4\pi^2 L_{c,SWR}^2 f_z^2} \\
G_{WHF}\left(f_z\right) &= \frac{2\sigma_{WHF}^2 L_{c,WHF}}{1+4\pi^2 L_{c,WHF}^2 f_z^2} \, .
\end{aligned}
\tag{3.3}
$$

The parameters describing the SWR (σ_{SWR} and $L_{c,SWR}$) are determined in section 3.4.1 using SEM images. Due to experimental limitations, a combination of the parameters describing the WHF (σ_{WHF} and $L_{c,WHF}$) will be extracted using optical measurements in section 3.4.2.

In order to analyze IBG phase noise, the model describing SWR and WHF must be linked to the variations of the local Bragg wavelength. Since the standard deviation of the Bragg wavelength is related to the effective index standard deviation, we write

$$\sigma_{\lambda_B} = 2\Lambda\sigma_n \, . \tag{3.4}$$

Considering both the presence of SWR and WHF noise sources, σ_n is given by

$$\sigma_n = \sqrt{2C_{SWR}^2\sigma_{SWR}^2 + C_{WHF}^2\sigma_{WHF}^2} \, , \tag{3.5}$$

instead of Eq (2.4), where C_{WHF} is the proportionality constants that link the waveguide height variations to an effective index variation. This parameter is evaluated around the waveguide average height using a finite element mode solver.

In analogy to the phase modulation of a carrier that introduces sidebands around the carrier frequency, spatial frequency components of grating phase noise introduce spectral distortions located at specific optical frequency bands of the grating spectrum. As the spatial frequency of the phase noise increases, the distortions will appear in frequency bands located farther away from the grating resonance [41]. Consequently, the grating spectral response is not affected by high frequency noise components because their impact will be outside the relevant optical bandwidth. Furthermore, because experimental measurements have a limited dynamic range, the distortions induced by high frequency noise content are often below the noise floor of the detection system. Thus, since only low spatial frequencies have an impact on the grating spectral response, the noise can be filtered to consider only such frequencies lower than the cut-off frequency, f_c, given by Eq. (2.10) [35], [41]. Considering that $\overline{\lambda_B} >> \Delta\lambda$, Eq. (2.10) can be simplified to

$$f_c \approx \frac{2n_g \Delta\lambda}{\overline{\lambda}_B^2}. \tag{3.6}$$

Since the integral of the power spectral density over the frequencies is, by definition, equal to the variance of the noise, the variance of the filtered noise, which has a significant impact on IBGs spectral response and is noted with "~", is defined by

$$\tilde{\sigma}^2 = \int_{-f_c}^{f_c} G_{\Delta x}\left(f_z\right) df_z = \frac{4\sigma^2 L_c f_c}{4\pi^2 L_c^2 f_c^2 + 1}. \tag{3.7}$$

In the special case where the cut-off frequency is significantly smaller than $(2\pi L_c)^{-1}$, $\tilde{\sigma}^2$ can be well approximated by $4\sigma^2 L_c f_c$. The filtered variances are thus given by

$$\begin{aligned} \tilde{\sigma}_{SWR}^2 &\approx 8n_g \frac{L_c \Delta\lambda}{\lambda_B^2} \sigma_{SWR}^2 \\ \tilde{\sigma}_{WHF}^2 &\approx 8n_g \frac{L_c \Delta\lambda}{\lambda_B^2} \sigma_{WHF}^2 \end{aligned} \tag{3.8}$$

and the filtered Bragg wavelength standard deviation $\tilde{\sigma}_{\lambda_B}$ is obtained by using Eq. (3.8) in Eqs. (3.4) and (3.5), such as

$$\tilde{\sigma}_{\lambda_B} = 2\Lambda \tilde{\sigma}_n = 2\Lambda \sqrt{2C_{SWR}^2 \tilde{\sigma}_{SWR}^2 + C_{WHF}^2 \tilde{\sigma}_{WHF}^2}, \tag{3.9}$$

where $\tilde{\sigma}_n$ is the filtered effective index standard deviation, which results in

$$\tilde{\sigma}_{\lambda_B} = \frac{8\Lambda\sqrt{n_g \Delta\lambda}}{\lambda_B} \sqrt{\left(C_{SWR}^2 L_{c,SWR} \sigma_{SWR}^2 + \frac{1}{2} C_{WHF}^2 L_{c,WHF} \sigma_{WHF}^2\right)}. \tag{3.10}$$

By using the parameters that describe the waveguide dimension fluctuations experimentally determined in section 3, Eq. (3.10) will be used in section 4 to compare the model to the experimentally retrieved Bragg wavelength standard deviations. Eq. (3.10) must be used instead of Eq. (3.4) since the experimental measurements of the Bragg wavelength were low-pass filtered by the optical characterization process because the noise floor of the spectral measurement hides the higher frequency content of the noise.

3.4 – Phase-noise characterization

As mentioned previously, the measurement of the low frequency content is critical for the modeling of IBG spectral responses. In section 3.1, the SWR parameters will be directly measured by stitching high-resolution images from a SEM. In section 3.2, the characterization of WHF will be done by optical measurements of IBGs. The parameters will be extracted using the results of section 3.1 and by reconstructing the grating structure using an integral layer peeling algorithm [73]. Through Eq. (9), the grating phase gives information on the WHF parameters but this method only allows the determination of the product $\sigma_{WHF} L_{c,WHF}^{1/2}$.Unfortunately, atomic force microscope (AFM) images could not be used to properly characterize the surface because, in order to measure low frequency components, the scan size should be made as large as possible. However, the mechanical properties of the piezoelectric element that moves the AFM probe near the surface introduce 2nd and 3rd order curvatures that are usually called “bow”. These phenomena increase with the scan size. As a result, the bow must be removed using a third order polynomial regression, which suppressed the low frequency contents that needs to be characterize.

3.4.1 – Characterization of sidewall roughness

The high resolution images needed to resolve the SWR random process having a σ_{SWR} of typically a few nanometers can be obtained with SEM images [95], [104], [109], [110]. The algorithm used in this chapter to determine the sidewall position follows closely the one presented in [95] and is summarized in section 3.4.1.1. However, those measurements require special care since high-resolution SEM pictures provide a relatively limited FOV. If the FOV is too small, L_c will be under-estimated. Consequently, to increase the FOV along the waveguide propagation axis without degrading the resolution, hundreds of successive images have been taken with an overlap between them of roughly half a FOV. An algorithm was developed to properly align them in order to obtain the waveguide width fluctuation over a length of ~ 100 μm. Section 3.4.1.2

presents the alignment algorithm while the retrieval of the SWR parameters is described in section 3.4.1.3.

Measurements reported in this section were made on uncorrelated straight SOI waveguides having nominal cross sections of 220 nm x 500 nm that were fabricated using 193 nm DUV photolithography (IMEC). The SEM was a Zeiss 1540XB CrossBeam. The picture magnification was 60 kX and the acceleration tension was 20 kV which results in a probe size of 1.1 nm. The FOV was about 1.9 μm along the waveguide axis.

3.4.1.1 – Waveguide edge determination

The algorithm used to determine the positions of the waveguide edges is based on a signal-threshold analysis, i.e. the edges are determined using a threshold value on the signal itself, as opposed to a derivate-threshold analysis that determines the edges using a threshold on the derivative signal. The derivative-threshold analysis has been discarded due to its higher noise sensitivity [95].

As can be seen in Fig. 28, the waveguide is defined by two bright lines. The algorithm can be applied either on the inner part or the outer part of the lines or could locate the position of the maximal brightness. However, it has been shown [95] that the retrieved edge functions using those three positions are alike. In this work, we chose to analyze the SWR using the outer part of the bright lines.

The first step after the image has been transformed into an array of pixel is to determine the pixel size (1.86 nm in this chapter; the picture length along the waveguide axis is $1024 \cdot 1.86$ nm = 1905 nm). The pixel size evaluation is done by the SEM and this value does not change from one picture to another. Afterward, since the image noise is white whereas the useful information is mostly composed of low frequencies, the images are low-pass filtered using a Gaussian filter having a size of 5 x 5 pixels [95]. Then, the average background intensity is subtracted to the filtered-picture and the intensity is normalized to the maximal intensity value of the waveguide edge. Consequently, the threshold value is a ratio smaller than 1 (0.2 in this chapter as shown by the black line in Fig. 29). Since the intensity might differ between the two waveguide walls, the normalization is done independently on both sides of the waveguide which explains the discontinuity at the center of the intensity profile shown in Fig. 29. At this point, the sidewall positions can be easily determined. Fig. 30 shows the top-down SEM image converted into a binary image with the retrieved sidewall positions.

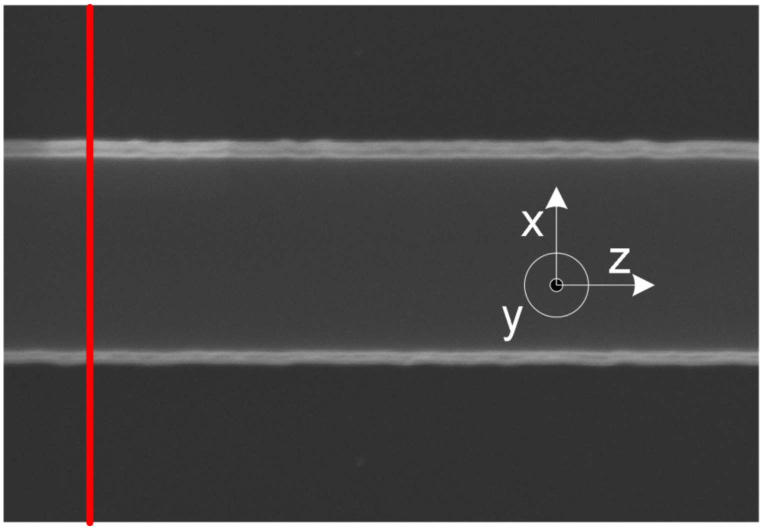

Fig. 28: Typical top-down SEM image of a photonic wire

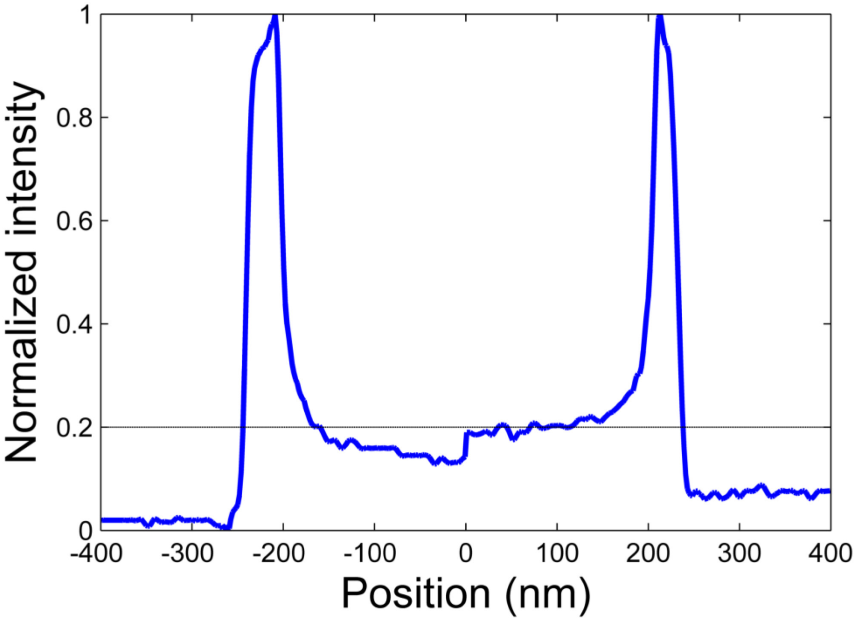

Fig. 29: Typical intensity profile of a pixel column (taken at the position of the red line in Fig. 28.

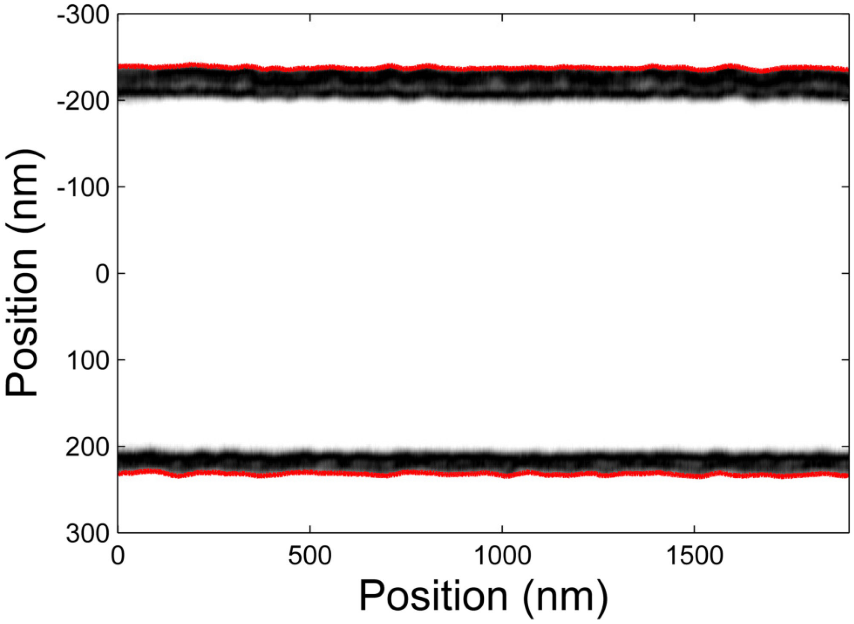

Fig. 30: Typical top-down SEM image converted into a binary image with the threshold shown by the black line in Fig. 29. The red lines are the outer waveguide sidewalls.

To conclude, pixel size up to 4 nm does not have significant impact on the edge position [95]. As a result, the resolution used for this measurement is sufficient for our purpose. Furthermore, the retrieved sidewall profile is not changing as a function of the threshold value [95], aside for a position shift (as long as the threshold is fixed to a value superior to the noise floor). However, since we are not interested by the absolute position of the sidewall but by its variation around its mean, as will be discussed in more details in the next subsection, the choice of the threshold has no impact on the waveguide width variation measurement.

3.4.1.2 – Picture alignment

Before aligning the pictures, the systematic source of error coming from the tilt that exists between the sample surface and the electron beam must be considered. Ideally, the beam would be at normal incidence on the silicon layer; however, a small residual tilt can have a major impact on the waveguide roughness analysis. The misalignment of the e-beam can be separated in three components; a rotation around the x-axis, the y-axis and the z-axis.

Rotation around the y-axis is the most obvious since it simply rotates the waveguide in the picture. Although this effect is often corrected by doing a linear fit of the retrieved sidewall function and by rotating numerically the picture accordingly, this cannot be done when analysing low frequency components since this operation suppresses an important portion of these low frequencies. Consequently, instead of correcting the picture misalignment and analysing the two sidewalls independently, it is wiser to analyse the waveguide width fluctuation instead, which is defined by removing w_0 to the waveguide width profile. This procedure cancels out the misalignment without influencing the retrieved SWR parameter since both sides of the waveguide are equally affected by this tilt and because the random processes affecting both sidewalls are identical. Therefore, the retrieved L_c parameter of the waveguide width fluctuation is the same as $L_{c,\mathrm{SWR}}$ while the retrieved σ should be divided by a factor $\sqrt{2}$ to obtain σ_{SWR}.

The rotation around the z-axis has a negligible impact since it simply reduce w_0 in a similar manner on every picture. Once again, we are not interested in the absolute width value. As a result, this error source is not relevant.

However, the rotation around the x-axis is critical. This tilt has a dramatic impact on the measured waveguide width fluctuation since it systematically increases the width on one side of the picture and reduces it on the other side. Obviously, this effect is very small and, when one analyzes one SEM picture at a time, this effect can easily be neglected. However, in this work, since a hundred pictures are put together, this effect adds up and must be removed. To this end, we superimposed every waveguide width fluctuation measurement from the different images as a function of pixel number as shown in Fig. 31. Since a random process with zero-mean is involved, the waveguide width fluctuation averaged over every picture should be equal to zero for every pixel. However, as can be seen from this figure, there is a small residual slope (in blue) which would result in a waveguide width variation of ~ 0.6 nm/picture (or equivalently 0.315 nm/µm) if this effect is not removed. Obviously, the left side of the sample was closer to the e-beam source than the right side for this measurement. It is interesting to evaluate what would be the Bragg wavelength chirp of a uniform grating if one was fabricated on this nominally constant waveguide. A grating having a length of 100 µm would have a waveguide width varying by about 30 nm. Thus, considering the effective index change of a waveguide having a width varying from 480 nm to 510 nm, the associate Bragg wavelength chirp of a uniform Bragg grating would be of the order of ~ 20 nm/100 µm (i.e. 2000 nm/cm). However, such chirp ratio has never been measured on a nominally straight waveguide (i.e. narrowband Bragg gratings can be fabricated with this technology [47], [102]). As a result, this slope is obviously a measurement artifact and has been removed on every picture. Finally, if the waveguide would have been designed in a tapered-shaped instead, this procedure would also have removed this linear width variation. However, since we are interested in the random process that affects the waveguide width, we can discard any source of systematic width variation.

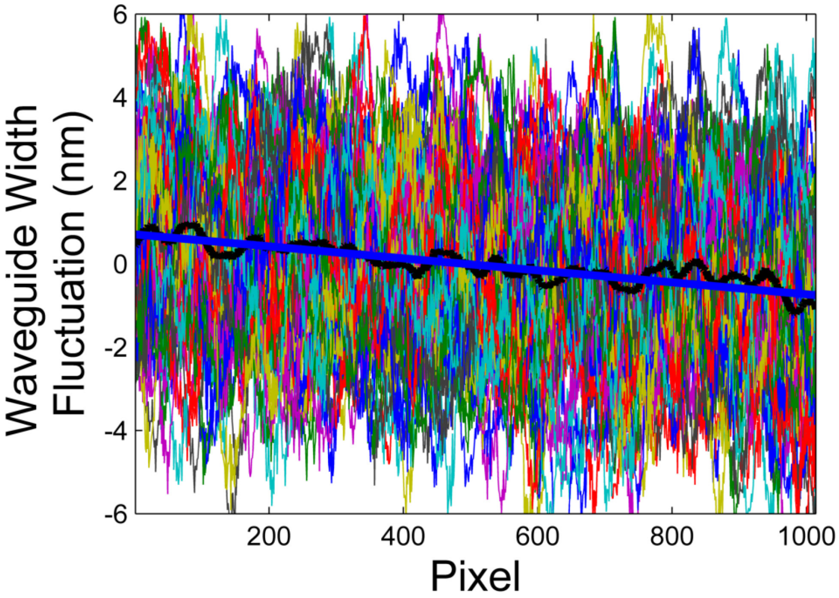

Fig. 31: Typical superposition of the waveguide width fluctuation from every image of a set of measurement. The thick blue line is the linear regression of the average waveguide width fluctuation per pixel (black curve).

The translation from one picture to another is about half a FOV. However, we must apply a correction to both w_0 and the waveguide axis (z-axis), in order to stitch together the images and be able to extract the width fluctuation profile over many tens of microns. For the z-alignment, the retrieved waveguide width of the M^{th} image is scanned over the $M - 1$ image until the fluctuations are matched. The optimal alignment corresponds to the position where the root mean square error is minimal. This is necessary because the translation stage of the SEM has a precision of about ± 0.3 μm. Fortunately the presence of high frequency components in the waveguide width measurement eases the alignment process.

An error in w_0 is introduced by the focus variations (working distance) from one picture to another. To illustrate this point, many pictures of a waveguide were taken at the same position but with the working distance being modified around the optimal value. Fig. 32 shows the superposition of the different measurements of waveguide width fluctuations once w_0 is removed. It can be noticed that the measured waveguide width fluctuations are not changing significantly, which means that a small error in the focus will not affect significantly the roughness analysis although, as shown in Fig. 33, w_0 is strongly modified. The waveguide image remains clear on a small range of working distance, which corresponds to a variation of the measured average waveguide width of about 5 nm. Sensitivity of waveguide width measurements to focus adjustments makes this parameter hard to characterize experimentally. As a result, because of this error in waveguide width measurement, a correction must be introduced which is simply done by adjusting the width of the image $M+1$ to the width of the M^{th} image. This procedure is not problematic since we are only interested in the waveguide width fluctuation. Once every images are properly aligned, the average width is removed which provides the waveguide width fluctuation.

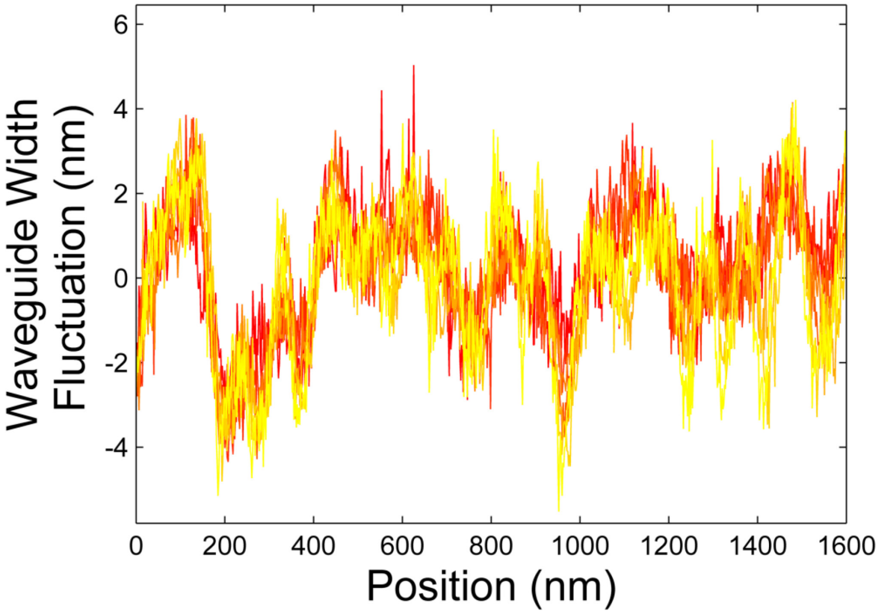

Fig. 32: Waveguide width fluctuation obtained from top-down SEM taken at the same location with different working distance.

The red, blue and green curves of Fig. 34 are typical results of waveguide width fluctuations retrieved from consecutive SEM measurements after a proper alignment. The good correspondence of the waveguide width fluctuations measured in overlapping regions gives good confidence in the precision of this technique. The black curve in Fig. 34 and Fig. 35 is the final profile that will be used from now on and was obtained by averaging the superimposed curves.

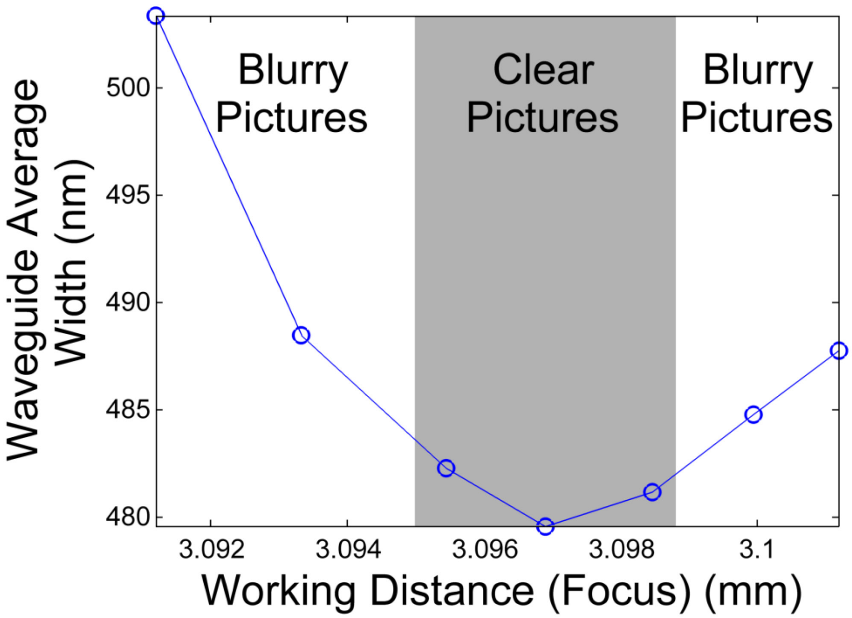

Fig. 33: Dependency of the average waveguide width caused by a variation of the working distance.

3.4.1.3 – Extraction of sidewall roughness parameters

To obtain the parameters σ_{SWR} and L_{SWR}, the autocorrelation of the waveguide width fluctuation function is calculated as displayed in Fig. 36. The amplitude at $\Delta z = 0$ is, by definition, the variance of the process (i.e. to obtain the SWR variance, this value must be divided by a factor 2). In the region $\Delta z < 1$ µm, the autocorrelation of the raw data experiences a very steep decay (identified by the red arrows). This region is associated to high frequency fluctuations and, since the high spatial frequency has no impact on IBG spectral response, the retrieved profile (in black in Fig. 35) can be low-pass filtered with a cut-off frequency of ~ 0.7 μm^{-1} (in blue in Fig. 35). This cut-off frequency has been optimized in order to suppress the steep decay around $\Delta z = 0$ while maintaining the other parts of the function unchanged as shown by the blue curve of Fig. 36. This part of the autocorrelation function that is removed can be obtained by analyzing a series of SEM images without the alignment procedure explained above. Those high frequency components are irrelevant for IBG analysis, but are critical to propagation loss calculations [104], [109]. The noise spatial frequency range relevant for propagation loss is discussed in [111]. Inversely, the low frequency components of waveguide width fluctuations discussed in this chapter are not important to characterize propagation loss.

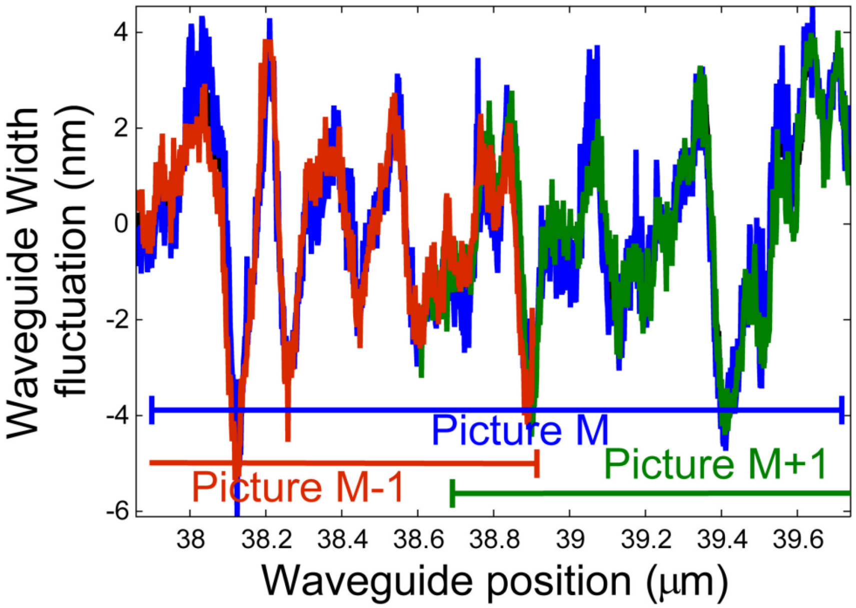

Fig. 34: Typical overlap of the waveguide width fluctuation between three consecutive images (red, blue and green). The black curve is the averaged waveguide width as a function of position.

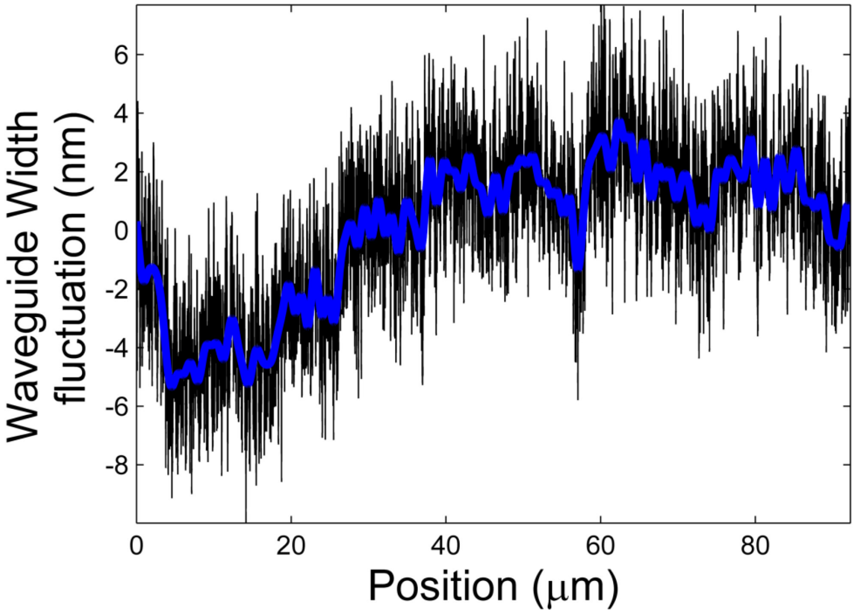

Fig. 35: Typical waveguide width fluctuation profile as a function of position. The black line is the raw data while the blue line is a filtered version of the waveguide width profile.

The red curve of Fig. 36 shows the autocorrelation, after filtering, modeled by a decaying exponential function. It should be mentioned that the filtered part of the waveguide width fluctuation measurement (high spatial frequencies), by itself, can also be modeled by a decaying exponential function as mentioned in [109], but obviously with a smaller autocorrelation length (a few tens to a few hundreds of nm). If one is interested to consider both the high and the low spatial frequencies of the waveguide SWR, the autocorrelation could be parameterized by the summation of two decaying exponential functions, with their respective set of parameters, σ_{SWR} and L_{SWR}.

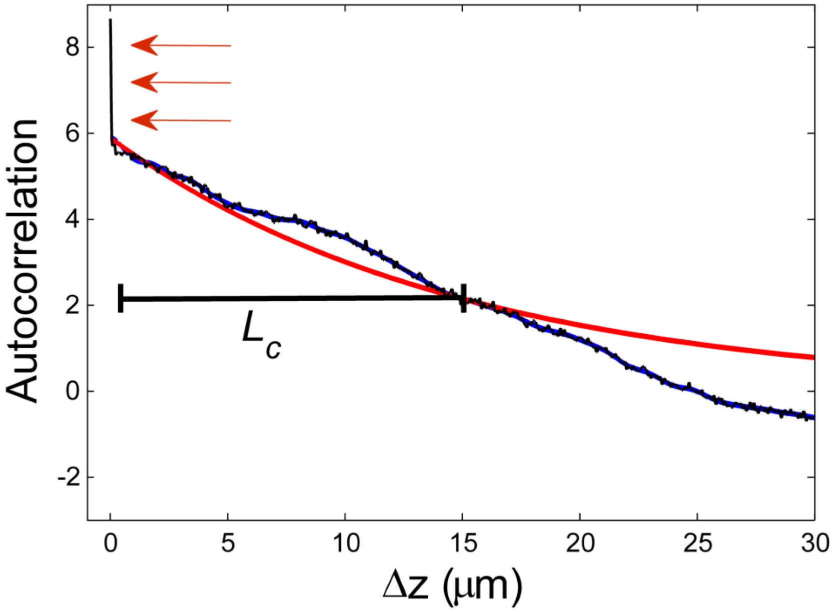

Fig. 36: Autocorrelation function of the waveguide width fluctuation of the filtered (blue) and unfiltered (black) curve of Fig. 35. The red curve is the decaying exponential autocorrelation fit.

The whole measurement procedure was repeated for seven photonic wires over a length of ~ 100 μm on three chips of the same wafer. The retrieved parameters are: σ_{SWR} = 1.8 nm ± 0.1 nm and L_{SWR} = 14 200 nm ± 600 nm[VIII]. The measurement length of 100 μm (i.e. 7x longer than the measured autocorrelation length) seems sufficient since it has been shown that the measurement length of a process to be characterized should be longer than the autocorrelation length by a factor in the range between three to eight [112]–[114][IX].

[VIII] The weak grating analysis presented in section 2.7 has been done for $L_{C,SWR}$ of a few nanometers, while the measured $L_{C,SWR}$ is about three order of magnitude larger. Fortunately, as mentioned in section 2.7, the approximation for small $L_{C,SWR}$ is still valid for values up to ~ 100 μm.

[IX] This point is studied in more detail in section 3.7.1

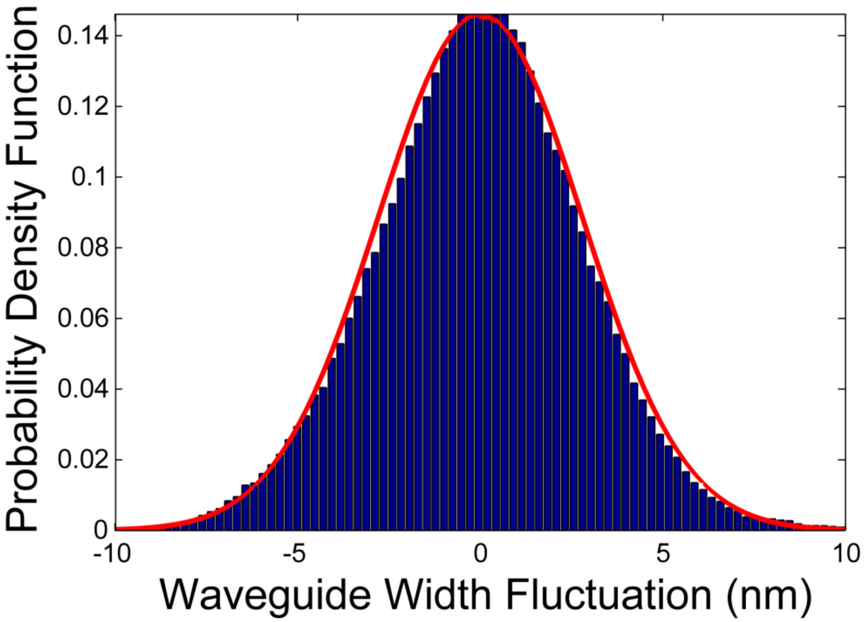

Fig. 37: Probability density functions of the SWR. The red curve is a Gaussian function.

Finally, as mentioned in section 2, the SWR is modeled by a random process with a normal distribution. This assumption is widely used for convenience since this kind of process can be easily handled mathematically. However, to our knowledge, this point has never been proven experimentally. To verify this affirmation, we considered the seven waveguide width profiles retrieved and plot a histogram (Fig. 37) to retrieve the probability density function of the process. The red curve is a Gaussian function with the width defined by the variance of the process. The overlap between the two confirms indeed that a normal distribution is an appropriate model for this kind of random process.

3.4.2 – Characterization of wafer height fluctuation

In this section, we use measurements of IBG spectral responses to estimate the phase-noise originating from WHFs. The IBGs samples were fabricated on the multimode section of a hybrid multimode/singlemode waveguide [98], [102] as shown in Fig. 4. The fabricated gratings used in this section are straight grating #1 and #2 described in Table 1 and Table 2. They were fabricated at IMEC. The $\lambda_B(z)$ and $\Delta n(z)$ profiles have been obtained using the characterization procedure described in section 1.6. The amplitude of a typical spectral response is shown in red in Fig. 38-a), while the retrieved grating profiles are displayed in Fig. 38-b) and c). The maximal grating reflectivity was designed to be very small to ease the convergence of the grating reconstruction algorithm[X]. The retrieved grating coupling amplitude and phase profiles, after appropriate filtering, are used to calculate the reconstructed spectral responses, showed by the black curve in Fig. 38-a), using a standard transfer matrix solution of the coupled mode equations. We confirm the precision of the retrieved λ_B and Δn profiles by obtaining a good correspondence between the reconstructed spectra and the measured ones. For the gratings studied in this chapter and the one shown in Fig. 38, the noise level allowed us to characterize the grating over a spectral band of roughly $\Delta\lambda = \pm 1$ nm around the resonances. As a result, a cut-off frequency of $f_c \approx 3\,000$ m^{-1} has been used.

Using Eq. (3.10) with the SWR parameters obtained in section 3.1 and the value of $\tilde{\sigma}_{\lambda_B}$ experimentally determined from measurements of IBGs fabricated on 1200 nm wide waveguides, the product $\sigma_{WHF} L_{c,WHF}^{1/2}$ can be estimated. A total of 11 gratings were measured on four different chips from two different wafers. We obtained $\tilde{\sigma}_{\lambda_B} = 0.17$ nm ± 0.01 nm resulting in $\sigma_{WHF} L_{c,WHF}^{1/2} =$ 6.6 x 10^{-13} m$^{3/2}$ using the calculated values C_{WHF} (3.6x10^{-3} nm^{-1}) and C_{SWR} (1.2x10^{-4} nm^{-1}) for these waveguides. This result is significantly lower than the experimentally determined product $2\sigma_{SWR} L_{c,SWR}^{1/2}$ =1.4 x 10^{-11} m$^{3/2}$ of the SWR. This means that, for a typical singlemode waveguide having a width of 500 nm, even though C_{WHF} (4.0x10^{-3} nm^{-1}) is about two times larger than C_{SWR} (1.9x10^{-3} nm^{-1}), SWR distortion is about one order of magnitude more damaging for IBGs spectral responses than WHF.

[X] The physical structure of strong gratings are harder to retrieve using inverse scattering algorithm since the optical wave is strongly reflected close to the input of the grating. As a result, very little optical power is reflected by the grating end thus making the reconstruction of the whole structure difficult. However, a lot of effort has been dedicated to solve this issue. In [73], the ILP algorithm used in this thesis, they successfully characterized grating having reflectivity of 99.99 %. However, in the work presented in this thesis, the grating reflectivity has been limited because of the high level of phase noise. As discussed in chapter 2, the spectral response of strong gratings (high κL) is more distorted by the phase noise. As a result, high phase fluctuations can be observed in the grating response and, since the algorithm is depending on the fast-Fourier transform algorithm, the obtained phase values must be unwrapped to provide the grating phase profile. If the wrong integer value of 2π is removed, the local evaluation of the Bragg wavelength will be wrong as well as the reconstructed profiles. Thus, to stay away from this problematic, weak gratings have been used.

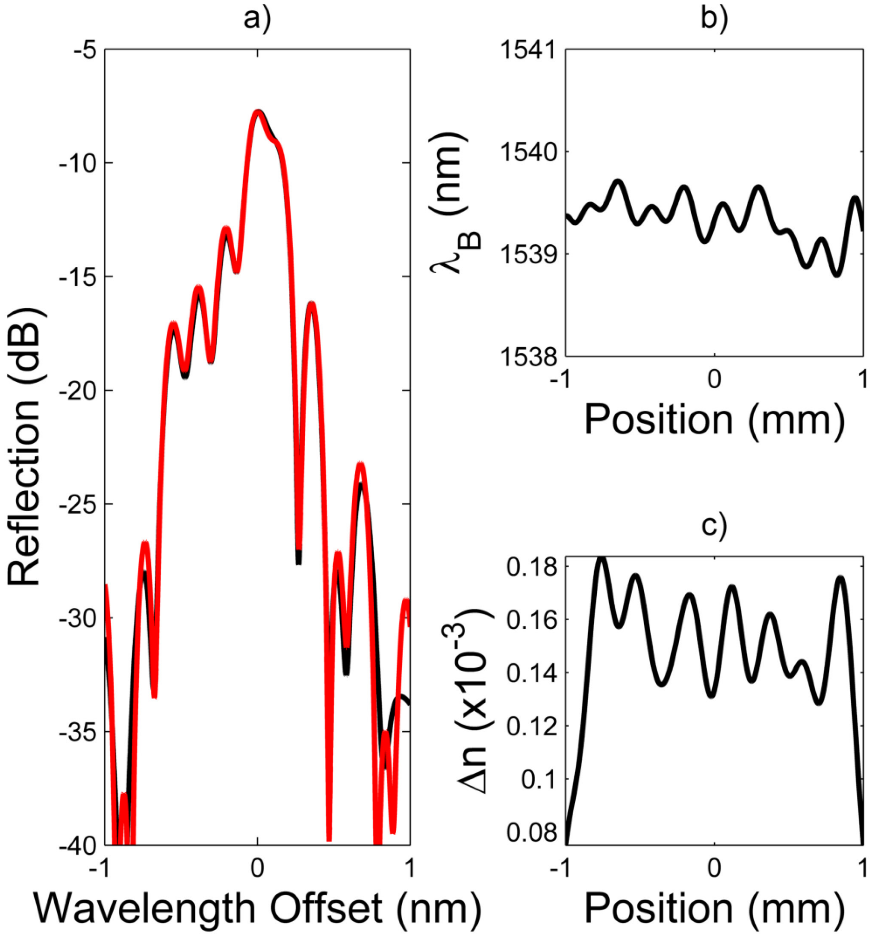

Fig. 38: a) Comparison of the experimental reflection spectrum of a typical straight grating on a 1200 nm wide waveguide (in red) with the reconstructed reflection spectrum (in black). Retrieved b) λ_B and c) Δn profiles, which are used to calculate the black curve of a).

3.5 – Phase-noise reduction techniques

Although an obvious way to reduce IBGs spectral distortions is to improve fabrication techniques to reduce the WHF, as discussed in [108], and the SWR, as discussed in [88], [89], [106], [107]. In the latter case, it is unclear if the proposed approaches, which are appropriate to reduce propagation losses, are compatible with the fabrication of corrugation based IBGs. These techniques optimize either the lithography, etching or post-etch process conditions in order to reduce the propagation losses, which are mainly influenced by spatial frequencies near the propagation constant of the guided mode [92]. Since the noise spatial frequencies that those techniques aim to remove are close to the grating spatial frequency, the grating corrugations will also be strongly suppressed during the fabrication process. Consequently, in this section we propose two approaches to reduce the phase noise by optimizing the design. The first one reduces the impact of SWR on IBGs spectra while the second one reduces the impact of WHFs.

3.5.1 – Reduction of the impact of sidewall roughness

The impact of SWR and WHF on the IBG phase noise is shown in Fig. 39 as a function of w_0. The curves were calculated for a waveguide with a 220 nm height using Eq. (3.10) with the experimentally determined parameter values for σ_{SWR}, L_{SWR} and $\sigma_{WHF} L_{c,WHF}^{1/2}$, and using a finite element mode solver to obtain $C_{SWR}(w_0)$ and $C_{WHF}(w_0)$. In Fig. 39, the red and the blue curves represent the respective contributions of the WHF and SWR impact on $\tilde{\sigma}_{\lambda_B}$, while the black curve shows their combined effect. Clearly, wider waveguide reduce considerably the IBG phase noise coming from SWR while leaving the impact of WHF unchanged. The cyan bars shows the value of $\tilde{\sigma}_{\lambda_B}$ determined from optical measurements of gratings in waveguides with w_0 = 1200 nm (i.e. the results used to obtain the product $\sigma_{WHF} L_{c,WHF}^{1/2}$ in the previous section) and in waveguides w_0 = 800 nm (a total of 14 gratings were measured on five different chips and two different wafers). The latter result is in good agreement with the theoretical curve, hence confirming the

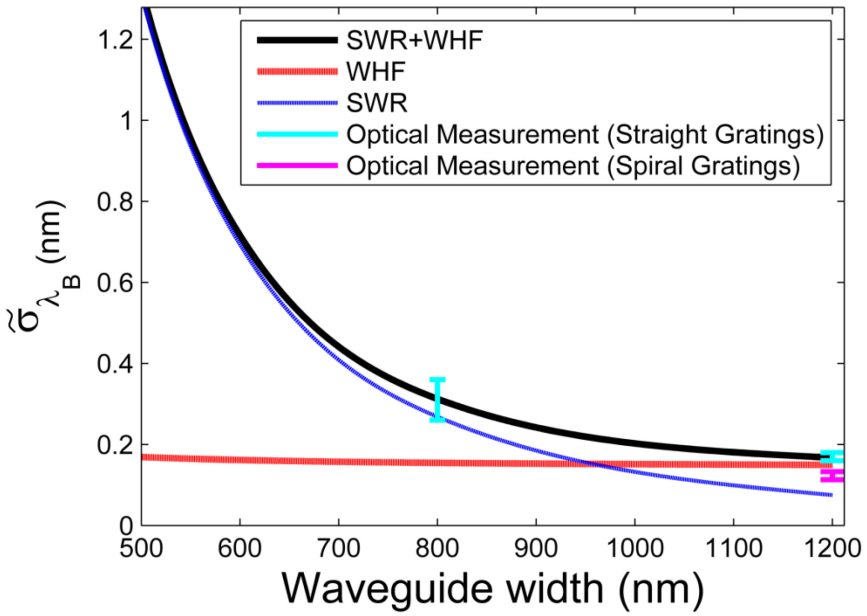

Fig. 39: Bragg wavelength standard deviation as a function of the waveguide width. The black curve contains both the impact of the SWR and the WHFs, while the blue and red curve takes those to effect independently. The cyan lines are the optical measurement of 2 mm-long IBGs while the purple line is the optical measurement for spiral IBGs.

validity of this model. As mentioned previously, the 1200 nm wide waveguides had an averaged Bragg wavelength standard deviation of $\tilde{\sigma}_{\lambda_B} = 0.17$ nm ± 0.01 nm while the 800 nm wide waveguides had a standard deviation of $\tilde{\sigma}_{\lambda_B} = 0.31$ nm ± 0.05 nm.

Since the fundamental mode becomes more strongly guided as w_0 increases, C_{SWR} decreases rapidly as shown on Fig. 3-b). It will be reduced by one order of magnitude when the waveguide width increases from 500 nm to 1050 nm when considering a waveguide thickness of 220 nm. As a result, as w_0 increases, the noise becomes dominated by WHF and the related Bragg wavelength standard deviation becomes

$$\tilde{\sigma}_{\lambda_{B,WHF}} \rightarrow \frac{8\Lambda C_{WHF}\sigma_{WHF}}{\lambda_B}\sqrt{\frac{n_g \Delta\lambda L_{c,WHF}}{2}} \tag{3.11}$$

which corresponds to the minimal amount of noise that can be obtained using hybrid single-mode waveguides [98], [102]. This approach allows a significant reduction of the phase noise but, as the calculations show, the improvement is limited by the level of WHF. Another motivation for designing IBGs in hybrid multimode/singlemode waveguides is the fact that the amount of backscattered light due to SWR is reduced as the waveguide width increases [78], i.e. when C_{SWR} is reduced. Considering that, in future work, longer grating structures with weaker coupling coefficients could be required to achieve integrated optical filters with elaborate spectral responses. As a result, backscattering noise could become problematic for standard singlemode waveguides (500 nm wide).

3.5.2 – Reduction of the impact of wafer height fluctuations

Considering that the phase noise that affects IBGs is composed of low frequency components and assuming that the autocorrelation length of the WHF is much longer than the SWR one, the fabrication of IBGs along a spiral as shown in Fig. 40 should reduce the WHF impact on the grating spectral response [83], [101]. With proper tuning of the grating period to compensate for the effective index variations caused by the curvature, as discussed in chapter 5 [101], those IBGs are as flexible as straight grating, provide highly compact devices and are less affected by phase noise.

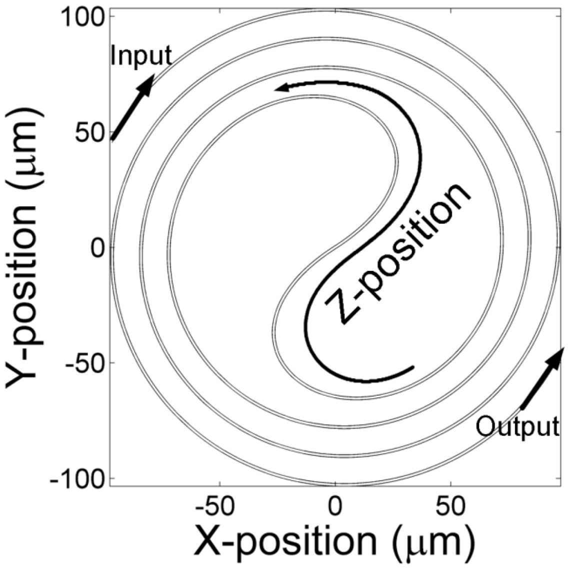

Fig. 40: Schematic of spiral IBGs

A total of nine spiral gratings on five different chips from the same wafer have been characterized. The detail of the spiral grating #3 parameters, fabricated at IME, is described in Table 3. The procedure to obtain the Bragg wavelength standard deviation is similar to the one described above for straight gratings. For this experiment, we obtained a Bragg wavelength standard deviation of 0.12 ± 0.01 nm. This result is indicated by the purple dot in Fig. 39 and can be compared to the straight grating result. It should be mentioned that, unlike the straight gratings, a layer of silica has been put on the wafer containing the spiral gratings. As a result, the improvement showed in Fig. 39 is probably underestimated due to the addition of a phase noise source caused by the possible presence of air-gaps between the waveguide and the silica layer. It should be mentioned that the top-cladding is causing a slight modification on C_{SWR} and C_{WHF}. The reduction of these parameters are responsible for about 10 % of the measured improvement of the Bragg wavelength standard deviation obtained with spiral gratings having an oxide top-layer while the remaining 90 % improvement is coming from the waveguide compactness.

To assess the impact of the SWR and the WHF reduction techniques on IBGs spectrum, a comparison is made in Fig. 41 between 2 mm-long straight gratings having widths of 800 nm and 1200 nm, with a spiral grating having a width of 1200 nm. The standard deviation of the Bragg wavelength of those gratings is 0.26 nm, 0.16 nm and 0.11 nm respectively, which makes them among the best of their category. The 3-dB bandwidths were respectively 0.22 nm (0.13 nm), 0.18 nm (0.13 nm) and 0.14 nm (0.12 nm). The value in parenthesis refers to the simulated 3-dB bandwidth of each design (presented in blue in Fig. 41). As can be seen from this figure, the use of wider straight waveguides improved the SLSR by ~ 3 dB and brought the grating 3-dB bandwidth closer to the design by ~ 0.04 nm. Furthermore, the improvement from 0.16 nm to 0.11 nm of the Bragg wavelength standard deviation obtained by using 1200 nm wide spiral-IBGs had a significant impact on the grating spectrum leading to a symmetrical main lobe that corresponds closely to the design (in blue). The SLSR has also been improved by ~ 3 dB compared to the straight 1200 nm wide IBGs and the first side-lobe corresponds more closely to the design. Fig. 42 presents the superposition of every Bragg wavelength measurements for the three types of IBG described above. The improvement due to the two phase-noise reduction techniques is clearly illustrated although further improvement could be achieved with even more compact spiral waveguides. In this work, the IBG strength was deliberately designed to be low in order to ease the reconstruction of the Bragg wavelength profile along the grating length but the two approaches could easily be extended to stronger grating filters.

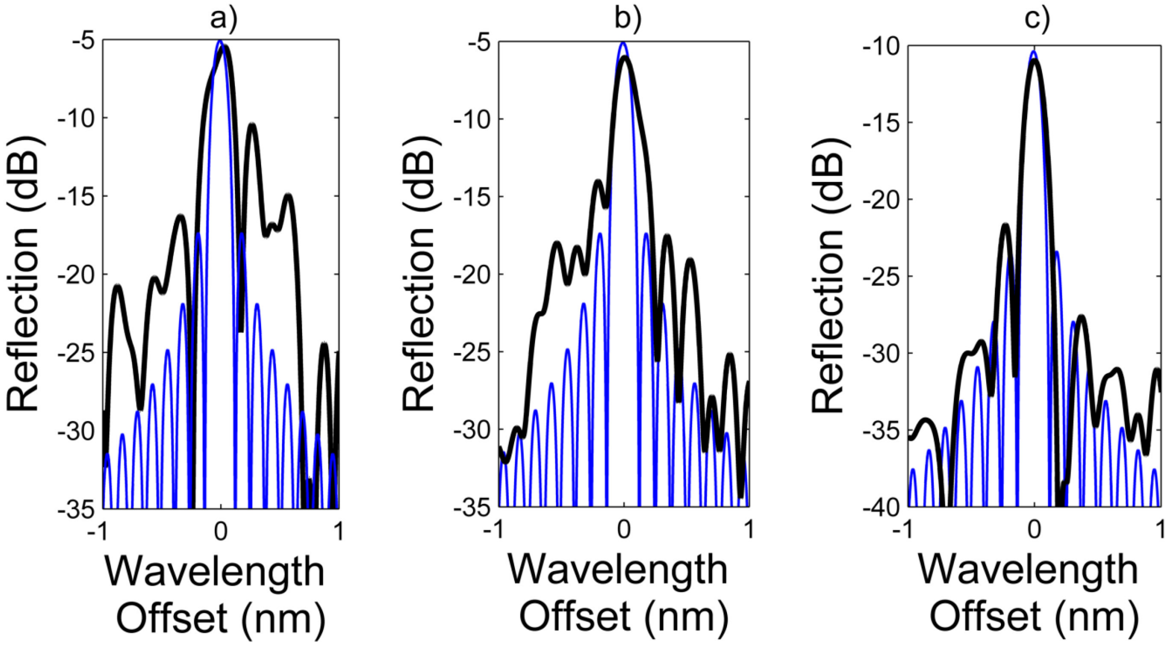

Fig. 41: Typical spectral response of 2 mm-long a) straight grating on a 800 nm wide waveguide, b) straight grating on a 1200 nm wide waveguide and c) spiral grating on a 1200 nm wide waveguide. The blue curves are the designs while the black curves are the experimental results.

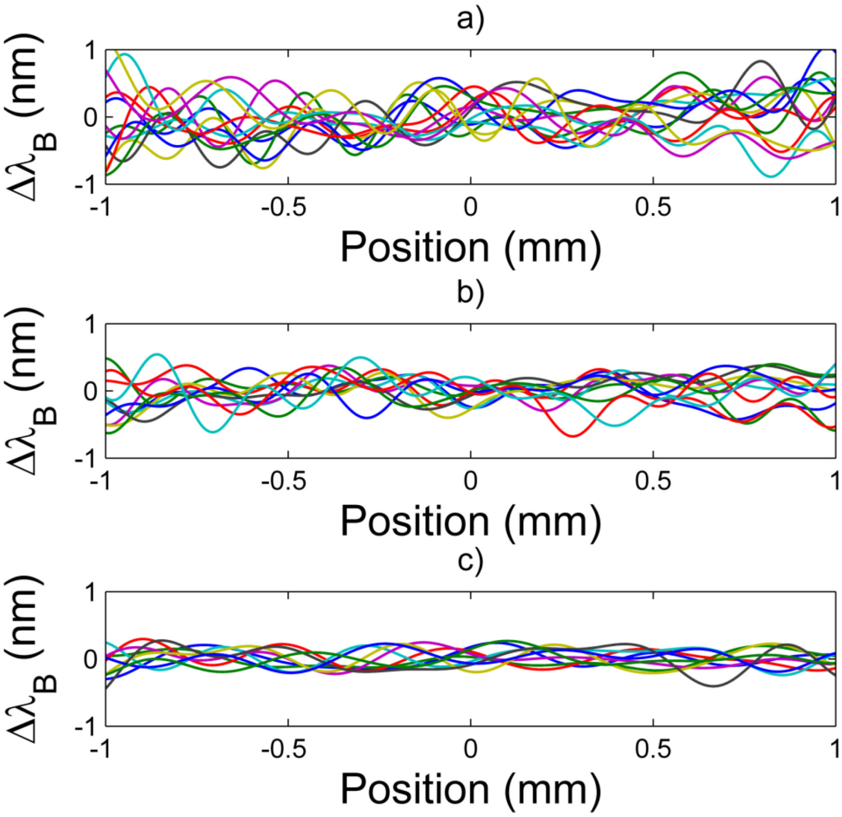

Fig. 42: Superposition of every Bragg wavelength fluctuation measurements for a) 800 nm straight waveguide, b) 1200 nm straight waveguide and c) 1200 nm spiral waveguide.

3.6 – Conclusion

In this chapter, we presented an improved technique to characterize SWR of silicon-on-insulator photonic waveguides and described how this phenomenon impacts the spectral response of IBGs. Many papers have discussed in length how to retrieve the sidewall roughness from SEM images. However, previously proposed technique could only be applied to single SEM image and, consequently, resulted in power spectral density described by an autocorrelation length of a few tens to a few hundreds of nm. In our work, we clearly show that there is also a significant portion of low frequency fluctuations. IBGs are predominantly influenced by the low spatial frequency content of the SWR whereas the high frequencies are relevant to characterize optical loss but are not sufficient to model and predict IBGs distortions. This chapter clearly demonstrates that, in addition to its amplitude, the spatial frequency content of SWR is of critical importance for IBG-based devices. Furthermore, the impact of the WHF on IBGs spectral response has been modeled and quantified for the first time.

This chapter also presented two techniques to improve IBG robustness to phase noise at the design step. The first one proposes the use of hybrid multimode/singlemode waveguides to reduce by more than one order of magnitude the effect of SWR on IBGs. The second one takes advantage of the fabrication of ultra-compact gratings in spiral waveguides to mitigate the impact of the silicon layer thickness variation.

These results are of importance because longer grating structures with weaker coupling coefficients are required in order to achieve integrated optical filters with elaborate spectral responses, both in amplitude and phase. Since longer gratings are more affected by phase noise, such demonstrations have been so far very limited. We believe that those phase-noise reduction techniques open the door to many new grating-based optical filter designs.

3.7 – Supplementary information

A few points should be added to this chapter: first, a thorough discussion should be made on the impact of the window size when characterizing the SWR autocorrelation length. Second, the numerical analysis presented in section 2.6 has been made with SWR parameters that do not model well the noise source of SOI waveguides; the SWR autocorrelation length is too small and the WHF phase noise source has been neglected. However, considering the results obtained in chapter 3 (σ_{SWR}, $L_{c,SWR}$, σ_{WHF} and $L_{c,WHF}$), the emulated IBGs can be converted to model IBGs on wider waveguide. This conversion is done below. Third, a discussion on the importance of a possible period noise is made. Finally, the autocorrelation shape obtained in Fig. 36 has been fitted with an exponential decaying function. However, a discussion on the exact shape of the autocorrelation function is made. Furthermore, the work presented in this chapter shows L_c values much larger than what is usually published in the literature. This aspect is also discussed in this section

3.7.1 – Window size

As stated in this chapter, the ratio (N_{Lc}) of the measurement length (or the window size) and the measured autocorrelation length should be larger by a factor between three to eight [112]–[114]. However, since this value is varying from reference to reference, we found necessary to analyse the impact of the measurement window with more attention. To do so, a white Gaussian noise has been generated and filtered with a Lorentzian function (as described by Eq. (2.3)) having a width defined by the measured autocorrelation length. To emulate the measurement taken in this chapter, the measurement window length was fixed at 100 µm and the generated autocorrelation length was varied between 2 µm and 100 µm which make N_{Lc} varied from 1 to 50. Using the generated noisy vector, the autocorrelation length was then calculated. The ratio between the calculated autocorrelation length and the generated autocorrelation length (α_{Lc}) is then calculated and plotted in Fig. 43 as a function of N_{Lc}. Each blue marker on this figure represents the average result obtained with 500 emulated data.

As can be seen in Fig. 43, $\alpha_{Lc} \rightarrow 1$ when the measured window is much larger than the autocorrelation length to characterize. The value $N_{Lc} = 8$ as stated in [113], [114] is indeed sufficient to obtain a very precise estimation of the autocorrelation length while a value of $N_{Lc} = 3$ as stated in [112] seems only sufficient to evaluate the order of magnitude of the autocorrelation length. As shown on this figure, the precision that can be obtain when using $N_{Lc} = 7$, the value used in this work, is higher than 90 %. Ideally, the measurement windows would have been slightly larger, but this parameter could not be easily increased since the precision of the SEM translation stage was not precise enough. As stated in this chapter, the precision of the translation

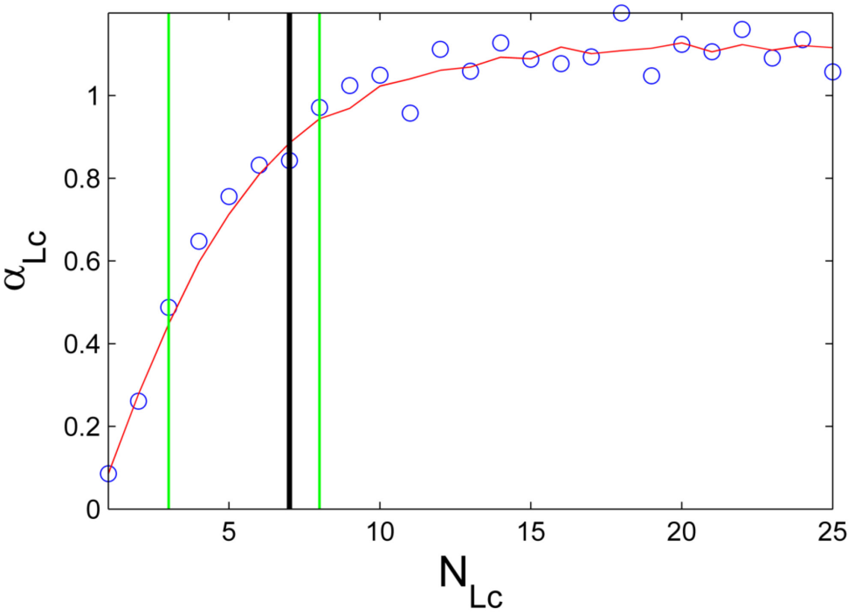

Fig. 43: α_{Lc} **is plotted in blue as a function of** N_{Lc}**. The red curve is a smoothed version of the blue markers while the black line is highlighting the** N_{Lc} **value used in this chapter and the green lines highlight the minimal** N_{Lc} **value suggested in [112]–[114].**

stage is about ± 0.3 µm. This value is not provided by the manufacturer but is the standard deviation of the *z*-translation correction that has been introduced on the data presented in this chapter. However, as the measurement window increases, the chance to have at least one translation offset larger than the FOV (1900 nm) increases. As a result, many measurements had to be thrown out. The impact of a 10 % variation of the autocorrelation length on the overall IBG phase noise is shown in Fig. 44. The proximity between the black and the red curve confirms that the use of a window length of ~ 100 µm was indeed appropriate to characterize the Bragg grating phase noise.

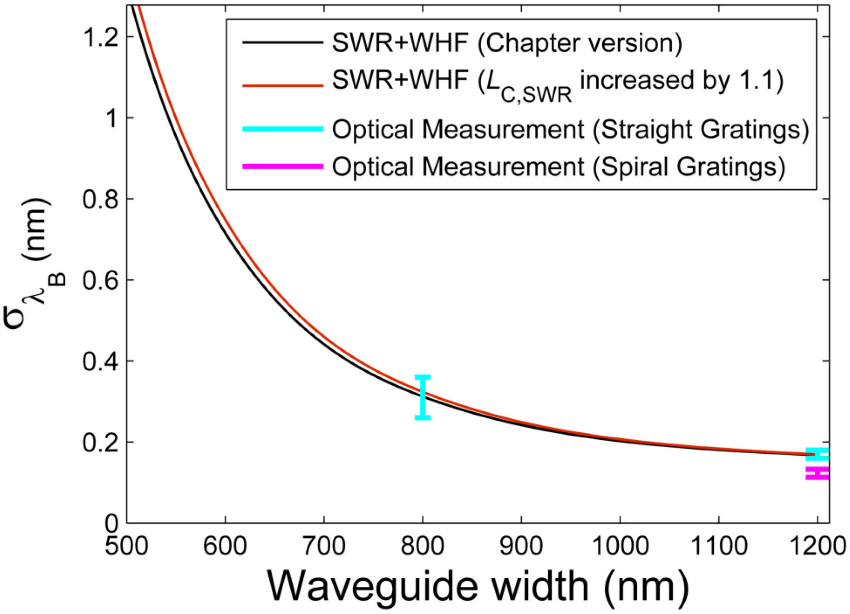

Fig. 44: Bragg wavelength standard deviation as a function of the waveguide width. The black curve contains both the impact of the SWR and the WHFs (already presented in Fig. 39) while the red curve presents the same result but with a larger $L_{c,SWR}$ (to consider a possible underestimation of the parameter due to the window size). The cyan lines are the optical measurement of 2 mm-long IBGs while the purple line is the optical measurement for spiral IBGs (already presented in Fig. 39).

3.7.2 – Emulation results

The emulation results obtained in section 2.6 were obtained using waveguide width and height of 500 nm x 220 nm and the phase noise parameters summarized in Table 4. Unfortunately, at the time, the values modeling the SWR were unknown and the WHF was neglected. As a result, those results are off. However, by calculating the $\tilde{\sigma}_{\lambda_B}$ values used in these simulations using Eq. (3.10) and by using these values, as well as the results presented in Fig. 39 (which takes into account the effect of WHF and uses properly characterized phase noise parameters), the emulation done in chapter 2 can be associated to IBGs made on hybrid waveguides. The widths that match $\tilde{\sigma}_{\lambda_B}$ are shown in Table 4 for three of the four emulation sets. The last one does not have any associated width since the WHF noise contribution, which does not vary significantly with the waveguide width, is higher than the emulated one.

Table 4: The inputs describe the phase noise characteristic used for the emulations presented in section 2.6 while the outputs is final standard deviation of the Bragg wavelength used in these simulations and the waveguide width that has the same emulation results considering the phase noise parameter measured in this chapter

Input					Output	
σ_{SWR}	$L_{c,SWR}$	σ_{WHF}	$L_{c,WHF}$	width	$\tilde{\sigma}_{\lambda_B}$	width
4 nm	300 nm	0 nm	-	500 nm	0.45 nm	680 nm
4 nm	50 nm	0 nm	-	500 nm	0.19 nm	1040 nm
2 nm	300 nm	0 nm	-	500 nm	0.23 nm	915 nm
2 nm	50 nm	0 nm	-	500 nm	0.10 nm	-

Furthermore, experimentally, the standard deviation of the central wavelength of IBG devices, measured over a full wafer, is of the order of several nanometers, which is a lot higher than the emulated gratings shown on Fig. 18-b). Even if the source of this wavelength shift is the same as the source of the spectral distortion discussed in chapters 2 and 3 (i.e. SWR and WHF), the spatial content that is responsible for the variability of the central wavelength of the IBGs is the very low spatial frequency, which has not been characterized in this third chapter. To model the central wavelength variability, one should characterize the SWR and the WHF on a wafer scale.

3.7.3 – Period noise

Finally, as stated in section 2.4, the impact of a period noise has been neglected in this thesis. However, as the SWR creates a waveguide width fluctuation which results in IBG phase noise, the same SWR could also create a period noise since each sidewall of the corrugations, parallel to the *x*-axis, can be moved in space around its designed value as shown by the horizontal arrows in Fig. 45. Consequently, strictly speaking, the impact of SWR should be analysed both on the waveguide (vertical arrows) and on the other corrugation sidewalls (horizontal arrows). However, since very small corrugation are required to obtain grating resonances, the fabricated IBG waveguide noise contribution can be approximated to be similar to the one of a simple waveguide.

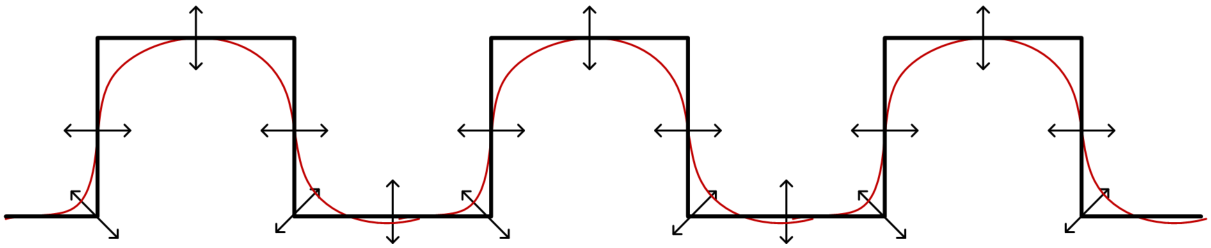

Fig. 45: The black line is an example of the shape of the corrugations of an IBG mask layout, the red lines shows a possible fabricated sidewall of an IBG while the arrows illustrate the position shifts of the sidewall that can happens after fabrication.

However, it should be mentioned that we do not expect the period phase noise to be significant even in the case of larger corrugation amplitudes since this effect will have negligible impact on IBGs spectral response. To confirm this point, let's consider that the corrugation central position is well modeled by a white Gaussian noise (i.e. the power spectral density is constant). Additionally, since the period is by definition the spacing between two corrugations, the period power spectral density will be composed of the initial white Gaussian noise power spectral density product by the linear function "$i\omega$" coming from the differentiation. As a result, if we consider only the low frequency content (below $f_c \approx 3\ 000\ \mathrm{m}^{-1}$ as it was done in section 3.4.2), according to simulations done with Matlab, the period standard deviation in this spectral range will be reduced by ~ $1\mathrm{x}10^{-4}$ compared to the initial white Gaussian noise which makes this phenomenon negligible.

3.7.4 – Autocorrelation shape and autocorrelation length

When considering Fig. 36, one can notice that the experimental decaying autocorrelation model [92] might not be the best fit to the experimental results. On one hand, introducing the Hurst factor [89] would add another fitting degree of freedom and could help to improve the match between the model and the experimental measurement. On the other hand, although this approach is not supported by a theoretical model, a linear regression seems to be a simple function that matches relatively well the result shown in Fig. 36. However, as shown in Fig. 46, the use of a linear model instead of an exponential decaying model does not modify significantly the impact of the phase noise on the grating spectral response. Fig. 46-a) shows the autocorrelation function, while Fig. 46-b) shows the associated power spectral density functions of both the exponential decaying model and the linear regression fit. Even if the shapes of the power spectral density function are slightly different from one another, the low frequency content that are relevant to IBGs spectral response (between the vertical dotted lines) have a similar amplitude. Thus the exact autocorrelation shape will not have a significant impact on the results presented in this chapter.

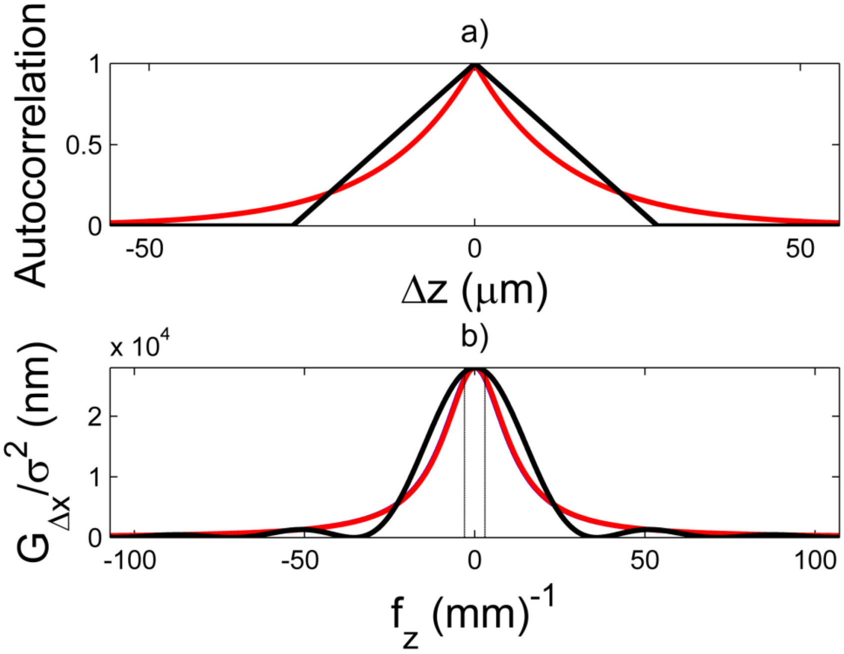

Fig. 46: a) Exponential decaying autocorrelation function (in red) and a linear fit (in black) and b) the associate power density function. The vertical dotted lines are the frequency content relevant for IBGs spectral response

Finally, unlike in many papers characterizing the SWR autocorrelation length [88], [89], [106], [111], where L_c is typically a few tens to a few hundreds of nanometers, the results presented in this chapter shows autocorrelation length of a few microns. However, this is due to the picture alignment procedure. When high resolution SEM pictures having a FOV of a few microns are analysed, the low frequency contents of the SWR are suppressed which reduces the L_c measurement. To confirm this point, the SEM images analysed in this chapter have been analysed without the picture alignment procedure and the resulting autocorrelation is shown in Fig. 47. The calculated autocorrelation length in that case is 42.2 nm and the noise standard deviation is 1.94 nm which agrees well with the results presented in the literature.

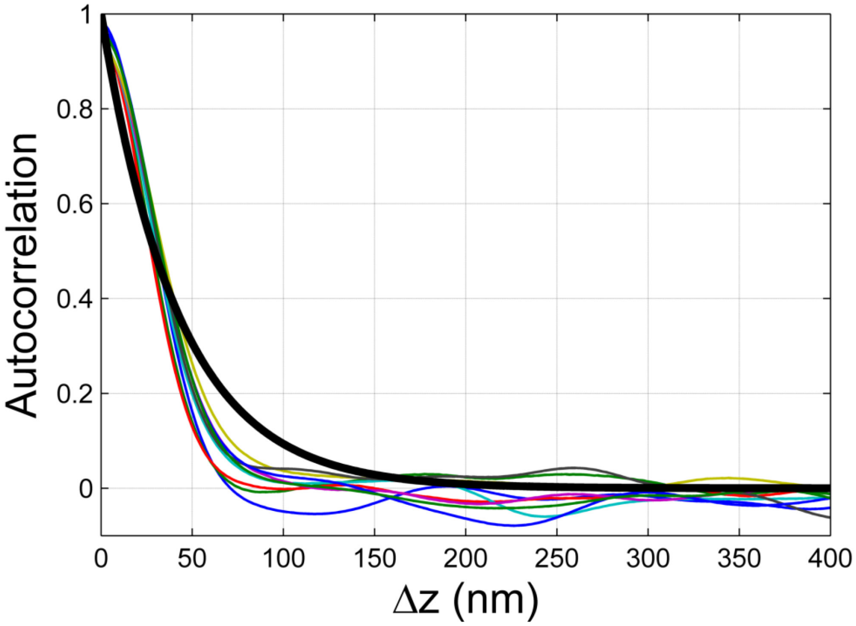

Fig. 47: Experimental autocorrelation function of the data presented in this paper but where the SEM images are analysed independently (without the picture alignment procedure). The thick black curve is the exponential fit having a 42.2 nm autocorrelation length.

Chapter 4: Apodized Silicon-on-Insulator Bragg Gratings

As shown on Fig. 3-b), the effective index of a photonic wire is varying non-linearly with the waveguide width. Similarly, the coupling coefficient associated with a recess variation is also non-linear. As a result, the spectral response of apodized grating fabricated with a recess varying approach will be distorted, both in phase and amplitude, by an offset of the average waveguide width or by a calibration error of the recess depth. Such an approach makes this kind of grating very sensitive to fabrication variation. A solution to this problem is to design gratings with uniform corrugation recess and uniform waveguide width. In this situation, an offset of the average waveguide width only shift the resonance and an offset in the recess amplitude will modify the maximal coupling coefficient value without adding distortion in these profiles. Furthermore, as discussed in section 1.6, when the grating complexity is increased, small local grating coupling coefficient are likely to be required. As a result, there is also strong motivation to develop apodisation techniques compatible with small κ values.

This chapter proposes two reliable apodization techniques solving these issues. However, the high amount of phase noise prevented the SLSR from reaching the expected design value. This last point was not fully discussed in this short paper, a reproduction of [102], which is why simulation results were added at the end of this chapter. This work was published in "*Photonics Technology Letters*" in 2012.

4.1 – Abstract

Accurate control of the apodization profile is still an issue for IBG filters fabricated in SOI because of the high modal confinement of these waveguides. In this chapter, we present two fabrication-friendly apodization techniques that are compatible with DUV lithography and can be used in mass-production of photonic-integrated circuits. These techniques are reliable even for weak effective index modulation amplitude, thus opening the door to the fabrication of long and elaborate grating structures.

4.2 – Introduction

IBGs find many applications in semiconductor lasers, on-chip interconnects, PICs, and so on. On one hand, IBGs in distributed-feedback lasers are typically short (hundreds of micrometers) and have strong reflectivity (coupling coefficient having value of a few hundreds of cm^{-1}). On the other hand, optical filters made with IBGs having lengths up to cm scale can provide on-chip phase engineering for dispersion or laser chirp compensation, pulse shaping for high-bit-rate optical communications, and channel selection for WDM applications. Recently, footprint reduction of long IBGs was proposed using curved waveguides [83], [84]. In all cases, grating apodization remains an issue.

Full control of the complex spectral responses of IBGs requires the development of reliable apodization techniques. Some previously studied techniques considered a change in the corrugation duty-cycle or recess amplitude to modify the local coupling coefficient [48], [49]. Unfortunately, in addition to the variation of the local coupling coefficient, these approaches often involve an important modification of the local effective index, which distorts the spectral response. To prevent these unwanted phase variations, it was proposed to simultaneously modify both the waveguide width and the amplitude of the grating corrugation recesses in order to independently control the coupling coefficient and average effective index profiles [50]. In principle, this approach is very flexible but, for long IBGs in SOI, the corrugation recesses are typically smaller than a few tens of nanometers and the precision of the lithographic process will limit the accuracy of the apodization technique. For research purposes, these IBGs can be fabricated using e-beam lithography, a very accurate but time consuming technique. However, for mass-production, CMOS processes typically use DUV lithography that offer enough precision to fabricate uniform IBGs, but have insufficient precision to apodize gratings by changing the amplitude of the corrugation recesses.

In this chapter, we investigate two apodization schemes that are CMOS compatible. The first one is based on the superposition of the two sidewall gratings while the second one relies on phase modulation of the grating. Both techniques rely on a modulation of the corrugation position rather than its recess amplitude. These apodization techniques are examined for the first time in SOI.

4.3 – Design and post processing

As shown in section 2.6.2 [41], the benefits of apodized gratings are strongly reduced when the noise on the Bragg wavelength is high. This effect is caused by the high index contrast of SOI waveguides and as mentioned in the previous chapter, a mean to reduce this phase noise in the design process is to implement the IBG in the multimode section of a hybrid multimode/singlemode waveguide [98] as shown in Fig. 4. The gratings used in this chapter are the 1200 nm wide straight gratings described in Table 1. For apodized gratings, a Gaussian apodization profile with a full-width at half maximum of 1 mm was used. To fully analyze the impact of the apodization schemes on the amplitude and phase profile of the IBGs, the recess amplitude had to be maintained constant. Consequently, the reflection of the apodized gratings is

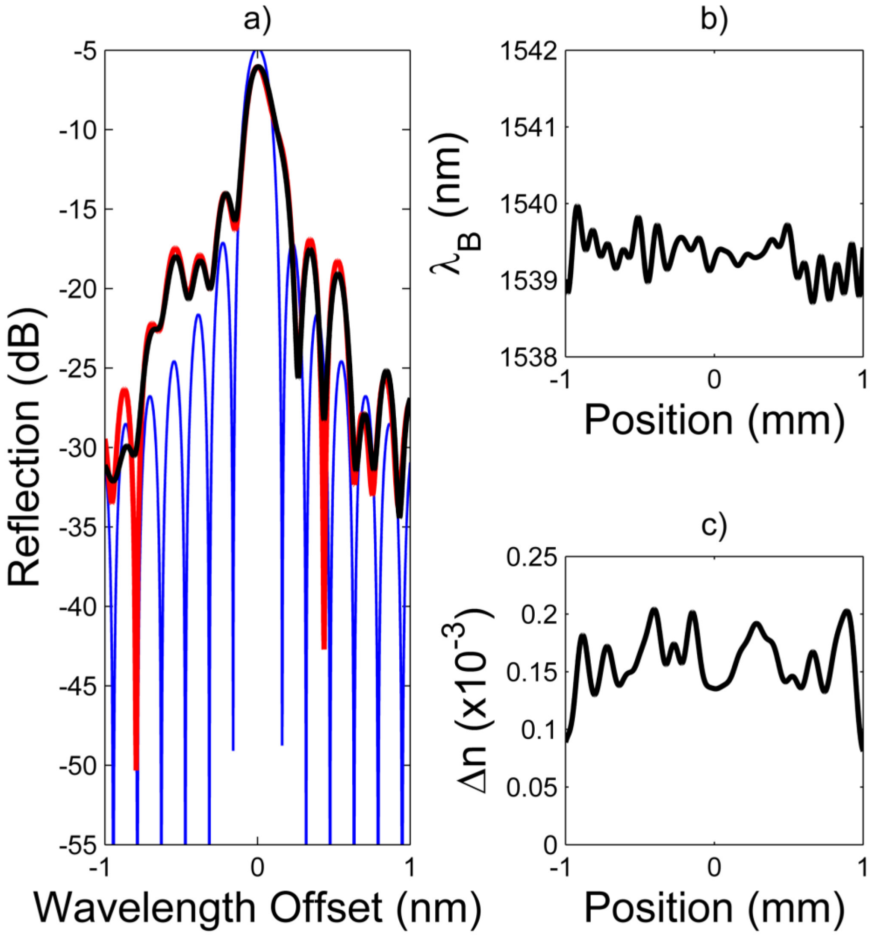

Fig. 48: a) Comparison of the experimental reflection spectrum of an unapodized grating (in red) with the reconstructed reflection spectrum (in black) and the designed spectrum (in blue). Retrieved b) λ_B and c) Δn profiles, which are used to calculate the black curve of a).

smaller compared to the unapodized ones due to the reduced value of the coupling coefficient integral over the grating length. The characterization of the grating has been done as described in section 1.6. The reconstructed spectra (in black in Fig. 48-a), Fig. 49-a) and Fig. 50-a)) are compared to the measured ones (in red) and to the designs (in blue). In [41], it was shown that only the phase noise with low spatial frequency has an impact on the IBG spectral response and that the cut-off frequency depends on the grating bandwidth. Therefore, the λ_B and Δn profiles were filtered by an ideal low-pass filter with a cut-off frequency of ~10 mm^{-1}, which corresponds to a spectral bandwidth of roughly ±3 nm around the Bragg wavelength.

Fig. 48-a) shows the results for an unapodized grating. The good correspondence between the experimental and the reconstructed curves, as well as the spatial uniformity of Δn, gives confidence in the technique used to retrieve the Bragg wavelength (shown in Fig. 48-b)) and Δn profiles (shown in Fig. 48-c)). The relatively low SLSR, ~ 8 dB (4 dB less than the design), is due to $\lambda_B(z)$ fluctuations that are likely caused by variations of the waveguide dimensions.

4.4 – Superposition-apodized Bragg gratings

The first apodization technique that we investigated relies on the superposition of two gratings that interfere to provide the desired apodization profile. This approach has already been tested in rectangular silica waveguides [115], but has never been studied for IBGs in highly confined waveguides such as SOI photonic wires. More specifically, this technique changes the relative phase of two grating structures, such that

$$n = n(\lambda) + \sum_{i=1}^{2} \frac{\Delta n_i}{2} \cos\left(\frac{2\pi}{\Lambda_i} z + \theta_i(z) + F_i(z) \right), \qquad (4.1)$$

where i = 1 and 2 refer to the left-hand-side and right-hand-side gratings, respectively. When both gratings are identical, aside from the phase functions $F_i(z)$ that are equal but opposite, $F_1(z) = -F_2(z) = F(z)$, Eq. (4.1) reduces to

$$n = n(\lambda) + \Delta n \cos\left(F(z)\right) \cos\left(\frac{2\pi}{\Lambda} z + \theta(z) \right). \qquad (4.2)$$

Consequently, the phase function *F*(*z*) must be equal to the arccosines of the target apodization profile. Fig. 49-a) shows a comparison between the measured, reconstructed, and designed grating spectra. Fig. 49-c) clearly shows that the fabricated apodization profile follows the target Gaussian profile, which confirms the robustness of this fabrication technique even for very small index modulation amplitude.

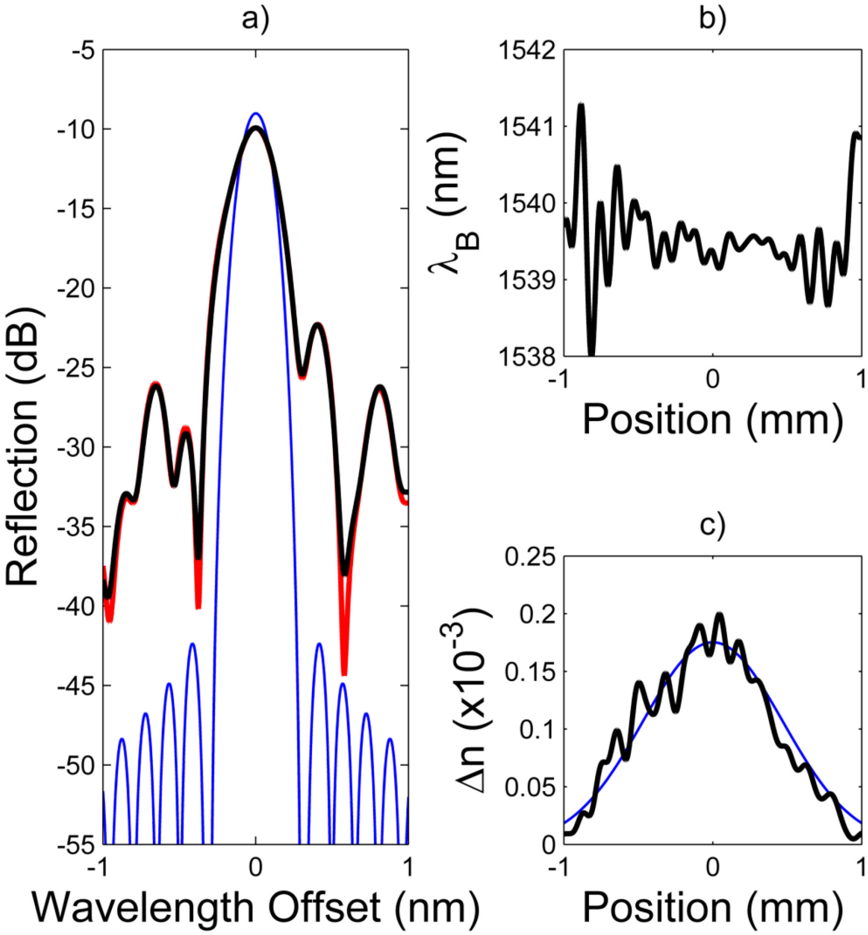

Fig. 49: a) Comparison of the experimental reflection spectrum of the superposition-apodized grating #1 (in red) with the reconstructed spectrum (in black) and the designed spectrum (in blue). Retrieved b) λ_B and c) Δn profiles, which are used to simulate the black curve of a). The blue curve in c) is the target apodization profile.

4.5 – Phase-apodized Bragg gratings

The second apodization technique, named phase-apodization, adds a slow modulation function in the phase function of the grating with a *z*-dependant amplitude [116]. In this case, both sidewall gratings are identical. The effective index of the grating can be expressed as

$$n = n(\lambda) + \Delta n \cos\left(\frac{2\pi}{\Lambda} z + \theta(z) + \phi(z) \sin\left(\frac{2\pi}{\Lambda_M} z \right) \right). \tag{4.3}$$

By expanding this equation with Fourier series and using the Bessel function integral definition, Eq. (4.3) becomes

$$n = n(\lambda) + \Delta n \sum_{m=-\infty}^{\infty} J_m(\phi(z)) \cos\left(\frac{2\pi}{\Lambda} z + m \frac{2\pi}{\Lambda_M} z + \theta(z) \right). \tag{4.4}$$

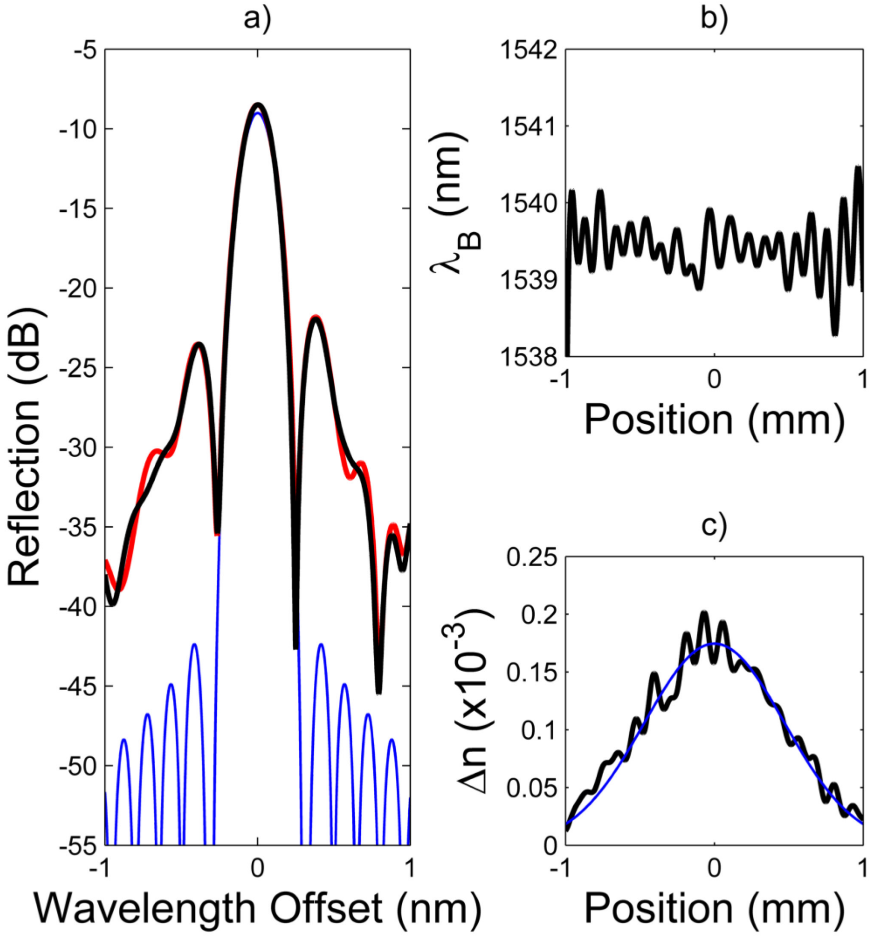

Fig. 50: a) Comparison of the experimental reflection spectrum of the phase-apodized grating #1 (in red) with the reconstructed spectrum (in black) and the designed spectrum (in blue). Retrieved b) λ_B and c) Δn profiles which are used to simulate the black curve of a), blue curve is the target apodization.

The desired apodized grating (m=0) is accompanied by Bragg grating structures ($|m| \geq 1$) at different resonant frequencies. The modulation period[XI] (Λ_M) must therefore be chosen small enough to prevent any perturbation of the desired grating resonance (m=0) by the satellite peaks ($m \neq 0$) induced by phase modulation but not too small to prevent distortions caused by inaccurate sampling. We find that Λ_M = 17.5 µm is a good tradeoff value. To apodize the 0th order grating, $\phi(z)$ must be equal to $J_0^{-1}(f(z))$, where $f(z)$ is the target apodization profile. Fig. 50 shows the result obtained for the phase-apodization scheme. Satellite peaks ($m = \pm 1$) are present at ± ~15 nm but are not displayed in Fig. 50.

4.6 – Discussion

For each apodization technique, we measured the spectral response of three grating samples. Table 5 displays the peak reflectivity, 3-dB and 5-dB bandwidths, and SLSR of each sample. Every sample follows the apodization design in a similar way as those shown in Fig. 49 and Fig. 50. These results show that the main reflection lobes of phase-apodized gratings match closely the design in terms of reflectivity and bandwidth. Fig. 49-b) and Fig. 50-b) suggest that the better spectral characteristics of phase-apodized gratings result from the lower effective index fluctuations displayed as Bragg wavelength fluctuations in the figures. This hypothesis was verified through numerical simulations, which showed that the effective index fluctuations in the superposition-apodization explained the spectral broadening and the reduced maximal reflectivity. We believe that this phase perturbation is related to the photolithographic process. The dose locally applied on the resist where the two gratings are in-phase slightly differs from the

---

[XI] According to Eq. (2.10), the wavelength spacing between the main Bragg resonance and the first satellite is well approximated by

$$\Delta\lambda = \frac{\overline{\lambda}_B}{1 + \Lambda_M \dfrac{\left(1 - 2n_1\Lambda\right)}{\Lambda}} = \frac{\overline{\lambda}_B^{\,2}}{\overline{\lambda}_B + 2n_g\Lambda_M},$$

or equivalently, the modulation period can be expressed as

$$\Lambda_M = \frac{\overline{\lambda}_B}{2n_g}\left(\frac{\overline{\lambda}_B}{\Delta\lambda} - 1\right).$$

dose applied where the two gratings are out of phase, which results in a slight variation of the average waveguide width; i.e. the Bragg wavelength is modified. Even if the coupling between the apodization and the effective index is small, this effect might be critical for applications that require nearly perfect control of the grating phase. Therefore, phase-apodization shows better promises for future applications. Although improved with respect to uniform gratings, the SLSR of both techniques is far from the expected 33 dB. This discrepancy is believed to be due to the aforementioned waveguide dimension fluctuations, which is still a major problem for the fabrication of phase sensitive devices on SOI[XII].

Table 5: Spectral measurement of IBG samples

	R_{max} (dB)	BW_{3dB} (GHz)	$BW_{5\,dB}$ (GHz)	SLSR (dB)
Design	-9.0	25.4	32.1	33.3
Super. #1	-9.9	34.5	45.3	12.4
Super. #2	-10.9	48.2	61.8	10.3
Super. #3	-9.7	30.7	40.7	13.1
Phase #1	-8.5	25.8	32.6	13.4
Phase #2	-8.1	24.9	31.5	13.8
Phase #3	-8.7	25.8	33.2	15.5

4.7 – Conclusion

We investigated two apodization techniques, superposition and phase modulation, for IBG fabrication in SOI. Both techniques present the advantage of having corrugation recess with constant amplitude along the grating, which facilitates fabrication with standard DUV lithography. Better results were obtained by apodization with phase-modulation. Precise apodization profiles can be realized even for gratings having very small index modulation amplitude, which would have been impossible using amplitude apodization. These results open the door to fabrication of the long grating structures necessary to design filters with elaborate spectral responses.

[XII] This point is discussed in more detail in section 4.8.

4.8 – Supplementary information

As mentioned in the discussion, the discrepancy between the design and the measured spectra are believed to be due to waveguide dimension fluctuations which create phase noise as stated in chapters 2 and 3. To confirm this point, the reconstructed profile of the apodized gratings obtained in sections 4.4 and 4.5 are used to simulate the spectrum of the retrieved apodized gratings, but without the phase noise contribution. To do that, the Bragg wavelength profile is artificially made constant to the average of the reconstructed profile. The results are presented in green in Fig. 51 and Fig. 52. As can be seen from these figures, it is the phase noise that dramatically distorts the grating spectra. When this phenomenon is removed, the spectra SLSR is

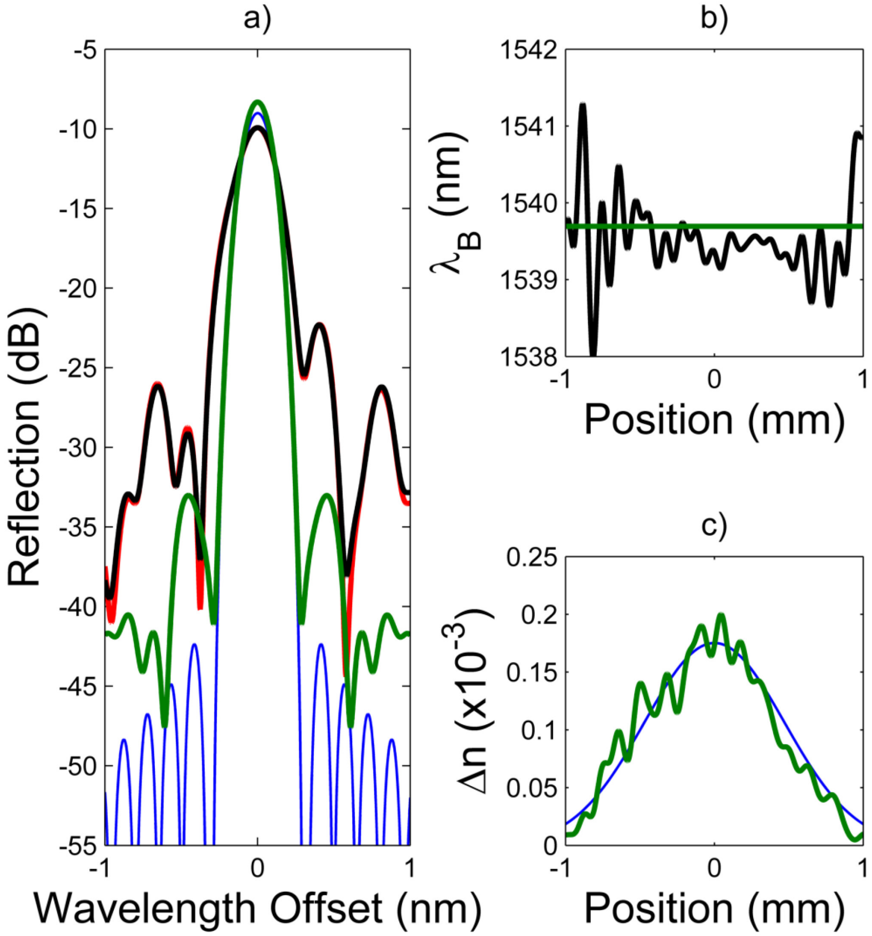

Fig. 51: a) Comparison of the experimental reflection spectrum of the superposition-apodized grating #1 (in red) with the reconstructed spectrum (in black) and the designed spectrum (in blue). Retrieved b) λ_B and c) Δn profiles, which are used to simulate the black curve of a). The blue curve in c) is the target apodization profile. This figure is a reproduction of Fig. 49 on which the simulated spectrum of the reconstructed apodization profile with an ideal Bragg wavelength profile is added in green.

improved by 11 dB and 16 dB for the superposition and phase apodisation technique respectively compared to their respective measured spectrum. A similar procedure has been done for an ideal apodisation profile but with the reconstructed phase noise profile, but the obtained spectra did not differ significantly from the experimental measurements, which confirm that the dominant impairment is phase noise rather than amplitude noise.

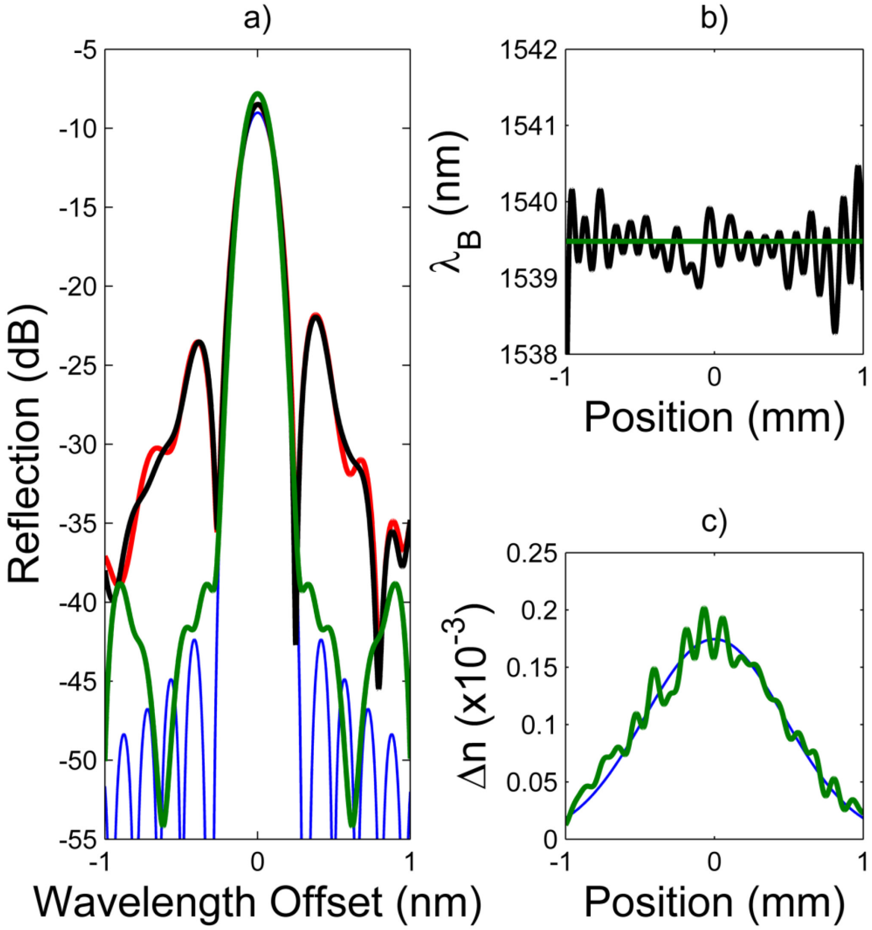

Fig. 52: a) Comparison of the experimental reflection spectrum of the phase-apodized grating #1 (in red) with the reconstructed spectrum (in black) and the designed spectrum (in blue). Retrieved b) λ_B and c) Δn profiles which are used to simulate the black curve of a), blue curve is the target apodization. This figure is a reproduction of Fig. 50 on which the simulated spectrum of the reconstructed apodization profile with an ideal Bragg wavelength profile is added in green.

Chapter 5: Integrated Bragg Gratings in Spiral Waveguides

In this chapter we discuss how the form factor of IBGs can be improved in order to be compatible with PIC chip size. This issue is particularly critical for filters with tailored optical responses like apodized or sampled gratings that typically are several millimeters long. The idea is to modify the strongly asymmetric grating aspect ratio into a symmetrical one by implementing the grating into a spiral-shaped waveguide. This chapter is a reproduction of a paper published in "*Optics Express*" in 2013 [101]. As discussed in chapter 3, it turns out that this approach is also a good solution to reduce the contribution of the wafer thickness fluctuations on IBGs phase distortion.

5.1 – Abstract

Over the last two decades, many filters requiring custom spectral responses were obtained from photo-inscribed FBGs because of the flexibility inherent to this technology. However, Bragg gratings in silicon waveguides have the potential to provide faster and more efficient tuning capabilities when compared to optical fiber devices. One drawback is that Bragg gratings filters with elaborate spectral amplitude and phase responses often require a long interaction length, which is not compatible with current integration trends in CMOS compatible photonic circuits. In this chapter, we propose to make Bragg gratings in spiral-shaped waveguides in order to increase their lengths while making them more compact. The approach preserves the flexibility of regular straight grating structures. More specifically, we demonstrate 2-mm long gratings wrapped in an area of 200 µm x 190 µm without any spectral degradation due to waveguide curvature. Furthermore, we interleave three spiral waveguides with integrated gratings thereby tripling the density and demonstrate good phase compensation for each of them. Finally, we show that this approach is compatible with phase-apodization of the grating coupling coefficient.

5.2 – Introduction

Optical filters with flexible and precisely tuned spectral responses are of great interest for many applications in communication and sensing. In the last two decades, FBG technology has been widely used to provide such custom optical filters. However, in recent years, the fabrication of Bragg gratings in silicon waveguides has become very appealing because CMOS technology provides a low-cost small-footprint platform on which several functions and devices can be integrated. Short and simple grating structures with strong coupling coefficients have already been demonstrated in SOI waveguides with good quality spectral responses and integration of such short uniform gratings on a four ports structure has allowed operating the gratings in reflection [32], [54]. Furthermore, demonstrations of tunable gratings using the thermo-optic and the electro-optic effects suggests potential use of these devices for modulation and switching [45], [57]. However, when elaborate spectral responses are needed long gratings must be used. Unfortunately, straight IBGs have an aspect ratio that can make them difficult to integrate efficiently in photonic integrated circuits. Furthermore, long straight gratings will be more affected by non-uniformities of fabrication processes including wafer thickness variations [105], [117]. There is therefore a strong interest to make compact grating structures having more convenient form factor that will provide increased flexibility in the design of photonic integrated circuits on SOI.

Huge research efforts have recently been deployed to minimize losses in curved photonic wires resulting in loss values lower than 0.01 dB/90° for singlemode waveguides with a radius of curvature of 5 µm [118]. Numerical simulations have also shown that hybrid multimode/single-mode waveguides should also exhibit such small bending losses [98], [119]. Those advances allow the work presented in this chapter, which focuses on the implementation of IBGs in spiral waveguides in order to increase grating length while improving its aspect ratio. When designing such spiral IBGs, the local radius of curvature is relatively large ($R > 20$ µm in this chapter) compared to the radius of curvature considered in [118], [119]. With such large radius of curvature, bending losses are not a concern compared to the induced effective index variation. As a result, the analysis of curved waveguides presented in this chapter focuses on preventing unwanted variations of the grating phase that would result in spectral distortion.

Several studies have addressed the modeling of bent waveguides. It has been shown that conformal transformations convert circularly curved step index waveguides with a constant radius of curvature and a 1D confinement to simple straight waveguides with modified refractive index profiles [120], [121]. Furthermore, the equivalent straight waveguide (ESW) approximation has extended this approach to waveguides having a 2D confinement [122]–[124]. Later on, it was shown that this approximation is also appropriate for photonic wires with $R > \sim 2$

μm [125]. In this work, we use this approach to model spiral IBGs by defining an equivalent straight grating that includes an effective index perturbation caused by the waveguide curvature. Then, the spectral response of spiral IBGs can be calculated using a 1-D simulator based on coupled mode equations.

The chapter is organized as follows. Firstly, we present the procedure to correct the effective index perturbation caused by the curvature when an IBG is implemented in a spiral waveguide on SOI. Afterwards, we show experimental results that compare compensated and uncompensated grating structures. The results confirm that the correction was successful and that spiral IBGs can be fabricated without spectral degradation. We further demonstrate a spiral configuration with interleaved waveguides that results in a highly compact IBG structure. Lastly, we address the apodization of spiral IBGs. When the Bragg grating length is increased, its coupling coefficient is usually reduced and this makes grating apodization more challenging because the modulation of the corrugation amplitude becomes limited by the precision of the fabrication process. However this difficulty can be overcome by using phase apodization as demonstrated in [102]. We show that spiral IBG structures are compatible with phase apodization.

5.3 – Waveguide and grating design

To improve IBGs compactness, a zigzag layout has been proposed in which the grating waveguide is bent in a succession of curved sections with uniform radius of curvature thus forming a series of s-shape waveguides [84]. Unfortunately, this approach adds a fair amount of propagation loss due to mode mismatch at the connection point between two curved sections where the center of rotation is moved. Furthermore, at those positions, there is a rapid modification of the effective index, which distorts the grating spectral response. These effects, that increase drastically when the radius of curvature is decreased or when the grating length is increased, strongly jeopardize the merit of this approach in terms of integration capability. Spiral waveguides, as shown in Fig. 53, do not induce significant losses since the radius of curvature is on average much larger, except near its center, and there is no discontinuity in the waveguide curvature, which alleviates coupling losses between waveguide sections. As a result, the spiral geometry makes it possible to design long waveguides with large radius of curvature while still improving significantly the compactness of the device. As for the effective index perturbation caused by the variation of the radius of curvature, we present in the remaining of this section an efficient technique to compensate this effect.

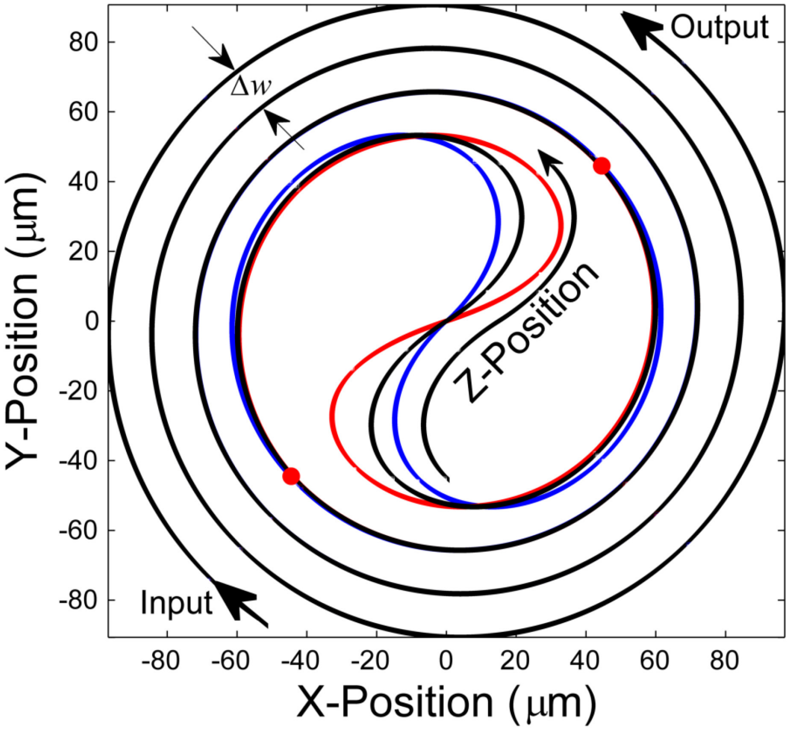

Fig. 53: Three different schematic of spiral gratings having α values of 0.3355, 0.671 and 1.0065 (red, black and blue curve respectively). The red dots represents the position where Δx_s becomes negligible.

As shown in [41], the spectrum of a long IBG is strongly distorted by the effect of SWR. This effect is enhanced by the high index contrast of SOI waveguides. A means to reduce this phase noise in the design process is to implement the IBG in the multimode section of a hybrid multimode/singlemode waveguide or in a rib waveguide. The first waveguide type was considered in this chapter. The detail of those 1200 nm wide spiral gratings are described in Table 3. The computer-aided design (CAD) mask is shown in Fig. 54-a) and an optical microscope image of the first row of the chip is shown in Fig. 54-b). This chip of 600 μm x 1400 μm has been covered by a silica cladding and contains 17 samples of 2-mm long gratings in spiral waveguides surrounded by 2 mm-long waveguides on each side of the IBGs. Since multimode waveguides are more sensitive to curvature losses, the radius of curvature should be larger than about 10 microns. Fortunately, as discussed previously, it is possible to design spiral gratings with small length-footprint ratio without using small radius of curvature.

In order to bend a straight grating into a spiral-shaped grating, three steps need to be taken: 1) a spiral waveguide of the required length is defined, 2) the grating is designed for the equivalent straight waveguides, which means that the grating incorporates the phase compensation term, and 3) the grating is geometrically mapped on the spiral. As mentioned earlier, this procedure uses the ESW approximation to transform the curved waveguide into an equivalent straight waveguide with a modified index profile. We detail below these three steps.

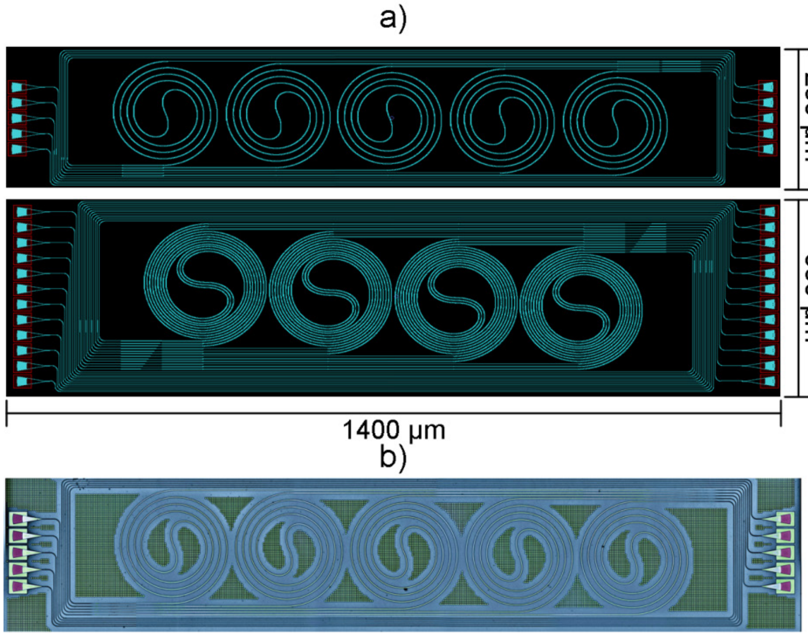

Fig. 54: a) CAD mask of the spiral IBGs used in this chapter (*α* value of 0.671); b) Optical microscope image of the first spiral-IBG row.

5.3.1 – Spiral waveguide definition

The *x* and *y* coordinates of the spiral are given by the real and imaginary parts of *S* defined by

$$S = R(\rho)e^{i|\rho|} - \Delta x_S\,, \tag{5.1}$$

where

$$R(\rho) = R_0\,\mathrm{sgn}(\rho) + \Delta w_s \rho/\pi\,, \tag{5.2}$$

$$\Delta x_s = R_0\,\mathrm{sgn}(\rho)e^{-|\rho|/\alpha}\,, \tag{5.3}$$

“sgn” is the sign function, Δw_s is the spacing between two consecutive waveguide in the spiral (as shown in Fig. 53) and ρ is the angle of rotation that increases along the spiral waveguide ($\rho = 0$ at the center). The term $R(\rho)e^{i|\rho|}$ is the spiral itself with a radius of curvature that is changing linearly with the angle of rotation. Without the Δx_s term in Eq. (5.1), the profile of the radius of curvature would be given by the black dotted line in Fig. 55 having a minimum value equal to R_0 at $\rho = 0$. A simple spiral could be designed by using an s-shaped waveguide having a radius of curvature of $R_0/2$ to connect a spiral waveguide defined by $R(\rho)e^{i\rho}$, with $\rho > 0$, to another one defined by $R(\rho)e^{i\rho}e^{i\pi}$ [83]. However, this leads to a discontinuity in the radius of curvature (jumping from R_0 to $R_0/2$). The addition of the term Δx_s in Eq. (5.1) avoids this discontinuity by smoothly shifting the center of rotation between the two spirals. Fig. 55 shows the numerically calculated profile of the radius of curvature, $R(z)$, as a function of the position on the spiral path from the input to the output of the waveguide (refer to by “z-position”[XIII]). When Δx_s becomes negligible, outside the red dots in Fig. 53 (located in this case at $\rho = \pm 5\pi/4$), the waveguide behaves as a simple spiral with a radius of curvature that increases linearly with ρ.

The profiles of the radius of curvature for three typical spirals are shown by the red, black and blue lines in Fig. 55 and the spiral themselves are presented in Fig. 53. $R_0 = 46.85$ µm and $\Delta w_s = 12.5$ µm for each spirals, while the α parameter, which controls the rate of change of the center of rotation as function of ρ, is respectively 0.3355, 0.671 and 1.0065. On one hand, when α is reduced, the minimum value of the radius of curvature of the spiral becomes smaller and, on the other hand, when α is increased, the radius of curvature increases significantly in the central portion of the spiral (around the location $[\mp 40, \pm 40]$ in Fig. 53 and at the z-position around ± 0.2 mm in Fig. 55) which decreases the waveguide spacing in this area. Consequently, α must be chosen carefully.

[XIII] In the previous chapters, the z-axis was referring to “axis of propagation” (as defined in the list of symbols) and the x-axis and y-axis were referring to the waveguide cross-section. Strictly speaking, the z-position definition still applies since it also refers to the axis of propagation. However, the x-position and y-position are not equivalent to the x-axis and y-axis defined in the previous chapters. The x-position and y-position are the real and imaginary axis of the complex plane where S is defined. As a result, the waveguide cross section coordinates are given by the local unitary tangential vector of S and the y-axis discussed in previous chapters.

Once the waveguide is defined, the local unitary normal vector, $\vec{N}$ is found numerically, which allows the calculation of the exact position of the waveguide sidewalls, i.e. $S \pm w_0\vec{N}/2$, and eventually allows the calculation of the position of the corrugation amplitudes.

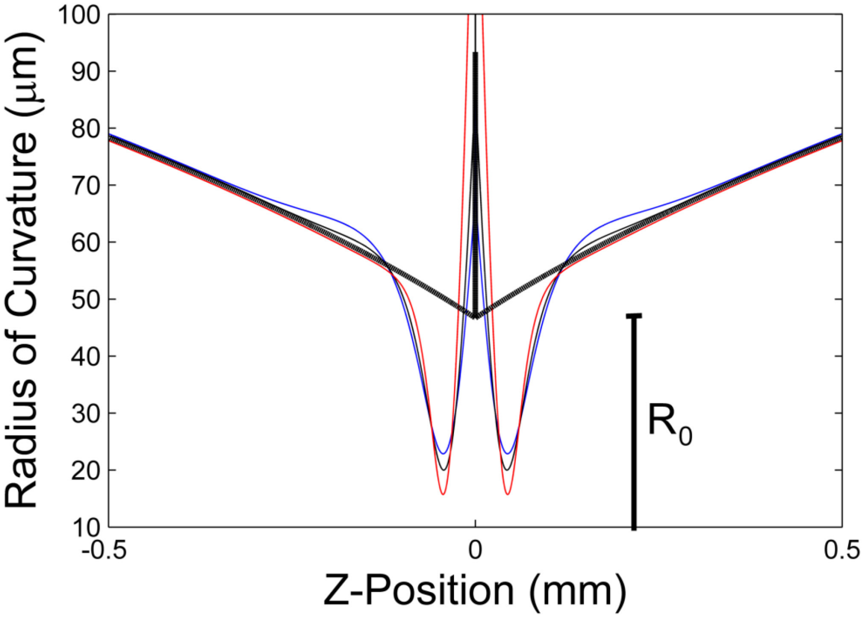

Fig. 55: a) Radius of curvature of the spirals shown in Fig. 53.

5.3.2 – Grating design

IBGs index profiles are given by

$$n(z) = n(\lambda) + \delta n\big(R(z)\big) + \Delta n \cos\left(\frac{2\pi}{\Lambda}z + \theta(z) + \Omega(z)\right), \qquad (5.4)$$

where $\delta n(R(z))$ is the effective index perturbation caused by the curvature, as shown in Fig. 56 for a waveguide of 1200 nm x 220 nm. The dependency of the waveguide effective index as a function of curvature was obtained using a finite elements mode solver simulator combined with the ESW approximation. The calculations take into account the specific profile of the radius of curvature calculated as a function of the *z*-position for the given spiral. The phase term $\Omega(z)$ in Eq. (5.4) is added to compensate for the effective index distortion $\delta n(R(z))$ caused by the spiral and is given by

$$\Omega(z) = \frac{2\pi}{n_0 \Lambda} \int_0^z dz' \delta n\left(R(z')\right). \qquad (5.5)$$

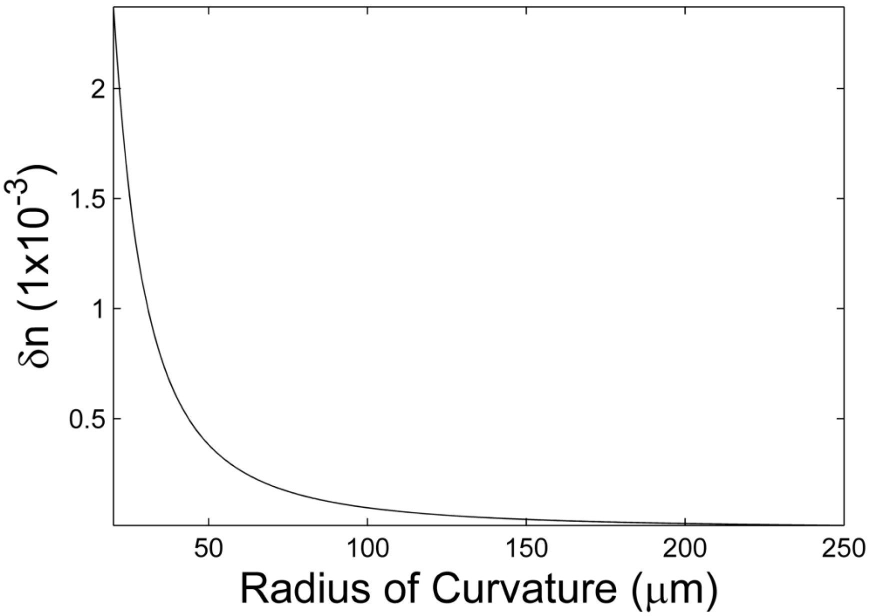

Fig. 56: Variation of the effective index of a 1200 nm x 220 nm silicon waveguide with top-oxyde as function of its radius of curvature.

The unbent position of each rectangular corrugation added on the side of the waveguide is obtained directly from the maximal values of every cycle of the cosine term in Eq. (5.4). The edge of the corrugation is then simply determined from the duty cycle.

The associated phase correction for the three spirals discussed previously is shown in Fig. 57. As can be seen on this figure, when the radius of curvature is large (on the sides), the phase function increases slowly since the effective index perturbation is very small. However, when the radius of curvature becomes smaller, the phase correction varies rapidly and the grating period must be decreased locally in order to compensate for the higher index of refraction. To illustrate the impact of the phase correction term, the grating local period, given by

$$\Lambda\left(z\right) = \frac{\Lambda}{\left[1 + \frac{\Lambda}{2\pi}\frac{\partial\theta(z)}{\partial z} + \frac{\Lambda}{2\pi}\frac{\partial\Omega(z)}{\partial z}\right]}, \qquad (5.6)$$

is displayed in Fig. 58. Despite the fact that the period correction is small, it has a significant impact on the phase function and on the grating spectra because of the integral in Eq. (5.5).

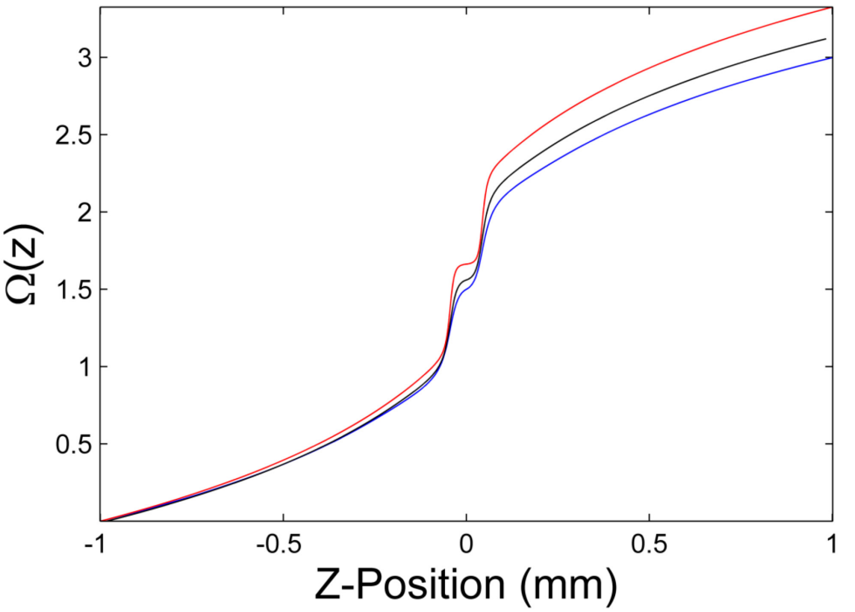

Fig. 57: Phase function that must be incorporated in the grating structure to compensate the effective index variation caused by the curvature of the spirals shown in Fig. 53.

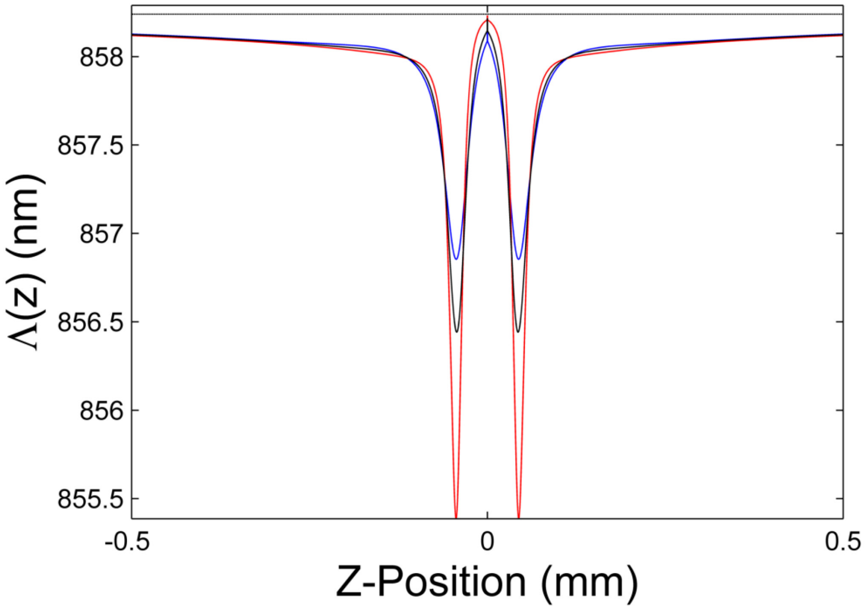

Fig. 58: The grating period of the spiral shown in Fig. 53. The black line is the uncorrected grating period.

5.3.3 – Mapping of the grating on the spiral

The last step of the mask design consists of mapping the grating corrugation profile of the straight waveguide onto the path of the spiral shape. The normal coordinate is calculated using $\vec{N}$ and the designed corrugation width. It should be noted that the coupling coefficient asymmetry associated with the gratings on the inner and outer side of a curved waveguide is negligibly small for the radius of curvature considered in this chapter (> 20 μm) and therefore, the corrugation amplitude has not been compensated [83].

5.4 – Grating characterization

As for the previous chapters, the complex spectral responses of every gratings was measured with a commercial optical frequency domain reflectometer to which we removed the coupling losses. The data processing that has been done to retrieve the $\lambda_B(z)$ and $\Delta n(z)$ profiles is described in section 1.6. The experimental measurements are shown in red in the following figures presenting experimental results (Fig. 59-a), Fig. 60-a), Fig. 62-a) and Fig. 63-a)). Once again, the grating reflectivity was designed to be small to ease the convergence of the grating reconstruction algorithm. However, it should be mentioned that spiral-IBGs are not limited to weak gratings. The corrugation recess amplitude can be increased as easily as for straight IBGs. The retrieved grating coupling amplitude and phase profiles, after appropriate filtering, are used to calculate the reconstructed spectral responses using a standard transfer matrix solution of the coupled mode equations (black curves in Fig. 59-a), Fig. 60-a), Fig. 62-a) and Fig. 63-a)). The good correspondence between the reconstructed spectra and the measured ones indicate that the λ_B and Δn profiles were retrieved with sufficient precision. More details on the post-processing procedure can be found in [35]. The designed grating spectral responses are shown in blue in Fig. 59-a), Fig. 60-a), Fig. 62-a) and Fig. 63-a). The grating spectra displayed in this chapter are typical results. Over thirty gratings have been characterized with similar responses.

5.5 – Experimental results and discussion

5.5.1 – Phase correction effect

We designed two uniform IBGs on a spiral having the following parameters: R_0 = 46.85 µm, Δw_s = 12.5 µm and α = 0.671 which results in spirals having a minimal radius of curvature of 20 µm, a length of 2 mm and an area of 200 µm x 190 µm. The spirals have the same parameters as those shown in Fig. 53 with α = 0.671.

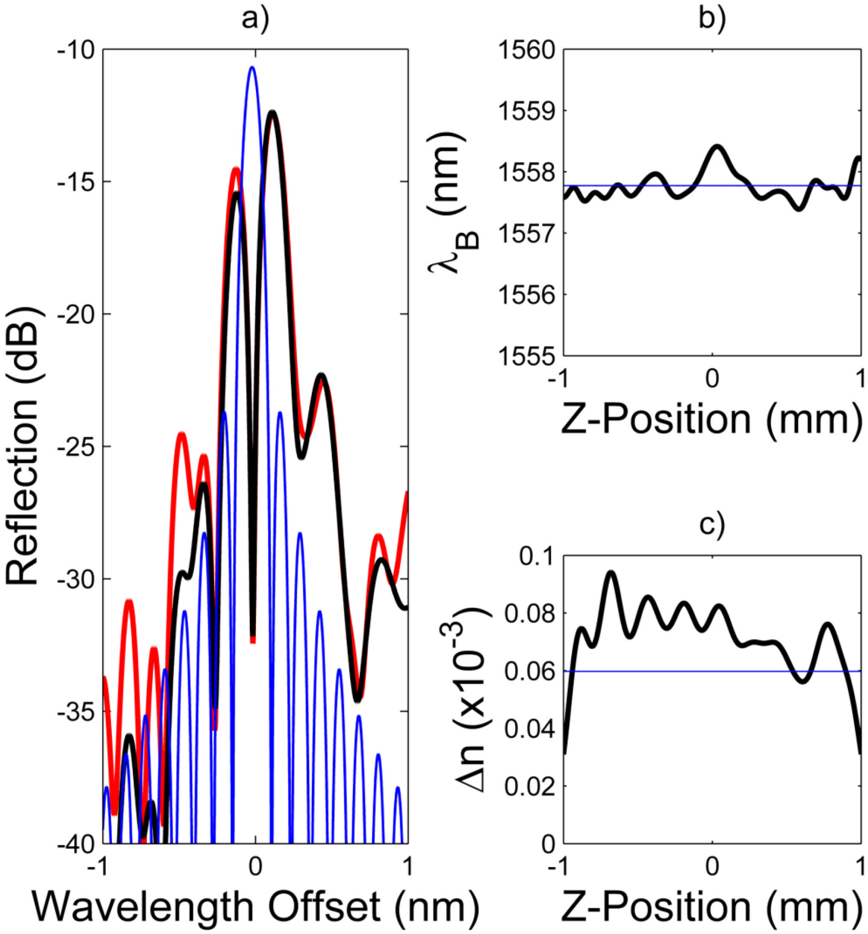

Fig. 59: a) Comparison of the experimental reflection spectrum of an uncompensated spiral IBG (in red) with the reconstructed reflection spectrum (in black) and the designed uniform grating response (blue curve). Retrieved b) λ_B and c) Δn profiles, which are used to calculate the black curve of a).

The first grating, presented in Fig. 59, was made without phase correction while the second grating, presented in Fig. 60, was designed with the phase correction. The spectral response of both measured and reconstructed gratings are shown in Fig. 59-a) and Fig. 60-a) while their retrieved physical profiles are shown in Fig. 59-b) and Fig. 59-c) and Fig. 60-b) and Fig. 60-c). As expected, the Bragg wavelength profile of the uncorrected grating shows a strong Bragg wavelength perturbation near its center. The spiral curvature acts as a distributed phase shift which results in a resonance in the grating bandgap as shown in Fig. 59-a). In this case, the distributed phase shift seems to be reasonably close to π since the resonance in the grating band is centered in the grating band, which might be of interest for some applications such as notch filters. Simulations of discrete phase-shifted gratings actually show that this asymmetry between the two main lobes can be obtained with a centered phase-shift of ~1.15π. However, for most

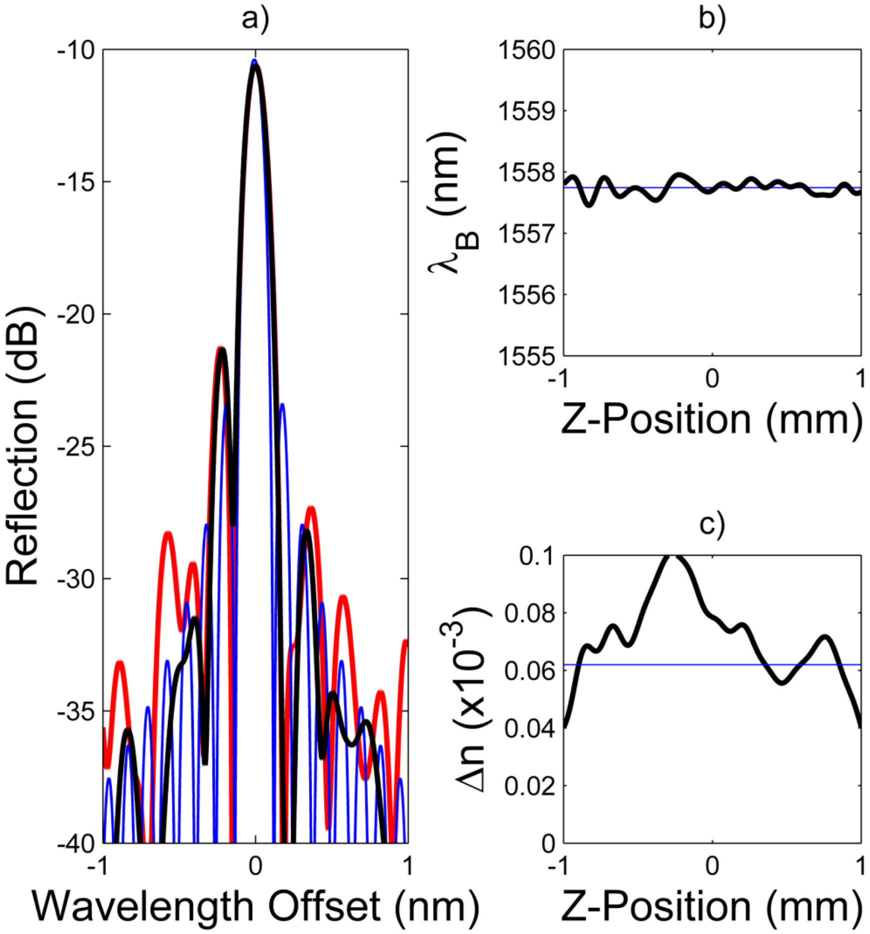

Fig. 60: a) Comparison of the experimental reflection spectrum of a phase compensated spiral IBG (in red) with the reconstructed reflection spectrum (in black) and the designed uniform grating response (blue curve). Retrieved b) λ_B and c) Δn profiles, which are used to calculate the black curve of a).

applications, the grating effective index should be corrected in order to prevent spectral distortions. Fig. 59-b) shows that the Bragg wavelength perturbation is cancelled out in the corrected grating displayed in Fig. 60-b) showing that the phase compensation approach is working properly. The grating SLSR shown in Fig. 60 (~10 dB) is slightly better than what has already been published for identical 2 mm-long straight grating [102]. Because the spiral grating is localized on a smaller area of the wafer, the phase noise created by silicon thickness variations is less likely to have an impact on the grating spectral response compared to gratings in straight waveguides.

Finally, it might seem odd that the phase shift in the Bragg wavelength profile of Fig. 59-b) does not experience a minimum at its center since the spiral is straight at this particular section of the grating and hence it should not experience phase distortion. However, Bragg gratings are not affected by the high frequency spatial components of the phase and index modulation profiles [35], [41]. Furthermore, only the low frequency components can be measured. As a result, the Bragg grating reconstruction acts as a low-pass filter which suppresses the localized minimum inside the spiral-induced distortion.

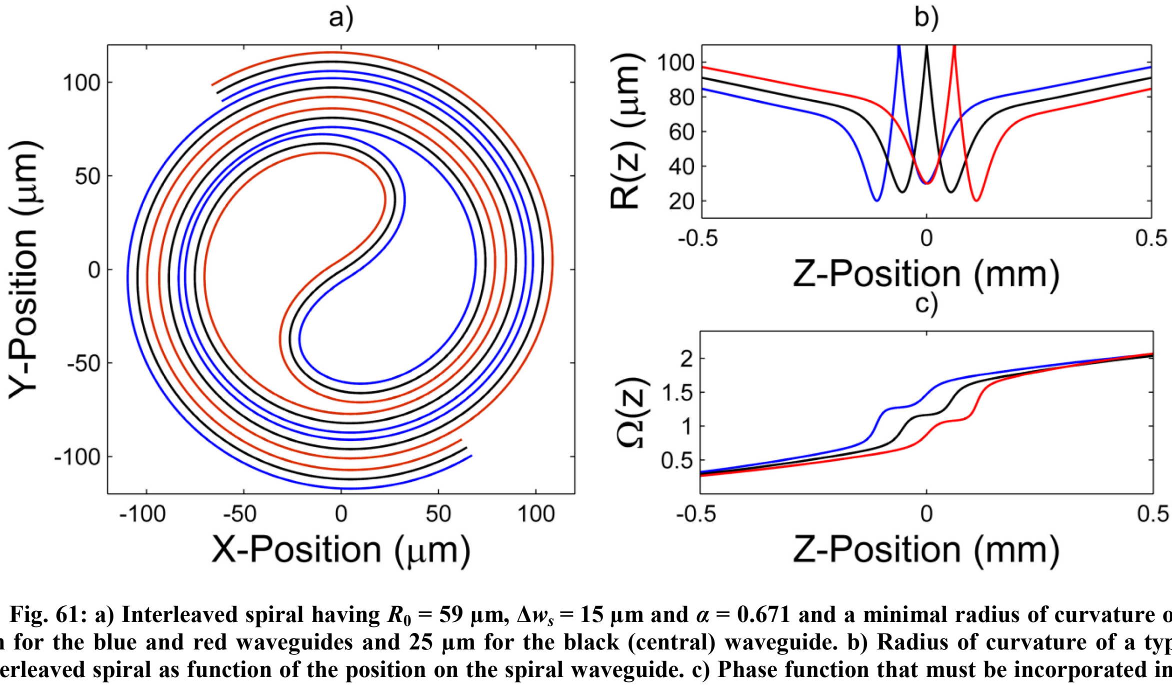

Fig. 61: a) Interleaved spiral having R_0 = 59 µm, Δw_s = 15 µm and α = 0.671 and a minimal radius of curvature of 20 µm for the blue and red waveguides and 25 µm for the black (central) waveguide. b) Radius of curvature of a typical interleaved spiral as function of the position on the spiral waveguide. c) Phase function that must be incorporated in the grating structure to compensate the effective index variation caused by the curvature

5.5.2 – Highly integrated gratings

In order to improve the grating integration factor, we designed a spiral structure consisting of three interleaved gratings. The addition of two other spirals (in red and blue in Fig. 61-a)) beside the central spiral (in black) is straightforward since the spiral function (*S*) and $\vec{N}$ are already known. As a result, the center of the side-spirals waveguides are defined by $S_{\pm} = S \pm (\Delta w/3)\vec{N}$. Aside from this detail, the design of those side-spiral gratings is exactly the same as discussed above. In this work, we chose spirals with R_0 = 59 µm, Δw_s = 15 µm, $\alpha = 0.671$ and $N = 1.345$ which gives three spirals spaced by 5 µm, having a minimal radius of curvature of 20 µm for the side-spirals and 25 µm for the central spiral, a path length of 2 mm (each spiral has the same total length) and a total area of 230 µm x 215 µm. It can be noticed that the total footprint of these

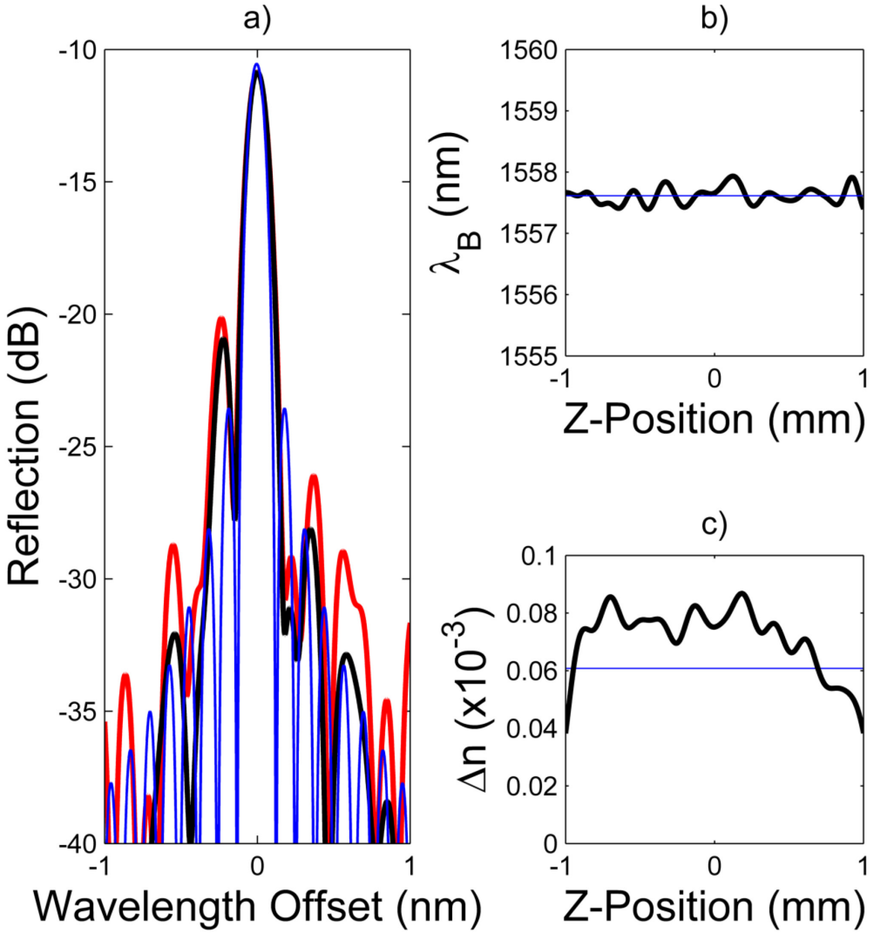

Fig. 62: a) Comparison of the experimental reflection spectrum of a compensated interleaved spiral IBG (in red) with the reconstructed reflection spectrum (in black) and the designed uniform grating response (blue curve). Retrieved b) λ_B and c) Δn profiles, which are used to calculate the black curve of a).

three IBGs is almost the same as the single spiral grating described in the previous section, thereby tripling the integration efficiency. The radius of curvature of the three gratings and their associated phase correction terms are shown in Fig. 61-b) and Fig. 61-c) respectively. As can be seen in Fig. 61-b), the central spiral has a symmetric radius of curvature profile. However, even if the side spirals experienced asymmetric profiles, their physical structure can be as easily compensated. Fig. 62 shows that the interleaved spiral does not affect significantly the grating spectrum as well as the fact that each waveguides are much closer than in the previous section. As it was the case for single-spiral, the correction phase term compensates well the effective index perturbation caused by the curvature; at least, the phase error has amplitude in the center portion of the grating that is smaller than the random phase noise observed near its input and output ends.

5.5.3 – Apodized gratings

Finally, since a full control of the complex spectral responses of IBGs requires reliable apodization techniques, the results presented in this last section confirms that spiral waveguides are compatible with the phase-apodization technique presented in [102]. Briefly, this technique adds a slow phase modulation in the grating structure with a z-dependent amplitude ($\phi(z)$). Consequently, the last term of Eq. (5.4) representing the grating can be written in the form

$$\Delta n \cos\left(\frac{2\pi}{\Lambda} z + \theta(z) + \Omega(z) + \phi(z)\sin\left(\frac{2\pi}{\Lambda_M} z\right)\right). \tag{5.7}$$

Phase modulation at a spatial frequency $1/\Lambda_m$ results in amplitude apodized grating with a spectral response having satellite resonances out of the band of interest when Λ_m is sufficiently small (in the present case $\Lambda_m = 17.5$ µm). Fig. 63-c) shows that the effective index modulation of the grating now follows the designed Gaussian profile with a 1 mm full-width at half maximum indicating that the correction applied to the grating does not affect the apodization profile.

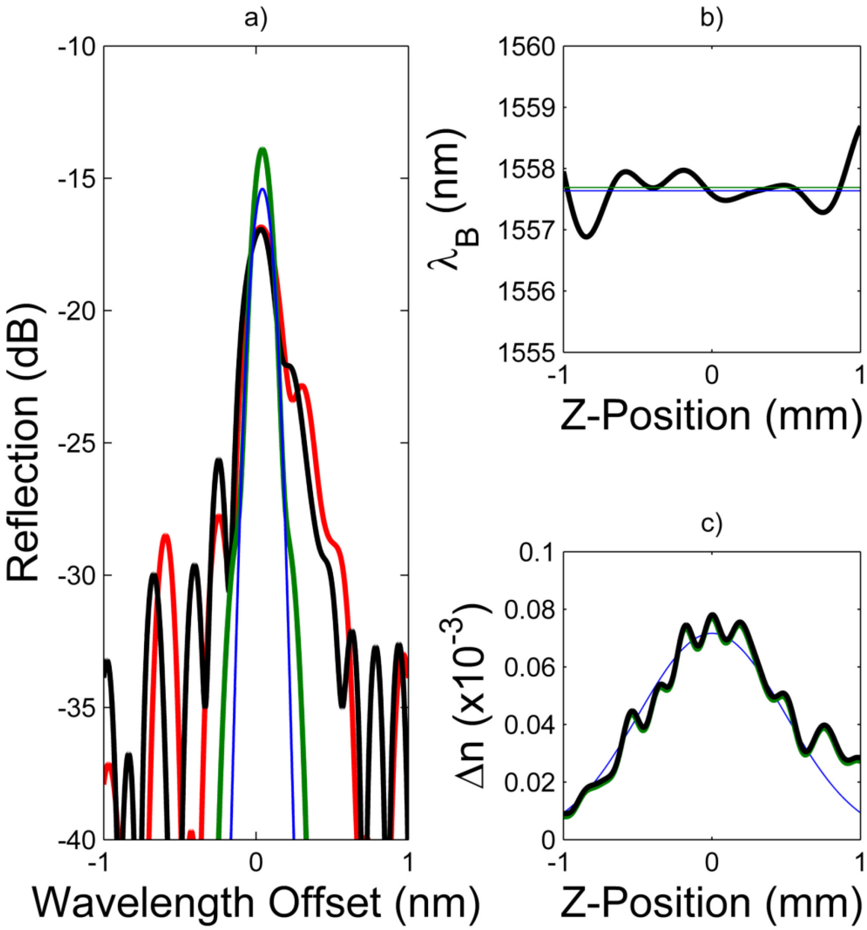

Fig. 63: a) Comparison of the experimental reflection spectrum of a compensated Gaussian-apodized CBG (in red) with the reconstructed reflection spectrum (in black). The blue curve is the spectrum obtained with the ideal Gaussian apodization profile shown in c) and an ideal Bragg wavelength while the green curve is the spectrum calculated with the noisy apodization profile but without phase noise (ideal Bragg wavelength). Retrieved b) λ_B and c) Δn profiles, which are used to calculate the black curve of a).

Unfortunately, IBGs in SOI usually experience a fair amount of phase noise, which prevents the apodization to properly reduce the side-lobe amplitude[XIV]. To confirm this point, the green curve of Fig. 63-a) presents the spectral response obtained using the grating apodization profile shown in Fig. 63-c), but with an ideal Bragg wavelength profile (no phase noise). As a result, the SLSR is decreased by more than 20 dB, which corresponds closely to the design (in blue). Consequently,

---

[XIV] As mentioned in chapter 3, spiral gratings should be more robust to phase noise. However, a comparison of Fig. 50 and Fig. 63 (i.e. straight and spiral apodized IBGs) does not show that apodized gratings have better performances in spiral waveguides. However, it should be mentioned that the grating shown in Fig. 63 is not the best one, but it is the only one that could be reconstructed with the algorithm presented in [73]. The weak reflectivity of the grating has created instabilities in the reconstruction and most IBGs in this category could not be reconstructed.

the variation of the apodization profile compared to the ideal design is not a major source of spectral distortion and we thus conclude that spiral IBGs are compatible with phase-apodization.

5.6 – Conclusion

We presented a simple procedure to design IBGs in a spiral configuration to improve their integration. We showed that IBGs in spiral waveguide can be fabricated without additional phase-noise or spectral distortions due to waveguide curvature. We further proposed an interleaved spiral configuration that allows fabrication of many gratings on the same chip section, thereby improving the integration factor. Finally, we have confirmed that this work is compatible with the phase-apodization technique needed for the fabrication of grating-based devices with elaborate spectral responses. Future work should consider the optimization of the waveguide spacing, Δw, in order to improve the compactness of the spiral-gratings. This work shows that as the quality of SOI wafers improves, long IBGs with high quality spectral characteristics will be achievable. This design approach can be used for various grating types and strengths thereby giving increased flexibility for the layout of photonic circuits.

Conclusion

In this work, several issues susceptible to prevent the conception and the fabrication of elaborate IBGs in SOI have been explored. In chapter 1.7 the parasitic reflections, which prevented the accurate characterization of IBGs spectral responses in reflection, have been successfully removed. Time filtering was introduced as a necessary step to use the reconstruction algorithms developed for FBGs. The ability to retrieve the grating coupling amplitude and phase was a key element for the remaining works of this thesis.

In chapter 2 and 3, the high level of phase noise in silicon IBGs has been thoroughly analysed for the first time. In chapter 2, the importance of SWR on IBGs spectral response has been modeled. Both the roughness amplitude and correlation length have been shown to be critical to IBGs performance. A technique to emulate IBG spectral responses in the presence of an imperfect waveguide has been proposed in order to evaluate the fabrication yield for IBGs fabricated in SOI photonic wires. Finally, an analytical study of SWR for weak gratings and small roughness variances was presented. A general analytical expression of the averaged spectrum in presence of the phase noise caused by SWR has been obtained, which could be used to analyze more complex weak gratings. Using weak uniform gratings as an example, an analytical expression for the standard deviation of the spectral response that gives information on the spread of the grating reflection spectra around the average was found. This analysis shows why the noise has a relatively small impact on the reflection strength at the Bragg wavelength while larger distortions appear on each side of the main reflection peak. The analytical expressions also help to evaluate how the spectral distortion depends on other grating parameters. Specifically, it was shown that it increases as the square of the integrated coupling coefficient, κL, but linearly with the standard deviation of the sidewall roughness, σ_{SWR}, and the effective index variation associate to a waveguide width variation, C_{SWR}, and as a square root function with the grating length, L, and the sidewall roughness autocorrelation length, $L_{c,SWR}$.

The results obtained in chapter 2 strongly suggest using hybrid multimode/singlemode waveguide to reduce the impact of SWR. However, in this situation, the WHF is becoming an important source of phase noise and, unfortunately, in the literature both SWR and WHF were not properly characterized processes in the context of IBGs. As a result, in chapter 3, a model that links the SWR and the WHF random processes to Bragg wavelength fluctuations observed in IBGs have been presented. A technique to characterize the low spatial frequency content of SWR which is critical to predict the quality of IBGs spectral response was proposed. It was also shown how to extract the parameters characterizing WHF from IBGs optical measurements. Finally, two techniques to improve IBG robustness to phase noise at the design step were proposed and experimentally characterized. First, the aforementioned hybrid multimode/singlemode waveguide was shown to reduce by more than one order of magnitude the effect of SWR on IBGs. Second, the fabrication of ultra-compact gratings in spiral waveguides mitigates the impact of the WHF.

As mentioned multiple times in this thesis, these results are of importance because longer grating structures with weaker coupling coefficients are required in order to achieve integrated optical filters with elaborate spectral responses, both in amplitude and phase. Since longer gratings are more affected by phase noise, such demonstrations have been so far very limited. We believe that these phase-noise reduction techniques open the door to many new grating-based optical filter designs.

Furthermore, in order to properly design an elaborate IBG spectral response, a perfect control over the grating coupling amplitude is required. In chapter 4, two apodization techniques for IBG fabricated in SOI were proposed. Both techniques present the advantage of having corrugation recesses with constant amplitude along the grating. This aspect improves the robustness to deep-UV lithography and fabrication errors. Furthermore, both techniques do no introduce distortions into the grating phase profile and they are compatible with gratings having small recesses.

Finally, the grating length required to design elaborate spectral response, which might go up to the cm-scale, is not compatible to most PIC device chip size. As a result, a simple procedure to design IBGs in a spiral configuration to improve their integration was presented. It was shown that IBGs in spiral waveguide can be fabricated without additional phase-noise or spectral distortions due to waveguide curvature. To further improve the integration factor, it was proposed to use an interleaved spiral configuration that allows the fabrication of many gratings on the same chip section. Finally, it has been confirmed that this work is compatible with the phase-apodization technique. This design approach can be used for various grating types and strengths thereby giving increased flexibility in the layout of photonic circuits.

To conclude, the work presented in this thesis addressed many issues in the fabrication of elaborate IBGs. But, "*can we translate the progress made in the last twenty years in FBG to the SOI platform?*". Unfortunately, this question cannot be answered positively for any design. Fibers are almost perfect waveguides and even with the reduction of the phase noise in SOI IBGs that has been achieved in this thesis, the phase noise property of FBGs are still orders of magnitude better. Since the phase noise robustness of IBGs was improved by about one order of magnitude, it means that IBGs length can be increased by about one or two order of magnitude, which ultimately can lead to the fabrication of more complex spectral response. As a result, the fabrication of grating structure having a millimeter scale length could be fabricate by using such phase noise reduction technique with the same quality than the usual hundreds of micron grating length. However, if the design requires longer gratings, the phase noise will likely be too important.

Further improvement could be realized by using immersed lithography techniques or extreme UV lithography. Such improved lithography technology is expected to be accessible soon to the photonic community since the fabrication technology of PIC is roughly 10 years behind the technology used by the electronics community. Furthermore, as it has been done for arrayed waveguide grating a few years ago [126], [127], where the path length error were thermally compensated, or for microring resonators, where the resonant wavelength can be either photo-adjust by exposing locally a photosensitive over-cladding material [128] or by thermal tuning, a possible approach to improve the spectral response quality of IBG could be to post-compensate the grating phase distortion. The first step in this direction is to be able to characterize gratings and this work has been done in this thesis. Assuming that the right technology can be found to do this post-correction, it could contribute to increase the fabricated grating length; i.e. hence the complexity of the spectral response. However, the next steps that should be done to properly test the technology is to fabricate IBGs with specific functionality and analyse the match between these elaborate gratings and their design.

Finally, in this thesis, since weak IBGs have been used to characterize the platform, the coupled mode theory described in chapter 1 was an appropriate model. However, when considering narrow photonic wires, the accuracy of this model is likely to be significantly reduced. As a result, future work should study the accuracy of modeling techniques. Furthermore, even if this theory is not supposed to be valid for high frequency spatial variation, it was shown in this thesis that, if the phase variation has small amplitude, the theory is still providing good results. However, since IBGs are typically short, it is likely that the spatial frequency of many grating structures will be relatively high by design (to obtain broadband reflector for example). Consequently, the precision of the theory should be analysed in these limits.

References

[1] R. Soref, “The past, present, and future of silicon photonics,” *IEEE J. Sel. Top. Quantum Electron.*, vol. 12, no. 6, pp. 1678–1687, 2006.

[2] I. P. Kaminow, L. Tingye, and A. E. Willner, *Optical fiber telecommunications V A: components and subsystems*. Elsevier Inc, 2008.

[3] G. T. Reed and C. E. J. Png, “Silicon optical modulators,” *Mater. Today*, vol. 8, no. 1, pp. 40–50, 2005.

[4] D. J. Thomson, F. Y. Gardes, J.-M. Fedeli, S. Zlatanovic, Y. Hu, B. P.-P. Kuo, E. Myslivets, N. Alic, S. Radic, G. Z. Mashanovich, and G. T. Reed, “50-Gb/s silicon optical modulator,” *IEEE Photon. Technol. Lett.*, vol. 24, no. 4, pp. 234–236, 2012.

[5] T. Baehr-Jones, R. Ding, Y. Liu, A. Ayazi, T. Pinguet, N. C. Harris, M. Streshinsky, P. Lee, Y. Zhang, A. E.-J. Lim, T.-Y. Liow, S. H.-G. Teo, G.-Q. Lo, and M. Hochberg, “Ultralow drive voltage silicon traveling-wave modulator,” *Opt. Express*, vol. 20, no. 11, pp. 12014–12020, mai 2012.

[6] J. Ding, H. Chen, L. Yang, L. Zhang, R. Ji, Y. Tian, W. Zhu, Y. Lu, P. Zhou, R. Min, and M. Yu, “Ultra-low-power carrier-depletion Mach-Zehnder silicon optical modulator,” *Opt. Express*, vol. 20, no. 7, pp. 7081–7087, Mar. 2012.

[7] P. Dong, C. Xie, L. Chen, L. L. Buhl, and Y.-K. Chen, “112-Gb/s monolithic PDM-QPSK modulator in silicon,” *Opt. Express*, vol. 20, no. 26, pp. B624–B629, Dec. 2012.

[8] A. Biberman, E. Timurdogan, W. A. Zortman, D. C. Trotter, and M. R. Watts, “Adiabatic microring modulators,” *Opt. Express*, vol. 20, no. 28, pp. 29223–29236, Dec. 2012.

[9] Y. Hu, X. Xiao, H. Xu, X. Li, K. Xiong, Z. Li, T. Chu, Y. Yu, and J. Yu, “High-speed silicon modulator based on cascaded microring resonators,” *Opt. Express*, vol. 20, no. 14, pp. 15079–15085, Jul. 2012.

[10] X. Xiao, X. Li, H. Xu, Y. Hu, K. Xiong, Z. Li, T. Chu, J. Yu, and Y. Yu, “44-Gb/s silicon microring modulators based on zigzag PN junctions,” *IEEE Photon. Technol. Lett.*, vol. 24, no. 19, pp. 1712–1714, 2012.

[11] J. C. Rosenberg, W. M. J. Green, S. Assefa, D. M. Gill, T. Barwicz, M. Yang, S. M. Shank, and Y. A. Vlasov, “A 25 Gbps silicon microring modulator based on an interleaved junction,” *Opt. Express*, vol. 20, no. 24, pp. 26411–26423, Nov. 2012.

[12] G. Li, X. Zheng, H. Thacker, J. Yao, Y. Luo, I. Shubin, K. Raj, J. E. Cunningham, and A. V. Krishnamoorthy, “40 Gb/s thermally tunable CMOS ring modulator,” in *2012 IEEE 9th International Conference on Group IV Photonics (GFP)*, 2012, pp. 1–3.

[13] W. Bogaerts, L. Liu, and G. Roelkens, “Technologies and building blocks for on-chip optical interconnects,” in *Integrated Optical Interconnect Architectures for Embedded Systems*, I. O’Connor and G. Nicolescu, Eds. Springer New York, 2013, pp. 27–78.

[14] A. W. Fang, B. R. Koch, R. Jones, E. Lively, D. Liang, Y. Kuo, and J. E. Bowers, “A distributed Bragg reflector silicon evanescent laser,” *IEEE Photon. Technol. Lett.*, vol. 20, no. 20, pp. 1667–1669, 2008.

[15] A. W. Fang, H. Park, O. Cohen, R. Jones, M. J. Paniccia, and J. E. Bowers, “Electrically pumped hybrid AlGaInAs-silicon evanescent laser,” *Opt. Express*, vol. 14, no. 20, pp. 9203–9210, Oct. 2006.

[16] G. Roelkens, D. Van Thourhout, R. Baets, R. Nötzel, and M. Smit, “Laser emission and photodetection in an InP/InGaAsP layer integrated on and coupled to a silicon-on-Insulator waveguide circuit,” *Opt. Express*, vol. 14, no. 18, pp. 8154–8159, Sep. 2006.

[17] R. E. Camacho-Aguilera, Y. Cai, N. Patel, J. T. Bessette, M. Romagnoli, L. C. Kimerling, and J. Michel, “An electrically pumped germanium laser,” *Opt. Express*, vol. 20, no. 10, pp. 11316–11320, May 2012.

[18] T.-Y. Liow, J. Song, X. Tu, A. E.-J. Lim, Q. Fang, N. Duan, M. Yu, and G.-Q. Lo, “Silicon optical interconnect device technologies for 40 Gb/s and beyond,” *IEEE J. Sel. Top. Quantum. Electron*, vol. 19, no. 2, pp. 8200312–8200312, 2013.

[19] B. Jalali, “Can silicon change photonics?,” *physica status solidi (a)*, vol. 205, no. 2, pp. 213–224, 2008.

[20] J. W. Goodman, F. J. Leonberger, S.-Y. Kung, and R. A. Athale, “Optical interconnections for VLSI systems,” *Proceedings of the IEEE*, vol. 72, no. 7, pp. 850 – 866, Jul. 1984.

[21] C. F. Lam, H. Liu, B. Koley, X. Zhao, V. Kamalov, and V. Gill, “Fiber optic communication technologies: What’s needed for datacenter network operations,” *IEEE Communications Magazine*, vol. 48, no. 7, pp. 32–39, 2010.

[22] J. Chan, G. Hendry, K. Bergman, and L. P. Carloni, “Physical-layer modeling and system-level design of chip-scale photonic interconnection networks,” *IEEE Transactions on Computer-Aided Design of Integrated Circuits and Systems*, vol. 30, no. 10, pp. 1507 –1520, Oct. 2011.

[23] “International technology roadmap for semiconductors - Interconnect,” 2011.

[24] M. Abtahi, M. Dastmalchi, S. LaRochelle, and L. A. Rusch, “Generation of arbitrary UWB waveforms by spectral pulse shaping and thermally-controlled apodized FBGs,” *J. Lightwave Technol.*, vol. 27, no. 23, pp. 5276–5283, 2009.

[25] J. Azana, “Ultrafast analog all-optical signal processors based on fiber-grating devices,” *IEEE Photonics Journal*, vol. 2, no. 3, pp. 359–386, 2010.

[26] Y. Painchaud, M. Lapointe, F. Trepanier, R. L. Lachance, C. Paquet, and M. Guy, “Recent progress on FBG-based tunable dispersion compensators for 40 Gb/s applications,” in *Optical Fiber Communication Conference. Optical Society of America*, 2007, pp. 1–3.

[27] S. Doucet, S. LaRochelle, and M. Morin, “Reconfigurable dispersion equalizer based on phase-apodized fiber Bragg gratings,” *J. Lightwave Technol.*, vol. 26, no. 16, pp. 2899–2908, 2008.

[28] B. F. Ventrudo, G. A. Rogers, G. S. Lick, D. Hargreaves, and T. N. Demayo, “Wavelength and intensity stabilisation of 980 nm diode lasers coupled to fibre Bragg gratings,” *Electron. Lett.*, vol. 30, no. 25, pp. 2147–2149, 1994.

[29] R. Slavik, I. Castonguay, S. LaRochelle, and S. Doucet, “Short multiwavelength fiber laser made of a large-band distributed Fabry-Pérot structure,” *IEEE Photon. Technol. Lett.*, vol. 16, no. 4, pp. 1017 –1019, Apr. 2004.

[30] I. Baumann, J. Seifert, W. Nowak, and M. Sauer, “Compact all-fiber add-drop-multiplexer using fiber Bragg gratings,” *IEEE Photon. Technol. Lett.*, vol. 8, no. 10, pp. 1331–1333, 1996.

[31] C. R. Giles, “Lightwave applications of fiber Bragg gratings,” *J. Lightwave Technol.*, vol. 15, no. 8, pp. 1391–1404, 1997.

[32] K. Ikeda, M. Nezhad, and Y. Fainman, “Wavelength selective coupler with vertical gratings on silicon chip,” *Appl. Phys. Lett.*, vol. 92, no. 20, pp. 201111–3, Mai 2008.

[33] D. T. H. Tan, “Optical pulse compression on a silicon chip—Effect of group velocity dispersion and free carriers,” *Appl. Phys. Lett.*, vol. 101, no. 21, p. 211112, 2012.

[34] W. Shi, X. Wang, C. Lin, H. Yun, Y. Liu, T. Baehr-Jones, M. Hochberg, N. A. F. Jaeger, and L. Chrostowski, “Silicon photonic grating-assisted, contra-directional couplers,” *Opt. Express*, vol. 21, no. 3, pp. 3633–3650, février 2013.

[35] A. D. Simard, Y. Painchaud, and S. LaRochelle, “Characterization of integrated Bragg grating profiles,” in *Bragg Gratings, Photosensitivity, and Poling in Glass Waveguides*, 2012, p. BM3D.7.

[36] R. Soref and B. Bennett, “Electrooptical effects in silicon,” *IEEE J. Quantum Electron.*, vol. 23, no. 1, pp. 123–129, 1987.

[37] Q. Fang, J. Song, X. Tu, L. Jia, X. Luo, M. Yu, and G. Lo, “Carrier-induced silicon waveguide Bragg grating filter based on ion implantation,” in *Optical Fiber Communication Conference. Optical Society of America*, 2013, p. OTu3C.8.

[38] T. E. Murphy, J. T. Hastings, and H. I. Smith, “Fabrication and characterization of narrow-band Bragg-reflection filters in silicon-on-insulator ridge waveguides,” *J. Lightwave Technol.*, vol. 19, no. 12, pp. 1938–1942, 2001.

[39] J. T. Hastings, M. H. Lim, J. G. Goodberlet, and H. I. Smith, “Optical waveguides with apodized sidewall gratings via spatial-phase-locked electron-beam lithography,” in *Papers from the 46th International Conference on Electron, Ion, and Photon Beam Technology and Nanofabrication*, Anaheim, California (USA), 2002, vol. 20, pp. 2753–2757.

[40] D. T. H. Tan, K. Ikeda, and Y. Fainman, “Cladding-modulated Bragg gratings in silicon waveguides,” *Opt. Lett.*, vol. 34, no. 9, pp. 1357–1359, Mai 2009.

[41] A. D. Simard, N. Ayotte, Y. Painchaud, S. Bedard, and S. LaRochelle, “Impact of sidewall roughness on integrated Bragg gratings,” *J. Lightwave Technol.*, vol. 29, no. 24, pp. 3693–3704, Dec. 2011.

[42] A. D. Simard, G. Beaudin, V. Aimez, Y. Painchaud, and S. LaRochelle, “Characterization and reduction of spectral distortions in silicon-on-insulator integrated Bragg gratings,” *Opt. Express*, vol. 21, no. 20, pp. 23145–23159, Oct. 2013.

[43] I. Giuntoni, D. Stolarek, H. Richter, S. Marschmeyer, J. Bauer, A. Gajda, J. Bruns, B. Tillack, K. Petermann, and L. Zimmermann, “Deep-UV technology for the fabrication of Bragg gratings on SOI rib waveguides,” *IEEE Photon. Technol. Lett.*, vol. 21, no. 24, pp. 1894–1896, 2009.

[44] I. Giuntoni, A. Gajda, M. Krause, R. Steingrüber, J. Bruns, and K. Petermann, “Tunable Bragg reflectors on silicon-on-insulator rib waveguides,” *Opt. Express*, vol. 17, no. 21, pp. 18518–18524, Oct. 2009.

[45] S. Honda, Z. Wu, J. Matsui, K. Utaka, T. Edura, M. Tokuda, K. Tsutsui, and Y. Wada, “Largely-tunable wideband Bragg gratings fabricated on SOI rib waveguides employed by deep-RIE,” *Electron. Lett.*, vol. 43, no. 11, pp. 630 –631, 2007.

[46] Guomin Jiang, Ruiyi Chen, Qiang Zhou, Jianyi Yang, Minghua Wang, and Xiaoqing Jiang, “Slab-modulated sidewall Bragg gratings in silicon-on-insulator ridge waveguides,” *IEEE Photon. Technol. Lett.*, vol. 23, no. 1, pp. 6–8, Jan. 2011.

[47] X. Wang, W. Shi, H. Yun, S. Grist, N. A. F. Jaeger, and L. Chrostowski, “Narrow-band waveguide Bragg gratings on SOI wafers with CMOS-compatible fabrication process,” *Opt. Express*, vol. 20, no. 14, p. 15547, Jun. 2012.

[48] C. Greiner, T. W. Mossberg, and D. Iazikov, “Bandpass engineering of lithographically scribed channel-waveguide Bragg gratings,” *Opt. Lett.*, vol. 29, no. 8, pp. 806–808, Avril 2004.

[49] D. Wiesmann, C. David, R. Germann, D. Emi, and G. L. Bona, “Apodized surface-corrugated gratings with varying duty cycles,” *IEEE Photon. Technol. Lett.*, vol. 12, no. 6, pp. 639–641, 2000.

[50] M. J. Strain and M. Sorel, “Integrated III–V Bragg gratings for arbitrary control over chirp and coupling coefficient,” *IEEE Photon. Technol. Lett.*, vol. 20, no. 22, pp. 1863–1865, 2008.

[51] V. Veerasubramanian, G. Beaudin, A. Giguere, B. Le Drogoff, V. Aimez, and A. G. Kirk, “Design and demonstration of apodized comb filters on SOI,” *IEEE Photonics Journal*, vol. 4, no. 4, pp. 1133–1139, Aug. 2012.

[52] W. Bogaerts, R. Baets, P. Dumon, V. Wiaux, S. Beckx, D. Taillaert, B. Luyssaert, J. Van Campenhout, P. Bienstman, and D. Van Thourhout, “Nanophotonic waveguides in silicon-on-insulator fabricated with CMOS technology,” *J. Lightwave Technol.*, vol. 23, no. 1, pp. 401–412, 2005.

[53] S. K. Selvaraja, W. Bogaerts, P. Dumon, D. Van Thourhout, and R. Baets, “Subnanometer linewidth uniformity in silicon nanophotonic waveguide devices using CMOS fabrication technology,” *IEEE J. Sel. Top. Quantum Electron.*, vol. 16, no. 1, pp. 316–324, 2010.

[54] Y. Painchaud, M. Poulin, C. Latrasse, N. Ayotte, M.-J. Picard, and M. Morin, “Bragg grating notch filters in silicon-on-insulator waveguides,” in *Bragg Gratings, Photosensitivity, and Poling in Glass Waveguides*, 2012, p. BW2E.3.

[55] K. A. Rutkowska, D. Duchesne, M. J. Strain, R. Morandotti, M. Sorel, and J. Azaña, “Ultrafast all-optical temporal differentiators based on CMOS-compatible integrated-waveguide Bragg gratings,” *Opt. Express*, vol. 19, no. 20, pp. 19514–19522, Sep. 2011.

[56] T. Chu, H. Yamada, S. Ishida, and Y. Arakawa, “Tunable optical add-drop multiplexer based on silicon photonic wire waveguides,” in *Optical Fiber Communication Conference. Optical Society of America*, 2006, pp. 1409–1411.

[57] W. Shi, X. Wang, C. Lin, H. Yun, Y. Liu, T. Baehr-Jones, M. Hochberg, N. A. F. Jaeger, and L. Chrostowski, “Electrically tunable resonant filters in phase-shifted contra-directional couplers,” in *2012 IEEE 9th International Conference on Group IV Photonics (GFP)*, 2012, pp. 78 –80.

[58] D. Taillaert, W. Bogaerts, P. Bienstman, T. F. Krauss, P. Van Daele, I. Moerman, S. Verstuyft, K. De Mesel, and R. Baets, “An out-of-plane grating coupler for efficient butt-coupling between compact planar waveguides and single-mode fibers,” *IEEE J. Quantum Electron.*, vol. 38, no. 7, pp. 949–955, 2002.

[59] F. Van Laere, T. Claes, J. Schrauwen, S. Scheerlinck, W. Bogaerts, D. Taillaert, L. O’Faolain, D. Van Thourhout, and R. Baets, “Compact focusing grating couplers for silicon-on-insulator integrated circuits,” *IEEE Photon. Technol. Lett.*, vol. 19, no. 23, pp. 1919–1921, 2007.

[60] X. Wang, W. Shi, M. Hochberg, K. Adam, E. Schelew, J. F. Young, N. A. F. Jaeger, and L. Chrostowski, “Lithography simulation for the fabrication of silicon photonic devices with deep-ultraviolet lithography,” in *9th International Conference on Group IV Photonics (GFP)*, 2012, pp. 288 –290.

[61] J. E. Sipe, L. Poladian, and C. M. de Sterke, “Propagation through nonuniform grating structures,” *J. Opt. Soc. Am. A:*, vol. 11, no. 4, pp. 1307–1320, Avril 1994.

[62] H. Kogelnik and C. V. Shank, “Coupled-wave theory of distributed feedback lasers,” *J. Appl. Phys.*, vol. 43, no. 5, pp. 2327–2335, Mai 1972.

[63] A. Yariv, “Coupled-mode theory for guided-wave optics,” *IEEE J. Quantum Electron.*, vol. 9, no. 9, pp. 919–933, 1973.

[64] J. Skaar, “Synthesis and characterization of fiber Bragg gratings,” Norwegian Univ. of Sci. Technol., 2000.

[65] T. Tamir and E. Garmire, *Integrated optics*. Berlin; New York: Springer-Verlag, 1979.

[66] L. Poladian, “Graphical and WKB analysis of nonuniform Bragg gratings,” *Phys. Rev. E*, vol. 48, no. 6, p. 4758, Décembre 1993.

[67] T. Erdogan, “Fiber grating spectra,” *J. Lightwave Technol.*, vol. 15, no. 8, pp. 1277–1294, 1997.

[68] H. Kogelnik, “Filter response of nonuniform almost-periodic structures,” *Bell Syst. Tech. J*, vol. 55, no. 1, pp. 109–126, 1976.

[69] L. A. Weller-Brophy and D. G. Hall, “Analysis of waveguide gratings: a comparison of the results of Rouard’s method and coupled-mode theory,” *JOSA A*, vol. 4, no. 1, pp. 60–65, 1987.

[70] Z. Wang, “Improved Rouard’s method for fiber and waveguide gratings,” *Optics Communications*, vol. 177, no. 1–6, pp. 245–250, Apr. 2000.

[71] S. E. Miller, “Coupled wave theory and waveguide applications,” *Bell Syst. Tech. J*, vol. 33, no. 3, p. D11, 1954.

[72] M. D. Greenberg, *Advanced engineering mathematics*, vol. 2. Prentice Hall New York, 1998.

[73] A. Rosenthal and M. Horowitz, “Inverse scattering algorithm for reconstructing strongly reflecting fiber Bragg gratings,” *IEEE J. Quantum Electron.*, vol. 39, no. 8, pp. 1018– 1026, Aug. 2003.

[74] G. H. Song, “Theory of symmetry in optical filter responses,” *J. Opt. Soc. Am. A*, vol. 11, no. 7, pp. 2027–2037, juillet 1994.

[75] L. Poladian, “Resonance mode expansions and exact solutions for nonuniform gratings,” *Phys. Rev. E*, vol. 54, no. 3, p. 2963, 1996.

[76] J. Skaar, Ligang Wang, and T. Erdogan, “On the synthesis of fiber Bragg gratings by layer peeling,” *IEEE J. Quantum Electron.*, vol. 37, no. 2, pp. 165–173, 2001.

[77] M. J. Strain, M. Gnan, G. Bellanca, R. M. De La Rue, and M. Sorel, “Retrieval of Bragg grating transmission spectra by post-process removal of spurious Fabry-Perot oscillations,” *Opt. Express*, vol. 17, no. 16, pp. 13493–13501, 2009.

[78] F. Morichetti, A. Canciamilla, C. Ferrari, M. Torregiani, A. Melloni, and M. Martinelli, “Roughness induced backscattering in optical silicon waveguides,” *Phys. Rev. Lett.*, vol. 104, no. 3, p. 033902, Jan. 2010.

[79] C. A. Barrios, “Electrooptic modulation of multisilicon-on-insulator photonic wires,” *J. Lightwave Technol.*, vol. 24, no. 5, p. 2146, 2006.

[80] F. Gan and F. X. Kartner, “High-speed silicon electrooptic modulator design,” *IEEE Photon. Technol. Lett.*, vol. 17, no. 5, pp. 1007–1009, May 2005.

[81] A. H. Atabaki, M. Soltani,, S. Yegnanarayanan, A. A. Eftekhar, and A. Adibi, “Optimization of metallic micro-heaters for reconfigurable silicon photonics,” in *The Conference on Lasers and Electro-Optics (CLEO) and The International Quantum Electronics Conference (IQEC)*, 2009, p. CThB4.

[82] M. W. Pruessner, T. H. Stievater, M. S. Ferraro, and W. S. Rabinovich, “Thermo-optic tuning and switching in SOI waveguide Fabry-Perot microcavities,” *Opt. Express*, vol. 15, no. 12, pp. 7557–7563, 2007.

[83] A. D. Simard, Y. Painchaud, and S. LaRochelle, “Integrated Bragg gratings in curved waveguides,” in *the 23rd Annual Meeting of the Photonics Society Denver, USA*, 2010, p. ThU3.

[84] S. Zamek, D. T. . Tan, M. Khajavikhan, M. Ayache, M. P. Nezhad, and Y. Fainman, “Compact chip-scale filter based on curved waveguide Bragg gratings,” *Opt. Lett.*, vol. 35, no. 20, pp. 3477–3479, 2010.

[85] K. K. Lee, D. R. Lim, H.-C. Luan, A. Agarwal, J. Foresi, and L. C. Kimerling, “Effect of size and roughness on light transmission in a Si/SiO2 waveguide: Experiments and model,” *Appl. Phys. Lett.*, vol. 77, no. 11, p. 1617, 2000.

[86] T. Barwicz and H. A. Haus, “Three-dimensional analysis of scattering losses due to sidewall roughness in microphotonic waveguides,” *J. Lightwave Technol.*, vol. 23, no. 9, p. 2719, 2005.

[87] C. Ciminelli, F. Dell’Olio, V. Passaro, and M. Armenise, “Fully three-dimensional accurate modeling of scattering loss in optical waveguides,” *Optical and Quantum Electronics*, vol. 41, no. 4, pp. 285–298, Mar. 2009.

[88] K. K. Lee, D. R. Lim, L. C. Kimerling, J. Shin, and F. Cerrina, “Fabrication of ultralow-loss Si/SiO2 waveguides by roughness reduction,” *Opt. Lett.*, vol. 26, no. 23, pp. 1888–1890, Décembre 2001.

[89] S. Sardo, F. Giacometti, S. Doneda, U. Colombo, M. D. Muri, A. Donghi, R. Morson, G. Mutinati, A. Nottola, M. Gentili, and M. C. Ubaldi, “Line edge roughness (LER) reduction strategy for SOI waveguides fabrication,” *Microelectron. Eng.*, vol. 85, no. 5–6, pp. 1210–1213, 2008.

[90] L. Poladian, F. Ladouceur, and P. D. Miller, “Effects of surface roughness on gratings,” *JOSA B*, vol. 14, no. 6, pp. 1339–1344, 1997.

[91] K. P. Yap, J. Lapointe, B. Lamontagne, A. Delage, A. Bogdanov, S. Janz, and B. Syrett, “SOI waveguide fabrication process development using star coupler scattering loss measurements,” in *Proceedings of SPIE*, Canberra, ACT, Australia, 2007, pp. 680014–680014–12.

[92] F. Ladouceur, J. D. Love, and T. J. Senden, “Measurement of surface roughness in buried channel waveguides,” *Electron. Lett.*, vol. 28, no. 14, pp. 1321–1322, 1992.

[93] K. Dossou and M. Fontaine, “A high order isoparametric finite element method for the computation of waveguide modes,” *Comput. Meth. Appl. Mech. Eng.*, vol. 194, no. 6–8, pp. 837–858, 2005.

[94] P. Pieter Dumon, “Ultra-compact integrated optical filters in silicon-on-insulator by means of wafer-scale technology,” Thesis Pieter Dumon, 2006.

[95] G. P. Patsis, V. Constantoudis, A. Tserepi, E. Gogolides, and G. Grozev, “Quantification of line-edge roughness of photoresists. I. A comparison between off-line and on-line analysis of top-down scanning electron microscopy images,” *J. Vac. Sci. Technol. B*, vol. 21, no. 3, pp. 1008–1018, Mai 2003.

[96] V. Constantoudis, G. P. Patsis, and E. Gogolides, “Photoresist line-edge roughness analysis using scaling concepts,” *J. Microlithogr. Microfabrication, Microsyst.*, vol. 3, no. 3, pp. 429–435, Juillet 2004.

[97] P. P. Naulleau and J. P. Cain, “Experimental and model-based study of the robustness of line-edge roughness metric extraction in the presence of noise,” *J. Vac. Sci. Technol., B*, vol. 25, no. 5, pp. 1647–1657, 2007.

[98] S. Spector, M. W. Geis, D. Lennon, R. C. Williamson, and T. M. Lyszczarz, “Hybrid multi-mode/single-mode waveguides for low loss,” *in Integrated Photonics Research, Optical Society of America*, 2004.

[99] M. A. Webster, R. M. Pafchek, G. Sukumaran, and T. L. Koch, “Low-loss quasi-planar ridge waveguides formed on thin silicon-on-insulator,” *Appl. Phys. Lett.*, vol. 87, no. 23, p. 231108, 2005.

[100] R. Kashyap, *Fiber Bragg gratings*. Academic Press, 1999.

[101] A. D. Simard, Y. Painchaud, and S. LaRochelle, “Integrated Bragg gratings in spiral waveguides,” *Opt. Express*, vol. 21, no. 7, pp. 8953–8963, avril 2013.

[102] A. D. Simard, N. Belhadj, Y. Painchaud, and S. LaRochelle, “Apodized silicon-on-insulator Bragg gratings,” *IEEE Photon. Technol. Lett.*, vol. 24, no. 12, pp. 1033 –1035, Jun. 2012.

[103] M. A. Schneider and S. Mookherjea, “Modeling transmission time of silicon nanophotonic waveguides,” *IEEE Photon. Technol. Lett.*, vol. 24, no. 16, pp. 1418 –1420, Aug. 2012.

[104] K. P. Yap, A. Delâge, B. Lamontagne, S. Janz, D.-X. Xu, J. Lapointe, P. Waldron, J. Schmid, P. Chow-Chong, E. Post, and B. Syrett, “Scattering loss measurement of SOI waveguides using 5X17 integrated optical star coupler,” *Integrated Optoelectronic Devices, International Society for Optics and Photonics*, pp. 64770J–1 – 64770J–11, février 2007.

[105] W. A. Zortman, M. R. Watts, and D. C. Trotter, “Determination of wafer and process induced resonant frequency variation in silicon microdisk-resonators,” in *Integrated Photonics and Nanophotonics Research and Applications*, 2009, p. IMC5.

[106] D. K. Sparacin, S. J. Spector, and L. C. Kimerling, “Silicon waveguide sidewall smoothing by wet chemical oxidation,” *J. Lightwave Technol.*, vol. 23, no. 8, p. 2455, 2005.

[107] J. Cai, Y. Wang, Y. Ishikawa, Y. Yamashita, Y. Kamiura, and K. Wada, “Hydrogen plasma treatment for Si waveguide smoothing,” in *8th IEEE International Conference on Group IV Photonics*, London, United Kingdom, 2011, pp. 95–97.

[108] S. K. Selvaraja, E. Rosseel, L. Fernandez, M. Tabat, W. Bogaerts, J. Hautala, and P. Absil, “SOI thickness uniformity improvement using corrective etching for silicon nano-photonic device,” in *in 8th IEEE International Conference on Group IV Photonics London, United Kingdom*, 2011, pp. 71–73.

[109] K. P. Yap, A. Delage, J. Lapointe, B. Lamontagne, J. H. Schmid, P. Waldron, B. A. Syrett, and S. Janz, “Correlation of scattering loss, sidewall roughness and waveguide width in silicon-on-insulator (SOI) ridge waveguides,” *J. Lightwave Technol.*, vol. 27, no. 18, pp. 3999 –4008, Sep. 2009.

[110] V. Constantoudis, G. P. Patsis, A. Tserepi, and E. Gogolides, “Quantification of line-edge roughness of photoresists. II. Scaling and fractal analysis and the best roughness descriptors,” *J. Vac. Sci. Technol. B*, vol. 21, no. 3, pp. 1019–1026, Mai 2003.

[111] T. Barwicz and H. I. Smith, “Evolution of line-edge roughness during fabrication of high-index-contrast microphotonic devices,” *J. Vac. Sci. Technol., B*, vol. 21, no. 6, pp. 2892–2896, 2003.

[112] V. Eswaran and S. B. Pope, “Direct numerical simulations of the turbulent mixing of a passive scalar,” *Phys. Fluids*, vol. 31, no. 3, pp. 506–520, Mar. 1988.

[113] S. B. Pope, *Turbulent flows*. Cambridge university press, 2000.

[114] P. L. O’Neill, D. Nicolaides, D. Honnery, and J. Soria, “Autocorrelation functions and the determination of integral length with reference to experimental and numerical data,” in *15th Australasian fluid mechanics conference, Sydney, Australia*, 2004.

[115] C. M. Greiner, D. Iazikov, T. W. Mossberg, B. McGinnis, R. Narevich, and A. Ticknor, “Engineering the spectral response of waveguide Bragg gratings patterned by deep ultraviolet nanolithography,” in *Integrated Optics: Devices, Materials, and Technologies XII*, San Jose, CA, USA, 2008, vol. 6896, p. 68960G–4.

[116] M. Poulin, A. Doyle, F. Trépanier, A. Mailloux, M. Guy, M. Morin, and J. Rothenberg, “Apodization of 25 and 50 GHz low dispersion FBG WDM filters by phase modulation coding of a phase mask,” in *Optical Fiber Communication Conference*, 2004.

[117] W. A. Zortman, D. C. Trotter, and M. R. Watts, “Silicon photonics manufacturing,” *Opt. Express*, vol. 18, no. 23, pp. 23598–23607, Nov. 2010.

[118] W. Bogaerts, P. Dumon, D. V. Thourhout, D. Taillaert, P. Jaenen, J. Wouters, S. Beckx, V. Wiaux, and R. G. Baets, “Compact wavelength-selective functions in silicon-on-insulator photonic wires,” *IEEE J. Sel. Top. Quantum Electron.*, vol. 12, no. 6, pp. 1394–1401, 2006.

[119] C. Koos, C. G. Poulton, L. Zimmermann, L. Jacome, J. Leuthold, and W. Freude, “Ideal bend contour trajectories for single-mode operation of low loss overmoded waveguides,” *IEEE Photon. Technol. Lett.*, vol. 19, no. 11, pp. 819–821, Jun. 2007.

[120] M. Heiblum and J. Harris, “Analysis of curved optical waveguides by conformal transformation,” *IEEE J. Quantum Electron.*, vol. 11, no. 2, pp. 75–83, 1975.

[121] T. E. Murphy, “Integrated optical grating-based matched filters for fiber-optic communications,” Massachusetts Institute of Technology, 1996.

[122] W. W. Lui, C.-L. Xu, T. Hirono, K. Yokoyama, and W.-P. Huang, “Full-vectorial wave propagation in semiconductor optical bending waveguides and equivalent straight waveguide approximations,” *J. Lightwave Technol.*, vol. 16, no. 5, p. 910, Mai 1998.

[123] S. S. A. Obayya, B. M. A. Rahman, and K. T. V. Grattan, “Full vectorial finite element modal solution of curved optical waveguides,” *Laser Phys. Lett.*, vol. 2, no. 3, pp. 131–136, 2005.

[124] B. M. A. Rahman, D. M. H. Leung, S. S. A. Obayya, and K. T. V. Grattan, “Numerical analysis of bent waveguides: bending loss, transmission loss, mode coupling, and polarization coupling,” *Appl. Opt.*, vol. 47, no. 16, pp. 2961–2970, Juin 2008.

[125] K. Kakihara, N. Kono, K. Saitoh, and M. Koshiba, “Full-vectorial finite element method in a cylindrical coordinate system for loss analysis of photonic wire bends,” *Opt. Express*, vol. 14, no. 23, pp. 11128–11141, Nov. 2006.

[126] H. Yamada, K. Takada, Y. Inoue, Y. Hibino, and M. Horiguchi, “10 GHz-spaced arrayed-waveguide grating multiplexer with phase-error-compensating thin-film heaters,” *Electron. Lett.*, vol. 31, no. 5, pp. 360–361, 1995.

[127] H. Yamada, K. Takada, and S. Mitachi, “Crosstalk reduction in a 10-GHz spacing arrayed-waveguide grating by phase-error compensation,” *J. Lightwave Technol.*, vol. 16, no. 3, p. 364, Mar. 1998.

[128] A. Canciamilla, S. Grillanda, C. Ferrari, F. Morichetti, A. Melloni, P. Velha, M. Sorel, J. Hu, J. Musgraves, K. Richardson, and others, “Visible light trimming of chalcogenide-assisted photonic integrated circuits,” in *Group IV Photonics (GFP), 2011 8th IEEE International Conference on*, 2011, pp. 56–58.

Appendix A: Coupled-Mode Equation Derivation

In this appendix, the derivation of the general coupled mode equations from the Maxwell equations is done. The final equation of this appendix is the starting point of section 1.3. The derivation closely matches the one presented by Kogelnick in [65].

A.1 – Simplification of Maxwell equations

Maxwell equations are

Faraday's law of electromagnetic induction	$\nabla \times \vec{E} = -\frac{\partial \vec{B}}{\partial t}$	(A.1)
Ampère's circuital law	$\nabla \times \vec{H} = \vec{J}_f + \frac{\partial \vec{D}}{\partial t}$	(A.2)
Gauss's law	$\nabla \cdot \vec{D} = \rho_f$	(A.3)
Gauss's law for magnetism	$\nabla \cdot \vec{B} = 0$	(A.4)

Where $\vec{E}$ is the electric field, $\vec{B}$ is the magnetic induction, $\vec{H}$ is the magnetic field, $\vec{D}$ is the electric displacement field, $\vec{J}_f$ is the free current density and ρ_f is the free charge density. Since no magnetic material is CMOS compatible, we can write the following constitutive equation:

$$\begin{aligned} \vec{B} &= \mu_0 \vec{H} \\ \vec{D} &= \varepsilon \vec{E} + \vec{P} \end{aligned} \tag{A.5}$$

where μ_0 is the free space permeability, ε is the permittivity and $\vec{P}$ is the polarisation field. Furthermore, since this thesis focus on passive devices, we consider an intrinsic silicon layer without the presence of current and free charges (i.e. $\vec{J}_f = 0$ and $\rho_f = 0$). Finally, let's consider a stationary solution, which can be written in the form

$$\begin{aligned} \vec{E}(t,x,y,z) &= \vec{E}(x,y,z)e^{-i\omega t} \\ \vec{H}(t,x,y,z) &= \vec{H}(x,y,z)e^{-i\omega t} \end{aligned} \tag{A.6}$$

where ω is the optical angular frequency. As a result, Maxwell's equations can be simplify to

$$\nabla\times\vec{E}(x,y,z)=i\omega\mu_0\vec{H}(x,y,z) \tag{A.7}$$

$$\nabla\times\vec{H}(x,y,z)=-i\omega\varepsilon\vec{E}(x,y,z)-i\omega\vec{P}(x,y,z) \tag{A.8}$$

A.2 – Excitation of modes

In this subsection, the simplified Maxwell Eqs. ((A.7) and (A.8)) are going to be used to describe the fields obtained from exciting sources. Later on, the resulting equations are going to be used to model coupling between modes of interest. If we consider two set of induced polarisation (labeled 1 and 2) and their associated field and we subtract the dot product of $\vec{H}_2^*$ with (A.7)$_1$ to the dot product of $\vec{E}_1$ with the complex conjugate of (A.8)$_2$, we obtain

$$\vec{H}_2^*\cdot\nabla\times\vec{E}_1-\vec{E}_1\cdot\nabla\times\vec{H}_2^*=i\omega\mu_0\vec{H}_1\cdot\vec{H}_2^*-\left(i\omega\varepsilon\vec{E}_1\cdot\vec{E}_2^*+i\omega\vec{E}_1\cdot\vec{P}_2^*\right) \tag{A.9}$$

Using $\nabla\cdot\left(a\times b\right)=b\cdot\left(\nabla\times a\right)-a\cdot\left(\nabla\times b\right)$, Eq. (A.9) gives

$$\nabla\cdot\left(\vec{E}_1\times\vec{H}_2^*\right)=i\omega\mu_0\vec{H}_1\cdot\vec{H}_2^*-i\omega\varepsilon\vec{E}_1\cdot\vec{E}_2^*-i\omega\vec{E}_1\cdot\vec{P}_2^* \tag{A.10}$$

Similarly, subtracting the dot product of $\vec{H}_1^*$ with the complex conjugate of (A.7)$_2$ to the dot product of $\vec{E}_2^*$ with (A.8)$_1$ gives

$$\begin{aligned}\nabla\cdot\left(\vec{E}_2^*\times\vec{H}_1\right)&=\vec{H}_1\cdot\nabla\times\vec{E}_2^*-\vec{E}_2^*\cdot\nabla\times\vec{H}_1\\&=-i\omega\mu_0\vec{H}_1\cdot\vec{H}_2^*+\left(i\omega\varepsilon\vec{E}_1\cdot\vec{E}_2^*+i\omega\vec{E}_2^*\cdot\vec{P}_1\right)\end{aligned}. \tag{A.11}$$

Summing Eq. (A.10) and (A.11) gives

$$\nabla\cdot\left(\vec{E}_1\times\vec{H}_2^*+\vec{E}_2^*\times\vec{H}_1\right)=i\omega\vec{E}_2^*\cdot\vec{P}_1-i\omega\vec{E}_1\cdot\vec{P}_2^* \tag{A.12}$$

Now, let's consider that the excitation source is coming from the field "1" (i.e. $\vec{P} = \vec{P}_1$ and $\vec{P}_2 = 0$) while the field "2" corresponds to a mode of interest. If we integrate over the guide cross-section, we obtain

$$\int_{-\infty}^{\infty}\int_{-\infty}^{\infty} dxdy\nabla\cdot\left(\vec{E}_1\times\vec{H}_2^* + \vec{E}_2^*\times\vec{H}_1\right) = i\omega\int_{-\infty}^{\infty}\int_{-\infty}^{\infty} dxdy\vec{E}_2^*\cdot\vec{P} \tag{A.13}$$

and if we split the transverse ("t" labels) and longitudinal ("z" labels) components of the left-hand side of (A.13)

$$\begin{aligned}&\int_{-\infty}^{\infty}\int_{-\infty}^{\infty} dxdy\nabla_t\cdot\left(\vec{E}_1\times\vec{H}_2^* + \vec{E}_2^*\times\vec{H}_1\right)_t\\ &+\int_{-\infty}^{\infty}\int_{-\infty}^{\infty} dxdy\frac{\partial}{\partial z}\cdot\left(\vec{E}_{t1}\times\vec{H}_{t2}^* + \vec{E}_{t2}^*\times\vec{H}_{t1}\right)_z = i\omega\int_{-\infty}^{\infty}\int_{-\infty}^{\infty} dxdy\vec{E}_2^*\cdot\vec{P}\end{aligned} \tag{A.14}$$

and use the divergence theorem, given by

$$\int_{-\infty}^{\infty}\int_{-\infty}^{\infty} dxdy\nabla_t\cdot\vec{g} = \oint_c ds\vec{g}\cdot\vec{a}_t \tag{A.15}$$

to show that the first term of Eq. (A.14) is null, we obtain

$$\int_{-\infty}^{\infty}\int_{-\infty}^{\infty} dxdy\frac{\partial}{\partial z}\cdot\left(\vec{E}_{t1}\times\vec{H}_{t2}^* + \vec{E}_{t2}^*\times\vec{H}_{t1}\right)_z = i\omega\int_{-\infty}^{\infty}\int_{-\infty}^{\infty} dxdy\vec{E}_2^*\cdot\vec{P}. \tag{A.16}$$

Since the waveguide modes form an orthogonal basis, it is possible to expend the field "1" in terms of the waveguide co-propagating (*a*) and contra-propagating (*b*) modes such as

$$\vec{E}_{1t} = \sum\left(a_v + b_v\right)\vec{E}_{tv} \qquad \vec{H}_{1t} = \sum\left(a_v - b_v\right)\vec{H}_{tv} \tag{A.17}$$

where a_v and b_v are z varying amplitude. Later on, the mode of interest is going to be selected. When the second field has a forward running mode, expressed by

$$\vec{E}_2 = \vec{E}_\mu e^{i\beta z} \qquad \vec{H}_2 = \vec{H}_\mu e^{i\beta z}, \tag{A.18}$$

inserting (A.17) and (A.18) into the left-hand side of (A.16) gives

$$
\begin{aligned}
&\int_{-\infty}^{\infty}\int_{-\infty}^{\infty} dxdy\frac{\partial}{\partial z}\cdot\left(\vec{E}_1\times\vec{H}_2^{*}+\vec{E}_2^{*}\times\vec{H}_1\right)_z \\
&=\int_{-\infty}^{\infty}\int_{-\infty}^{\infty} dxdy\frac{\partial}{\partial z}\cdot\left(\sum\left(a_\nu+b_\nu\right)\vec{E}_{t\nu}\times\vec{H}_\mu^{*}e^{-i\beta z}+\vec{E}_\mu^{*}e^{-i\beta z}\times\sum\left(a_\nu-b_\nu\right)\vec{H}_{t\nu}\right)_z \\
&=\int_{-\infty}^{\infty}\int_{-\infty}^{\infty} dxdy\begin{pmatrix} e^{-i\beta z}\sum\left(a_\nu^{'}+b_\nu^{'}\right)\vec{E}_{t\nu}\times\vec{H}_\mu^{*}-i\beta e^{-i\beta z}\sum\left(a_\nu+b_\nu\right)\vec{E}_{t\nu}\times\vec{H}_\mu^{*} \\ +e^{-i\beta z}\vec{E}_\mu^{*}\times\sum\left(a_\nu^{'}-b_\nu^{'}\right)\vec{H}_{t\nu}-i\beta e^{-i\beta z}\vec{E}_\mu^{*}\times\sum\left(a_\nu-b_\nu\right)\vec{H}_{t\nu} \end{pmatrix} \\
&=e^{-i\beta z}\sum\left(a_\nu^{'}+b_\nu^{'}\right)\int_{-\infty}^{\infty}\int_{-\infty}^{\infty} dxdy\vec{E}_{t\nu}\times\vec{H}_\mu^{*}-i\beta e^{-i\beta z}\sum\left(a_\nu+b_\nu\right)\int_{-\infty}^{\infty}\int_{-\infty}^{\infty} dxdy\vec{E}_{t\nu}\times\vec{H}_\mu^{*} \\
&+e^{i\beta z}\sum\left(a_\nu^{'}-b_\nu^{'}\right)\int_{-\infty}^{\infty}\int_{-\infty}^{\infty} dxdy\vec{E}_\mu^{*}\times\vec{H}_{t\nu}-i\beta e^{-i\beta z}\sum\left(a_\nu-b_\nu\right)\int_{-\infty}^{\infty}\int_{-\infty}^{\infty} dxdy\vec{E}_\mu^{*}\times\vec{H}_{t\nu}
\end{aligned}
$$

The orthogonally relation allows us to ignore every modes where μ ≠ ν. As a result, we have

$$
\begin{aligned}
&\int_{-\infty}^{\infty}\int_{-\infty}^{\infty} dxdy\frac{\partial}{\partial z}\cdot\left(\vec{E}_1\times\vec{H}_2^{*}+\vec{E}_2^{*}\times\vec{H}_1\right)_z \\
&=\frac{1}{2}e^{-i\beta z}\left(a_\mu^{'}+b_\mu^{'}\right)-\frac{1}{2}i\beta e^{-i\beta z}\left(a_\mu+b_\mu\right) \\
&+\frac{1}{2}e^{-i\beta z}\left(a_\mu^{'}-b_\mu^{'}\right)-\frac{1}{2}i\beta e^{-i\beta z}\left(a_\mu-a_\mu\right). \\
&=a_\mu^{'}e^{-i\beta z}-a_\mu i\beta e^{-i\beta z} \\
&=\frac{\partial A_\mu}{\partial z}
\end{aligned}
$$

The last equation is obtained with this following change of variable:

$$
a=A\exp\left(i\beta z\right)\qquad b=B\exp\left(-i\beta z\right) \tag{A.19}
$$

which modify the field of Eq. (A.17) to

$$
\begin{aligned}
\vec{E}_{1t}&=\sum\left(A_\nu\exp\left(i\beta_\nu z\right)+B_\nu\exp\left(-i\beta z\right)\right)\vec{E}_{t\nu} \\
\vec{H}_{1t}&=\sum\left(A_\nu\exp\left(i\beta_\nu z\right)-B_\nu\exp\left(-i\beta_\nu z\right)\right)\vec{H}_{t\nu}
\end{aligned} \tag{A.20}
$$

To sum up, inserting (A.20) and (A.18) into (A.16) gives

$$
\frac{\partial A_\mu}{\partial z}=i\omega\int_{-\infty}^{\infty}\int_{-\infty}^{\infty} dxdy\vec{E}_\mu^{*}e^{-i\beta_\mu z}\cdot\vec{P}\,. \tag{A.21}
$$

Similarly, when the second field has a backward running mode, expressed by

$$\vec{E}_{2t} = \vec{E}_{-\mu} e^{-i\beta z} = \vec{E}_{\mu} e^{-i\beta z} \qquad \vec{H}_{2t} = \vec{H}_{-\mu} e^{-i\beta z} = -\vec{H}_{\mu} e^{-i\beta z}\ , \tag{A.22}$$

inserting (A.20) and (A.22) into the (A.16) gives

$$\frac{\partial B_{\mu}}{\partial z} = -i\omega \int_{-\infty}^{\infty} \int_{-\infty}^{\infty} dxdy \vec{E}^{*}_{-\mu} e^{i\beta_{\mu} z} \cdot \vec{P}\ . \tag{A.23}$$

Eqs. (A.21) and (A.23) show the change of amplitude experienced by the mode μ resulting of an excitation described by the polarisation field. Those equations are the basis of many coupled-modes physical problems.

A.3 – Calculation of the polarisation

The specific problem of interest for this thesis concerns a periodic perturbation of the waveguide structure. At this point, more attention must be accorded to the polarisation, related to the electrical field by

$$\vec{P} = \Delta\varepsilon \vec{E}\ . \tag{A.24}$$

where $\Delta\varepsilon$ is the deviation of the permittivity from the nominal distribution which induces a polarisation. Since the orthogonal relation only apply to the transverse field components, the z-component must be treated with special care. On one hand, considering Eqs. (A.17) and (A.24), the transverse component of the polarisation is given by

$$\vec{P}_t = \Delta\varepsilon \vec{E}_t = \Delta\varepsilon \sum \left(a_v + b_v\right) \vec{E}_{tv}\ . \tag{A.25}$$

On the other hand, the z-component of the polarisation is given by

$$\vec{P}_z = \Delta\varepsilon \vec{E}_z \tag{A.26}$$

To evaluate the z-component of the electric field, Eqs. (A.8) and (A.24) are combined to give

$$\nabla_t \times \vec{H}_t = i\omega \left(\varepsilon + \Delta\varepsilon\right) \vec{E}_z \tag{A.27}$$

As a result,

$$\vec{P}_z = \frac{\Delta\varepsilon}{i\omega\left(\varepsilon + \Delta\varepsilon\right)} \nabla_t \times \vec{H}_t \,. \tag{A.28}$$

Combining the previous result with Eq. (A.17) gives

$$\vec{P}_z = \frac{\Delta\varepsilon}{i\omega\left(\varepsilon + \Delta\varepsilon\right)} \sum \left(a_\nu - b_\nu\right) \nabla_t \times \vec{H}_{t\nu} = \frac{\varepsilon\Delta\varepsilon}{\left(\varepsilon + \Delta\varepsilon\right)} \sum \left(a_\nu - b_\nu\right) \vec{E}_{z\nu} \,. \tag{A.29}$$

A.4 – General coupled-mode equations

In order to obtain the coupled mode equations, the polarisation equations, found in the previous section, must be inserted into Eqs. (A.21) and (A.23), which results in

$$\begin{aligned}
\frac{\partial A_\mu}{\partial z} &= i\omega \int_{-\infty}^{\infty} \int_{-\infty}^{\infty} dxdy e^{-i\beta_\mu z} \cdot \sum \left(\Delta\varepsilon \left(a_\nu + b_\nu\right) \vec{E}_{t\nu} \vec{E}_{t\mu}^* + \frac{\varepsilon\Delta\varepsilon}{\left(\varepsilon + \Delta\varepsilon\right)} \left(a_\nu - b_\nu\right) \vec{E}_{z\nu} \vec{E}_{z\mu}^* \right) \\
\frac{\partial B_\mu}{\partial z} &= -i\omega \int_{-\infty}^{\infty} \int_{-\infty}^{\infty} dxdy e^{i\beta_\mu z} \cdot \sum \left(\Delta\varepsilon \left(a_\nu + b_\nu\right) \vec{E}_{t\nu} \vec{E}_{t\mu}^* - \frac{\varepsilon\Delta\varepsilon}{\left(\varepsilon + \Delta\varepsilon\right)} \left(a_\nu - b_\nu\right) \vec{E}_{z\nu} \vec{E}_{z\mu}^* \right)
\end{aligned} \tag{A.30}$$

where the following symmetry equations has been used to express the mode $\vec{E}_{-\mu}^*$ in terms of $\vec{E}_\mu^*$

$$\begin{array}{ll}
\vec{E}_t\left(z\right) = \vec{E}_t\left(-z\right) & \vec{E}_z\left(z\right) = -\vec{E}_z\left(-z\right) \\
\vec{H}_t\left(z\right) = -\vec{H}_t\left(-z\right) & \vec{H}_z\left(z\right) = \vec{H}_z\left(-z\right)
\end{array} . \tag{A.31}$$

Eq. (A.30) can be simplified by defining a tangential and longitudinal coupling coefficient, such as

$$\begin{aligned}
\mathrm{K}_{\mu\nu}^t &= \frac{\pi}{\lambda} \left[\frac{2c}{n(\lambda)} \int_{-\infty}^{\infty} \int_{-\infty}^{\infty} dxdy \Delta\varepsilon \vec{E}_{t\nu} \vec{E}_{t\mu}^* \right] \\
\mathrm{K}_{\mu\nu}^z &= \frac{\pi}{\lambda} \left[\frac{2c}{n(\lambda)} \int_{-\infty}^{\infty} \int_{-\infty}^{\infty} dxdy \frac{\varepsilon\Delta\varepsilon}{\varepsilon + \Delta\varepsilon} \vec{E}_{z\nu} \vec{E}_{z\mu}^* \right]
\end{aligned} , \tag{A.32}$$

and by using Eq. (A.19) where $n(\lambda)$ is the effective index of the mode. As a result, we obtain

$$\frac{\partial A_\mu}{\partial z} = i\sum\left(\left(A_\nu\, \mathrm{e}^{i\beta_\nu z} + B_\nu\, \mathrm{e}^{-i\beta_\nu z}\right)e^{-i\beta_\mu z}\mathrm{K}^{t}_{\mu\nu} + \left(A_\nu\, \mathrm{e}^{i\beta_\nu z} - B_\nu\, \mathrm{e}^{-i\beta_\nu z}\right)e^{-i\beta_\mu z}\mathrm{K}^{z}_{\mu\nu}\right)$$

$$\frac{\partial B_\mu}{\partial z} = -i\sum\left(\left(A_\nu\, \mathrm{e}^{i\beta_\nu z} + B_\nu\, \mathrm{e}^{-i\beta_\nu z}\right)e^{i\beta_\mu z}\mathrm{K}^{t}_{\mu\nu} - \left(A_\nu\, \mathrm{e}^{i\beta_\nu z} - B_\nu\, \mathrm{e}^{-i\beta_\nu z}\right)e^{i\beta_\mu z}\mathrm{K}^{z}_{\mu\nu}\right)$$

$$\frac{\partial A_\mu}{\partial z} = i\sum\left(A_\nu\left(\mathrm{K}^{t}_{\mu\nu} + \mathrm{K}^{z}_{\mu\nu}\right)e^{-i\left(\beta_\mu - \beta_\nu\right)z} + B_\nu\left(\mathrm{K}^{t}_{\mu\nu} - \mathrm{K}^{z}_{\mu\nu}\right)e^{-i\left(\beta_\mu + \beta_\nu\right)z}\right) \tag{A.33}$$

$$\frac{\partial B_\mu}{\partial z} = -i\sum\left(A_\nu\left(\mathrm{K}^{t}_{\mu\nu} - \mathrm{K}^{z}_{\mu\nu}\right)e^{i\left(\beta_\mu + \beta_\nu\right)z} + B_\nu\left(\mathrm{K}^{t}_{\mu\nu} + \mathrm{K}^{z}_{\mu\nu}\right)e^{i\left(\beta_\mu - \beta_\nu\right)z}\right) \tag{A.34}$$

The previous equations can be used to obtain the change of amplitude of the μ^{th} mode resulting from a permittivity deformation. These equations are the starting point of section 1.3.

Appendix B: Sidewall Roughness Modeling

This appendix has been published with the paper “Impact of Sidewall Roughness on Integrated Bragg Gratings” presented in chapter 2.

B.1 – Detuning distribution autocorelation

To obtain information on *E*(*rr**), which is the mean value of the grating reflection amplitude, we need information on the detuning distribution autocorrelation. The detuning distribution is given by

$$\delta_j\left(z\right)=2\int_0^z dz'\frac{\sqrt{2}\pi C_{SWR}}{n_0\Lambda}\Delta x\left(z'\right)=\frac{2\sqrt{2}\pi C_{SWR}}{n_0\Lambda}\int_0^z dz'\Delta x\left(z'\right),$$

consequently, the autocorrelation function is given by

$$\begin{aligned}R_{\delta_j}(z,\zeta)&=E\left[\delta_j(z)\delta_j(\zeta)\right]\\&=\left(\frac{2\sqrt{2}\pi C_{SWR}}{n_0\Lambda}\right)^2 E\left[\int_0^z dz'\Delta x\left(z'\right)\int_0^\zeta d\zeta'\Delta x\left(\zeta'\right)\right]\\&=\left(\frac{2\sqrt{2}\pi C_{SWR}}{n_0\Lambda}\right)^2\int_0^z dz'\int_0^\zeta d\zeta' E\left[\Delta x\left(\zeta'\right)\Delta x\left(z'\right)\right]\\&=\left(\frac{2\sqrt{2}\pi C_{SWR}\sigma}{n_0\Lambda}\right)^2\underbrace{\int_0^z dz'\int_0^\zeta d\zeta'\exp\left(\frac{-\left|z'-\zeta'\right|}{L_{c,SWR}}\right)}_{I_1}\end{aligned}$$

Considering the case where z < ζ, we obtain

$$\begin{aligned}I_1&=\int_0^z dz'\left[\underbrace{\int_0^{z'} d\zeta'\exp\left(\frac{-\left(z'-\zeta'\right)}{L_{c,SWR}}\right)}_{I_2}+\underbrace{\int_{z'}^\zeta d\zeta'\exp\left(\frac{\left(z'-\zeta'\right)}{L_{c,SWR}}\right)}_{I_3}\right]\\I_2&=\int_0^{z'} d\zeta' e^{-z'/L_{c,SWR}}e^{\zeta'/L_{c,SWR}}=L_c e^{-z'/L_{c,SWR}}\left(e^{z'/L_{c,SWR}}-1\right)\\&=L_c\left(1-e^{-z'/L_{c,SWR}}\right)\end{aligned}$$

$$\begin{aligned} I_3 &= \int_{z'}^{\zeta} d\zeta' e^{z'/L_{c,SWR}} e^{-\zeta'/L_{c,SWR}} = -L_c e^{z'/L_{c,SWR}} \left(e^{-\zeta/L_{c,SWR}} - e^{-z'/L_{c,SWR}} \right) \\ &= -L_c \left(e^{-\zeta/L_{c,SWR}} e^{z'/L_{c,SWR}} - 1 \right) \end{aligned}$$

$$\begin{aligned} I_1 &= \int_0^z dz' \left(I_2 + I_3 \right) \\ &= \int_0^z dz' \left(L_{c,SWR} \left(1 - e^{-z'/L_{c,SWR}} \right) - L_{c,SWR} \left(e^{-\zeta/L_{c,SWR}} e^{z'/L_{c,SWR}} - 1 \right) \right) \\ &= \int_0^z dz' \left(2L_{c,SWR} - L_{c,SWR} e^{-z'/L_{c,SWR}} - L_{c,SWR} e^{-\zeta/L_{c,SWR}} e^{z'/L_{c,SWR}} \right) \\ &= 2L_{c,SWR} \int_0^z dz' - L_{c,SWR} \int_0^z dz' e^{-z'/L_{c,SWR}} - L_{c,SWR} e^{-\zeta/L_{c,SWR}} \int_0^z dz' e^{z'/L_{c,SWR}} \\ &= 2L_{c,SWR} z + L_{c,SWR}^2 \left(e^{-z/L_c} - 1 \right) - L_{c,SWR}^2 e^{-\zeta/L_{c,SWR}} \left(e^{z/L_{c,SWR}} - 1 \right) \end{aligned}$$

If we consider small L_c values, we obtain $I_1 \approx 2L_{c,SWR} z$. Similarly, since the autocorrelation equation is symmetric for z and ζ, when z > ζ $I_1 \approx 2L_{c,SWR} \zeta$ which gives $I_1 \approx 2L_{c,SWR} \min(z, \zeta)$. Consequently, the autocorrelation function is given by

$$R_{\delta_f}(z, \zeta) = 2L_{c,SWR} \left(\frac{2\sqrt{2}\pi C_{SWR}\sigma}{n_0 \Lambda} \right)^2 \min(z, \zeta) \qquad \text{(B.1)}$$

B.2 – Derivation of O(4)

The term involving the fourth order moment of *δ(z)*, *O(*4*)*, is given by

$$O(4) = L_{z_1}^{+} L_{z_2}^{-} L_{z_3}^{+} L_{z_4}^{-} E\left[\delta_f(z_1) \delta_f(z_2) \delta_f(z_3) \delta_f(z_4) \right] \qquad \text{(B.2)}$$

where *L*, the linear operator describing the integral over the grating structure, is given by

$$L_{z_i}^{\pm} = \int_{-L/2}^{L/2} dz_i \kappa e^{\pm 2i\delta z_i} \qquad \text{(B.3)}$$

and where the fourth order moment of *δ(z)* is given by

$$\begin{aligned} E[\ldots] = {} & E\left[\delta_f(z_1) \delta_f(z_2) \right] E\left[\delta_f(z_3) \delta_f(z_4) \right] \\ & + E\left[\delta_f(z_1) \delta_f(z_3) \right] E\left[\delta_f(z_2) \delta_f(z_4) \right] \\ & + E\left[\delta_f(z_1) \delta_f(z_4) \right] E\left[\delta_f(z_2) \delta_f(z_3) \right] \end{aligned} \qquad \text{(B.4)}$$

Using the definition of the detuning distribution autocorrelation given by Eq. (B.1) and integrating over z_1 to z_4, $O(4)$ is given by

$$O(4)=\left(\frac{2\sqrt{2}\pi C_{FEM}\sigma\kappa L}{n_0\Lambda}\right)^4\frac{4L_{c,SWR}^2L^2}{\left(2\delta L\right)^4}\left[2\left(2\cos^2\left(\delta L\right)-\frac{\sin\left(2\delta L\right)}{\delta L}\right)^2\right.$$
$$\left.+\left(\frac{\sin\left(2\delta L\right)}{2\delta L}-1\right)^2+\left(\sin\left(2\delta L\right)+\frac{\cos\left(2\delta L\right)-1}{\delta L}\right)^2\right] \qquad \text{(B.5)}$$